

Short-range sea ice forecast with a regional coupled sea-ice–atmosphere–ocean model

Dissertation

zur Erlangung des Doktorgrades der Naturwissenschaften
an der Fakultät für Mathematik, Informatik und Naturwissenschaften
Fachbereich Geowissenschaften der Universität Hamburg

vorgelegt von

Andrea M. U. Gierisch

aus München

Hamburg, 2014

Tag der Disputation: 30. Januar 2015

Folgende Gutachter empfehlen die Annahme der Dissertation:

Prof. Dr. K. Heinke Schlünzen

Prof. Dr. Lars Kaleschke

Abstract

Connected with climate change, sea ice in the Arctic is reducing. This opens new possibilities for ship traffic, for instance along the Northern Sea Route. For navigators to find the best route through these partly ice-covered waters, forecasts of the sea ice conditions for a few days are required. For this purpose, a short-range sea ice forecast system, HAMMER, is set up and some relevant features are discussed in this thesis.

In order to determine which physical processes have to be considered in a short-range model, the relevance of processes that affect sea ice is investigated. To do so, the impact-timescale is calculated which indicates how quickly a process can affect the target property of sea ice, which here are ice drift, ice concentration, and ice thickness. Furthermore, the variability of the process' effect is evaluated by a newly developed measure: the update-timescale. This indicates how frequently the process has to be updated (i.e. recalculated) in a numerical model. The results reveal that some processes like the lateral melt of ice floes can be neglected for short-range forecasts. Moreover, most processes have to be updated only every 30 minutes or even less frequently.

To correctly simulate the interaction processes of sea ice with its surrounding, HAMMER applies a coupling to an ocean model as well as to an atmosphere model. The setup of this system is presented, in combination with two numerical optimisations that reduce the computational costs. A) A time-split approach in the atmosphere model METRAS decouples the calculation of cloud-microphysical processes from the main model time step. Thus, the time step can be increased during precipitation events, which yields a speed-up of 10%. B) A new algorithm to solve the ice drift equation is developed. By enhanced coupling of the ice drift components u and v during the iterative procedure, numerical instabilities can be avoided. Because of the resultant decrease of required iterations the amount of computational time required by the sea ice model relative to the atmosphere model is reduced from 50% to 5%. The simulation results remain quasi-unchanged for A) and B).

The optimised model system, HAMMER, was applied to operationally forecast sea ice conditions in the Barents Sea in March 2014. The simulated ice concentration is evaluated using hit rates. They reveal that HAMMER performs worse than a persistence forecast, especially in regions with high ice concentration. The benefit of HAMMER is shown by a new evaluation technique that addresses the navigability of randomly chosen ship routes. Even though HAMMER forecasts navigable routes to be non-navigable more often than persistence does, it can reduce danger for some types of ships because it can better forecast non-navigable routes.

Zusammenfassung

Das Meereis in der Arktis nimmt bedingt durch den Klimawandel immer weiter ab, was neue Möglichkeiten für die Schifffahrt eröffnet, z.B. auf der Nordostpassage. Um in diesen teilweise eisbedeckten Gewässern die beste Route zu finden, benötigen die Kapitäne Meereisvorhersagen für die nächsten Tage. Solche können mit dem Kurzfrist-Meereisvorhersagesystem HAMMER erstellt werden, dessen Eigenschaften in dieser Arbeit vorgestellt werden.

Um herauszufinden, welche physikalischen Prozesse in Kurzfristmodellen berücksichtigt werden müssen, wird die Relevanz von Meereisprozessen untersucht. Dazu wird die Einflusszeitskala berechnet, die angibt, wie schnell der jeweilige Prozess Einfluss auf die Zielgröße – hier Eisdrift, Eisdicke und Eiskonzentration – nehmen kann. Außerdem wird eine Aktualisierungszeitskala eingeführt, durch die die Variabilität der Prozesse bewertet werden kann. Sie gibt an, wie oft jeder Prozess in numerischen Modellen aktualisiert (neu berechnet) werden muss. Die Ergebnisse zeigen, dass manche Prozesse wie z.B. das seitliche Schmelzen von Eisschollen bei Kurzfristvorhersagen vernachlässigt werden können. Außerdem müssen die meisten Prozesse nur alle 30 Minuten oder seltener neu berechnet werden.

Um die Wechselwirkungen zwischen Meereis und seinen umgebenden Systemen richtig darzustellen, ist das Eismodell von HAMMER sowohl mit dem Ozean als auch mit der Atmosphäre gekoppelt. Nach der Beschreibung dieses Modellsystems werden zwei numerische Optimierungen vorgestellt, die den Rechenaufwand reduzieren. A) Durch ein Zeitsplitverfahren im Atmosphärenmodell METRAS können die wolkenmikrophysikalischen Prozesse unabhängig vom generellen Modellzeitschritt berechnet werden, der somit während Regenphasen erhöht werden kann. Dadurch wird das Modell um 10% schneller. B) Ein neuer Algorithmus für die Lösung der Eisdriftgleichung wird entwickelt. Dieser verhindert numerische Instabilitäten, indem er die u - und v -Komponenten der Eisdrift im iterativen Lösungsprozess mehr miteinander verquickt. Damit sinkt die Zahl der nötigen Iterationen, wodurch das Eismodell nur noch 5% statt 50% der Rechenzeit verglichen mit dem Atmosphärenmodell benötigt. Die Simulationsergebnisse ändern sich bei A) und B) so gut wie nicht.

Mit dem optimierten Modellsystem HAMMER wurden im März 2014 operationelle Eisvorhersagen für die Barentssee erstellt. Die Evaluierung der simulierten Eiskonzentrationen ergibt, dass HAMMER schlechter abschneidet als Persistenzvorhersagen. Dies gilt vor allem für Regionen mit hoher Eiskonzentration. Der Nutzen von HAMMER zeigt sich bei einer neuen Evaluationsmethode, die auf die Befahrbarkeit von zufällig gewählten Schiffsrouten abzielt. Zwar hält HAMMER schiffbare Routen öfter als Persistenzvorhersagen für nicht befahrbar, dafür sagt es aber nicht-schiffbare Routen zuverlässiger voraus und bewahrt damit manche Schiffe vor Gefahr.

Contents

Abstract	iii
Zusammenfassung	iv
Contents	v
List of Figures	viii
List of Tables	x
1 Introduction	1
2 Time scales of processes affecting sea ice	6
2.1 Introduction	6
2.2 Basic equations	8
2.2.1 Ice drift speed	9
2.2.2 Ice concentration	10
2.2.3 Ice thickness	14
2.2.4 Processes and their characteristic strength	16
2.3 Impact-timescales	19
2.3.1 Derivation of impact-timescale	20
2.3.2 Values for input variables	20
2.3.3 Resulting impact-timescales	21
2.3.4 Discussion of determined impact-timescales	28
2.4 Update-timescales	29
2.4.1 Error induced by keeping processes constant	30
2.4.2 Characteristic values used	32
2.4.3 Temporal development of errors	35
2.4.4 Determination of update-timescale	35
2.4.5 Dependency of the update-timescales on ice thickness and ice concentration	38
2.4.6 Discussion of determined update-timescales	44
2.5 Conclusion	48
3 Development of the short-range forecast system	50
3.1 Model system	50
3.1.1 Sea ice model MESIM	50
3.1.2 Coupling to the atmosphere model METRAS	54
3.1.3 Coupling to the ocean model HAMSOM	54

3.1.4	Input data for the model system	55
3.1.4.1	Boundary values	56
3.1.4.2	Initial values	57
3.2	Model optimisations	58
3.2.1	New solver for the momentum equation in MESIM	58
3.2.1.1	Theoretical background and new algorithm	59
3.2.1.2	Performance tests	64
3.2.2	Timesplitting of cloud-microphysics in METRAS	69
3.2.2.1	Optimisation approaches	71
3.2.2.2	Performance tests	74
4	Application and evaluation of the model system	79
4.1	Application of the model system during the IRO-2 experiment phase	79
4.1.1	Experiment and model setup	79
4.1.2	Exemplary results	82
4.2	Predicted ice concentration	87
4.2.1	Calculation of hit rates	87
4.2.2	Results	89
4.2.2.1	Impact of the time of model initialisation on hit rates	91
4.2.2.2	Comparison of hit rates between model and persistence forecasts	94
4.2.2.3	Day-to-day variability of the model quality	99
4.2.3	Discussion	104
4.3	Predicted navigability of artificial ship routes	106
4.3.1	Method for determining threat indices	107
4.3.1.1	Determination of random ship routes	107
4.3.1.2	Definition of navigability	110
4.3.1.3	Used model data, observation data, and comparison data	111
4.3.1.4	Calculation of threat indices	112
4.3.2	Results and discussion	113
5	Conclusions & Outlook	118
	Acknowledgements	120
A	Derivation of the ice thickness equation from equations of ice concentration and ice volume	122
A.1	Case I: Divergent ice drift or partly ice covered sea	122
A.2	Case II: Convergent ice drift of unbroken ice cover	122

B Derivation of the characteristic values for internal forces, INT, and open water production due to shear, OWS	123
B.1 Internal forces, INT	123
B.2 Open water production due to shear, OWS	123
C Comparison of sea ice models MESIM and VICE	124
D Correction method for SMOS ice thickness data	128
E Supplementary material to the hit rate analysis	129
E.1 Assessment of the error tolerance using quantiles	129
E.2 Influence of clouds and water vapour on observed sea ice concentration	131
F Random generator for artificial ship routes	136
List of Symbols	137
List of Acronyms	144
References	145
Erklärung	154

List of Figures

1.1	Northern Sea Route and Suez Canal Route.	3
1.2	Diagram of processes that affect sea ice quantities.	4
2.1	Sketch of an ice floe in a grid cell, illustrating H and h	9
2.2	Sketch of a 1D ice floe.	13
2.3	Impact-timescales for first-year ice and multi-year ice.	24
2.4	Temporal error development for ice drift when keeping processes constant.	36
2.5	Schematic diagram of the error limit function and the error development when a process is updated regularly.	37
2.6	Update-timescales of processes depending neither on \mathcal{A} nor on \mathcal{H}	39
2.7	Update-timescales of processes depending only on \mathcal{A}	40
2.8	Update-timescales of processes depending only on \mathcal{H}	42
2.9	Update-timescales of processes depending on \mathcal{A} and \mathcal{H}	45
3.1	Quantities exchanged between MESIM and atmosphere/ocean.	53
3.2	Boundary values for MESIM/METRAS+HAMSOM from external models.	57
3.3	Number of iterations of the previous and the new SOR-algorithm.	67
3.4	Δu^i during SOR-iteration at 06:07 UTC comparing previous and new algorithm.	68
3.5	pSOR vs. OPER: BIAS, RMSE, and 99-percentile for A and H	70
3.6	woTS vs. OPER: BIAS & 99-percentile for cloud and rain water content.	76
3.7	woTS vs. OPER: HITRATE for 10-m wind, BIAS & 99-percentile for A and H	78
4.1	Modeldomains of MESIM-METRAS and HAMSOM with track of R/V Lance.	80
4.2	Simulated ice concentration development.	83
4.3	Daily temperatures at Edgeøya, Kongsøya, and Kvitøya in March 2014.	84
4.4	Simulated ice drift in comparison to simulated 10-m wind.	85
4.5	Simulated temperature transport and ice concentration on 29/03.	86
4.6	Simulated cloud water content and net shortwave radiation on 22/03.	87
4.7	Hit rate of simulated ice concentration vs. AMSR2 for fc06 and fc18.	90
4.8	Hit rate difference of fc18 to fc06.	91
4.9	Hit rate difference for the pairs fc18–fc06 and fc06 ₊₁ –fc18, average over all runs.	93
4.10	Hit rate of ice concentration from persistence forecast by AMSR2.	96
4.11	Difference of hit rates from the model- vs. persistence-forecasts.	96
4.12	Difference of hit rates model vs. persistence for three SIC ranges.	98
4.13	Distribution of ice concentration values in satellite observations.	100
4.14	Hit rate of fc06-runs, separately for SIC<5% and for SIC>85%.	101
4.15	Tendency of fraction of highly ice-covered (SIC85 _{SAT}) cells.	103
4.16	Daily mean ice drift speed, direction and divergence.	105
4.17	Exemplary, randomly chosen artificial ship routes.	108

4.18	Scatterplots of H vs. A for Lance's track.	111
4.19	Threat indices HIT, COR, MIS, and FAL for forecasted navigability on 25/03. . .	114
4.20	Threat indices for forecasted navigability as average for 13/03 until 30/03. . . .	115
4.21	Difference of time-averaged threat indices between HAMMER and persistence. . .	116
4.22	Difference of spatially-averaged threat indices between HAMMER and persistence.	116
D.1	Transformation function $g(A)$ for SMOS ice thickness data.	129
E.1	80%-quantiles of the difference between simulated and observed ice concentration.	130
E.2	Ice concentration from 21-23 March 2014 observed by AMSR2.	132
E.3	Total column cloud water and total column water vapour on 22/03.	134

List of Tables

2.1	Characteristic values for variables and expressions.	17
2.2	Formulas for characteristic strengths of processes.	18
2.3	Ranges of characteristic values for the forcing variables.	22
2.4	Values of constants used in the calculations.	23
2.5	Selected target impacts $\Delta\chi$ for the target variables.	23
2.6	Characteristic change rates and minimum and maximum of the forcing variables.	33
2.7	Values of the initial state of the forcing variables.	34
2.8	Summary of update-timescales.	47
3.1	Comparison of wall-clock time for previous and new SOR algorithm.	69
3.2	Simulations used for time split evaluation.	74
3.3	Ratio of computational speed of OPER-runs and woTS-runs.	75
4.1	Contingency table	107
C.1	Comparison of sea ice models MESIM and VICE.	124

1 Introduction

Sea ice is a fascinating element of the climate system. Essentially, it is only frozen sea water floating on top of the ocean, but it has many interesting features. Like every ice, it can only exist at sufficiently low temperatures: those below the freezing point of sea water. Thus, sea ice mainly exists close to the earth's poles, in the Arctic and the Antarctic, where it grows and shrinks again, following the annual cycle. It is important not only for animals like the polar bear and as habitat for many sorts of algae living at the bottom of sea ice. It also affects atmosphere and ocean for example by altering the salt content of water masses or by insulating the cold air from the relatively warm sea water. This effect is enhanced if the sea ice bears a layer of snow on top.

Furthermore, sea ice has a special micro-structure that originates from the salt of the frozen sea water. This causes small salt-water bubbles (brine pockets) in the ice or even a whole net of brine channels. On a larger scale, sea ice can take various forms, depending on its history. In the very first state of freezing, single ice crystals are floating in the ocean surface layer. This frazil ice can further evolve to nilas if the ocean is very calm or to grease ice in wavy conditions. If the latter solidifies, it forms pancake ice. With ongoing freezing conditions, the sea ice would grow thicker and can cover large parts of the ocean. This sea ice cover, however, is not static but it can be moved and distorted by winds and ocean currents. Then, on the one hand, the sea ice can break up into single ice floes, or so-called leads can open in the ice. On the other hand, if the sea ice is pushed together, it might pile up and build pressure ridges.

If the temperatures increase above the freezing point, the sea ice is induced to melt. Then, it does not simply become thinner and eventually disappears, but various processes will shape this progress. For example, melt water can collect on top of the ice and form melt ponds. Or it can percolate down in the ice flushing out the salty brine. After the summer months some sea ice will have been gone; some parts of it, however, survive and are then called second-year ice or multi-year ice—in contrast to the first-year ice, which melts during the first summer.

This multi-year ice can be found especially at the Greenland-side of the Arctic Ocean (AARI, 2014), where it is gathered by the prevailing sea ice drift. In average, it is thicker than first-year ice, because of two reasons; On the one hand it grows thermodynamically during recurrent freezing periods, on the other hand it also gets piled up dynamically.

The amount of multi-year ice in the Arctic continuously decreased during the last years (NSIDC, 2012). Likely, this is connected to climate change. The global warming certainly reduces the total amount of sea ice, regardless whether or not it finally even passes a tipping point (NOTZ,

2009). In any case, climate models predict the temperatures to increase above average in the polar regions. A reason for this polar amplification could be linked to the sea ice: The ice–albedo feedback describes the effect that a reduction of the sea ice area reduces the average albedo so that more radiation from the sun can be absorbed. This process raises the temperatures and thus leads to enhanced sea ice melt.

The reduction of sea ice is most recognisable when measuring its extent in the Arctic. The Antarctic sea ice behaves slightly different and will not be focus of this thesis. The lowest Arctic sea ice extent that has ever been observed by satellites was measured on 16 September 2012. However, not only the sea ice extent or the sea ice area make climate changes apparent. The sea ice also becomes thinner in average, and multi-year ice disappears. This sea ice melt does not contribute to the global sea level rise, but it has many other implications. One often mentioned example is that the low-saline melt water could influence the thermohaline circulation. But it is not only earth scientists who keep a very close eye on these developments; also the economy becomes more and more interested in the sea ice reduction. Large oil and gas reserves below the ice-covered Arctic Ocean are tempting to be explored. Moreover, the retreating sea ice cover will open new routes for shipping through the Arctic.

There are two main routes that lead through the Arctic from Europe to the Bering Strait: The Northwest Passage along the Canadian coast and the Northern Sea Route along the Siberian coast. While the first often features dangerous sea ice conditions (STEWART et al., 2007), the latter is more interesting for ship traffic because it is open more frequently and for longer time periods. It was navigable for several years in a row and with climate change, the yearly ice-free season is predicted to further prolong by up to 6 months until 2100 (KHON et al., 2010). Already now, the Northern Sea Route is used by dozens of ships each year¹. The reason why this northern route is so profitable for shipping companies is depicted in Figure 1.1: The Northern Sea Route is much shorter than the traditional route via the Suez Canal. The sea ice map shows the minimum of the sea-ice-covered area in 2014, which reveals that the conditions are indeed appealing: The Northern Sea Route meets the sea ice only rarely. Nevertheless, sea ice can pose a threat to traversing ships, especially if the ice conditions are more heavy during early summer or late autumn. As accidents in this sensitive environment and in these remote areas are fatal, they should be prevented at any cost. This could be achieved by not navigating there. If navigation is non avoidable, at least the location of the sea ice and its properties have to be known as accurate as possible.

¹The Northern Sea Route Information Office registered 41, 46, and 71 transits in 2011, 2012, and 2013, respectively (http://www.arctic-lio.com/nsr_transits).

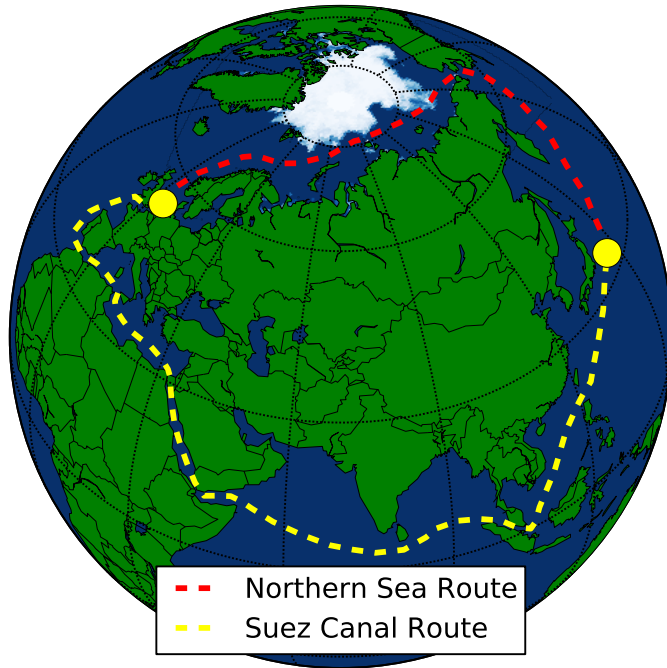


Figure 1.1: Sketch of route options between destinations in western Europe and eastern Asia: Standard route via Suez Canal (yellow) and Northern Sea Route (red). The background colour indicates land areas in green, water in blue, and the sea ice concentration on 17 September 2014 based on ASI-SSMI data (KALESCHKE et al., 2001; SPREEN et al., 2008) ranging from white (fully ice-covered) to blue (open ocean).

The prerequisites to find the best and safest route for ships sailing through sea ice is to forecast future sea ice conditions. Thus, the aim of this thesis is to set up such a forecasting system and to discuss its relevant features. First of all, the route planning requires sea ice forecasts for a few days, so-called *short-range* forecasts. Furthermore, the spatial resolution should be high enough to recognise the sea ice features that are important for ships.

To make such forecasts, it is at first necessary to know which (physical) processes affect the properties of sea ice. With this knowledge, a forecast model can be designed appropriately to simulate the sea ice behaviour with the adequate complexity. Relevant properties that represent the state of sea ice are the ice drift, the thickness of the sea ice, its temperature and salinity, and the ice concentration, which is the fraction of the ocean that is covered by sea ice. The processes that affect these sea ice properties are illustrated schematically in Figure 1.2, without any claim of being exhaustive. The meaning of many of the processes (arrows and text) and of the depicted quantities (ellipses) is explained later in this thesis. The diagram should primarily raise an impression about the complexity of the interactions. At the same time, it becomes clear that sea ice quantities (red ellipses) are also influenced by processes that are governed by the atmosphere (yellow) or the ocean (blue).

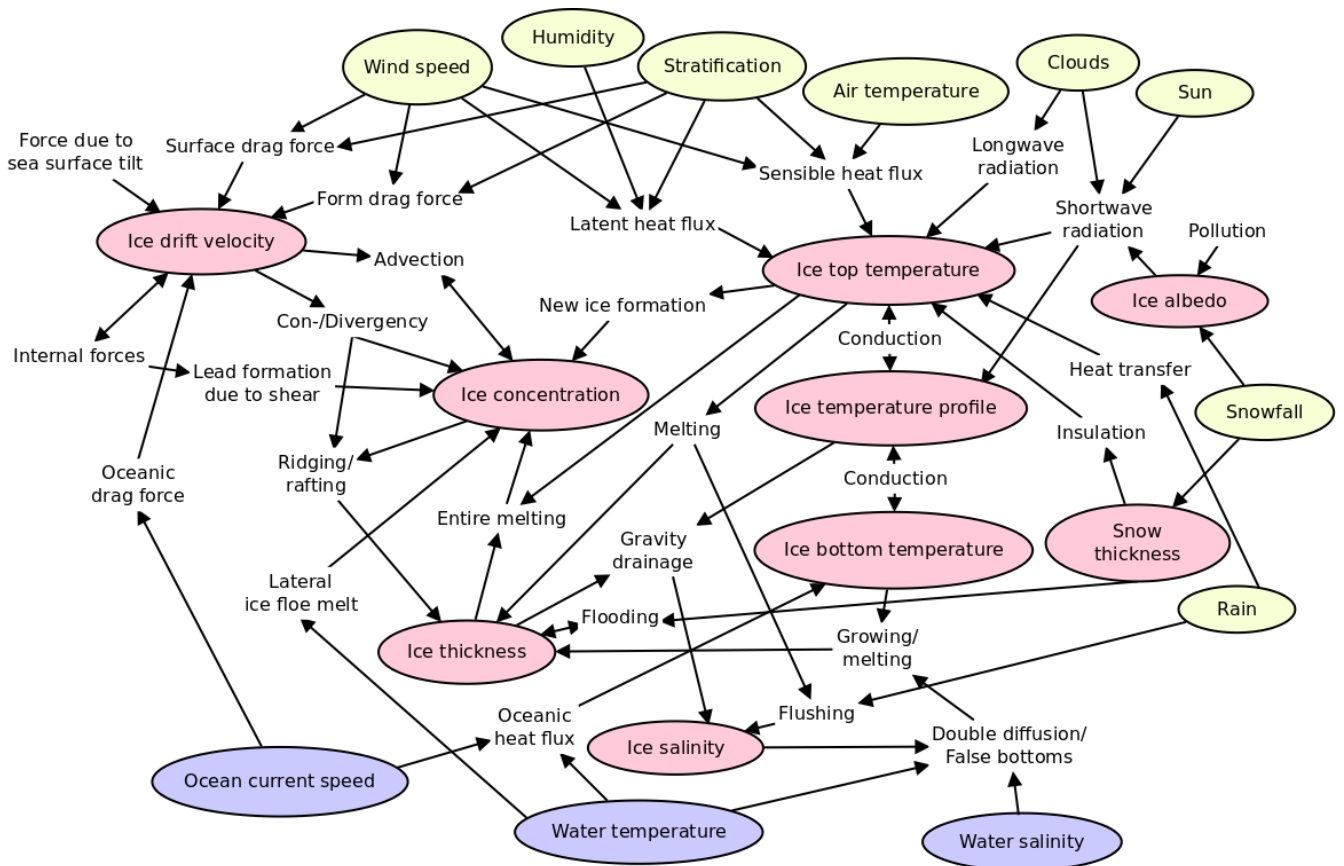


Figure 1.2: Conceptual model of physical processes (text between arrows) that affect sea ice quantities (red ellipses). Some processes also involve atmospheric quantities (yellow ellipses) or oceanic quantities (blue ellipses).

All these processes take place with different rates, some slower and some faster. Thus, they also have different effects on the sea ice quantities. Therefore, the question arises whether all of these processes are relevant for short-range forecasts. This issue is addressed in Chapter 2. The investigations there are twofold. Firstly, the time-scales of processes that affect sea ice properties are analysed in order to rate their relevance. Secondly, the time variability of a process' intensity is investigated because this could be used for optimisation of sea ice forecast models.

For simulating the processes, various numeric sea ice models have been developed. Their focus can be very different as is the selection of processes they simulate. Not all models are made for short-range forecasts, but many are used for climate simulations. Their simulation areas usually cover the whole Arctic and/or Antarctic. Other models focus on a specific region and simulate sea ice only in this limited area. Still others simulate the sea ice evolution at one point only. These 1D-models focus more on the temperature profile within the ice and connected thermodynamic processes like freezing and melting. The drift of sea ice and its deformation,

in contrast, are simulated by dynamic models. Many well-known sea ice models consider both dynamic and thermodynamic processes. Also the sea ice model that is used in the sea ice forecasting system presented here can simulate both types of processes.

For simulating the sea ice dynamics, sea ice models use different approaches depending on the spatial scale of the simulations. In the large scale, sea ice can be treated as continuum like it is done in the frequently used approach by HIBLER (1979). For smaller scales (<10 km), different approaches have been developed, as summarised by KWOK and COON (2006), that can, for example, account for the anisotropy of the sea ice cover or that regard discrete ice floes. Nevertheless, the HIBLER-model is still commonly applied also at these small scales. This also holds for the sea ice model used in this thesis.

As indicated by Figure 1.2, the sea ice properties are influenced by the external systems atmosphere and ocean. In order to correctly simulate the according processes, sea ice models are often coupled to an ocean model (MELLOR and HÄKKINEN, 1994). A coupling to an atmosphere model is less common but pursued for some models (e.g. the MI-IM model; RØED and DEBERNARD, 2004). Only very few operational sea ice services apply sea ice models that are coupled to atmosphere models (DINESSEN et al., 2011). They use weather forecasts as forcing data but do not take into account that the sea ice might change the state of the atmosphere. As DIERER and SCHLÜNZEN (2005) and HEBBINGHAUS et al. (2007), however, showed that the location of the sea ice can indeed influence the local wind field, a coupling of sea ice and atmosphere can be considered to be important for the high-accuracy sea ice forecasts that are demanded by navigators. Therefore, importance is attached to applying a coupling with both ocean and atmosphere in the proposed sea ice forecast system. The elements of this model system called HAMMER, its main features and the associated data flow are described in Section 3.1.

Since forecasts in general are time-critical, models should be computationally efficient to produce the forecasts well in time. Furthermore, if the computational costs of a model can be reduced, its resolution could be increased in return. This would allow for the simulation of more small-scale features, which are relevant for ship navigation. Thus, HAMMER was inspected for options to reduce its computational time by numerical optimisations. Two of these optimisations together with efficiency tests are discussed in Section 3.2

In order to test the performance of HAMMER, it is applied in a realistic setting in Chapter 4. During a two-week experiment in March 2014, HAMMER was run operationally to route an ice-going vessel in the Barents Sea. The generated forecasts of the sea ice conditions are used to evaluate the model skill: Is HAMMER able to correctly predict the sea ice concentration and to advise navigators about the navigability of ship routes? The answer is discussed in Sections 4.2 and 4.3. Main conclusions of this thesis and some suggestions for a further improvement of HAMMER are given in Chapter 5.

2 Time scales of processes affecting sea ice

This chapter is in preparation to be submitted as independent scientific paper. Therefore, it contains its own introduction and conclusion sections.

2.1 Introduction

Sea ice can be seen as a complex system defined by state variables like ice thickness, ice concentration and ice drift velocity. These state variables are influenced by surrounding systems and are interconnected with each other. For example, the wind influences the ice drift, and the convergence of sea ice drift causes the ice concentration to increase. These interconnections are named physical *processes*. They include both internal and external processes, the first acting within the sea ice system, the latter connecting surrounding systems to the sea ice. The most important external systems for sea ice are atmosphere and ocean. For example, DIERER et al. (2005) showed a strong influence of atmospheric cyclones on the sea ice cover in the Fram Strait. The ocean plays an important role during melting by supplying heat to the sea ice (STEELE et al., 2010), and the ocean can influence the ice drift, for example by the effect of tides (KOENTOPP et al., 2005).

In order to study and forecast the various processes affecting sea ice, various sea ice models have been developed that simulate thermodynamic and dynamic processes. They range from global models like CICE (HUNKE et al., 2013) or LIM (VANCOPPENOLLE et al., 2009), that were developed for climate simulations, to regional sea ice models for short-range ice forecasts (listed in DINESSEN et al. (2011)). HIROMB (WILHELMSSON, 2002), for example, was applied to predict small scale (3 nautical miles) sea ice features for ship navigation (KOTOVIRTA et al., 2009).

Although most of the sea ice models are based on the sea ice physics equations introduced by HIBLER (1979) (hereinafter “H79”), the sea ice models are used for various applications covering completely different spatial and temporal scales. The question arises, if all processes are relevant for both long-range and short-range simulations or if some processes can be simplified or omitted for some applications.

A simplification of the modelled sea ice system could reduce the computational time. This is useful for both short-range sea ice forecasts and long-term climate simulations. For example, the forecast of an optimised short-range model can be provided to the customer more quickly. Models for climate simulations can benefit from an optimisation since they have to be efficient to simulate

multiple centuries (HUNKE et al., 2010). A first step towards optimisation would be to identify the relevant processes. Subsequent steps can be numerical and/or technical model improvements like the replacement of the traditional viscous–plastic rheology (H79) by the elastic–viscous–plastic rheology (HUNKE and DUKOWICZ, 1997) or, more technically, the parallelisation of the model code.

Information about the relevance of a process for a certain sea ice variable can be obtained by scale analyses. This means, characteristic values are used in the equations of the sea ice variables. The magnitude of different terms can thereby be estimated and compared with each other to determine the relevance of single processes. Such a scale analysis was conducted by LEPPÄRANTA (2011a) for the ice drift equation. It showed that the drift speed of ice floes is primarily governed by the wind, the ocean current and the resistance caused by adjacent ice floes. The advection of ice drift momentum, however, plays a minor role for the ice drift.

The motivation for the present study is to extend LEPPÄRANTA’s study for the variables ‘ice concentration’ and ‘ice thickness’. All required prognostic equations and the corresponding processes will be compiled in Section 2.2. Furthermore, the aim of the study is to identify not only the relative importance of the processes, but also the absolute time after which the impact of a process becomes relevant. For this purpose, an “*impact-timescale*” will be introduced in Section 2.3.1 that specifies how long a process has to be active to considerably influence its target variable. If the forecast period is shorter than the impact-timescale, the process can be neglected. An example from the atmosphere makes the meaning of the impact-timescale conceivable: the change of seasons is negligible for a 3-day weather forecast, but not for climate simulations. Values of impact-timescales for sea ice processes will be determined for typical sea ice conditions in Section 2.3. These “typical sea ice conditions” certainly cover a range of different conditions, thus, also the sensitivity of the impact-timescale to variations of the environmental conditions will be investigated.

Beside neglecting a process in a model, there is another way to simplify the calculations: In the case that the strength of a process does not change over time, its value could be determined at the beginning of the simulation and then be kept constant during the whole simulation period. A common example in meteorology is the vertical acceleration by gravity: The gravitational constant is first determined (maybe according to the latitude) and then applied throughout the whole simulation. To make use of this feature for model optimisation, an “*update-timescale*” will be introduced in Section 2.4 that defines the time period during which the strength of a process can be treated as constant. After this time has elapsed, the value of the process’ strength has to be recalculated (i.e. “updated”) in order to avoid too large errors in the model simulation. Resulting values for the update-timescale will be discussed with regard to their dependency on prevailing conditions of ice concentration and ice thickness.

The scale analyses presented here are applicable to sea ice models that are based on the H79-equations. For single specifications (e.g. parametrisations) the paper draws on the model MESIM (BIRNBAUM (1998); DIERER et al. (2005); SCHLÜNZEN et al. (2012)). MESIM is chosen because it is utilised—in conjunction with regional ocean and atmosphere models—for operational short-range sea ice forecasts. Reducing the complexity of the MESIM model using impact-timescale and update-timescale might result in a speed-up of the model without loss of forecast quality. This promotes fast delivering of forecast products to customers. How the findings of this study could be used for sea ice model optimisations is discussed in Section 2.5.

2.2 Basic equations

This study focuses on the three sea ice properties ice drift speed v [m/s], ice concentration A [%] (also known as compactness of the ice) and ice thickness H [m]. These are the quantities which common sea ice models simulate at each grid cell of their model domain. Usually, however, models do not calculate the ice thickness H directly but they derive it from the prognosed ice volume per unit area. This quantity is called h and can be interpreted as an average ice thickness that would result if all ice in the grid cell were equally distributed over the whole grid area. Figure 2.1 illustrates the distinction of H and h : A square grid cell is covered by an ice floe of thickness H with 50% ice concentration (Figure 2.1a) and 25% ice concentration (Figure 2.1b), respectively. The ice volume per unit area, h , appears as the height of the dashed box, which fills the whole grid cell area. Mathematically, H and h are connected by the ice concentration A :

$$h = A \cdot H \tag{2.1}$$

The actual ice thickness H is more suitable than the ice volume per unit area h for the users of sea ice forecasts (like e.g. navigators of icebreakers). Therefore, this study will focus on H rather than on h .

The analyses of the impact-timescale and the update-timescale are based on prognostic equations of the so-called *target variables* v , A , and H . As a basis, the equations are taken from H79 because several sea ice models are based on them, e.g. ROMS (BUDGELL (2005); HEDSTRÖM (2009)), VICE (ÓLASON and HARMS, 2010), NAOSIM (KARCHER et al., 2003) and MESIM (DIERER et al., 2005). Deviations from HIBLER’s equations and additional parametrisations used in this study will be explained in the next sections.

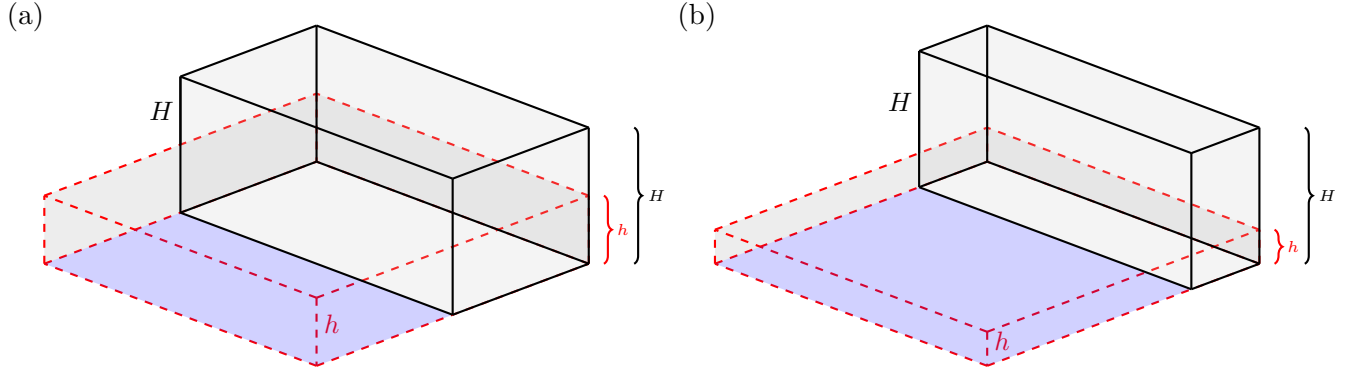


Figure 2.1: Sketch of a square grid cell containing an ice floe (black box) with thickness H covering (a) 50% and (b) 25% of the grid cell area. The resulting ice concentration, A , is 50% and 25%, respectively, with water at the remaining area (blue). The red, dashed box illustrates the meaning of h : It is the height of the ice if all ice volume was redistributed over the whole grid cell.

2.2.1 Ice drift speed

The ice drift speed is calculated from the momentum equation of sea ice as given in H79. Regarding the wind stress term and the ocean stress term, CONNOLLEY et al. (2004) pointed out that both terms are not correctly treated by HIBLER's momentum equation for conditions with low ice concentrations. Even though they note that the influence on model results is small, the corrected equation will be used in this theoretical study in order to correctly describe the dependency of wind and ocean stress on the ice concentration. This corrected equation is also used by HAAPALA et al. (2005). To convert this momentum equation to an equation for ice drift, it is divided by the mass of ice per unit area, ρh , using the density of sea ice ρ .

$$\frac{\partial \vec{v}}{\partial t} = \underbrace{-\vec{v} \cdot \nabla \vec{v}}_1 - \underbrace{f \vec{k} \times \vec{v}}_2 + \underbrace{\frac{A}{\rho h} \vec{\tau}_a}_3 + \underbrace{\frac{A}{\rho h} \vec{\tau}_w}_4 - \underbrace{g\beta}_5 + \underbrace{\frac{1}{\rho h} \nabla \cdot \underline{\sigma}}_6 \quad (2.2)$$

Equation (2.2) describes the local change of the ice drift velocity \vec{v} as result of six processes: 1) the advection of momentum, 2) the Coriolis force calculated from the Coriolis parameter f by utilising \vec{k} , the unit vector normal to the surface, 3) the acceleration due to wind stress $\vec{\tau}_a$, 4) the acceleration due to ocean stress $\vec{\tau}_w$, 5) the acceleration caused by the tilt β of the sea surface, requiring the gravitational constant g , and 6) internal forces in the ice pack calculated from the divergence of the stress tensor $\underline{\sigma}$.

In accordance with H79, the following simple parametrisations for the external forces are used

in the present study:

$$\vec{\tau}_a = \rho_a C_a |\vec{v}_{ag}| \exp(i\theta_a) \vec{v}_{ag} \quad (2.3)$$

$$\vec{\tau}_w = \rho_w C_w |\vec{v}_{wg} - \vec{v}| \exp(i\theta_w) (\vec{v}_{wg} - \vec{v}) \quad (2.4)$$

$$g\beta = -f(\vec{k} \times \vec{v}_{wg}) \quad (2.5)$$

Required are the geostrophic wind velocity \vec{v}_{ag} , the geostrophic ocean current velocity \vec{v}_{wg} , densities of air ρ_a and sea water ρ_w , drag coefficients for air C_a and sea water C_w as well as turning angles between sea ice drift direction and wind direction θ_a and ocean current direction θ_w , respectively.

The internal forces are parametrised by HIBLER's viscous-plastic rheology:

$$\sigma_{ij} = 2\eta\epsilon_{ij} + \delta_{ij} \left\{ (\zeta - \eta) (\epsilon_{11} + \epsilon_{22}) - \frac{P}{2} \right\} \quad \text{for } i, j \in \{1, 2\} \quad (2.6)$$

$$\text{with } P = P^* h C(A) \quad (2.7)$$

$$\text{and } C(A) = e^{-C^*(1-A)} \quad (2.8)$$

The ij -component of the stress tensor $\underline{\sigma}$ is calculated from a bulk viscosity ζ , a shear viscosity η , the Kronecker delta δ_{ij} , the ice strength P (requiring the empirical constants P^* and C^*) and the strain rate tensor

$$\epsilon_{ij} = \frac{1}{2} \left(\frac{\partial u_i}{\partial x_j} + \frac{\partial u_j}{\partial x_i} \right) \quad \text{for } i, j \in \{1, 2\} \quad (2.9)$$

of the ice drift velocity $\vec{v} = (u_1, u_2)$.

With this, the prognostic equation for the ice drift velocity is:

$$\begin{aligned} \frac{\partial \vec{v}}{\partial t} = & -\vec{v} \cdot \nabla \vec{v} - f\vec{k} \times \vec{v} + \frac{A}{\rho h} \rho_a C_a |\vec{v}_{ag}| \exp(i\theta_a) \vec{v}_{ag} \\ & + \frac{A}{\rho h} \rho_w C_w |\vec{v}_{wg} - \vec{v}| \exp(i\theta_w) (\vec{v}_{wg} - \vec{v}) - f(\vec{k} \times \vec{v}_{wg}) + \frac{1}{\rho h} \nabla \cdot \underline{\sigma} \end{aligned} \quad (2.10)$$

2.2.2 Ice concentration

The prognostic equation for the ice concentration A

$$\frac{\partial A}{\partial t} = -\nabla \cdot (A\vec{v}) - Q_S + Q_N + Q_L \quad (2.11)$$

looks like a common conservation equation, but actually describes the sea ice behaviour empirically (MELLOR and KANTHA, 1989) as ice concentration is not a physically conserved quantity. Especially, the equation becomes invalid if A were to increase above 100%. The first term describing the effects of ice advection and diverging drift is in detail discussed in MELLOR and

KANTHA (1989). Furthermore, the ice concentration is dynamically reduced by creation of open water during shear, Q_S , and thermodynamically by lateral melting of ice floes, Q_L . Formation of new ice, Q_N , enlarges the sea ice area. The parametrisations for these terms are presented in the next sections.

Parametrisation of open water production due to shear Q_S

The sink term Q_S in Equation (2.11) accounts for the effect that open water areas arise in the ice pack if it experiences shear stress. It basically represents ridging and rafting effects. In the original publication of HIBLER's model in 1979 this term was not included. He introduced it firstly in 1984 with the parametrisation

$$Q_S = \psi_s(\dot{\epsilon}) \cdot C(A) \quad \text{with} \quad (2.12)$$

$$\psi_s(\dot{\epsilon}) = 0.5 \cdot (\Delta - \nabla \cdot \vec{v}) \quad \text{and} \quad (2.13)$$

$$\Delta = \sqrt{\dot{\epsilon}_I^2 + (\dot{\epsilon}_{II}/e)^2} \quad (2.14)$$

$e = 2$ is the aspect ratio of the yield curve ellipse of H79. $\dot{\epsilon}_I = \dot{\epsilon}_{11} + \dot{\epsilon}_{22}$ and $\dot{\epsilon}_{II} = \sqrt{(\dot{\epsilon}_{11} - \dot{\epsilon}_{22})^2 + 4\dot{\epsilon}_{12}^2}$ represent the invariants *divergence* and *shear* of the strain rate tensor $\dot{\epsilon}_{ij}$ (Equation (2.9)). Combining Equations (2.12)-(2.14) yields

$$Q_S = 0.5 \cdot \left(\sqrt{\dot{\epsilon}_I^2 + (\dot{\epsilon}_{II}/e)^2} - \dot{\epsilon}_I \right) \cdot C(A) \quad (2.15)$$

The function $C(A)$ models the dependency of Q_S on the ice concentration. The formulation for $C(A)$ that was used by HIBLER (1984) is not exactly the same as in Equation (2.8), that is used in the momentum equation. However, as they resemble each other very well, this study follows the approach of HARDER (1994) who applies the function for $C(A)$ from Equation (2.8) for both, the momentum equation as well as for Q_S .

Parametrisation of new ice formation Q_N

One of the two thermodynamic processes in Equation (2.11) is the increase of ice concentration due to new ice formation, Q_N . For it, the parametrisation by H79 is used:

$$Q_N = \frac{1 - A}{h_0} f(0) \quad (2.16)$$

h_0 is the demarcation thickness² and $f(0)$ is the growth rate of new ice. This notation is used to distinguish the growth rate $f(0)$ for new ice ($H=0$) from the growth/melt rate $f(H)$ for existing ice of thickness H . If the environmental conditions do not allow for ice generation, then $f(0)$ is zero.

Parametrisation of lateral melt of ice floes Q_L

The other thermodynamic process in Equation (2.11) is the lateral melt of ice floes, expressed by Q_L . The parametrisation originally proposed by H79 is based on the assumption that the thicknesses of ice floes in a grid cell are distributed linearly between 0 and $2H$ if the mean ice thickness of the floes is H . If the constant (vertical) melt rate $f(H) \leq 0$ is applied to all these ice floes with thicknesses ranging from 0 to $2H$ equally, the thinner parts of the ice pack will melt entirely, which, in turn, decreases the ice concentration. Therefore, the vertical melt rate $f(H)$ directly influences the lateral melt, Q_L , here in the parametrisation by H79:

$$Q_L \stackrel{\text{H79}}{=} Q_{Lh} = \frac{A}{2H} \cdot f(H) \quad (2.17)$$

If the environmental conditions do not allow for ice melting, then $f(H)$ is zero.

This approach by H79 does not take into account the water temperature or a floe distribution, but the ice area is simply reduced proportionally to the vertical melt rate. STEELE (1992), however, found a large influence of different floe geometries on lateral melt rates. Therefore, an alternative parametrisation is also applied in this study, in addition and in comparison to Equation (2.17). It is the parametrisation that is used by MESIM and it is based on laboratory investigations of the heat flux at melting vertical ice walls: According to MAYKUT and PEROVICH (1987), JOSBERGER (1979) (hereinafter “J79”) found that the equation for the vertically averaged lateral melt rate M_r can be parametrised as

$$M_r = m_1 \Delta T_w^{m_2} \quad (2.18)$$

ΔT_w represents the elevation of the water temperature above the freezing point. For the parameters m_1 and m_2 , the values found by J79 are taken ($m_1=2.85 \cdot 10^{-7} \text{m s}^{-1} \text{K}^{-1.36}$ and $m_2=1.36$) because BIRNBAUM (1998) states that these values will result in the most realistic melt rates for the model MESIM.

²The demarcation thickness is used by H79 to differentiate between “thin ice” and “thick ice”. “Thin ice” includes open water and ice floes with an ice thickness H lower than h_0 . For consistency reasons with literature, the demarcation thickness is named h_0 although it specifies an ice thickness (H) rather than an ice volume per unit area (h). The role of h_0 in the parametrisation of new ice formation is to specify the thickness level up to which the newly formed ice is piled up by notionally pushing it together. The area that is covered by this imaginary ice pile defines the ice concentration increase Q_N .

From the melt rate M_r of J79 the change of ice concentration, Q_L , can be derived by geometrical considerations. For 2D ice floes, this was done by STEELE (1992) (his Equation (8)):

$$\frac{\partial A}{\partial t} = \frac{\pi}{\alpha L} A \cdot (-M_r) \quad (2.19)$$

where $\pi/\alpha L$ represents a perimeter-to-area ratio of 2D ice floes with the nomenclature of STEELE (1992). The perimeter is defined as the sides of the floe where lateral melting takes place. In the present study however—in common with MESIM—, ice floes are not considered as 2D- but only as 1D-objects. Thus, a linear ice floe of length L_i and (arbitrary) width δ melts on the 2 sides of length δ (schematically depicted in Figure 2.2). This results in a “perimeter”-to-area ratio of $2\delta/\delta L_i$ for 1D ice floes replacing the term $\pi/\alpha L$ of 2D ice floes. With this, the change in ice concentration by lateral melt becomes for the J79-parametrisation

$$Q_L \stackrel{\text{J79}}{=} Q_{L_j} = -\frac{2}{L_i} A m_1 \Delta T_w^{m_2} \quad (2.20)$$

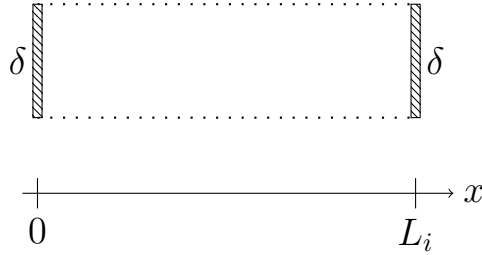


Figure 2.2: Sketch of a 1D ice floe of length L_i . Melting takes place at both shaded sides of length δ .

Final equation for ice concentration

Merging the parametrisations for Q_S (Equation (2.15)), Q_N (Equation (2.16)), and Q_L (Equations (2.17) and (2.20)) into Equation (2.11), the final prognostic equation for the ice concentration in a grid cell reads

$$\frac{\partial A}{\partial t} = -\nabla \cdot (A\vec{v}) - 0.5 \cdot \left(\sqrt{\epsilon_I^2 + (\epsilon_{II}/e)^2} - \epsilon_I \right) \cdot C(A) + \frac{1-A}{h_0} f(0) + \left\{ \begin{array}{l} \frac{A}{2H} \cdot f(H) \\ -2 \frac{A}{L_i} m_1 \Delta T_w^{m_2} \end{array} \right\} \quad (2.21)$$

The curly brackets hold the two different parametrisations of the lateral melt that will be used in this study.

2.2.3 Ice thickness

Derivation of the general equation (dynamic terms)

The prognostic equation for ice thickness H can be derived by combining the prognostic equation for ice concentration A and the conservation equation for ice mass per unit area ρh . Assuming that sea ice density is constant, the equation for mass conservation turns into an equation for conservation of sea ice volume per unit area, $h=AH$, (H79)

$$\frac{\partial AH}{\partial t} + \nabla(AH\vec{v}) = S_h \quad (2.22)$$

S_h subsumes all source and sink terms of ice volume per unit area that will be introduced later. By analogously summarising source and sink terms of ice concentration in S_A , Equation (2.11) is written as

$$\frac{\partial A}{\partial t} + \nabla(A\vec{v}) = S_A \quad (2.23)$$

Subtracting Equation (2.23) from Equation (2.22) yields a prognostic equation for ice thickness H (Appendix A.1):

$$\frac{\partial H}{\partial t} = -\vec{v}\nabla H + \frac{1}{A}S_h - \frac{H}{A}S_A \quad \text{if } A < 1 \quad (2.24)$$

It expresses that the ice thickness can be changed by advection of ice with different thickness ($-\vec{v}\nabla H$), by increase of the ice volume ($A^{-1}S_h$) or by spreading of ice over a different area ($-HA^{-1}S_A$).

However, this equation is only valid as long as the empirical law for the change of ice concentration (Equation (2.23)) is applicable. In the case that the sea surface is completely covered by sea ice (i.e. $A=1$) and convergent ice drift would lead to an unrealistic further increase of ice concentration, the restriction $A \leq 1$ has to be applied and thus $\partial A/\partial t \stackrel{!}{=} 0$ is used instead of Equation (2.23). This leads to a different equation for H (Appendix A.2):

$$\frac{\partial H}{\partial t} = -\vec{v}\nabla H - \underbrace{H\nabla \cdot \vec{v}}_a - \underbrace{\frac{\vec{v}H}{1}\nabla A}_b + S_h \quad \text{if } A=1 \quad (2.25)$$

In this case, two new terms appear: the ice thickness can increase by ridging or rafting of convergent ice (a) and decrease by advection of ice concentration (b). Term b is always negative because $A=100\%$ at the particular grid cell and thus only ice with *less* concentration can be advected from neighbouring cells. Hence, this term counteracts the increase of ice thickness by convergence.

Parametrisation of thermodynamic terms

In order to achieve a full equation for the ice thickness, the thermodynamic terms have to be specified. The ice volume per unit area can change by two thermodynamic processes: the production of new ice, V_{newice} , and the accretion or melting of already existing ice, $V_{existice}$:

$$S_h = V_{newice} + V_{existice} \quad (2.26)$$

These processes are parametrised by H79 as

$$V_{newice} = (1 - A) \cdot f(0) \quad (2.27)$$

$$V_{existice} = A \cdot f(H) \quad (2.28)$$

These parametrisations represent that new ice is generated with the rate $f(0)$ in the open water areas described by $(1 - A)$ and that the existing ice in the areas of A grows with the rate $f(H)$. If it is too warm to freeze sea water, $f(0)$ is zero, and if ice is melting, $f(H)$ becomes negative. As this study does not comprise thermodynamic models, simply, the values of the growth and melt rate f are taken from THORNDIKE et al. (1975), which were also used by H79. In order to make continuous calculations possible, the discrete values given by THORNDIKE et al. (1975) are interpolated utilising a fitting-function of the form $a/(b \cdot x + c)$ for the growth rate and a function of the form $a \cdot \exp((b \cdot x + c)^{-1})$ for the melt rate.

During melting conditions, ice floes can melt at their top or bottom ($V_{existice\updownarrow}$) as well as at their sides ($V_{existice\leftrightarrow}$). Both of these processes are included in HIBLER's parametrisation of $V_{existice} = A \cdot f(H)$ ($= V_{existice\updownarrow} + V_{existice\leftrightarrow}$). By applying Equation (2.17), he assumes that simply half of the ice volume loss $V_{existice}$ occurs at the floe sides, the other half reduces the floes' thickness.

When applying the parametrisation of J79, however, the change of ice volume by lateral melt is taken into account independently from vertical ice thickness changes. Thus, the ice thickness does not change if floes are melting laterally. Hence, the melt rate $f(H)$ describes only the ice loss at the top and the bottom of ice floes.

$$V_{existice\updownarrow} = A \cdot f(H) \quad (2.29)$$

The volume per unit area that is additionally lost at the sides of ice floes, $V_{existice\leftrightarrow}$, can be calculated from the reduction of the ice concentration Q_{L_j} (Equation (2.20)) by multiplication with the ice thickness of the melting ice floes:

$$V_{existice\leftrightarrow} = H \cdot Q_{L_j} \quad (2.30)$$

Final equation for ice thickness

A final prognostic equation for the ice thickness in a grid cell shall be compiled that covers all possible cases described in the last paragraphs: melting or freezing, the parametrisation of lateral melt by either H79 or J79, and the special case of a converging unbroken ice cover. Hence, the final equation is derived from the combination of the general Equations (2.24) and (2.25). For S_A , the parametrisations described in Section 2.2.2 are used. Applying the thermodynamic terms S_h from Equation (2.26) with the new ice formation given in Equation (2.27) and the change of old ice volume given either in Equation (2.28) or in Equations (2.29) and (2.30), respectively, yields

$$\frac{\partial H}{\partial t} = -\vec{v} \cdot (\nabla H) - H \nabla \cdot \vec{v} - \vec{v} H \nabla A + \frac{1}{2} f(H) + \left[1 - \frac{H}{h_0} \right] \frac{1-A}{A} \cdot f(0) + \frac{H}{A} Q_S \quad (2.31)$$

The red terms are only active if $A=1$ under **converging drift**, the blue terms are active if $A<1$, and the green factor appears from H79's parametrisation during **melt** if $A<1$.

2.2.4 Processes and their characteristic strength

In the last sections, the prognostic equations (2.10), (2.21), and (2.31) were introduced, that describe the development of the sea ice state in a grid cell, more exactly the development of the ice drift speed, the ice concentration, and the ice thickness. Each of these three variables is substitutionally called *target variable* $\chi \in \{\vec{v}, A, H\}$ hereafter. The prognostic equation for each target variable can, in general, be expressed in the form

$$\frac{\partial \chi}{\partial t} = \sum_i P_i \quad (2.32)$$

because the change of each target variable is caused by a superposition of different *processes* P_i . For example, the processes “wind stress” and “ocean stress” alter the target variable “ice drift speed”, or the processes “lateral melting” and “new ice formation” alter the target variable “ice concentration”.

For the further theoretical assessment, the processes are simplified and condensed in a way commonly used in scale analyses (PIELKE SR (2002), LEPPÄRANTA (2011a)): The variables (and even entire expressions) are replaced by their characteristic values. In this way, the magnitude of the terms in the equations resembles typical applications and, thus, the characteristic behaviour and influence of the particular processes can be studied. Table 2.1 shows how variables and terms of Equations (2.10), (2.21), and (2.31) are replaced by their characteristic values. Gradients of variables are discretised by use of a characteristic length scale for horizontal changes. Also, characteristic values were derived for more complex expressions; this can be found in Appendix B. Constants like e.g. the densities do not have to be replaced because their values are definite.

Table 2.1: Approximation of variables and expressions by their characteristic values used in the scale analyses.

Variable	Characteristic value	Expression	Characteristic value
\vec{v}	\mathcal{U}	$\nabla\vec{v}$	$\mathcal{U}/\mathcal{L}_U$
A	\mathcal{A}	∇A	$\mathcal{A}/\mathcal{L}_A$
H	\mathcal{H}	∇H	$\mathcal{H}/\mathcal{L}_H$
\vec{v}_{ag}	\mathcal{U}_{ag}		
\vec{v}_{wg}	\mathcal{U}_{wg}		
L_i	\mathcal{L}_i		
ΔT_w	$\Delta\mathcal{T}_w$		
Expression		Characteristic value	
$(\rho h)^{-1} \nabla \cdot \underline{\sigma}$		$(P^* C(\mathcal{A})) / (\mathcal{L}_\sigma \rho)$	
$0.5 \cdot \left(\sqrt{\dot{\epsilon}_I^2 + (\dot{\epsilon}_{II}/e)^2} - \dot{\epsilon}_I \right) \cdot C(A)$		$\lambda \mathcal{E}_{II}^* C(\mathcal{A})$	

Once characteristic values are introduced for all variables and expressions in the prognostic equations, the magnitude of each term, that belongs to a process P_i , can be determined. This magnitude is called (*characteristic*) *strength* \mathcal{P}_i in this study because the magnitude of a term in the prognostic equations indicates the effectiveness of its corresponding process. How the characteristic strength can be calculated from the characteristic values is listed in column 4 of Table 2.2 for each process of all prognostic equations (Eq.(2.10), (2.21), or (2.31), respectively) in the same order as given there. Column 2 provides a description of the process and column 3 defines an abbreviation for the process' name for later use.

For the momentum equation, the present study follows the scale analysis approach of LEPPÄRANTA (2011a), who does not consider the direction of the ice drift but only its absolute value: the drift speed U . Consequently, after the vectorial ice drift velocity is reduced to the scalar drift speed, the strengths of the processes do not depend on any rotating features: the turning angles θ_a and θ_w disappear from wind stress, AST, and ocean stress, OST, respectively, and the term $\vec{k} \times$ is not present in the strength of the acceleration by Coriolis force, COR, nor by the sea surface tilt, TIL.

Further on, in the formula for OST, the sign between \mathcal{U}_{wg} and \mathcal{U} might seem suspicious. The term in brackets in its original form $(\vec{v}_{wg} - \vec{v})^2$ would require information about the direction of

Table 2.2: Typical strength (column 4) of each process, in the order of occurrence in the prognostic equations (Eq.(2.10), (2.21), and (2.31)) (column 1). Column 2 provides a description of the process and column 3 defines an abbreviation for the process' name.

Eq.	Description of process P_i	Name	Typical strength \mathcal{P}_i
U	Advection of ice drift speed U	ADV	$\frac{U \cdot U}{\mathcal{L}_U}$
	Acceleration by Coriolis force	COR	fU
	Acceleration by atmospheric stress (wind)	AST	$\frac{\rho_a C_a}{\rho \mathcal{H}} \mathcal{U}_{ag}^2$
	Acceleration by ocean stress (current)	OST	$\frac{\rho_w C_w}{\rho \mathcal{H}} (\mathcal{U}_{wg} + U)^2$
	Acceleration by sea surface tilt	TIL	fU_{wg}
	Acceleration by internal forces	INT	$\frac{P^* C(\mathcal{A})}{2 \mathcal{L}_\sigma \rho}$
A	Advection of ice concentration A	ADV	$\frac{UA}{\mathcal{L}_A}$
	Change of A by divergent or convergent drift	DIV	$\frac{AU}{\mathcal{L}_U}$
	Reduction of A by open water creation due to shear	OWS	$\lambda \dot{\mathcal{E}}_{II} C(\mathcal{A})$
	Reduction of A by lateral melt (2 parametrisations)	LAMh	$\left\{ \begin{array}{l} \frac{A}{2\mathcal{H}} \cdot f(\mathcal{H}) \\ \frac{A}{2 \mathcal{L}_i} m_1 \Delta \mathcal{T}_w^{m_2} \end{array} \right\}$
		LAMj	
Increase of A due to formation of new ice	NEW	$\frac{1-A}{h_0} f(0)$	
H	Advection of ice thickness H	ADV	$\frac{UH}{\mathcal{L}_h}$
	Increase of H due to ridging/rafting if $A=1$	DIV	$[\mathcal{A}] \cdot \frac{HU}{\mathcal{L}_U}$
	(Vertical) melt or accretion of ice	GRW	$f(\mathcal{H})$
	Change of mean ice thickness by new ice formation	NEW	$\left \left[1 - \frac{\mathcal{H}}{h_0} \right] \frac{1-A}{A} \cdot f(0) \right $
	Increase of H when A is reduced by OWS	OWS	$\frac{\mathcal{H}}{A} \lambda \dot{\mathcal{E}}_{II} C(\mathcal{A})$

the ocean current and the ice drift. The value could range from $(|\overrightarrow{v_{wg}}| - |\vec{v}|)^2$ to $(|\overrightarrow{v_{wg}}| + |\vec{v}|)^2$. For the purpose of the present study, i.e. determining the relevance of different processes, the maximally possible value should be used. Thus, the upper bound $(\mathcal{U}_{wg} + \mathcal{U})^2$ is used for OST.

From the ice thickness equation Equation (2.31) the third term is disregarded to simplify the study. It is only active if $A=100\%$ and if convergent ice drift would lead to further, unrealistic increase of A . In this case, it reduces the increase of H if ice with low concentration is advected. However, it will never decrease H because then the prerequisites would not be fulfilled for it to become active in the first place. This means that the magnitude of this advection term (third term in Equation (2.31)) never exceeds the magnitude of the convergency term (second term in Equation (2.31)). Hence, only the latter is analysed afterwards.

Regarding the ice thickness processes, there are four more specialities that have to be explained: First, the red coloured terms in Equation (2.31) are only active if the ocean is fully ice-covered ($A=1$). To ensure that the strength of these terms is set to zero for $A<1$, the factor $[\mathcal{A}]$ is introduced in DIV. $[\mathcal{A}]$ is 1 if $A=1$, and 0 otherwise. Second, the green coloured factor $1/2$ in Equation (2.31) is only active if the lateral melt is parametrised following H79. Thus, this volatile factor is disregarded and does not appear in GRW because it is sufficient to use the upper bound of the process' strength, as just explained. Third, the f -function in GRW should specify either the growth rate or the melting rate, whatever is applicable. In order to avoid case differentiations and complying with the aim that upper bounds of the process' strengths should be determined, f is composed as combination of the growth and melt rates: For each ice thickness value, the larger one of the two absolute values of growth and melt rate is taken. And forth, the process of new ice formation, NEW, can either decrease or increase the ice thickness H , depending on the magnitude of H compared to the prescribed demarcation thickness h_0 . If new ice of thickness h_0 is produced within a field of thicker (thinner) ice than h_0 , the mean ice thickness would decrease (increase). Thus, the absolute value is used for the strength of this process, NEW, in order to obtain only positive values.

2.3 Impact-timescales

In Section 2.2 different processes P_i were introduced that influence the three target variables $\chi \in \{\vec{v}, A, H\}$. Each of these processes has its particular strength, thus some processes might influence the target variable more than other ones. In order to compare the impact-potential of the different processes, a so-named *impact-timescale* is introduced. It specifies how long it takes for a process to change the target variable by a certain amount. The motive is that a process can be rated “unimportant” if it has a large impact-timescale and thus needs much more time than other processes to achieve the same change of χ . Such a slow process with large impact-timescale

could be neglected for simulations with prognosis periods well below the impact-timescale. This simplifies the modelled system and reduces computational costs.

2.3.1 Derivation of impact-timescale

The impact-timescale can be derived from the prognostic Equation (2.32) for each target variable χ . Each process P_i contributes to the total change of χ . Assuming that the processes do not interact with one another, $\partial\chi/\partial t$ can be split up as

$$\frac{\partial\chi}{\partial t} = \sum_i \left. \frac{\partial\chi}{\partial t} \right|_i \quad (2.33)$$

where

$$\left. \frac{\partial\chi}{\partial t} \right|_i = P_i \quad (2.34)$$

represents that amount of the change in χ which is caused by the process P_i . By discretising and reordering, Equation (2.34) can be used to calculate the time that every process P_i needs to cause a certain impact $\Delta\chi$. This time is named impact-timescale \mathfrak{I}_i and it is determined from the characteristic strength \mathcal{P}_i of the process P_i by

$$\mathfrak{I}_i = \frac{\Delta\chi}{\mathcal{P}_i} \quad (2.35)$$

In order to compare the impact-timescales of all processes against each other, the same target impact (requested change) $\Delta\chi$ is used for all processes.

Calculation of \mathfrak{I}_i in this way implies two assumptions: 1) The strength, \mathcal{P}_i , of the investigated process P_i is constant during the time \mathfrak{I}_i , or to be precise \mathcal{P}_i specifies the average strength during this time. 2) During the time \mathfrak{I}_i , the different processes contribute linearly to changes in χ , which means they do not interact with one another. These assumptions are generally not fulfilled in nature but this simplified approach still provides an indication about the relative impact of the different processes.

2.3.2 Values for input variables

Before Equation (2.35) can be utilised to calculate the impact-timescale for all processes of the three prognostic equations, the strength, \mathcal{P}_i , of each process has to be determined. It depends on the characteristic value of different variables as shown in Table 2.2. These variables that define the magnitude of the processes are named *forcing variables*. Usually, there does not exist one characteristic value for each forcing variable but rather a range of characteristic values. The ranges chosen for this study are listed in Table 2.3. With these values for the forcing

variables and required constants (Table 2.4) the characteristic strength of each process \mathcal{P}_i can be calculated. This can then be used to calculate the impact-timescale \mathfrak{I}_i (Equation (2.35)).

For the impact-timescale calculation, also the target impact $\Delta\chi$ has to be prescribed. The same value $\Delta\chi$ is used for each process so that the relevance of the processes can be compared with each other. By choosing values for $\Delta\chi$ that reflect the desired accuracy of the sea ice model the processes can be rated with respect to their absolute relevance for the model simulation. Certainly, the desired accuracy depends on the purpose of the simulation, which for the present study is short-range sea ice forecasting in the Barents Sea region. Therefore, the accuracy is selected according to the needs of ship navigation, following the recommendations of the IICWG (2007): The ice concentration at each grid point should be predicted correctly to $\pm 10\%$ and the ice thickness to ± 10 cm. The accuracy for the ice drift speed can be deduced from the desired accuracy of the position of ice features (e.g. the ice edge). It is set to 5 km for a 3-day simulation, which corresponds to a deviation of one grid spacing in MESIM. To achieve this, the accuracy of the ice drift speed has to be $2 \cdot 5$ km/3 days if the error is assumed to increase linearly³. The mentioned accuracies are used as target impact $\Delta\chi$ for the calculations of the impact-timescales as summarised in Table 2.5.

2.3.3 Resulting impact-timescales

The impact-timescale is calculated from Equation (2.35) for every process of the prognostic equations (Table 2.2) separately. The calculation is repeated for all possible values of the respective forcing variables (Table 2.3), thus yielding a wide range of resultant impact-timescales for each process. In order to study how the impact-timescale is influenced by different ice conditions, the large range of possible characteristic values for the ice thickness \mathcal{H} is split up into the interval from 0.1 m to 2 m for first-year ice (including young ice; WMO, 1970) and the interval from 2 m to 3.5 m for multi-year ice. Likewise, the impact-timescales are calculated separately for different ice concentrations \mathcal{A} : low (1% to 30%), intermediate (30% to 80%), high (80% to 99%) and fully-covered (100%).

The findings are summarised in Figure 2.3 where the resultant range of impact-timescales is shown for each process. The results are split up in two graphics, one for first-year ice (Figure 2.3a) and one for multi-year ice (Figure 2.3b). The different categories of ice concentration can be distinguished by their colour and fill pattern.

³If the ice drift speed increases linearly from 0 km/day to ($2 \cdot 5$ km/3 days) within 3 days, the ice moves 5 km in 3 days. The same applies for the drift speed *error*.

Table 2.3: Ranges of characteristic values for the forcing variables.

Forcing variable	Range minimum	Range maximum	Comment
Ice drift speed \mathcal{U}	7.5 cm/s	20 cm/s	^a
Ice concentration \mathcal{A}	1 %	100 %	^b
Ice thickness \mathcal{H}	0.1 m	3.5 m	^c
Length scales $\mathcal{L}_U, \mathcal{L}_\sigma, \mathcal{L}_A$ and \mathcal{L}_H	10 km	1000 km	^d
Shear deformation $\dot{\mathcal{E}}_{II}$	10^{-7} s^{-1}	$1.5 \cdot 10^{-6} \text{ s}^{-1}$	^e
Water temperature above freezing point $\Delta\mathcal{T}_w$	0 K	1 K	^f
Length of ice floes \mathcal{L}_i	10 m	1000 m	^g
Geostrophic wind speed \mathcal{U}_{ag}	3 m/s	15 m/s	^h
Geostrophic ocean current \mathcal{U}_{wg}	1.5 cm/s	7.5 cm/s	ⁱ

^a HALLER et al. (2014): Median drift speed in Central Arctic and in Fram Strait.

^b Ice concentration of 0 % is not allowed, because in this case ice thickness/drift are not defined.

^c 10 cm is the lower bound of *Young Ice* (i.e. consolidated and not frazil ice) (WMO, 1970); 3.5 m is taken as mean thickness of old ice (MASLANIK et al., 2007). In Section 2.3.3, the range is split up into the interval 0.1–2 m, defined as first-year ice, and the interval 2–3.5 m, defined as multi-year ice.

^d adopted from LEPPÄRANTA (2011a).

^e MARSAN et al. (2004): Mean deformation rate at scale 160-320 km and 85%-percentile of deformation rate at 13-20 km scale (Assuming that shear rate and deformation rate are of the same scale).

^f Measurements during the Marginal Ice Zone Experiment (MIZEX) (MAYKUT and PEROVICH, 1987).

^g Ranging from small floes at the outer part of the MIZ (VINJE and KVAMBEKK, 1991) to almost closed pack ice.

^h Calculations from ECMWF analyses during drift experiment of DAMOCLES (HALLER et al., 2013).

ⁱ KWOK et al. (2013) found currents below 1–2 cm/s over most of the Arctic Ocean. The maximum is estimated from plots in KWOK and MORISON (2011) and KWOK et al. (2013).

Table 2.4: Values of constants used in the calculations.

Parameter	Symbol	Value	Comment
Density of sea ice	ρ	910 kg/m ³	^a
Density of air	ρ_a	1.3 kg/m ³	^a
Density of sea water	ρ_w	1000 kg/m ³	^a
Ice strength parameter	C^*	20	^a
Drag coefficient for air	C_a	$1.2 \cdot 10^{-3}$	^b
Drag coefficient for sea water	C_w	$5.5 \cdot 10^{-3}$	^b
Coriolis parameter	f	$1.43 \cdot 10^{-4}$ 1/s	^c
Demarcation thickness	h_0	30 cm	^d
Ice strength parameter	P^*	20000 N/m ²	^a

^a SCHRÖDER (2005)

^b HIBLER (1979)

^c valid for 80° N

^d BJORNSSON et al. (2001)

Table 2.5: Selected target impacts $\Delta\chi$ for the target variables.

Target variable	Target impact $\Delta\chi$	Explanation
Ice drift speed	$\Delta U = 2 \cdot 5000 \text{ m} / (3 \cdot 86400 \text{ s})$ $\approx 0.04 \text{ m/s}$	Position of the ice edge predicted correctly to the accuracy of 1 grid spacing (5 km) after a 3-day simulation.
Ice concentration	$\Delta A = 0.1$	Ice concentration predicted correctly to the accuracy of 10% (IICWG, 2007).
Ice thickness	$\Delta H = 0.1 \text{ m}$	Ice thickness predicted correctly to the accuracy of 10 cm (IICWG, 2007).

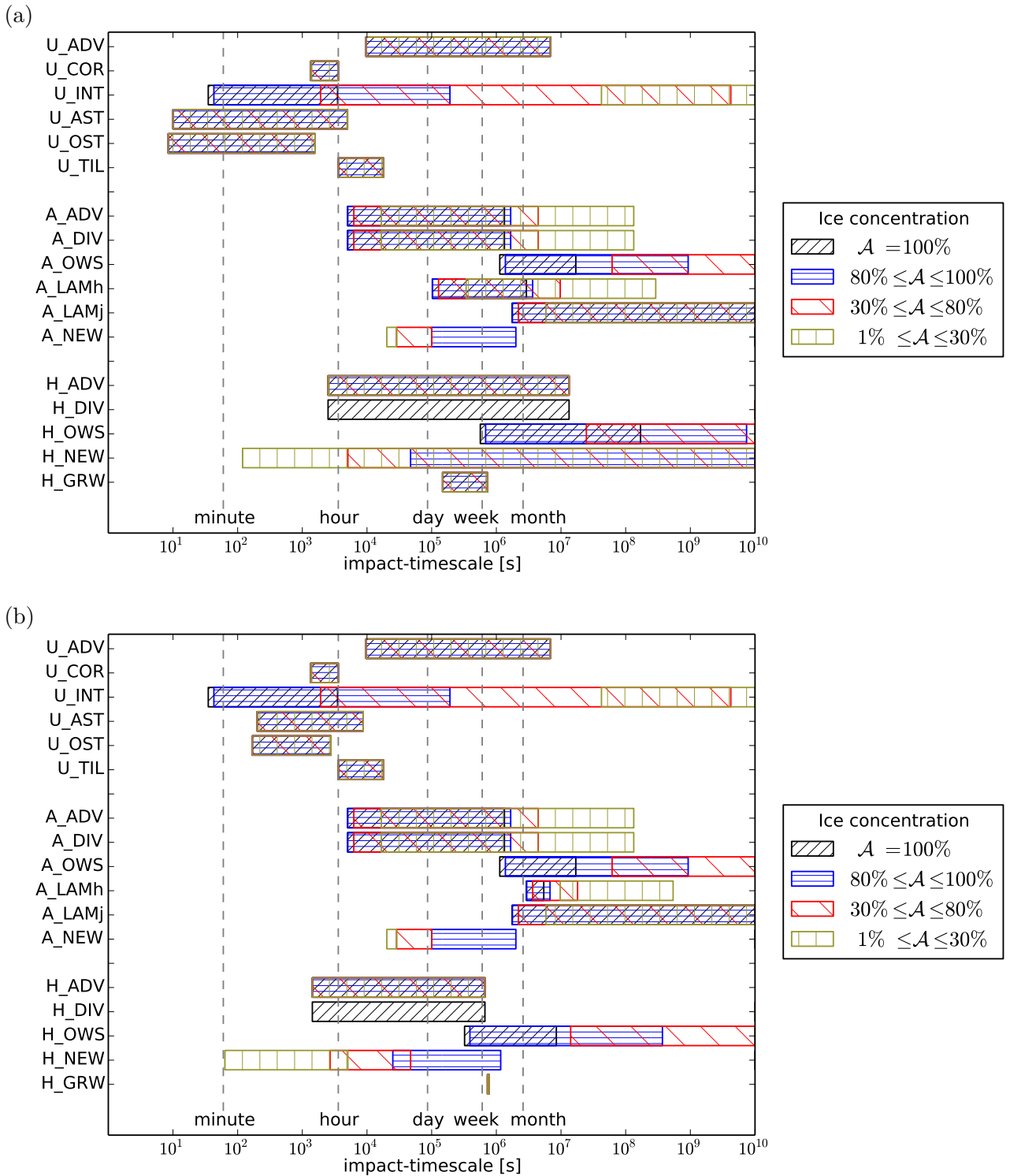


Figure 2.3: Ranges of impact-timescales \mathfrak{I}_i for (a) first-year ice and (b) multi-year ice. The bars show the possible values of \mathfrak{I}_i for all processes in the prognostic equations of U (upper part), A (middle part) and H (lower part) that result from applying ranges of characteristic values for the forcing variables. The ranges of applied ice concentration values are highlighted by different colour/pattern. The x-axis is limited to 10^{10} s and dashed lines mark common time units.

First-year ice

For the equation of ice drift speed, the impact-timescales of the processes (marked with “U_” in Figure 2.3a) do not depend on ice concentration except for the internal forces, **INT**. These can cause changes of $\Delta U \approx 4 \text{ cm s}^{-1}$ in the ice drift speed in less than 1 hour if the ocean is fully ice-covered. In less dense ice conditions however, the ice is more free to move and thus internal forces in the ice can hardly built up. This results in large impact-timescales for low ice concentrations. The process of momentum advection, **ADV**, is also slow compared to the remaining processes. At least several hours up to months are necessary for ADV to induce the ΔU , depending on the prevailing drift speed and its spatial gradient. The Coriolis force, **COR**, or the downhill-slope force of the tilted sea surface, **TIL**, are able to provoke the same change in only about one hour. The stresses by atmospheric winds, **AST**, and by ocean currents, **OST**, need even less: These forces could accelerate the ice to 4 cm s^{-1} in less than a minute in the case of very thin ice because the mass of the ice is so small that the inertia effect, that has to be overcome, is very small.

These results compare well with the summary of LEPPÄRANTA (2011a) who rates the terms of the momentum equation by their characteristic scale: The advection has a scale of 10^{-4} Pa and thus it is less relevant than COR, TIL (both 10^{-2} Pa), AST and OST (both 10^{-1} Pa). This behaviour is reflected by the impact-timescales that state a quick impact of AST and OST on U . The internal forces, INT, have a fairly large impact-timescale for $\mathcal{A} < 80\%$, which also corresponds to LEPPÄRANTA (2011a).

The middle part of Figure 2.3a shows the impact-timescales of the processes for the prognostic equation of ice concentration (marked with “A_”). A change of $\Delta A = 10 \%$ can be provoked by advection of ice, **ADV**, or diverging/converging drift, **DIV**, in about one hour in favourable conditions. The position of the right side of the bars, however, indicates that it also can take several weeks if the ice conditions inhibit ADV and DIV. This is the case if the spatial distribution of ice concentration and drift is homogeneous so that \mathcal{L}_A and \mathcal{L}_U are large, which decreases ADV and DIV, respectively (Table 2.2). **OWS** has also an impact-timescale of more than several weeks. It denotes the process, that open water areas arise if leads are created by shear stress within the ice. If the ice concentration is very low, there is little possibility for shear stress and open-water creation, thus the impact-timescale is very large for $\mathcal{A} < 80\%$. Similar impact-timescales are valid for **LAMj**, i.e. the process of lateral melt of ice floes in the formulation of J79 that takes into account the size of the ice floes. The impact-timescales for LAMj are hardly sensitive to \mathcal{A} but rather to the floe size \mathcal{L}_i , which explains the range of the bar: If the floes are small, there is a large melting area at the floes’ sides which amplifies the process. If the floe size \mathcal{L}_i is very large, however, the lateral melt of ice, LAMj, is small (Table 2.2) which leads to very large impact-timescales. Interesting is the comparison of LAMj to the other parametrisation of

the same process, namely **LAMh** by H79. In this case, the lateral melt rate does not depend on the size of ice floes, but it is set to a certain fraction of the vertical melt rate. If the ice is thin, the relative melt rate $f(\mathcal{H})/\mathcal{H}$ is high. Thus, a large area of ice (Equation (2.17)) disappears by melting, especially if the ice concentration is high. This causes the lower impact-timescale of LAMh compared to LAMj. Which of these two parametrisations is more accurate cannot be evaluated here. At least, the results correspond to the statement of MAYKUT and PEROVICH (1987) that the parametrisation by J79 underestimates the lateral melt rate compared to a field measurement. The process **NEW**, that specifies the formation of new ice in open water areas, has an impact-timescale of hours to weeks. This range is mostly generated by variations of \mathcal{A} : New ice formation is less effective if most of the area is already covered with ice. The impact-timescale of NEW is, however, also sensitive to the choice of the demarcation thickness h_0 . If new ice is accumulated only up to a thickness of 10 cm instead of 30 cm, which might happen in calm situations, the ocean surface could freeze over more rapidly. This results in a smaller impact-timescale.

Summing up, the ice concentration can be changed fastest by ADV and DIV, if the conditions are favourable, or by formation of new ice, NEW, in large open water areas. In contrast, OWS and LAM are comparatively slow.

The impact-timescales of the processes that affect the ice thickness are shown in the bottom part of Figure 2.3a (marked with “H_”). The advection of ice thickness, **ADV**, can cause a change of $\Delta H = 10$ cm in various times. Its impact-timescale depends mainly on the length scale of ice thickness changes, \mathcal{L}_H , which leads to an intensification of ADV if \mathcal{L}_H is low (Table 2.2). The possible range of impact-timescales from one hour to several months is equally resulting for the process **DIV**, i.e. the increase of ice thickness by piling-up of ice during convergent ice drift. However, this process becomes only active, if the ocean is fully ice-covered and the convergence cannot be compensated by an increase of ice concentration. The ice thickness can also be changed thermodynamically by accretion or vertical melting of ice, **GRW**. The growth and melt rates from THORNDIKE et al. (1975) yield impact-timescales of several days for GRW, independent of the current ice concentration. Much faster may act the process of new ice formation, **NEW**. It does not only alter the ice concentration but also causes changes of the ice thickness, ΔH . As H specifies the average thickness of ice floes, it will decrease if new, thin ice is added to a grid cell. Thus, this process has a low impact-timescale especially if the open water areas are large (\mathcal{A} is low). The bar in Figure 2.3a reveals that the impact-timescale of NEW can also be very large. This is the case, if the mean ice thickness, which is varied between 0.1 m and 2 m (Table 2.3), by chance equals the thickness of the newly formed ice (i.e. the demarcation thickness h_0). Then, new ice formation cannot alter the mean ice thickness which results in infinitely large impact-timescales. This points out that for NEW, the impact-timescale is more

a result of the definition of H , being a mean value, than results of a physical process. This issue, however, is only present for sea ice models that define only one ice thickness value per grid cell. If a model does differentiate between several ice thickness classes, only the mean ice thickness of the class for the thinnest ice would change. All other classes are not affected by new ice formation. So, the impact-timescale for NEW strongly depends on the model characteristics. The process **OWS** increases the ice thickness as a consequence of the open water production due to shear. If leads open up during shear, the remaining ice cover becomes thicker by ridging or rafting. Figure 2.3a, however, shows that this impact is very slow and a ΔH of 10 cm can at the best be achieved after one week. This is the consequence of the large impact-timescale which was found for OWS when acting on A . It demonstrates that OWS is a slow process in general.

In total, the mean ice thickness is quickest affected by ADV, DIV, and NEW, depending on the particular conditions. GRW might become important for longer simulations, while OWS has a too large impact-timescale to be relevant for short-range forecasts.

Multi-year ice

In the case that the ice thickness exceeds 2 m (multi-year ice), the resulting impact-timescales differ from the ones for thinner (first-year) ice in some aspects. The comparison of Figure 2.3a and Figure 2.3b affirms that the processes of the ice drift equation do not depend on the ice thickness, except for AST and OST. These processes embodying atmospheric and oceanic stresses are slower for thicker ice because then the same external force has to accelerate more ice mass. Thus, the impact-timescales of AST and OST for an acceleration by $\Delta U \approx 4 \text{ cm s}^{-1}$ increase to at least 100 s for the chosen characteristic values. This is still short compared to the other processes, so AST and OST, together with INT, are the dominating processes also for thick ice.

In the equation for ice concentration, only LAMh, the lateral melt of ice floes in the parametrisation by H79, depends on the ice thickness. LAMh is parametrised to be a portion of the relative vertical melt rate $f(\mathcal{H})/\mathcal{H}$. For thick ice, the relative melt rate is small and thus LAMh is little effective. The impact-timescale of LAMh then exceeds one month, which is close to the value of the other parametrisation LAMj.

The most extensive dependencies on ice thickness occur in the prognostic equation for the ice thickness itself. The impact-timescale of every process changes if the ice is thicker. However, the general picture of the relevance of the processes remains unchanged. The fastest process, NEW, has an even lower impact-timescale if the ice is thicker. This, however, again is an effect of the definition of H being an average value: If the same area of new ice is generated in a field of thicker ice, the average ice thickness in this ice field is reduced more than if the existing ice was

thinner and closer to h_0 , the thickness of the newly formed ice. Further, the impact-timescale of NEW is not only lower for multi-year ice but it also does not become infinite as it does for first-year ice. The reason is that multi-year ice, defined as ice being thicker than 2 m, is thicker than h_0 . Thus, it is not possible that the mean ice thickness remains unchanged by new ice formation. The processes ADV and DIV also have a lower impact-timescale for thicker ice. DIV depends on \mathcal{H} (Table 2.2) because the accumulation of ice by convergent drift is more efficient the more ice mass is transported. ADV can faster produce the ΔH because the spatial distribution of ice thickness ∇H is assumed to correlate with \mathcal{H} (Table 2.1). The impact-timescale of OWS is slightly reduced for thicker ice because, then, more ice mass is redistributed when the same area of leads opens up as in regions with thinner ice. The process of thermodynamic vertical growth or melting of ice (GRW) is the only process whose impact-timescale increases for increasing ice thickness. This effect is not caused by the melt rate, which is almost independent from ice thickness, but from the growth rate: thick ice grows slower than thin ice because it insulates itself more effectively from the cold atmosphere. Therefore, the impact-timescale of GRW is increased to more than a week for thick ice.

2.3.4 Discussion of determined impact-timescales

In Section 2.3.3, the calculated impact-timescales were presented. They indicate how long each process needs for changing its corresponding target variable U , A or H by $\approx 4 \text{ cm s}^{-1}$, 10% or 10 cm, respectively. The results depend on the environmental conditions. Therefore, ranges of impact-timescales are presented rather than single values. These arise only from variations of the forcing variable values and do not represent any uncertainty that could stem from empirically determined constants of parametrisations.

By comparing the impact-timescales of all processes, their respective relevance for the target variable can be estimated. If the chosen value of $\Delta\chi$ specifies the desired accuracy, also the absolute relevance of the processes in a sea ice simulation can be rated. This is done here exemplarily for a short-range forecast of sea ice conditions over 3 days, as it is planned to be conducted with the model MESIM. All processes of the ice drift equation have impact-timescales shorter than 3 days. This means that each of them can change the ice drift speed considerably within 3 days. Thus, none of them can be disregarded totally in the simulation. However, internal forces, INT, and the advection of momentum, ADV, are only relevant under certain conditions: If the ice concentration is below 80%, INT has a larger impact-timescale than 3 days. ADV depends on \mathcal{L}_U (Table 2.2), and thus it is not relevant if the characteristic length scale for changes in the drift speed is small.

When it comes to the ice concentration as target variable, the open water production due to

shear, OWS, is so slow that it does not induce any notable influence within 3 days. However, this reflects only the effect on A . In addition, open water areas produced by OWS would also affect e.g. the sensible heat flux to the atmosphere. As already a change of 1% in ice concentration can alter the near-surface temperature up to 3.5 K (LÜPKES et al., 2008), OWS might still play an important role in coupled atmosphere-ice models. The lateral melting of ice floes also has a large impact-timescale, especially for thick multi-year ice. In case of thinner ice, the result depends on the chosen parametrisation. These findings correspond to STEELE (1992), who showed that lateral melt is only important for ice floes smaller than 30 m in diameter. All other processes affecting A have, in general, to be considered in a 3-day simulation, as do most of the processes affecting the ice thickness H . Only OWS acts so slow that it is not relevant for an ice thickness forecast for 3 days. The thermodynamic growth, GRW, is unimportant for multi-year ice, which is indeed known to grow dynamically by ridging/rafting rather than thermodynamically (FLATO, 1995). Other processes like e.g. DIV are only relevant in certain conditions, but they cannot generally be disregarded.

The presented analysis can help identifying relevant processes for certain applications. However, it is sometimes difficult to estimate the characteristic values of the input variables correctly. This regards for example the spatial gradients of various quantities. In this study, a characteristic length scale for changes is set for each gradient, but other approaches might be necessary to define more reliable values. Additionally, the two assumptions have to be kept in mind that were made during the derivation of the impact-timescales. Firstly, no interactions between processes are permitted, so they are treated as if they would act independently and solely. The importance of these interactions might be non-negligible, so an investigation by a model study that considers interactions would be required. Secondly, it is assumed that the strength of each process is constant with time. How fast the strength of processes changes if the forcing variables vary, will be analysed in Section 2.4.

2.4 Update-timescales

Section 2.3 discussed the relevance of the processes that affect ice drift speed, ice concentration and ice thickness. Rating them with the impact-timescale revealed that few processes can be neglected, which reduces the complexity of a sea-ice model only slightly. Therefore, an other possibility for simplification is introduced in this section.

Even though a process cannot be neglected, its strength might be constant for a characteristic time. This can be taken advantage of in the following way: The model calculates the magnitude of the process' term initially, and then uses it in the prognostic equation for several model time steps. The magnitude of the process' term is recalculated only after a certain characteristic

time, the so-named *update-timescale*. It quantifies for how long each process can be treated as constant in time. In other words, the update-timescale is a measure of how fast the strength of each process changes over time.

An example can illustrate the advantages of large update-timescales for model optimisation: if ice drift was stationary, the Coriolis force COR, which indeed is relevant for the prognostic equation of ice drift, would be constant over time. Then it would be sufficient to calculate the value of COR only once and reuse it in the prognostic equation every time step. If the ice drift changes slowly, COR has to be recalculated at some point. If it has a large update-timescale, however, the recalculations are rare, which saves computational costs without losing accuracy in the forecast results.

2.4.1 Error induced by keeping processes constant

For deriving the update-timescale, first the error has to be determined that arises from keeping a process constant. This is done by introducing an integral function that describes the temporal development of the error: Investigating the prognostic equations of the target variables $\chi \in \{\vec{v}, A, H\}$, it is obvious that the strength of each process depends on one or more forcing variables (e.g. the wind speed or the ice concentration, see Table 2.2). Every forcing variable is collectively called ψ hereafter, like target variables are called χ . Each process P_i depends on an own set of forcing variables $\psi \in \mathcal{F}_i$.

$$P_i = P_i(\mathcal{F}_i) = P_i(\{\psi_1, \psi_2, \dots, \psi_{m(i)}\}) \quad (2.36)$$

The value of each forcing variable changes over time. Thus, Equation (2.34) can by use of Equation (2.36) be written as

$$\left. \frac{\partial \chi}{\partial t} \right|_i = P_i(\mathcal{F}_i) = P_i(\{\psi_1(t), \psi_2(t), \dots, \psi_{m(i)}(t)\}) \quad (2.37)$$

Two cases are assumed for each process: In case I, all forcing variables $\psi \in \mathcal{F}_i$ are set to a constant value. Thus, the strength of the process \mathcal{P}_i is also constant. In case II, the forcing variables change over time in a linear manner:

$$\text{Case I: } \psi = \Psi = \text{const} \quad \forall \psi \in \mathcal{F}_i \quad (2.38)$$

$$\text{Case II: } \psi(t) = \Psi \pm \dot{\Psi} \cdot t \quad \forall \psi \in \mathcal{F}_i \quad (2.39)$$

Ψ is a characteristic value for the forcing variable ψ and $\dot{\Psi}$ is a value for a characteristic temporal change of ψ . Equation (2.37) is integrated over time for each process P_i and for both cases I and II. In this, special attention has to be paid to processes which depend on several forcing

variables. In case I, all forcing variables are set constant but in case II, each of them is changing according to Equation (2.39) at the same time. Accidentally, a change of one forcing variable just cancels the change caused by another forcing variable. This effect is undesired because the *maximal* error is to be identified that could arise from keeping processes constant. Thus to avoid cancellation, first, the impact of each forcing variable ψ on its associated process is examined: would the strength of the process increase or decrease if ψ increases? With this knowledge, the changes of the forcing variables can be combined in such way that the strength \mathcal{P}_i is either increased by *every* forcing variable or decreased by *every* forcing variable. To achieve this, the appropriate sign in Equation (2.39) is used for each forcing variable. In case II^\oplus the signs are chosen so that \mathcal{P}_i increases while in case II^\ominus , the changing forcing variables all contribute to a decrease of \mathcal{P}_i .

Equation (2.37) is integrated over time for case II^\oplus and case II^\ominus separately. The resulting values $\chi_i^{\text{II}^\oplus}(t)$ and $\chi_i^{\text{II}^\ominus}(t)$, respectively, specify the development of the target variable where the forcing variables change with time. In contrast, $\chi_i^{\text{I}}(t)$, for case I, represents the development that would emerge if the forcing was constant. The difference between both cases

$$E(t)_i = \max \left(\left| \chi_i^{\text{I}}(t) - \chi_i^{\text{II}^\oplus}(t) \right|, \left| \chi_i^{\text{I}}(t) - \chi_i^{\text{II}^\ominus}(t) \right| \right) \quad (2.40)$$

can thus be interpreted as the maximum error that arises from the assumption of constant forcing variables.

Two assumptions are made during this derivation: First, the processes do not interact with each other so that Equation (2.37) can be integrated for each process separately. Second, the forcing variables in case II are supposed to change linearly over time, which is a crude approximation. Despite these assumptions, the study should reveal some indications for the process' sensitivity on changing forcing variables.

The integration of Equation (2.37) to calculate the development of the target variables is conducted numerically. Usually, the time step, Δt , has to be chosen small enough to ensure numerical stability of the integration algorithm (DURRAN, 2010). This is different for Equation (2.37) because it is not a differential equation. Even though it stands for the differential equations (2.10), (2.21), and (2.31)), it represents a simplification of them because the target variables on the left hand side are dissociated from the forcing variables on the right hand side. Target variables and forcing variables are treated as independent from each other even though they may represent the same physical quantity. As χ does not appear on the right hand side, the integration of Equation (2.37) does not require considerations about the numerical stability of the solution algorithm. The length of the time step, Δt , only determines the accuracy of the numerical quadrature, i.e. how accurate the integral $\int_a^b \chi(t)dt$ is approximated by the sum $\sum_{t=a}^b \chi(t)\Delta t$.

The time step, Δt , is set to 0.1 seconds for all numerical calculations which regard the update-timescales. This value proved to be small enough for an accurate numeric integration as the results stay the same even if a larger time step $\Delta t=1$ s were used.

2.4.2 Characteristic values used

With the method introduced above, the error development can be determined for each process. For this, the strengths \mathcal{P}_i are calculated according to Table 2.2, however with a small modification to NEW: The formula that calculates the impact of NEW on H contains an absolute value because no negative values were desired for the impact-timescale calculation. For the update-timescale calculation, however, a change of the sign of a process matters during time integration. Thus, the absolute value of NEW is disregarded hereafter. For all other processes, the sign of the process does not change within the time integration. Thus, no attention has to be paid to their sign: No matter if Equation (2.37) were integrated using $-\mathcal{P}_i$ instead of \mathcal{P}_i , the error calculation (Equation (2.40)) would yield the same result because the sign is cancelled out by the absolute value.

For the calculation of the errors, two sets of characteristic values are required. Firstly, values for characteristic temporal changes $\dot{\Psi}$ of the forcing variables have to be set. In order to avoid underestimation of the error development, a value for a *characteristic maximum change* shall be used. By this, Equation (2.40) yields an upper bound of the resulting error. The final decision about which forcing variables are treated as time-dependent and what is their assumed change rate, has to be made adequately for each intended application; the values used in this study are listed in Table 2.6. The application of a change rate to a forcing variable can lead to unrealistic values. To avoid this, the forcing variables are bound to the minimum and maximum values given in Table 2.6. These values do not specify the range of *characteristic* values like in Table 2.3, but they are rather chosen to represent the range of *possible* and realistic values. They rely on considerations about which magnitudes are rather unlikely to occur in the Barents Sea. Furthermore, ice concentration and ice thickness are prevented to become zero wherever they appear in the denominator of a process. There, the minimum ice concentration is set to 1% and the minimum ice thickness to 1 mm.

Secondly, characteristic values Ψ have to be found for the “initial state” from which the integration starts. Here, the values were chosen so that they lie in the range given in Table 2.3. The initial values for Ψ are listed in Table 2.7. The choice of the initial state—especially of ice concentration and ice thickness—can highly influence the resulting error developments. Thus, Section 2.4.5 will enlarge upon the dependency of the update-timescale on the initial values of A and H .

Table 2.6: Values of characteristic change rates (column 2) of the forcing variables used in the calculations. Column 3 and 4 specify the allowed range for changed forcing variables.

Forcing variable	Change rate $\dot{\Psi}$		Minimum for Ψ	Maximum for Ψ
Ice drift speed	$\frac{0.2 \text{ m/s}}{6 \cdot 3600 \text{ s}}$	<i>a</i>	0 m/s	0.7 m/s
Ice concentration	$\frac{100\% \cdot 0.1 \text{ m/s}}{5000 \text{ m}}$	<i>b</i>	0 %	100 %
Ice thickness	$\frac{1 \text{ m} \cdot 0.1 \text{ m/s}}{5000 \text{ m}}$	<i>c</i>	0 m	4 m
Shear deformation	$\frac{1 \cdot 10^{-6} \text{ s}^{-1}}{86400 \text{ s}}$	<i>d</i>	0 s ⁻¹	$1 \cdot 10^{-4} \text{ s}^{-1}$
Water temperature above freezing point	$\frac{1 \text{ K}}{10 \cdot 86400 \text{ s}}$	<i>e</i>	0 K	5 K
Geostrophic wind speed	$\frac{1 \text{ m/s}}{3600 \text{ s}}$	<i>f</i>	0 m/s	30 m/s
Geostrophic ocean current	$\frac{1 \text{ cm/s}}{86400 \text{ s}}$	<i>g</i>	0 cm/s	20 cm/s

^aThe ice drift of 0.1 m/s changes its sign within half of a M2-tidal-period (6 hours). This value corresponds to the maximum ice drift found in the time series in CHMEL et al. (2010).

^bA non-broken ice cover ($A=100\%$) is advected with a speed of 0.1 m/s into an ice-free grid cell of length $\Delta x=5000$ m.

^cA non-broken ice cover of 1 m thickness is advected with a speed of 0.1 m/s into an ice-free grid cell of length $\Delta x=5000$ m.

^dThe ice dynamics with a characteristic value of $1 \cdot 10^{-6} \text{ s}^{-1}$ for the shear changes within 1 day.

^eWhile ice is present, water temperature changes slowly with 1 K within 10 days.

^fWind speed changes by 1 m/s in 1 hour. This is the 95-percentile of hourly wind speed data (10 m height) measured during SHEBA (<http://www.atmos.washington.edu/~roode/SHEBA.nc.readme.html>).

^gThe geostrophic current is rather stationary, thus a change of 1 cm per day is assumed.

Table 2.7: Values of the initial state of the forcing variables used in the calculations.

Value Ψ of forcing variables for the initial state		
Ice drift speed \mathcal{U}	0.1 m/s	^a
Ice concentration \mathcal{A}	90 %	^b
Ice thickness \mathcal{H}	1 m	^c
Length scales $\mathcal{L}_U, \mathcal{L}_\sigma, \mathcal{L}_A$ and \mathcal{L}_H	100 km	^d
Shear deformation $\dot{\mathcal{E}}_{II}$	$0.75 \cdot 10^{-6} \text{ s}^{-1}$	^e
Water temperature above freezing point $\Delta\mathcal{T}_w$	0.5 K	^e
Length of ice floes \mathcal{L}_i	100 m	^d
Geostrophic wind speed \mathcal{U}_{ag}	9 m/s	^e
Geostrophic ocean current \mathcal{U}_{wg}	4.5 cm/s	^e

^aThis is the characteristic value usually used for ice drift (LEPPÄRANTA, 2011b).

^bA rather high value is used so that internal forces are relevant. Update-timescales for different values of \mathcal{A} are presented in Section 2.4.5.

^cUpdate-timescales for different values of \mathcal{H} are presented in Section 2.4.5.

^dMean order of magnitude of characteristic values as given in Table 2.3.

^eMean value within the range of characteristic values as given in Table 2.3.

2.4.3 Temporal development of errors

The error that arises if a certain processes is spuriously treated as stationary, is calculated from Equation (2.40) by using the values given in Section 2.4.2. Exemplarily, the results for the ice drift equation are shown in Figure 2.4. The dashed lines depict the error that occurs if single processes are kept constant. At the beginning of the integration, the errors are zero, and they grow with increasing time. If, for example, AST is kept constant by fixing the wind speed and the ice thickness (Table 2.2), then the inaccurate value of AST would induce a deviation in the ice drift speed of 1 cm/s after about 20 minutes. If the ocean stress (OST) is kept constant, the same deviation is generated after 17 minutes already. The reason is i.a. that OST depends on three instead of two forcing variables (\vec{v}_{wg} , \vec{v} , and H for OST instead of \vec{v}_{ag} and H for AST) that all would change over time and thus contribute to the total error.

It is noticeable that in general those processes that have a small impact-timescale (Figure 2.3) also cause errors quickly, for example like AST, OST and COR compared to ADV. A small impact-timescale implies that the process has a large impact on the target variable; hence, also errors associated with this process will affect the target variable quickly. An exception is TIL: although its impact-timescale is only a bit larger than that of COR, it will cause errors very much slower, simply because its forcing variable does change slowly. This kind of information is contained in the update-timescale.

2.4.4 Determination of update-timescale

Figure 2.4 shows how the error increases with time, that is introduced by assuming processes to be constant. At a certain time, the error will eventually become so large that it noticeably affects the result of the simulation. In order to avoid this, and to keep the error below a given limit E_{max} after the simulation time t_{sim} , the process' value has to be updated regularly, i.e. its strength has to be recalculated every now and then. This section explains how the length of this update interval can be determined.

If a process is permanently kept constant, the induced error normally increases over time. In general, it cannot be assumed that the growth of the error slows down by itself at some time. This implies that e.g. after half of the simulation period, t_{sim} , an error not more than half of the total allowed limit, E_{max} , should be accumulated. Generalised this means that the error $E(t)$ after any time t of the simulation must not exceed a fraction of t/t_{sim} of the total error E_{max} . The development of the allowed error $\hat{E}(t)$ thus can be represented as the straight line

$$\hat{E}(t) = \frac{E_{max}}{t_{sim}} \cdot t \quad (2.41)$$

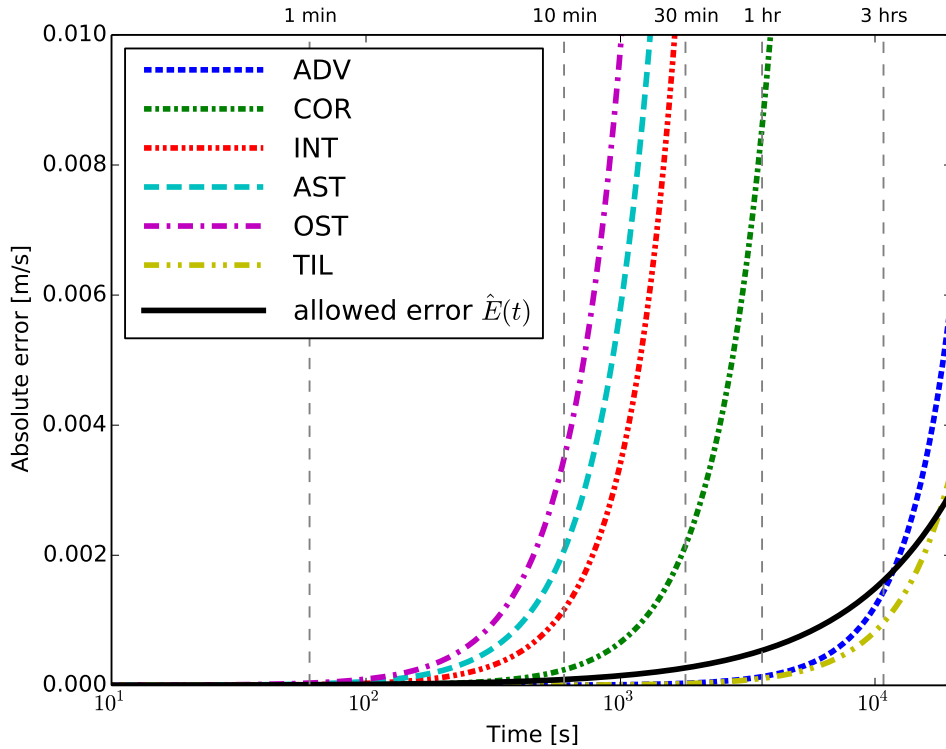


Figure 2.4: Temporal development of the error in the predicted ice drift speed that arises if the particular process (dashed line) is kept constant. The solid line represents the development of the allowed error $\hat{E}(t)$ mentioned in Section 2.4.4.

which is shown as black, solid line in Figure 2.4 (Note the logarithmic scale.). If the process is kept constant only for a certain time t_{upd} and is then updated, the error accumulation is intermitted and starts again. This behaviour is schematically depicted in Figure 2.5 for some fictional process. In order to certainly meet the given limit E_{max} at the end of the simulation, the error curve has to stay below the straight line $\hat{E}(t)$. This is achieved by updating the process as soon as its error reaches the straight line. Thus, the update time t_{upd} can be determined from the intersection point of the original error curve $E(t)$ and its limiting function $\hat{E}(t)$.

For calculating the update times, the total limit E_{max} and the simulation time t_{sim} have to be chosen according to the planned application. For the present study, the same accuary values as used in Section 2.3.2 for the impact-timescale analysis (Table 2.5) are selected for E_{max} regarding ice drift speed, ice concentration and ice thickness, respectively. These error limits shall be met after a simulation time, t_{sim} , of 3 days.

With these values, the update times can be determined for all processes of the prognostic equations for ice drift speed, ice concentration and ice thickness. The error development is calculated

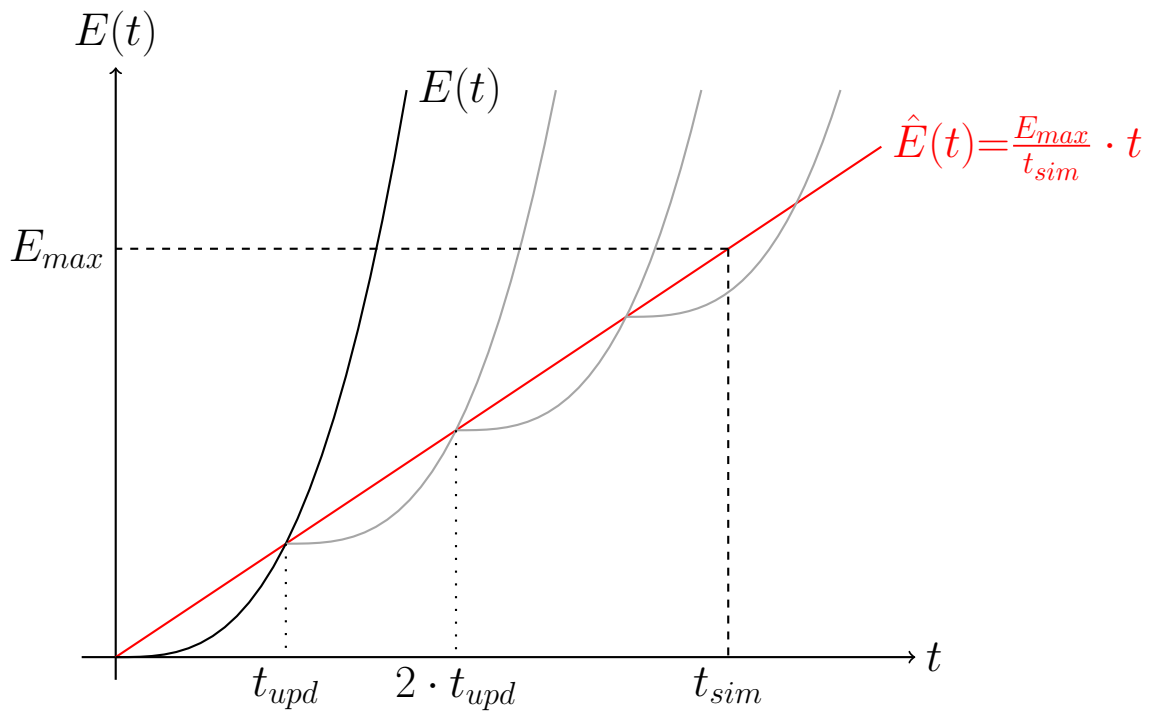


Figure 2.5: Schematic diagram of the temporal error development $E(t)$ (black) of a fictional process if its strength is kept permanently constant. If the process is recalculated after the update interval t_{upt} , its actual error (grey) will never exceed the error limit function $\hat{E}(t)$ (red). In this way, the predefined total allowed error E_{max} at the end of the simulation t_{sim} can be met.

numerically from Equation (2.40) for each process and the intersection point with the error limit function Equation (2.41) is determined. The time after which the intersection point is reached specifies the update-interval that states how long the process can be treated as constant. The results are presented and discussed in Sections 2.4.5 and 2.4.6.

2.4.5 Dependency of the update-timescales on ice thickness and ice concentration

The update-intervals introduced in Section 2.4.4 provide information about how long each process can be treated as constant during the simulation. Their values vary for different environmental conditions (initial states). Especially the prevailing ice concentration and ice thickness can strongly affect the results. Moreover, these quantities are highly variable within a model domain. In order to study their impact, the update-timescales are calculated for initial ice concentrations \mathcal{A} between 0% and 100% and for initial ice thicknesses \mathcal{H} between 0 m and 4 m. The results are presented in the next paragraphs.

Update-timescales of processes depending neither on \mathcal{A} nor on \mathcal{H}

There are three processes which do neither depend on ice concentration nor on ice thickness. These are the advection of momentum, **ADV**, the effect of the Coriolis force, **COR**, and the acceleration by the tilted ocean surface, **TIL**. They all affect the target variable ice drift speed. Their update-timescales can be seen in Figure 2.6. If it is required that the ice edge is predicted with an accuracy of 5 km after 3 days of simulation (Table 2.5), the advection of momentum could be assumed to be constant for 3 hours before its value has to be updated. TIL is almost constant for 5 hours, while the Coriolis force should be recalculated every 4 minutes.

The results show that the update-timescale is controlled by two effects: On the one hand, processes like TIL, whose forcing variables change very slowly, are relatively stationary and thus have a large update-timescale. On the other hand, also processes with fast changing forcing variables can have a large update-timescale if their impact on the target variable is weak. This relevance for the target variable is rated by the impact-timescale (Section 2.3), so that impact-timescale and update-timescale may be correlated. This is e.g. true for ADV and COR: Both depend only on the drift speed \mathcal{U} , which varies equally for both ADV and COR. However, the update-timescale of ADV is much larger than that of COR because the impact-timescale of ADV is larger (Figure 2.3). Any error induced by spuriously keeping ADV constant will affect the target variable less (compared to COR), which allows for longer update intervals.

Comparing COR with TIL however shows that the update-timescale still can provide information in addition to that of the impact-timescale: Even though the impact-timescale of TIL is only

slightly larger than that of COR (Figure 2.3), their update-timescales are very different. This is a consequence of the slowly varying forcing variable \mathcal{U}_{wg} , that impacts TIL. Because the forcing variable of COR, \mathcal{U} , varies a lot faster, COR has to be updated earlier than TIL. So, the update-timescale carries exactly this kind of information: How often a process has to be recalculated because of its changing forcing variables.

Using the current parametrisation, TIL does not include any tidal effects but rather reacts on large scale changes of the geostrophic ocean current speed \mathcal{U}_{wg} . Tides would influence the ocean surface elevation on much shorter timescales, so if their effect were considered in the analysis, TIL would be more variable. This would lead to a shorter update-timescale.

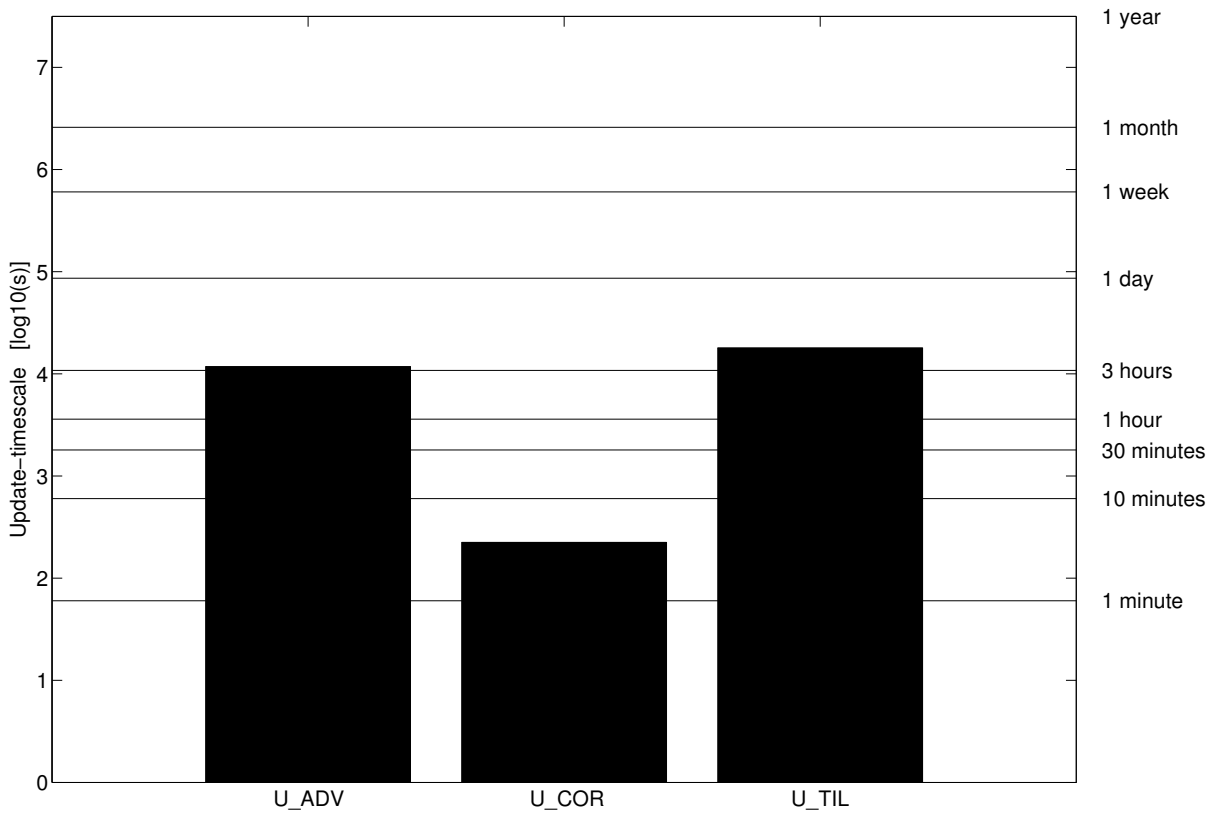


Figure 2.6: Update-timescales of processes depending neither on ice concentration nor on ice thickness. The prefix letter specifies the corresponding target variable of the process.

Update-timescales of processes depending on \mathcal{A} , but not on \mathcal{H}

Six processes of Table 2.2 show a dependency on the ice concentration, \mathcal{A} , and not on the ice thickness, \mathcal{H} . One of them, the effect of internal forces, INT, influences the target variable drift speed; the others contribute to the prognostic equation of ice concentration. In Figure 2.7, the calculated update-timescales are displayed for each process. They are a function of the initial

ice concentration (Table 2.7), that is varied between 0% and 100%. The applied error limit is $\pm 10\%$ after a 3-day simulation. The \mathcal{A} -dependency is not visible for **LAMj** because the update-timescale is always larger than 1 year. This corresponds to the large impact-timescale that was found for LAMj (Figure 2.3). The update-timescale of new ice formation, **NEW**, is about 2 hours and does not depend on \mathcal{A} . Even though the strength of NEW is influenced by \mathcal{A} , there is no influence on the update-timescale because this term cancels in the error calculation (subtraction in Equation (2.40)). Therefore, the time after which NEW has to be recalculated is only controlled by the assumed change rate $\dot{\Psi}$ for ice concentration (Table 2.6) and not by the chosen initial value of \mathcal{A} .

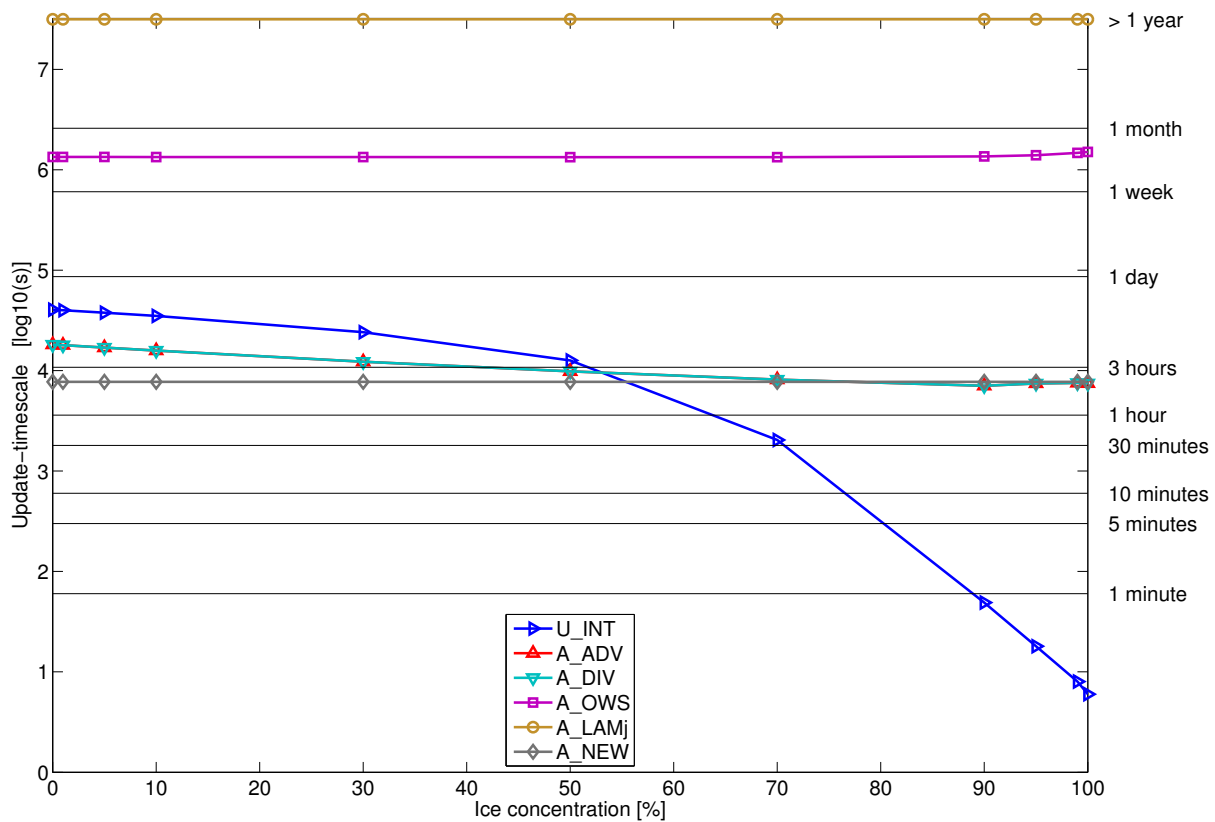


Figure 2.7: Update-timescales of processes depending on ice concentration but not on ice thickness. The prefix letter specifies the corresponding target variable of the process. The initial value is varied between 0% and 100%.

The update-timescale of the open water production due to shear, **OWS**, is quite large regardless of \mathcal{A} and has a value of about 16 days. Advection of ice concentration, **ADV**, and the change of ice concentration by divergence or convergence, **DIV**, have the same update-timescale because the parameters to calculate their characteristic strengths are set equal. For low ice concentration, ADV and DIV can be kept constant for 5 hours. If the concentration increases, more ice is

available to be advected or to be collected by convergence. Thus, variations of the drift speed \mathcal{U} , that acts as forcing variable of ADV and DIV, are the more important the larger \mathcal{A} becomes. Therefore, ADV and DIV should be updated already after 2 hours in regions with high ice concentration.

INT is the only process in Figure 2.7 that affects the ice drift speed as target variable. It has a much more pronounced \mathcal{A} -dependency of its update-timescale than the other processes in this figure. In cases of low ice concentration, the update-timescale is up to 11 hours; it decreases to 3.5 hours at 50% ice concentration and drops below 1 minute for $\mathcal{A} > 90\%$. This behaviour corresponds well to the impact-timescale: INT can quickly impact the drift speed if the ice concentration is high (Figure 2.3). Additionally, the errors arising from keeping \mathcal{A} constant in time are the more relevant for INT the higher the ice concentration because the $C(\mathcal{A})$ -function (Equation (2.8)) is not linear. In consequence, INT should be recalculated very quickly. Indeed, many algorithms for calculation of the ice drift speed use iterative methods in conjunction with the internal forces.

Update-timescales of processes depending on \mathcal{H} but not on \mathcal{A}

Four processes of Table 2.2 depend on the ice thickness, \mathcal{H} , and not on the ice concentration, \mathcal{A} . Their update-timescales are calculated for initial ice thicknesses between 0 m and 4 m. The results are shown in Figure 2.8. The processes ADV and GRW affect the prognostic equation of ice thickness, for which the error limit after a 3-day simulation was set to 10 cm. For **GRW**, the vertical growth or melt of ice, the update-timescale suggests recalculations after 1 hour for very thin ice. For thick ice, however, the process has to be updated only every 3 days. The reason is that for thin ice, the growth rate changes a lot if the thickness changes slightly, while for thicker ice, the growth rate is less sensitive. Thus, keeping \mathcal{H} constant leads to errors more quickly if the ice is thin than if it is thick.

The \mathcal{H} -dependency is reversed for the advection of ice thickness, **ADV**. Following the results in Figure 2.8, ADV can be kept constant for 5 hours if the ice is thin. If the ice thickness is large, more ice mass is available to be advected. Thus, an inaccurate value of the forcing variable ice drift speed, \mathcal{U} , which is responsible for the advection, induces larger errors if the ice is thick. Therefore, the update-timescale of ADV decreases to 30 minutes for thick ice (4 m).

The other two processes in Figure 2.8, **OST** and **AST**, affect the ice drift speed as target variable. For ice with 4 m thickness, the results show update-timescales of 1 and 2 minutes, respectively. For thin ice, the update-timescales approach zero. Thin ice has a low ice mass, so varying forcing variables like wind and current can affect the drift speed more efficiently for thin ice than if they had to accelerate the large ice mass of thick ice. Even though one objective

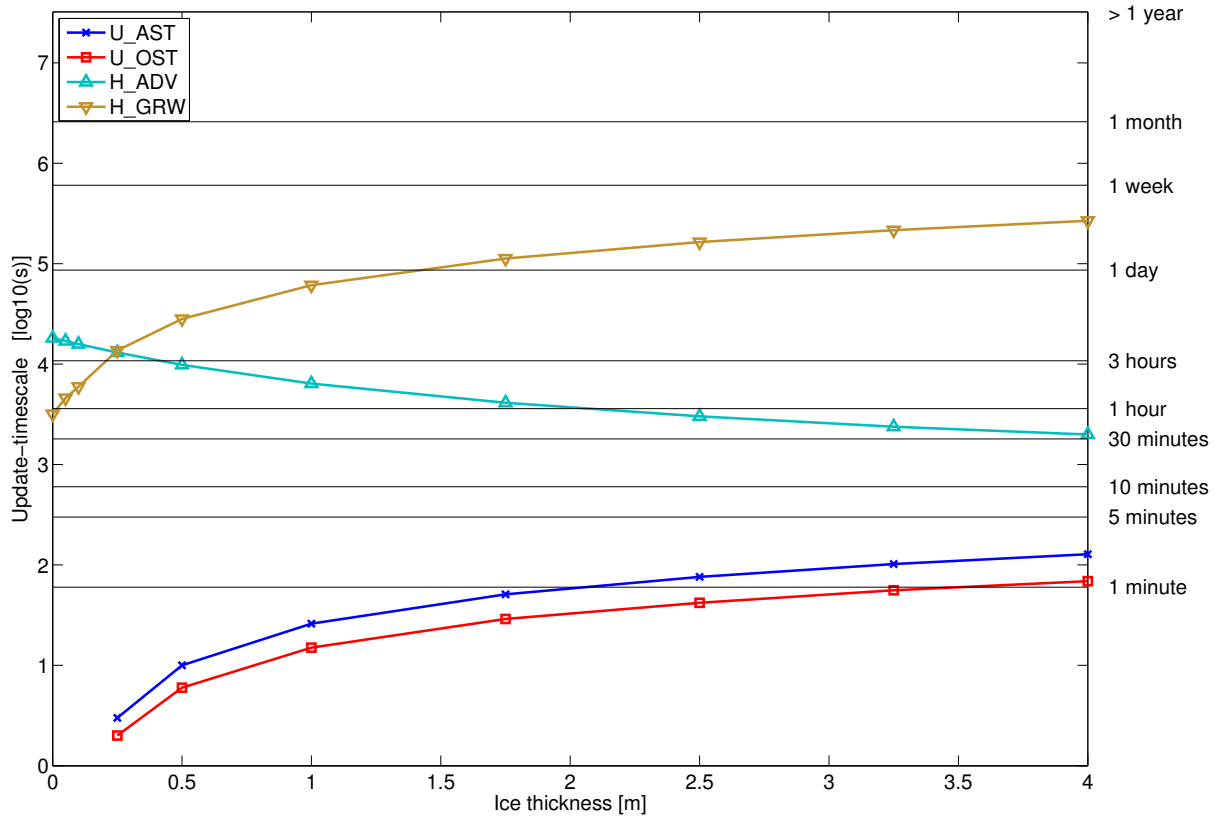


Figure 2.8: Update-timescales of processes depending only on ice thickness but not on ice concentration. The prefix letter specifies the corresponding target variable of the process. The initial value is varied between 0 m and 4 m.

of the study is to determine *upper bounds* of the errors which results in lower bounds for the update-timescales, the values appear to be implausibly small: For most models, they are smaller than the typical model time step. However, they are not wrong per se, but the results point to the limits of this theoretical analysis: The assumption that processes do not interact with each other is invalid for AST and OST. In reality, if the wind freshens, the ice would be accelerated, which in turn would increase the friction between ice and ocean. Likewise, the internal forces INT would compensate for an increased drift speed by providing additional friction. By this, the forces in the momentum equation are in a quasistatic equilibrium (KLEINE and SKLYAR, 1995, page 193). However, as these moderating interactions between different processes are not accounted for, the analysis suggests very small update-timescales. Another reason might be that the values for the characteristic change of the forcing variables (Table 2.6) lead to an overestimation of the errors. The applied values are rather valid for short time periods. The timescale analysis implicitly assumes that these change rates would last for the whole simulation. All the more, the resulting update-timescales have to be read as lower bounds for the updating

intervals. Nonetheless, the general statement that the update-timescales of OST and AST are small, might not be that wrong. Observations show that in some cases the ice drift reacts quickly to changing winds (BRÜMMER et al., 2003). Keeping AST constant for too long could then lead to large errors.

Update-timescales of processes depending on \mathcal{A} and \mathcal{H}

The update-timescale of four processes depends on the environmental conditions for both ice concentration and ice thickness. Three of them belong to the prognostic equation of ice thickness, the other one affects the ice concentration. The latter is **LAMh**, i.e. H79's parametrisation of lateral melt of ice floes. Figure 2.9a shows its update-timescales for the initial state varied as combinations of ice concentration (between 0% and 100%) and ice thickness (between 0 m and 4 m). The update-timescale of LAMh strongly depends on \mathcal{H} : The thinner the ice the smaller is the update-timescale; for 5 cm thick ice, the update-timescale is 12 minutes for fully ice-covered situations and 40 minutes for open water. For 4-m-thick ice, LAMh has to be updated only every 2 days. This behaviour is very consistent with the calculated impact-timescales. This suggests that the \mathcal{A} -and- \mathcal{H} -dependency of the update-timescales is governed by the \mathcal{A} -and- \mathcal{H} -dependency of the impact-timescale of LAMh. For ice thinner than 5 cm, the determined update-timescale is surprisingly small. This results from the parametrisation approach: In contrast to LAMj (Figure 2.7), the lateral melt with the parametrisation LAMh is directly connected to the vertical ablation of ice floes by the conversion factor $\mathcal{A}/2\mathcal{H}$. Thus, if the ice is thin, the magnitude of LAMh is large, and it is very sensitive to \mathcal{A} and \mathcal{H} . Therefore, small deviations cause large errors. Thus, the short update interval for very thin ice is necessary not because of a high variability of the process but rather because of the parametrisation approach of LAMh that has \mathcal{H} in the denominator.

The processes shown in Figures 2.9b, 2.9c, and 2.9d belong to the prognostic equation for ice thickness. The update-timescale of the change of ice thickness related to shear in the ice cover, **OWS**, is shown in Figure 2.9b. It is only weakly depending on the initial state of ice concentration and ice thickness, and it ranges from 2.5 days to 4.5 days. Recalling that the impact-timescale of OWS is larger than several days (Figure 2.3) explains also the large update-timescale: An erroneous value of OWS, that is induced by keeping OWS constant, has only little effect on the target variable H because OWS has such a small impact on H as stated by its impact-timescale. Hence in general, a large impact-timescale prevents that errors affect the target variable, and, thus, it promotes large update-timescales.

The process that changes the mean ice thickness in a grid cell if new ice is forming, **NEW**, has to be updated much earlier: Figure 2.9c shows that its update-timescales typically are about half an hour. Only for thin ice with high ice concentration, errors that arise from keeping the process

constant are less important and the update interval can be increased to 5.5 hours. For small ice concentrations, however, the update-timescale is very low. The reason is that in this case NEW is very sensitive to changes of the forcing variables because of the small \mathcal{A} in the denominator (Table 2.2). A conspicuous local maximum is located at an ice thickness of about 30 cm, which was chosen as demarcation thickness. Similarly to the impact-timescale, the update-timescale is increased here because the mean ice thickness is insensitive to errors during new ice formation if the ambient ice thickness equals the ice thickness of the newly formed ice. Furthermore, the update-timescale increases for initial ice thickness approaching 0 m. This feature is connected to the limitation that the forcing variable \mathcal{H} cannot decrease below 0 m: As soon as \mathcal{H} reaches 0 m, the forcing does not change any further, such that keeping the process constant does not lead to larger errors. The fact that the update-timescale of NEW is quite small for a thermodynamic process is not due to physical properties of the process. It is rather connected to the approach of using only one ice thickness value H , that represents the *mean* ice floe thickness in a grid cell. Another model approach, e.g. used by BIRNBAUM (1998), allows for several ice thickness categories. This means that several ice thickness values exist for a grid cell and that each of them represents the mean floe thickness of its corresponding category, e.g. 'new ice', 'thin ice', and 'thick ice'. With this approach, new ice growth, NEW, would only affect the thickness of the 'new ice'-category and not that of the 'thick ice'-category. For these target variables, the timescales would look different than for H .

Figure 2.9d shows the update-timescale of the ice thickness change by convergent ice drift, **DIV**. It is not distinctly depending on the ice thickness but rather on ice concentration: In cases with much open water, DIV can be kept constant for up to 14 hours. If the ice concentration increases, DIV has to be recalculated more often. The reason is that DIV only becomes active if the ice concentration is 100%. If the initial value of the ice concentration is already very high, it is more likely that the model develops a closed ice cover and that DIV has to be activated. If DIV is not recalculated often enough, this regime change can be missed. Thus, the update-timescale is low for high initial ice concentrations. Only for thin ice below 20 cm, the update-timescale does not drop below 3 hours: Even if the onset of DIV is missed for thin ice, there is not much ice volume available that could be piled-up and that could effectively change the ice thickness during convergence. Therefore, the error stays small for thin ice and the update-timescale is large.

2.4.6 Discussion of determined update-timescales

The update-timescale provides information about the time interval after which the strength of a particular process has to be recalculated so that a proposed accuracy of the target variable

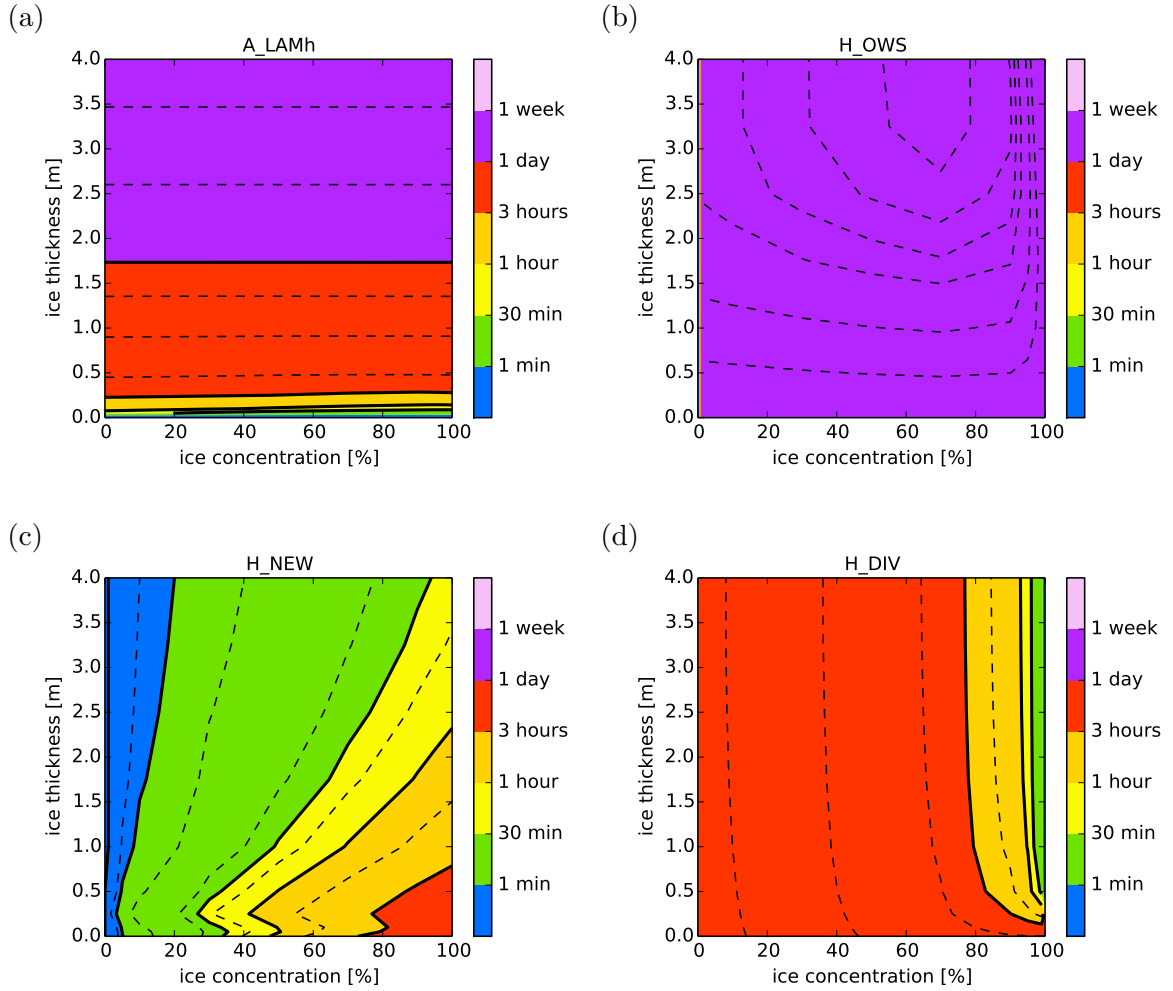


Figure 2.9: Update-timescales of processes depending on ice concentration and ice thickness: (a) A_LAMh; (b) H_OWS; (c) H_NEW; (d) H_DIV. The prefix letter specifies the corresponding target variable of the named process. The dashed lines are additional isolines at arbitrary intervals to highlight the contour shape. The initial state is varied between 0% and 100% for ice concentration and between 0 m and 4 m for ice thickness. The used steps are for ice concentration 0%, 1%, 5%, 10%, 30%, 50%, 70%, 90%, 95%, 99%, and 100% and for ice thickness 0 m, 0.05 m, 0.10 m, 0.25 m, 0.50 m, 1.00 m, 1.75 m, 2.50 m, 3.25 m, and 4.00 m.

will be achieved. The values of the update-timescales that are found for the given initial state (Table 2.7) and a set of characteristic change rates of forcing variables (Table 2.6) are summarised in Table 2.8. If the update-timescale depends on ice concentration and/or ice thickness, the resulting minimum value is given. The summary reveals that the update-timescales can be very different, also for processes contributing to the same prognostic equation. The largest update-timescales are found in the ice concentration equation for OWS and LAMj. In the ice thickness equation, also OWS has to be updated only rarely. Regarding the ice drift equation, the processes ADV and TIL have comparatively long update-timescales.

This knowledge can be valuable for model optimisation. A large update-timescale of a process indicates that its strength only has to be recalculated once in a while. Thus, computational costs can be saved without losing model accuracy. The implementation in the model could be realised by a time-splitting method, which allows for calculation of different processes with different time steps like e.g. applied by SKAMAROCK and KLEMP (1994).

Even though the update-timescale is naturally correlated to the impact-timescale, it carries some additional information which can be used by modellers: If a process is not negligible (i.e. it has a low impact-timescale), its update-timescale can still be so large that it is justified to keep the process constant. This is the case for the process TIL as the present study revealed. Its impact-timescale is only slightly larger than that of the Coriolis force, which means that TIL has an considerable impact on the ice drift speed. Despite TIL cannot be neglected, the update-timescale of more than 5 hours indicates that the model could be simplified by recalculating the value of TIL only every 5 hours.

The update-timescale results have to be interpreted with care because some assumptions made are not fulfilled in nature. For example, the change of forcing variables is assumed to be linear. This is certainly not true for long time periods. As the change rate was selected to represent a characteristic *maximal* change, the assumed linearity leads to an overestimation of the total change. Hence, the resulting update-timescales might be too short and less frequent updating could still be sufficient to meet the proposed model accuracy. In contrast, the update-timescale can also be underestimated: The analysis neglects feedbacks of processes whose target variable also appears as their forcing variable. An example is new ice formation NEW, that increases the ice concentration. If there is much open-water as initial state, NEW is very strong because the ice concentration \mathcal{A} appears after the minus sign in Table 2.2. Thus, the intense new ice formation closes the open water area quickly. In turn, NEW becomes weaker because the open water fraction $(1 - \mathcal{A})$ is reduced. In this study, however, this feedback is not taken into account but the forcing variable \mathcal{A} is varied according to its given characteristic change rate value. For self-reinforcing processes, this shortcoming could underestimate the necessary update-timescale.

Table 2.8: Summary of update-timescales for the processes of the prognostic equations for ice drift speed (Equation (2.10)), ice concentration (Equation (2.21)), and ice thickness (Equation (2.31)) (column 1). For processes whose update-timescale depends on ice concentration and/or ice thickness a minimum value is given. Abbreviations of process' names (column 2) are explained in Table 2.2.

Eq.	Process	Update-timescale
U	ADV	3 hours
	COR	6 minutes
	AST	< 2 minutes
	OST	< 1 minute
	TIL	5 hours
	INT	5 minutes if $\mathcal{A} < 80\%$ ≤ 50 seconds, if $\mathcal{A} \geq 90\%$
A	ADV	2 hours
	DIV	2 hours
	OWS	15 days
	LAMh	40 minutes if $\mathcal{H} > 5$ cm ≤ 12 minutes if $\mathcal{H} \leq 5$ cm
	LAMj	> 1 year
	NEW	2 hours
H	ADV	30 minutes
	DIV	45 minutes if $\mathcal{A} \leq 95\%$ ≤ 9 minutes if $\mathcal{A} \geq 99\%$
	GRW	50 minutes
	NEW	3 minutes if $\mathcal{A} \geq 20\%$ ≤ 20 seconds if $\mathcal{A} \leq 10\%$
	OWS	2.5 days if $\mathcal{A} \geq 1\%$

The analysis of the update-timescale furtheron does not consider the whole range of possible variability of a process. Not all parameters that determine the process' strength have been varied using a characteristic change rate of forcing variables. Yet, also parameters that are used as constants during the analysis actually vary in nature. For example C_a , the drag coefficient between wind and sea ice in AST, shows "considerable day-to-day variability" (OVERLAND and COLONY, 1994). The negligence of such variations could at worst reduce the actual update-timescale.

2.5 Conclusion

With the presented methods, impact-timescales and update-timescales of physical processes can be determined. The analysis is conducted in the present study for the prognostic equations of ice drift speed, ice concentration and ice thickness for a specific set of environmental conditions. The **impact-timescale** turns out to be one week or longer for 1) lateral melting of ice floes parametrised according to JOSBERGER (1979) (LAMj), 2) open water production due to shear within the ice drift field (OWS), and 3) accretion or melt (GRW) of thick ice. The **update-timescale** of the processes affecting the ice drift speed is in the region of minutes, excluding the advection of momentum (ADV) and the acceleration by sea surface tilt (TIL), which have update-timescales of 3 and 5 hours. The processes contributing to the ice concentration equation and ice thickness equation have update-timescales larger than 2 hours and 30 minutes, respectively. Exceptions arise not by physics but from the formulation of the process parametrisation. This occurs for the lateral melt of ice floes parametrised by HIBLER (1979) (LAMh) and the formation of new ice (NEW) in regions with much open water.

Utilising the information given by impact-timescale and update-timescale, numerical models can be inspected for optimisation possibilities. A model that is based on the equations presented in this study and that is applied for the given environmental conditions could thus be streamlined in two ways: a) Concluding from their impact-timescales, LAMj and OWS are irrelevant for the modelling result so they could be disregarded. The same is true for GRW if the model domain does not include thin ice. b) Concluding from their update-timescale, the strength of TIL and the momentum advection, ADV, does only have to be recalculated every 3 and 5 hours, respectively. Meanwhile, their value can be kept constant. For the equations of ice concentration and ice thickness, a time-splitting scheme might be appropriate: Because of LAMh and NEW, which have small update-timescales, the equations have to be evaluated frequently (in the order of minutes). The other processes, however, do only have to be recalculated every 2 hours for the ice concentration equation and every 30 minutes for the ice thickness equation, respectively.

This study is limited by the assumption that the processes and prognostic equations act in-

2.5 Conclusion

dependently from each other. In reality, for example, newly formed ice will also be subjected to advection, or it will be rafted during convergence. Additionally, ice concentration changes will affect the internal forces and thus alter the ice drift. These effects are not taken into account by the impact-timescales and update-timescales, and a further study is needed to rate the importance of these interactions for the timescales.

The presented methods can also be extended to other prognostic equations. For example, instead of the mean ice floe thickness of a grid cell, a study could analyse the processes that determine the ice thickness distribution in a grid cell. BITZ (2008) states that those equations indeed are increasingly used in recent sea ice models.

3 Development of the short-range forecast system

Sea ice is changing on different time scales (Chapter 2), and accurate forecasts of its behaviour are demanded from different users ranging from climate scientists to shipping companies. Sea ice predictions can be produced by means of numerical models. Thus, in Section 3.1, a numerical model system is introduced which is able to simulate the sea ice behaviour that is relevant for shipping activities. This implies the need for high spatial resolution and the ability to simulate sea ice changes at time scales of the order of days. Hence, resulting from Chapter 2, the model system has to consider impacts from both the atmosphere and the ocean. Such a complex model system requires much computational efforts. Nevertheless, sea ice forecasts are the more valuable the earlier they can be provided. Thus, two optimisations of the model system, which reduce the computational costs, are presented in Section 3.2.

3.1 Model system

The model system used in this study was developed by members of the University of Hamburg during the project IRO-2 “Ice Forecast and Route Optimisation”. As basis of this model system called HAMMER (HAMburger für Mesoskalige Eisvorhersage und Routenoptimierung) there were two appropriate sea ice models available for which expertise existed within the project group. A comparison of both models’ features is given in Appendix C and lead to the decision for the model MESIM. In this section, the layout of the model system, HAMMER, based on MESIM is described as it is used throughout the remaining parts of this thesis.

3.1.1 Sea ice model MESIM

MESIM is a mesoscale sea ice model that was developed by BIRNBAUM (1998) from a large scale model from FISCHER (1995) and HARDER (1996). The dynamic part of MESIM originates from the sea ice model by HIBLER (1979), while the thermodynamic part follows the approach of MAYKUT and UNTERSTEINER (1971). After some improvements concerning boundary conditions and the calculation of the surface temperature (DIERER, 2002) MESIM has successfully been applied for investigations of the interaction between sea ice and Arctic cyclones (DIERER et al., 2005).

Basically, MESIM solves the three main sea ice equations discussed in Chapter 2: Equation (2.2) being the prognostic equation for ice drift velocity, \vec{v} , Equation (2.11) as prognostic equation for the ice concentration, A , and Equation (2.22), which gives the ice volume per unit area, h

(Figure 2.1). The main difference is that MESIM categorises the ice into 4 ice classes, c , according to its thickness (< 10 cm, 10 cm – 40 cm, 40 cm – 1 m, and > 1 m). This means that in one grid cell there can be up to 4 types of ice, each with a specific ice concentration, A_c , and a specific ice volume per unit area, h_c . Naturally, they total to the overall ice concentration A and ice volume per unit area, h , as

$$\sum_c A_c = A \quad (3.1)$$

and

$$\sum_c h_c = h \quad (3.2)$$

Therefore, MESIM actually solves the prognostic equations Equation (2.11) and Equation (2.22) for each ice class separately. These can be written in the following way

$$\frac{\partial A_c}{\partial t} = -\nabla \cdot (A_c \vec{v}) + S_{A,c} \quad (3.3)$$

$$\frac{\partial h_c}{\partial t} = -\nabla \cdot (h_c \vec{v}) + S_{h,c} \quad (3.4)$$

where a similar nomenclature to that in Equation (2.23) is used: $S_{A,c}$ subsumes all source and sink terms of ice concentration in ice class c and $S_{h,c}$ subsumes all source and sink terms of ice volume per unit area in ice class c . METRAS considers the same sources and sinks as described in Sections 2.2.2 and 2.2.3: Open water formation due to shear, new ice formation, growth or melt of existing ice, and lateral melt of ice floes. For latter, the parametrisation of J79 is used.

In order to determine the growth and melt rates that were prescribed as $f(0)$ and $f(H)$ in Chapter 2, MESIM has a thermodynamic module that uses the approach of MAYKUT and UNTERSTEINER (1971). Their one-dimensional multilayer model allows for non-linear temperature gradients within the ice (and the snow) which favours the accurate simulation of the ice surface temperature. Thus, the amount of melting or growing ice can be determined realistically. However, this feature could not be made use of during this study due to technical problems, that remained unresolvable during the limited study period. Therefore, the thermodynamic part of MESIM will not be described here but information about it can be found in BIRNBAUM (1998) and SCHLÜNZEN et al. (2012).

In addition to the budget equation for ice concentration and ice volume per unit area, MESIM has two further sets of prognostic equations: Firstly, the length of ice floes in each ice class can be simulated. It changes by lateral melt of ice floes and by the advection of different ice floes. Secondly, snow can lie on top of the ice floes of all ice classes. The snow thickness influences the heat flux through the ice in the thermodynamic module. MESIM takes care of the correct dynamical redistribution of the snow during the simulation.

For determining transport processes in the budget equation, MESIM calculates the ice drift velocity from Equation (2.2). The internal forces are parametrised by the viscous-plastic rheology of HIBLER (1979) as shortly explained after Equation (2.6). A more detailed description of this rheology and the used elliptic yield curve can be found in ÓLASON (2012). Different parametrisations compared to those defined in Chapter 2 are used in MESIM for the wind stress $\vec{\tau}_a$ and the ocean stress $\vec{\tau}_w$. They are quite sophisticated and do take into account not only the respective speeds of wind, current, and ice but also the stratification of the atmospheric boundary layer as well as the so-called form drag. An additional drag from the wind acts on the freeboard of the ice floes because they jut out of the water surface. The same applies for the draught of the ice floes which provides a target for the ocean current. These effects are taken into account by the parametrisations in MESIM. The equations are applied for each ice class c separately. Afterwards, total values for $\vec{\tau}_a$ and $\vec{\tau}_w$ are calculated as averages over all ice classes weighted by their particular ice concentration A_c .

The parametrisation of wind stress in each ice class c is

$$\vec{\tau}_{a,c} = \left[\tau_{a,s,c} + \frac{1}{A} \tau_{a,f,c} \right] \cdot \frac{\vec{v}_{a,s}}{|\vec{v}_{a,s}|} \quad (3.5)$$

with the surface drag contribution

$$\tau_{a,s,c} = \rho_a u_{*,c}^2 \quad (3.6)$$

and with the form drag contribution

$$\tau_{a,f,c} = 0.5 \rho_a \frac{1}{L_{i,c} + L_{w,c}} \left(1 - \exp(-0.18 \frac{L_{w,c}}{H_{f,c}}) \right)^2 \frac{u_{*,w}^2}{\kappa^2} \int_{z_{0,w}}^{H_{f,c}} \left[\ln \left(\frac{z}{z_{0,w}} \right) - \psi_{m,w} \right]^2 dz \quad (3.7)$$

The parametrisation of the ocean stress for each ice class c is

$$\vec{\tau}_{w,c} = \rho_w c_{sd,w} \left[1 + 0.5 \frac{H_{d,c}}{L_{i,c} + L_{w,c}} \left(\frac{1}{\kappa} \left(\ln \frac{H_{d,c}/\exp(1)}{z_{0,oc}} \right) \left(1 - \exp(-0.18 \frac{L_{w,c}}{H_{d,c}}) \right) \right)^2 \right] \cdot |\vec{v}_{w,s} - \vec{v}| \cdot \left[(\vec{v}_{w,s} - \vec{v}) \cos(\phi_w) + \vec{k} \times (\vec{v}_{w,s} - \vec{v}) \sin(\phi_w) \right] \quad (3.8)$$

For a detailed derivation and explanation of these equations see BIRNBAUM (1998). Here, it is only important which input variables determine the value of $\vec{\tau}_{a,c}$ and $\vec{\tau}_{w,c}$. First, there are some **constants and parameters**: the density of air, ρ_a , the density of sea water, ρ_w , the von-Karman constant, κ , the roughness length of water surfaces with respect to air, $z_{0,w}$, the roughness length of ice with respect to water $z_{0,oc}$, the surface-drag coefficient between ice and ocean, $c_{sd,w}$, and the turning angle between sea ice drift and ocean current direction θ_w . Second, quantities describing the **sea ice properties**: the ice concentration, A , and the ice drift velocity, \vec{v} . Additionally for each ice class the length of ice floes, $L_{i,c}$, the distance between ice floes, $L_{w,c}$, the height of the ice floe freeboard, $H_{f,c}$, and the draught of the ice floes, $H_{d,c}$. These quantities are determined by MESIM itself. In contrast, Equations (3.5)–(3.8) also contain quantities that

3.1 Model system

depend on the state of **atmosphere or ocean**. They include: the horizontal wind velocity close to the surface, $\overrightarrow{v_{a,s}}$, the horizontal ocean current velocity close to the surface, $\overrightarrow{v_{w,s}}$, the friction velocity over an ice surface of class c , $u_{*,c}$, the friction velocity over a water surface, $u_{*,w}$, and the stability function of the atmospheric boundary layer over water surfaces for momentum, $\psi_{m,w}$.

The stress equations (3.5)–(3.8) emphasise that the sea ice model needs information about atmosphere and ocean. Ocean data are also required to determine the acceleration of the ice by the downhill force. For this, the tilt *beta* of the sea surface has to be accessible. In order to provide these information, MESIM is coupled to an atmosphere model (METRAS) and an ocean model (HAMSOM). They, in return, require information about the sea ice state from MESIM. A summary of the exchanged quantities is given by Figure 3.1. Thermodynamic sea ice processes are omitted, however, because this part of the model is not used in the study. The variables that are provided by MESIM (arrows in the centre part) and those variables that are exchanged directly between atmosphere and ocean (arrows on the right hand side) are discussed in Sections 3.1.2 and 3.1.3.

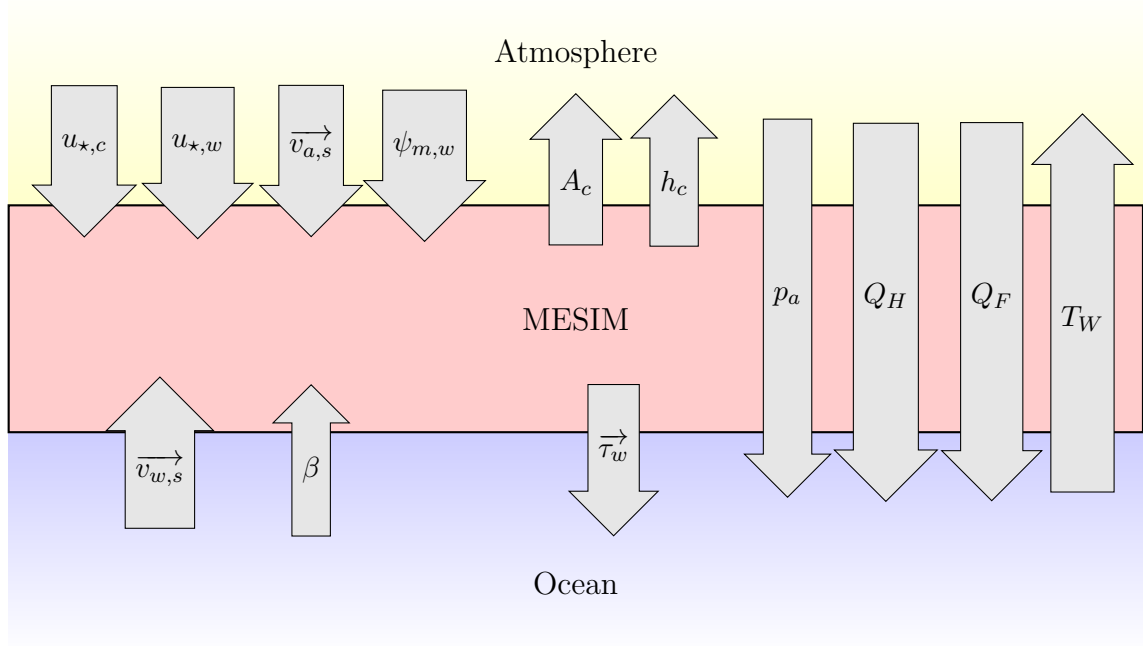


Figure 3.1: Illustration of the quantities that are exchanged between MESIM and the surrounding systems atmosphere and ocean.

3.1.2 Coupling to the atmosphere model METRAS

Information about the atmosphere is generated by the numerical model METRAS (MEsocale TRAnsport and Stream model, SCHLÜNZEN (1990); SCHLÜNZEN et al. (2012)). This is a three-dimensional, non-hydrostatic model that applies the Boussinesq approximation. It solves the Reynolds-averaged Navier-Stokes equations in combination with the anelastic continuity equation and budget equations for potential temperature, humidity, cloud- and rain-water, and pollutants.

METRAS has a special feature which is very advantageous for the simulation of the air above ice-covered oceans: It allows for multiple surface cover types within one grid cell. The fluxes between the boundary layer and the different surfaces are calculated separately and their aggregated effect is determined at the so-called “blending height” (VON SALZEN et al., 1996). This makes it for example possible to simulate realistic heat fluxes from a small fraction of open water (leads) within an almost closed ice pack. Indeed, these small openings can have large effects on the atmospheric boundary layer (LÜPKES et al., 2008).

A further advantage of taking METRAS as the atmosphere model for MESIM is that MESIM was actually made for being coupled to METRAS. When BIRNBAUM adapted a large scale sea ice model for the mesoscale in 1998, she directly coupled it to METRAS using the online integrated coupling approach. At it, she payed attention to the correct treatment of the different grids of MESIM and METRAS, namely Arakawa-B grid and Arakawa-C grid, respectively. Additionally, she implemented a time control between the two models because METRAS has an adaptive time step while MESIM runs with a fixed time step of 1 minute. Thus, there now exists a fast connection between MESIM and METRAS.

METRAS provides MESIM with the required information about wind velocity, friction velocities and a stability function of the atmospheric stratification (Figure 3.1). To determine these, METRAS requests information about the state of the surface. With the knowledge about A_c and h_c , i.e. the fraction of a grid cell that is covered by ice of a specific thickness, METRAS is able to calculate the fluxes of heat, momentum and moisture between the surfaces and the atmosphere. For this, the temperatures of the individual ice surfaces are determined with the force-restore method by DEARDORFF (1978) as explained in DIERER (2002). In contrast, the temperature of the water surfaces between the ice floes is procured from the ocean model.

3.1.3 Coupling to the ocean model HAMSOM

An ocean model is not only necessary to provide a water temperature, T_W , to METRAS but also to provide MESIM with the surface ocean current velocity, $\overrightarrow{v_{w,s}}$, and the sea surface slope, β .

For this task, the 'HAMburg Shelf Ocean Model' HAMSOM is used which is a three-dimensional mesoscale model and thus suitable for the desired application because of its fine horizontal and vertical resolution (POHLMANN, 2006). To simulate the water flow, HAMSOM solves the equation of motion, approximated by the hydrostatic equation in the vertical, in combination with the incompressible continuity equation. Further, temperature and salinity of the sea water are calculated from the equation of the state of sea water and transport equations for temperature and salinity. More information about HAMSOM and especially about the semi-implicit approaches for free surface waves and vertical diffusion can be found in BACKHAUS (1985) and POHLMANN (1996), respectively. Latter also discusses the formulations for the turbulent bottom and surface layer.

In order to simulate all processes appropriately, HAMSOM needs information regarding the sea surface, namely surface heat flux, Q_H , fresh water flux, Q_F , atmospheric pressure, p_a , and the mechanical surface stress, $\vec{\tau}_w$, either caused by wind or drifting ice. In earlier versions, HAMSOM calculated these fluxes from bulk formulae, but when coupling it to MESIM, DOBRYNIN and FOCK (2013, personal communication) enabled a direct exchange of the fluxes. This exchange is accomplished with online access coupling through the *OASIS Coupler*⁴, which also takes care of the time control of HAMSOM and MESIM/METRAS.

A problem arises from the different grid types of HAMSOM and MESIM, the first basing on the longitude–latitude coordinate system, the latter on a conformal grid with metre as the unit of measurement. This not only makes it necessary to interpolate between both systems, but it also results in model domains that never can be congruent. Because of numerical reasons, the HAMSOM domain was chosen to be smaller than the MESIM domain. Therefore, additional input data are required for those regions which are not covered by HAMSOM.

3.1.4 Input data for the model system

The model system, consisting of MESIM, METRAS, and HAMSOM, simulates the behaviour of sea ice, atmosphere and ocean not globally but in a limited area of about one million square kilometre. Therefore, the models have to be nested into large scale simulations. They receive these information at their lateral boundaries so that the solution in the interior of the model domains can be assimilated to the large scale values. Additionally, the initial state of sea ice, atmosphere and ocean has to be known at the beginning of the simulation.

⁴<https://verc.enes.org/oasis>

3.1.4.1 Boundary values

An overview about the boundary values that are required by the model system is given in Figure 3.2. External large scale models (green) provide various information (grey arrows) to the model system. The atmospheric part of the online-integrated-coupled models METRAS and MESIM receives data about large scale weather forecasts from the IFS model run at ECMWF (ECMWF, 2014c). The three-dimensional fields of the potential temperature, Θ_a , horizontal wind velocity, \vec{v}_a , humidity, q_a , and liquid water content, q_c , are provided to METRAS through a nudging approach. Because the momentum equation for wind needs to be solved spanning the whole model domain, it is not feasible to only prescribe the outermost boundary values. Rather a transition zone is established at the outer model domain in which the quantities are 'nudged' towards the large scale values. In this study, the nudging procedure as adapted by SCHOETTER (2013) is applied.

The sea ice model requires information about large scale sea ice properties at the boundaries for the case that ice drifts into the model domain. Then, values for the ice concentration, A , the ice volume per unit area, h , and the snow volume per unit area, h_s , are prescribed at the outermost grid cells. From there, this information is advected by the ice drift into the inner model domain. As MESIM uses different ice classes, the large scale values of A , h , and h_s are assigned to an ice class in accordance to the ice thickness h/A . All other ice classes at this grid cell remain empty. Provided are the data by the Arctic-wide assimilation system ICEDAS (developed within IRO-2 based on NAOSIM (KAUKER et al., 2003)). It includes a sea ice model and an ocean model, and it is forced with the same atmospheric data from ECMWF as METRAS.

The ocean component of ICEDAS is used to generate lateral boundary values for HAMSOM. It provides it with temperature and salinity profiles, T_o and S_o . As ICEDAS does not include tides, this information is separately obtained from the tidal model FES2004 (LYARD et al., 2006) and combined with the sea surface height data, ζ , of ICEDAS before it is passed to HAMSOM. Additionally, ICEDAS produces input data for the lower boundary of MESIM/METRAS for those areas which are not supplied by HAMSOM. These data are passed to the OASIS coupler so that MESIM receives them concurrently with the data from HAMSOM as complete fields. This concerns the three quantities 1) current velocity at the surface, $\vec{v}_{w,s}$, 2) the sea surface slope, β , that is determined from the sea surface height, ζ , from ICEDAS and FES2004, and 3) the water surface temperature, T_W , which is needed by METRAS.

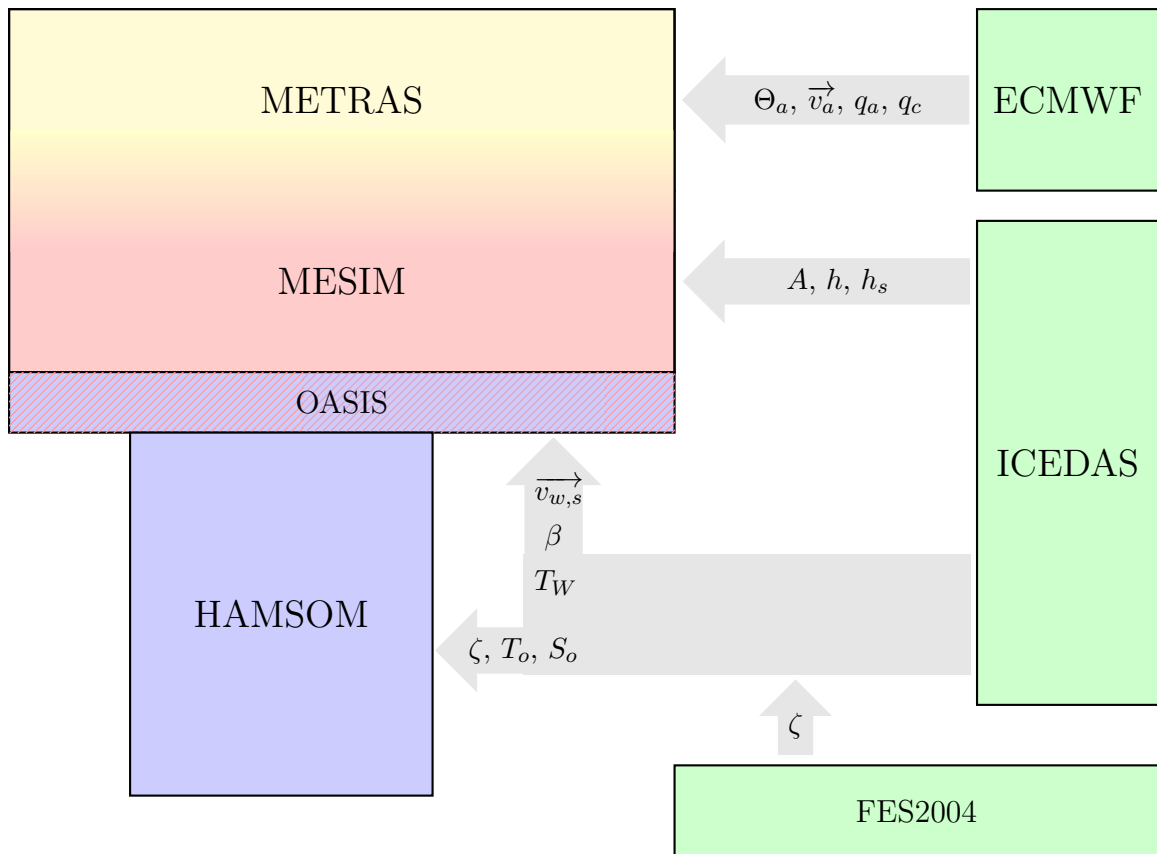


Figure 3.2: Overview of all time-varying boundary values (grey arrows) that are required by the model system MESIM/METRAS + HAMSOM coupled via OASIS. The sources of the data are external large scale models (green).

3.1.4.2 Initial values

In addition to the boundary values, another set of input data is necessary: The initial values from which the model system starts its calculations. For the atmospheric part, a one-dimensional version of METRAS calculates an initial vertical profile for all prognostic variables which is then spread over the whole model domain. As input for the 1D-model, fix points for the profile are taken from the IFS model at ECMWF. HAMSOM does not need any special initial data because it is run continuously: After a spin-up run, which lasted for several months and was conducted by DOBRYNIN (2014, personal communication), HAMSOM is always started from its previous simulation results.

MESIM needs initial data for ice concentration, ice thickness, snow thickness, as well as ice drift velocity. The latter is also adopted from previous model simulations, while the other are mostly determined from satellite observations. A more detailed description of these data follows

in Section 4.1. That section addresses the application of the full model system, as introduced in this section, to an actual case in the Arctic.

3.2 Model optimisations

Such a complex system like HAMMER needs quite some computational resources. If they can be reduced, the forecasts can be provided earlier and for lower costs to the customers like navigators. Therefore, several optimisations were made by the HAMMER team. Unfortunately, the investigations of Chapter 2 did not reveal any extensive potential for optimisations regarding the modelled physical processes. Therefore, the speed-up of HAMMER was mainly accomplished by numerical and technical optimisations.

First of all, large parts of MESIM were parallelised by the use of OpenMP. By distributing the computational load to multiple processors, the same calculations can be accomplished in less wall-clock time. The same was done in METRAS with the iterative solver for the pressure equation. As this task required special knowledge about block-parallelisation, it was conducted by Hendryk Bockelmann of the Deutsches Klimarechenzentrum (DKRZ). Instead, hardly any effort was made to debug the thermodynamic module of MESIM because the used approach of MAYKUT and UNTERSTEINER (1971) is known to be very computationally intensive anyway. As determined in Chapter 2, only the formation of new ice would be a relevant thermodynamic process at the timescale of the planned forecast lead time. Thus, this drawback to not simulate new ice growth was taken in order to allow for quick simulations.

Two further optimisations in the numerical scheme of HAMMER were developed in this thesis. These will be presented in Sections 3.2.1 and 3.2.2.

3.2.1 New solver for the momentum equation in MESIM

The first optimisation concerns the algorithm which is used to solve the momentum equation of sea ice drift (Equation (2.2)). This equation is highly non-linear because of the viscous-plastic parametrisation of the internal stress terms, which even involve spatial gradients. Thus, the momentum equation cannot be solved explicitly, or only by using very small time steps (BOUILLON et al., 2009), but it requires an implicit or mostly iterative solution technique. In the following section, the equation system is derived from the momentum equation for which the former solving algorithm is presented thereafter. The new algorithm is introduced afterwards.

3.2.1.1 Theoretical background and new algorithm

The aim is to solve the momentum equation of drifting ice in the form:

$$\rho h \frac{\partial \vec{v}}{\partial t} = \rho h \left[-\vec{v} \cdot \nabla \vec{v} - f \vec{k} \times \vec{v} \right] + \vec{\tau}_a + \vec{\tau}_w - \rho h g \beta + \nabla \cdot \underline{\sigma} \quad (3.9)$$

Note that the correction for the wind and ocean stress terms that was suggested by CONNOLLEY et al. (2004) is not applied here. Defining the mass of sea ice per unit area

$$M := \rho h \quad (3.10)$$

and applying the sea surface tilt parameterisation

$$g \beta = -f(\vec{k} \times \vec{v}_{wg}) \quad (3.11)$$

the x and y component of Equation (3.9) become

$$\begin{aligned} M \frac{\partial u}{\partial t} &= -Mu \frac{\partial u}{\partial x} - Mv \frac{\partial u}{\partial y} + Mfv + \tau_{ax} + \tau_{wx} - Mfv_{wg} + (\nabla \cdot \underline{\sigma})_x \\ M \frac{\partial v}{\partial t} &= -Mu \frac{\partial v}{\partial x} - Mv \frac{\partial v}{\partial y} - Mfu + \tau_{ay} + \tau_{wy} + Mfu_{wg} + (\nabla \cdot \underline{\sigma})_y \end{aligned} \quad (3.12)$$

The water stress

$$\vec{\tau}_w = \rho_w C_w |\vec{v}_{wg} - \vec{v}| \exp(i\theta_w) (\vec{v}_{wg} - \vec{v}) =: W \exp(i\theta_w) (\vec{v}_{wg} - \vec{v}) \quad (3.13)$$

is linearised by using the absolute value of the velocity difference $|\vec{v}_{wg} - \vec{v}|$ from the previous time step. This factor is combined with the sea water density, ρ_w , and the drag coefficient, C_w , to form the constant W . Splitting Equation (3.13) up into its x- and y-components yields

$$\tau_{wx} = W [(u_{wg} - u) \cos \theta_w - (v_{wg} - v) \sin \theta_w] \quad (3.14)$$

$$\tau_{wy} = W [(u_{wg} - u) \sin \theta_w + (v_{wg} - v) \cos \theta_w] \quad (3.15)$$

or in expanded form

$$\tau_{wx} = -Wu \cos \theta_w + Wv \sin \theta_w + Wu_{wg} \cos \theta_w - Wv_{wg} \sin \theta_w \quad (3.16)$$

$$\tau_{wy} = -Wu \sin \theta_w - Wv \cos \theta_w + Wu_{wg} \sin \theta_w + Wv_{wg} \cos \theta_w \quad (3.17)$$

Note that the x-component of the water stress depends not only on u but also on v because of the effect of the turning angle, θ_w , between water drag and resulting ice drift.

The internal forces $\nabla \cdot \underline{\sigma}$ are parametrised following HIBLER (1979) by

$$\begin{aligned} \sigma_{ij} &= 2\eta \epsilon_{ij} + \delta_{ij} \left\{ (\zeta - \eta) (\epsilon_{11} + \epsilon_{22}) - \frac{P}{2} \right\} \quad \text{and} \\ \epsilon_{ij} &= \frac{1}{2} \left(\frac{\partial u_i}{\partial x_j} + \frac{\partial u_j}{\partial x_i} \right) \end{aligned} \quad (3.18)$$

The 4 components of the stress tensor are:

$$\begin{aligned}
 \sigma_{11} &= \zeta \frac{\partial u}{\partial x} + \zeta \frac{\partial v}{\partial y} + \eta \frac{\partial u}{\partial x} - \eta \frac{\partial v}{\partial y} - \frac{P}{2} \\
 \sigma_{12} = \sigma_{21} &= \eta \frac{\partial u}{\partial y} + \eta \frac{\partial v}{\partial x} \\
 \sigma_{22} &= \zeta \frac{\partial u}{\partial x} + \zeta \frac{\partial v}{\partial y} + \eta \frac{\partial v}{\partial y} - \eta \frac{\partial u}{\partial x} - \frac{P}{2}
 \end{aligned} \tag{3.19}$$

The x- and y-components of the internal stresses $\nabla \cdot \underline{\sigma}$ can thus be calculated from

$$\begin{aligned}
 \{\nabla \cdot \underline{\sigma}\}_x &= \frac{\partial \sigma_{11}}{\partial x} + \frac{\partial \sigma_{21}}{\partial y} \\
 &= \frac{\partial}{\partial x} \left(\zeta \frac{\partial u}{\partial x} + \zeta \frac{\partial v}{\partial y} + \eta \frac{\partial u}{\partial x} - \eta \frac{\partial v}{\partial y} \right) + \frac{\partial}{\partial y} \left(\eta \frac{\partial u}{\partial y} + \eta \frac{\partial v}{\partial x} \right) - \frac{\partial}{\partial x} \left(\frac{P}{2} \right)
 \end{aligned} \tag{3.20}$$

$$\begin{aligned}
 \{\nabla \cdot \underline{\sigma}\}_y &= \frac{\partial \sigma_{12}}{\partial x} + \frac{\partial \sigma_{22}}{\partial y} \\
 &= \frac{\partial}{\partial x} \left(\eta \frac{\partial u}{\partial y} + \eta \frac{\partial v}{\partial x} \right) + \frac{\partial}{\partial y} \left(\zeta \frac{\partial u}{\partial x} + \zeta \frac{\partial v}{\partial y} + \eta \frac{\partial v}{\partial y} - \eta \frac{\partial u}{\partial x} \right) - \frac{\partial}{\partial y} \left(\frac{P}{2} \right)
 \end{aligned}$$

The local rate of change of the x- and y-components of the drift vector, namely u and v , are discretised using the values at the old time step $n - 1$ and at the new current time step n :

$$M \frac{\partial u}{\partial t} = M \frac{u^n - u^{n-1}}{\Delta t} = M \frac{u^n}{\Delta t} - M \frac{u^{n-1}}{\Delta t} \tag{3.21}$$

$$M \frac{\partial v}{\partial t} = M \frac{v^n - v^{n-1}}{\Delta t} = M \frac{v^n}{\Delta t} - M \frac{v^{n-1}}{\Delta t} \tag{3.22}$$

When using Equations (3.16), (3.17), (3.20), (3.21) and (3.22), the full equations for u and v (Equation (3.12)) can be specified as

$$\begin{aligned}
 M \frac{u}{\Delta t} - M \frac{u^{n-1}}{\Delta t} &= - M u^{n-1} \frac{\partial u}{\partial x} - M v^{n-1} \frac{\partial u}{\partial y} + M f v + \tau_{ax} - M f v_{wg} \\
 &\quad - W \cos \theta_w u + W \sin \theta_w v + W \cos \theta_w u_{wg} - W \sin \theta_w v_{wg} \\
 &\quad + \frac{\partial}{\partial x} \left(\zeta \frac{\partial u}{\partial x} + \zeta \frac{\partial v}{\partial y} + \eta \frac{\partial u}{\partial x} - \eta \frac{\partial v}{\partial y} \right) + \frac{\partial}{\partial y} \left(\eta \frac{\partial u}{\partial y} + \eta \frac{\partial v}{\partial x} \right) - \frac{\partial}{\partial x} \left(\frac{P}{2} \right) \\
 M \frac{v}{\Delta t} - M \frac{v^{n-1}}{\Delta t} &= - M u^{n-1} \frac{\partial v}{\partial x} - M v^{n-1} \frac{\partial v}{\partial y} - M f u + \tau_{ay} + M f u_{wg} \\
 &\quad - W \sin \theta_w u - W \cos \theta_w v + W \sin \theta_w u_{wg} + W \cos \theta_w v_{wg} \\
 &\quad + \frac{\partial}{\partial x} \left(\eta \frac{\partial u}{\partial y} + \eta \frac{\partial v}{\partial x} \right) + \frac{\partial}{\partial y} \left(\zeta \frac{\partial u}{\partial x} + \zeta \frac{\partial v}{\partial y} + \eta \frac{\partial v}{\partial y} - \eta \frac{\partial u}{\partial x} \right) - \frac{\partial}{\partial y} \left(\frac{P}{2} \right)
 \end{aligned} \tag{3.23}$$

For better readability, the time level index n is omitted and only $n - 1$ is explicitly mentioned. Colours highlight occurrences of u in red, v in blue, and spatial gradients of u or v in green.

Reordering Equation (3.23) and separating terms containing u and v yields

$$\begin{aligned}
 u \cdot \left[\frac{M}{\Delta t} + W \cos \theta_w \right] + v \cdot [-Mf - W \sin \theta_w] = \\
 M \frac{u^{n-1}}{\Delta t} + \tau_{ax} - M f v_{wg} + W \cos \theta_w u_{wg} - W \sin \theta_w v_{wg} - \frac{\partial}{\partial x} \left(\frac{P}{2} \right) \\
 + \frac{\partial}{\partial x} \left(\zeta \frac{\partial u}{\partial x} + \zeta \frac{\partial v}{\partial y} + \eta \frac{\partial u}{\partial x} - \eta \frac{\partial v}{\partial y} \right) + \frac{\partial}{\partial y} \left(\eta \frac{\partial u}{\partial y} + \eta \frac{\partial v}{\partial x} \right) - M u^{n-1} \frac{\partial u}{\partial x} - M v^{n-1} \frac{\partial u}{\partial y} \\
 u \cdot [Mf + W \sin \theta_w] + v \cdot \left[\frac{M}{\Delta t} + W \cos \theta_w \right] = \\
 M \frac{v^{n-1}}{\Delta t} + \tau_{ay} + M f u_{wg} W \sin \theta_w u_{wg} + W \cos \theta_w v_{wg} - \frac{\partial}{\partial y} \left(\frac{P}{2} \right) \\
 + \frac{\partial}{\partial x} \left(\eta \frac{\partial u}{\partial y} + \eta \frac{\partial v}{\partial x} \right) + \frac{\partial}{\partial y} \left(\zeta \frac{\partial u}{\partial x} + \zeta \frac{\partial v}{\partial y} + \eta \frac{\partial v}{\partial y} - \eta \frac{\partial u}{\partial x} \right) - M u^{n-1} \frac{\partial v}{\partial x} - M v^{n-1} \frac{\partial v}{\partial y}
 \end{aligned} \tag{3.24}$$

When applying following abbreviations

$$\begin{aligned}
 d_u &= \frac{M}{\Delta t} + W \cos \theta_w \\
 d_v &= \frac{M}{\Delta t} + W \cos \theta_w \\
 a &= Mf + W \sin \theta_w \\
 r_u &= \frac{\partial}{\partial x} \left(\zeta \frac{\partial u}{\partial x} + \zeta \frac{\partial v}{\partial y} + \eta \frac{\partial u}{\partial x} - \eta \frac{\partial v}{\partial y} \right) + \frac{\partial}{\partial y} \left(\eta \frac{\partial u}{\partial y} + \eta \frac{\partial v}{\partial x} \right) - M u^{n-1} \frac{\partial u}{\partial x} - M v^{n-1} \frac{\partial u}{\partial y} \\
 r_v &= \frac{\partial}{\partial x} \left(\eta \frac{\partial u}{\partial y} + \eta \frac{\partial v}{\partial x} \right) + \frac{\partial}{\partial y} \left(\zeta \frac{\partial u}{\partial x} + \zeta \frac{\partial v}{\partial y} + \eta \frac{\partial v}{\partial y} - \eta \frac{\partial u}{\partial x} \right) - M u^{n-1} \frac{\partial v}{\partial x} - M v^{n-1} \frac{\partial v}{\partial y} \\
 f_x &= M \frac{u^{n-1}}{\Delta t} + \tau_{ax} - M f v_{wg} + W \cos \theta_w u_{wg} - W \sin \theta_w v_{wg} - \frac{\partial}{\partial x} \left(\frac{P}{2} \right) \\
 f_y &= M \frac{v^{n-1}}{\Delta t} + \tau_{ay} + M f u_{wg} W \sin \theta_w u_{wg} + W \cos \theta_w v_{wg} - \frac{\partial}{\partial y} \left(\frac{P}{2} \right)
 \end{aligned} \tag{3.25}$$

Equation (3.24) can be written as

$$\begin{aligned}
 d_u \cdot u - a \cdot v &= r_u + f_x \\
 a \cdot u + d_v \cdot v &= r_v + f_y
 \end{aligned} \tag{3.26}$$

The d -terms represent all processes in which the velocity component depends on itself, whereas the a -terms represent all processes in which u depends on v and vice versa. f represents terms that are independent from u and v , and r collects all terms that contain spatial derivations of

u or v . Discretisation of these spatial derivations reveals that they depend on the velocities of the neighbouring grid cells. The orange framed terms, however, are discretised such that they also depend on the velocity at the local grid point. Therefore, parts of these framed terms are actually transferred to the d -terms.

Using the definition of the b -terms as

$$\begin{aligned} b_u &= \frac{1}{d_u} \\ b_v &= \frac{1}{d_v} \end{aligned} \tag{3.27}$$

Equations (3.26) are divided by d_u and d_v , respectively:

$$\begin{aligned} u - a \cdot b_u \cdot v &= (r_u + f_x) \cdot b_u =: s_u \\ a \cdot b_v \cdot u + v &= (r_v + f_y) \cdot b_v =: s_v \end{aligned} \tag{3.28}$$

This is a linear system of equations for u and v with the right hand sides defined as s -terms. It can also be expressed by matrices:

$$\begin{pmatrix} 1 & -a \cdot b_u \\ a \cdot b_v & 1 \end{pmatrix} \cdot \begin{pmatrix} u \\ v \end{pmatrix} = \begin{pmatrix} (r_u + f_x) \cdot b_u \\ (r_v + f_y) \cdot b_v \end{pmatrix} \tag{3.29}$$

Solving Equation (3.28) for u and v yields:

$$\begin{aligned} \tilde{u} := u &= \frac{s_u + a \cdot b_u \cdot s_v}{1 + a^2 b_u b_v} \\ \tilde{v} := v &= \frac{s_v - a \cdot b_v \cdot s_u}{1 + a^2 b_u b_v} \end{aligned} \tag{3.30}$$

This coupled system of equations is solved with the successive-overrelaxation (SOR) method. Here, \tilde{u} and \tilde{v} are temporary values of the drift components. From these, the actual values of u and v are calculated for each iteration step applying the overrelaxation coefficient w that represents the weighting factor between the old drift components and the temporary new values. (see Algorithm 1 for details.) During the SOR procedure, the grid cells are divided into two groups. Because of their distribution within the domain, which represents a checkerboard pattern, they are called *black* and the *white*. The a , b and f -terms are treated as constants during the SOR-operation.

Algorithm 1 shows the general procedure of the SOR algorithm as implemented previously. In this pseudo-code, f denotes arbitrary functions, and it is only used to show the dependency of the variables without repeating the lengthy equations. New values for u and v are calculated alternately for black and white until the solution does not change anymore, which means that

3.2 Model optimisations

the changes Δu and Δv are smaller than the threshold $vrmax=10^{-4}$ ms $^{-1}$ at every grid cell. This whole SOR procedure actually is run twice for each time step. That means, the values determined for u^n and v^n that are determined after the first run of the SOR are not the final velocities. They are only utilised to calculate

$$\begin{aligned} u^{n-1/2} &= 0.5 \cdot (u^{n-1} + u^n) \\ v^{n-1/2} &= 0.5 \cdot (v^{n-1} + v^n) \end{aligned} \quad (3.31)$$

which are valid at the centred time between $n-1$ and n . These, in turn, are used in the second run of the SOR for all non-linear terms like the ocean stress and the r -terms. Hereby, the step to proceed the original velocities, u^{n-1} and v^{n-1} , to the final ones, u^n and v^n , is based on the centred velocities. This is at least a better approximation of the non-linearity than relying only on the original velocities. The algorithm for the two SOR runs, however, is identical because only the matrix elements (a , $b_{u,v}$, $r_{u,v}$, and $f_{x,y}$) have a different value in the second run.

Algorithm 1 SOR algorithm as implemented previously. Differences to the later introduced new algorithm (Algorithm 2) are highlighted red.

```

Calculate  $a$ ,  $b_u$ ,  $b_v$ ,  $f_x$ ,  $f_y$  based on  $u^{n-1}$  and  $v^{n-1}$ 
 $i \leftarrow 0$ 
 $u_{\{b,w\}}^i \leftarrow u^{n-1}$ ,  $v_{\{b,w\}}^i \leftarrow v^{n-1}$  ▷ First guess for  $u$  and  $v$ 
while  $verr \geq vrmax$  do
5:    $i \leftarrow i + 1$ 
      First colour black, index  $b$ 
           $r_{u,b}^i \leftarrow f(u_w^{i-1}, v_w^{i-1}, v_b^{i-1})$  and  $r_{v,b}^i \leftarrow f(v_w^{i-1}, u_w^{i-1}, u_b^{i-1})$  ▷ Equation (3.25)
           $s_{u,b}^i \leftarrow f(r_{u,b}^i)$  and  $s_{v,b}^i \leftarrow f(r_{v,b}^i)$  ▷ Equation (3.28)
           $\tilde{u}_b^i \leftarrow f(s_{u,b}^i, s_{v,b}^i)$  and  $\tilde{v}_b^i \leftarrow f(s_{u,b}^i, s_{v,b}^i)$  ▷ Equation (3.30)
10:   $\Delta u_b^i \leftarrow w \cdot (\tilde{u}_b^i - u_b^{i-1})$  and  $\Delta v_b^i \leftarrow w \cdot (\tilde{v}_b^i - v_b^{i-1})$ 
           $u_b^i \leftarrow u_b^{i-1} + \Delta u_b^i$  and  $v_b^i \leftarrow v_b^{i-1} + \Delta v_b^i$ 
      Second colour white, index  $w$ 
           $r_{u,w}^i \leftarrow f(u_b^i, v_b^i, v_w^{i-1})$  and  $r_{v,w}^i \leftarrow f(v_b^i, u_b^i, u_w^{i-1})$  ▷ Equation (3.25)
           $s_{u,w}^i \leftarrow f(r_{u,w}^i)$  and  $s_{v,w}^i \leftarrow f(r_{v,w}^i)$  ▷ Equation (3.28)
15:   $\tilde{u}_w^i \leftarrow f(s_{u,w}^i, s_{v,w}^i)$  and  $\tilde{v}_w^i \leftarrow f(s_{u,w}^i, s_{v,w}^i)$  ▷ Equation (3.30)
           $\Delta u_w^i \leftarrow w \cdot (\tilde{u}_w^i - u_w^{i-1})$  and  $\Delta v_w^i \leftarrow w \cdot (\tilde{v}_w^i - v_w^{i-1})$ 
           $u_w^i \leftarrow u_w^{i-1} + \Delta u_w^i$  and  $v_w^i \leftarrow v_w^{i-1} + \Delta v_w^i$ 
      Calculate the ERROR
           $verr \leftarrow \max(|\Delta u_b^i|, |\Delta v_b^i|, |\Delta u_w^i|, |\Delta v_w^i|)$ 
20: end while
 $u^n \leftarrow \bigcup \{u_b^i, u_w^i\}$ ,  $v^n \leftarrow \bigcup \{v_b^i, v_w^i\}$ 

```

The problem with the previously implemented SOR algorithm is that the calculation of the u -

component is executed “at the same time” as for the v -component, meaning not necessarily on parallel processors but with the same state of the input variables as basis. This becomes clear in line 7, where the old value v_b^{i-1} is used to calculate r_u , and the old value u_b^{i-1} is used to calculate r_v . Eventually, new values, u_b^i and v_b^i , are calculated independently from one another. This can lead to numerical instabilities and oscillating solutions during the iteration as was observed in applications of MESIM.

To overcome this issue, the algorithm was altered slightly so that the coupling between u - and v -components is better taken into account. As can be seen in Algorithm 2, the calculation order is permuted so that the v -components are calculated *after* the new u^i is determined. Hereby, the new value of u^i is directly used for the calculation of r_v^i (lines 16 and 29). In this way, the solution of v cannot decouple from u . This reduced the number of required iterations enormously as will be demonstrated in Section 3.2.1.2.

As may be noticed already, the permutation of the calculation order caused another change in the used iteration levels: The calculation of \tilde{u}^i used the new values s_v^i in Algorithm 1 (lines 9 and 15), which is not possible anymore in Algorithm 2 (lines 12 and 25). However, the difference should not be large because the “new” value, s_v^i , that was used previously in Algorithm 1, was also (like in Algorithm 2) based on the old u^{i-1} . Moreover, no problems appeared from this during tests.

The shown version of Algorithm 2 first calculates the u -components and consecutively the v -components. However, this order is not predefined and can be interchanged. It was proven by tests that the order indeed has no important influence on the solution. Nevertheless, to prevent any on-sidedness of the solution, the order is switched at each time step, i.e. the SOR starts with the calculation of u at every even time step, n , and with v at every odd time step.

3.2.1.2 Performance tests

The new SOR algorithm for solving the ice drift momentum equation is tested for its effectiveness in terms of computational time. Besides, it is checked whether the simulation results remain the same. The simulations that are used for this purpose come from an experiment phase, during which HAMMER produced sea ice forecasts operationally. As the detailed setup of these simulations is not relevant for the effectiveness study, only a very short overview is given in the next paragraph. The more interested reader is referred to Section 4.1, in which the model setup is explained in detail and exemplary simulation results are shown.

HAMMER was run operationally from 13/03/2014 until 30/03/2014 to simulate the sea ice con-

3.2 Model optimisations

Algorithm 2 New SOR algorithm. Differences to the original algorithm (Algorithm 1) are highlighted red.

```

Calculate  $a, b_u, b_v, f_x, f_y$  based on  $u^{n-1}$  and  $v^{n-1}$ 
 $i \leftarrow 0$ 
 $u_{\{b,w\}}^i \leftarrow u^{n-1}, v_{\{b,w\}}^i \leftarrow v^{n-1}$  ▷ First guess for  $u$  and  $v$ 
 $s_{v,b}^i \leftarrow f(v_w^i, u_w^i, u_b^i)$  ▷ Initialisation
5:  $s_{v,w}^i \leftarrow f(v_b^i, u_b^i, u_w^i)$  ▷ Initialisation
while  $v_{err} \geq v_{rmax}$  do
     $i \leftarrow i + 1$ 
    First colour black, index  $b$ 
     $u$  Equation
10:    $r_{u,b}^i \leftarrow f(u_w^{i-1}, v_w^{i-1}, v_b^{i-1})$ 
        $s_{u,b}^i \leftarrow f(r_{u,b}^i)$ 
        $\tilde{u}_b^i \leftarrow f(s_{u,b}^i, s_{v,b}^{i-1})$  ▷ Equation (3.30)
        $\Delta u_b^i \leftarrow w \cdot (\tilde{u}_b^i - u_b^{i-1})$ 
        $u_b^i \leftarrow u_b^{i-1} + \Delta u_b^i$ 
15:    $v$  Equation
        $r_{v,b}^i \leftarrow f(v_w^{i-1}, u_w^{i-1}, u_b^i)$ 
        $s_{v,b}^i \leftarrow f(r_{v,b}^i)$ 
        $\tilde{v}_b^i \leftarrow f(s_{u,b}^i, s_{v,b}^i)$  ▷ Equation (3.30)
        $\Delta v_b^i \leftarrow w \cdot (\tilde{v}_b^i - v_b^{i-1})$ 
20:    $v_b^i \leftarrow v_b^{i-1} + \Delta v_b^i$ 
    Second colour white, index  $w$ 
     $u$  Equation
        $r_{u,w}^i \leftarrow f(u_b^i, v_b^i, v_w^{i-1})$ 
        $s_{u,w}^i \leftarrow f(r_{u,w}^i)$ 
25:    $\tilde{u}_w^i \leftarrow f(s_{u,w}^i, s_{v,w}^{i-1})$  ▷ Equation (3.30)
        $\Delta u_w^i \leftarrow w \cdot (\tilde{u}_w^i - u_w^{i-1})$ 
        $u_w^i \leftarrow u_w^{i-1} + \Delta u_w^i$ 
     $v$  Equation
        $r_{v,w}^i \leftarrow f(v_b^i, u_b^i, u_w^i)$ 
30:    $s_{v,w}^i \leftarrow f(r_{v,w}^i)$ 
        $\tilde{v}_w^i \leftarrow f(s_{u,w}^i, s_{v,w}^i)$  ▷ Equation (3.30)
        $\Delta v_w^i \leftarrow w \cdot (\tilde{v}_w^i - v_w^{i-1})$ 
        $v_w^i \leftarrow v_w^{i-1} + \Delta v_w^i$ 
    Calculate the ERROR
35:    $v_{err} \leftarrow \max(|\Delta u_b^i|, |\Delta v_b^i|, |\Delta u_w^i|, |\Delta v_w^i|)$ 
end while
 $u^n \leftarrow \cup \{u_b^i, u_w^i\}, \quad v^n \leftarrow \cup \{v_b^i, v_w^i\}$ 

```

ditions in the Barents Sea. On each day, two forecast runs were started, one for 06 UTC and one for 18 UTC. Each of these produced sea ice forecasts for 138 hours (>5 days). These 36 operationally conducted simulations are named OPER-runs hereafter and are used as reference. They comprise all possible optimisations that were developed for HAMMER.

The OPER-runs are rerun for the present study using the previous SOR algorithm; thus they are named pSOR-runs. These are compared to the OPER-runs, which include the new SOR algorithm. For the pSOR-runs, it was made sure that each run was initialised identically to the OPER-runs. This is not a given because the ocean model, HAMSOM, runs continuously throughout all OPER-runs. Thus for the pSOR-runs, HAMSOM has to be restarted each day with the same initialisation data as the OPER-runs. For the following performance analyses, it appears to be sufficient to evaluate only the first 24 hours of the forecasts. Also, only the simulations which started at 06 UTC were considered, thus a total of 18 simulations. All simulations are conducted on the machine “Blizzard” at DKRZ. A whole node is employed in order that the computation time cannot be influenced by potential co-users of the same node.

The first feature to be investigated is the number of iterations that are used by the SOR-algorithms to converge to a solution with a preset accuracy. Figure 3.3a shows how many iterations are needed in average for all 18 pSOR-runs in the course of the simulation. The green line specifies the iteration number for the first SOR-run for the centred velocities, the black line gives the iterations of the second SOR-run required to find the final velocities (as explained in Section 3.2.1.1). Even though the iteration number decreases with time when the system adjusts itself, its magnitude of about 1000 is astonishing. Comparing it to the new SOR-algorithm (Figure 3.3b), the improvement becomes clear: In average, the new SOR-algorithm only needs 10–20 iterations for the first SOR-run after a short adjustment-time. Further on, the iterations needed for the second SOR-run are even less which indicates that the system is well-settled. This is also confirmed by the fact that the iteration number quickly drops again after the peak caused by the restart of the model system after 6 hours. Also after the 15-minutes-peaks, which are caused by the coupling with HAMSOM, the iteration number decreases quickly.

The reason for the large number of iterations with the previous SOR-algorithm are oscillations of the solution caused by the insufficient coupling between u and v . An example is presented in Figure 3.4 for 29/03/2014 at 06:07 UTC, i.e. short after the simulation start. Figure 3.4 shows the development of the solution during the iteration process for pSOR (left) and OPER (right) during the first SOR-run. More precisely, the plots show the value of Δu^i , which is the change of the u -component between iteration step $i - 1$ and i . The smaller the absolute value of Δu^i the more the solution is converged. After the first iteration (Figures 3.4a,e), both algorithms considerably change the u -component. After 5 iterations (Figures 3.4b,f), both algorithms still behave similarly and the changes become smaller. After 15 iterations (Figures 3.4c,g), the

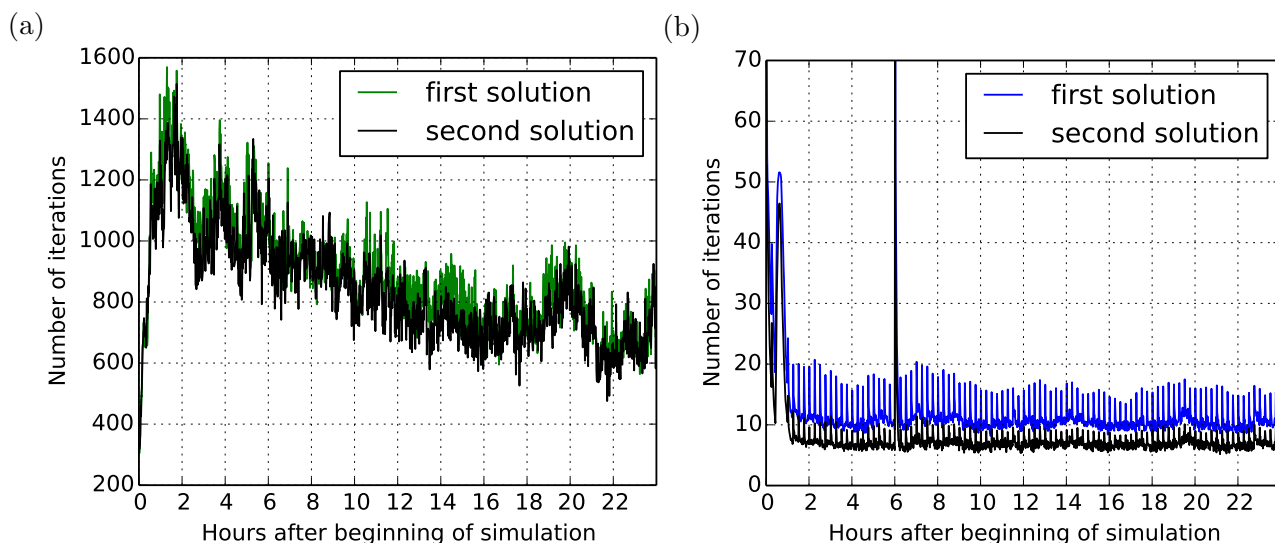


Figure 3.3: Number of iterations used by (a) the previous SOR-algorithm and (b) the new SOR-algorithm during the course of the simulation as average over all 06-UTC runs. Note the different y-axis scales. The peak in (b) at 6 hours reaches a value of 180 iterations.

changes are again smaller, however, small spots appear in the pSOR-run. After 34 iterations (Figures 3.4d,h), these spots are intensified and show an oscillation-typical red-blue pattern. In contrast, the new SOR-algorithm does not create instabilities and does hardly change the solution anymore. After few more iterations the new SOR-algorithm has found the solution, while the previous SOR-algorithm needs a lot more iterations to degrade the instabilities again.

The prevention of oscillations by the new SOR-algorithm reduces the number of iterations which is in turn reflected by the computational time needed for the whole simulation. To measure the computational time, the “SC Timer Lib”⁵ was applied in the source code. It measures the wall-clock time spent within the specified part of the code with “as little overhead as possible”⁵. Table 3.1 shows the fraction of computational time that is spent within the sea-ice model compared to the complete model run with MESIM-METRAS. HAMSOM is neglected here because it runs in parallel to MESIM-METRAS anyway. The fraction numbers indicate the average values for the first 24-hour-forecasts of all 18 runs, pSOR-runs in the first row and OPER-runs in the second row. Similarly to the iteration numbers, the time spent in MESIM is reduced by a factor of 10. Furthermore, the dynamic model part with the new SOR-algorithm only needs 1.8% of the total computational time for calculating the ice drift velocity. This is less than half of the time needed for the full sea-ice model.

⁵provided by the Deutsches Klimarechenzentrum (DKRZ). Documentation was available on 2014/11/17 at <https://doc.redmine.dkrz.de/sct/html/>.

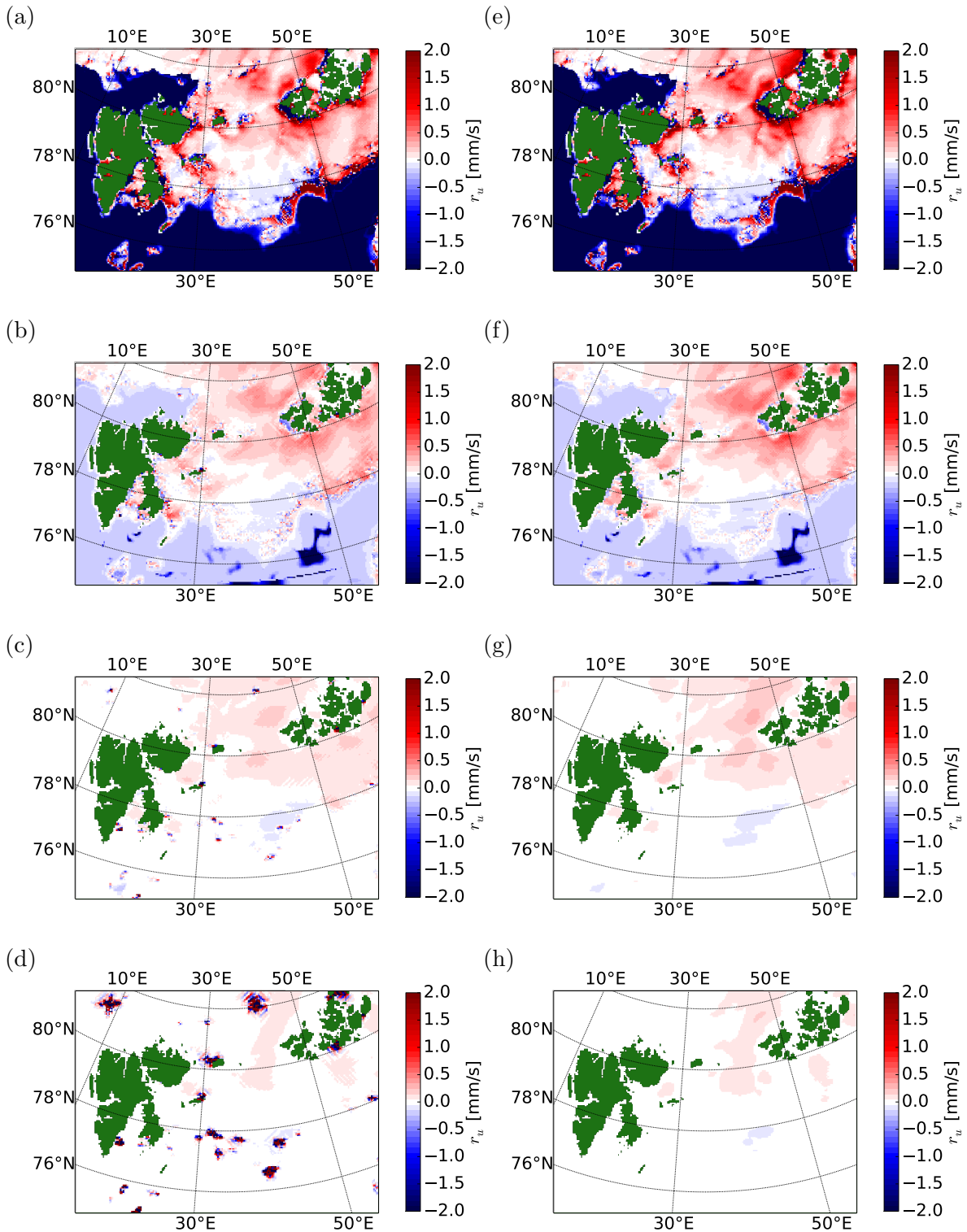


Figure 3.4: Δu^i after (a,e) one, (b,f) five, (c,g) 15, and (d,h) 34 iterations in the first SOR-run as comparison between the previous SOR-algorithm, (a,b,c,d), and the new SOR-algorithm, (e,f,g,h) for 06:07 UTC on 29/03/2014. Green areas depict land.

Table 3.1: Comparison of computational time needed for previous and new SOR algorithm. Given is the fraction of wall-clock time spent for the sea-ice model MESIM and for those parts of it that calculate the ice drift velocity \vec{v} . The time spent for the total model system MESIM-METRAS is used as reference.

	MESIM-METRAS	MESIM	Calculation of \vec{v}
Previous SOR algorithm	100%	49%	47%
New SOR algorithm	100%	4.8%	1.8%

Hence, the new SOR-algorithm brings a tremendous speed-up of the model. And yet, the question arises if the simulated ice conditions are still reasonable. Therefore, the model results of pSOR-runs and OPER-runs are compared with each other. For quantifying the differences, BIAS and RMSE are calculated. These measures are suggested by SCHLÜNZEN and SOKHI (EDITORS) (2008) for evaluation of cloud cover, so they are used here because of the similarity of cloud cover and ice cover. The development of BIAS and RMSE during the simulation as average of all runs is shown in Figures 3.5a and 3.5c for ice concentration, A , and in 3.5b and 3.5d for ice thickness, H . In general, the error increases with simulation time as would be expected. Within 24 hours however, both BIAS and RMSE stay small compared to the magnitude of A and H .

Even if the 99-percentile of the absolute value of the deviations is calculated (Figures 3.5e and 3.5f), these values are small and not relevant for customers of the forecasts. Moreover, it might be possible that the previous SOR-algorithm did not simulate the ice conditions totally correct so that the results generated by the new SOR-algorithm deviate from them because they are actually better. Therefore, it is concluded from the performance investigations in this section that the new SOR-algorithm is much more efficient while retaining model quality. Thus, its application in the operational runs is justified.

3.2.2 Timesplitting of cloud-microphysics in METRAS

In order to take full advantage of the optimisation of the ice drift model, an additional optimisation is implemented in the atmospheric part METRAS. Tests with METRAS during the development phase of HAMMER revealed that METRAS is quite slow as soon as precipitation occurs in the simulation. In this case, the adaptive time step of METRAS becomes low, which increases the amount of required computations and thus hinders a timely forecast. To avoid this, the time step calculation is improved twofold. These concepts are explained in the last parts of Section 3.2.2.1 after an overview of the previously implemented procedure was given.

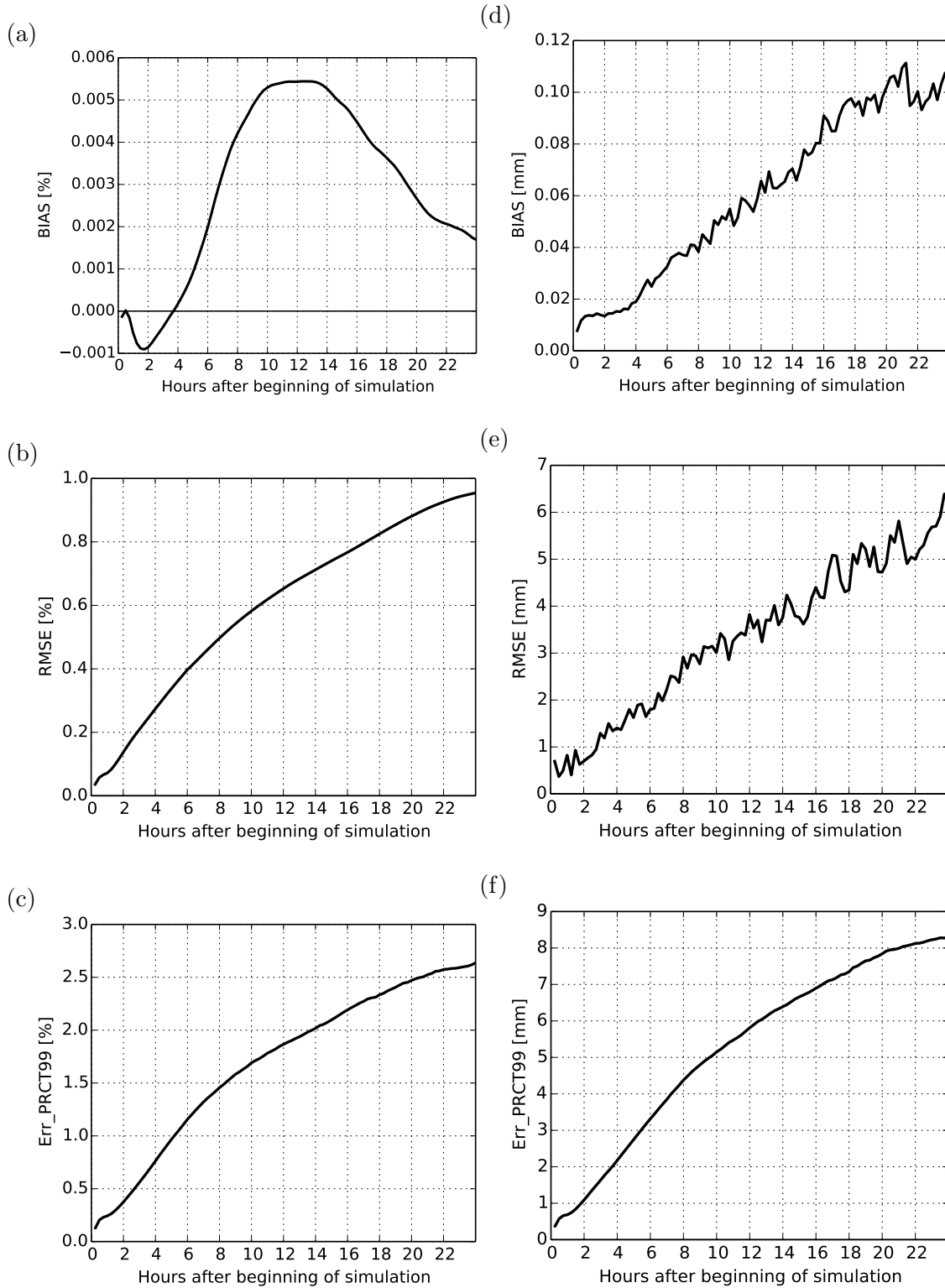


Figure 3.5: Comparison of model results for (a,b,c) ice concentration, A , and (d,e,f) ice thickness, H . The deviation between pSOR-runs and OPER-runs is quantified by (a,d) BIAS, (b,e) RMSE, and (c,f) the 99-percentile of the absolute value of the differences. Shown is the time development of these measures as mean of the 18 06-UTC runs.

In Section 3.2.2.2, the performance of the optimised model version is tested.

3.2.2.1 Optimisation approaches

Determination of the model time step

In METRAS, the length of the time step, Δt , is recalculated regularly to adapt it to the actual requirements of the simulated processes. Hereby, following processes are considered: Advection and diffusion in x-,y-,and z-direction, respectively, accretion of rain droplets, and sedimentation of rain droplets. Each of these processes, \mathfrak{P} , limits the time step. If only one of them would be active at a time, the respective allowed time steps would be:

$$\text{Advection in x-direction} \quad \Delta t_{Adv_x} = \frac{\Delta x}{u_a} \cdot CFL \quad (3.32)$$

$$\text{Advection in y-direction} \quad \Delta t_{Adv_y} = \frac{\Delta y}{v_a} \cdot CFL \quad (3.33)$$

$$\text{Advection in z-direction} \quad \Delta t_{Adv_z} = \frac{\Delta z}{w_a} \cdot CFL \quad (3.34)$$

$$\text{Diffusion in x-direction} \quad \Delta t_{Dif_x} = \frac{\Delta x^2}{4 \cdot 1.3 \cdot K_{hor}} \quad (3.35)$$

$$\text{Diffusion in y-direction} \quad \Delta t_{Dif_y} = \frac{\Delta y^2}{4 \cdot 1.3 \cdot K_{hor}} \quad (3.36)$$

$$\text{Diffusion in z-direction (explicit)} \quad \Delta t_{Dif_z} = \frac{\Delta z^2}{4 \cdot 1.3 \cdot K_{ver}} \quad (3.37)$$

$$\text{Diffusion in z-direction (implicit)} \quad \Delta t_{Dif_z} = \frac{\Delta z^2}{2 \cdot 1.3 \cdot K_{ver}} \quad (3.38)$$

$$\text{Accretion} \quad \Delta t_{Acc} = 0.42 \cdot q_r^{-0.875} \quad (3.39)$$

$$\text{Sedimentation} \quad \Delta t_{Sed} = 0.014 \cdot \Delta z \cdot \sqrt{\frac{\rho_a}{\rho_s}} \cdot \left(\frac{\rho_a}{1000} \cdot q_r \right)^{-0.1905} \quad (3.40)$$

The time steps are, thus, restricted not only by the grid resolution (Δx , Δy , and Δz) but also by time varying quantities: the wind components, u_a , v_a , and w_a , the horizontal and vertical diffusion coefficients, K_{hor} and K_{ver} , the air density, ρ_a , and the rain water content, q_r . $\rho_s=1.29 \text{ kg/m}^{-3}$ is a reference air density. The time step restriction for vertical diffusion depends on the numerical scheme that is chosen (explicit: Adams–Bashforth; implicit: Crank–Nicolson). The decision about the numerical scheme is taken online by the model itself.

When METRAS determines the total time step, it first evaluates Equations (3.32)-(3.40) at each grid cell. Then, it is assumed that all these processes, \mathfrak{P} , act simultaneously and in the same

direction. Hence, the total time step is calculated as

$$\Delta t = \frac{1}{\sum_{\mathfrak{P}} \frac{1}{\Delta t_{\mathfrak{P}}}} \quad (3.41)$$

Adaption of time step calculation to treatment of physical processes

To calculate the time step by Equation (3.41) implies that all processes listed in equations (3.32)-(3.40) are treated as concurrent. As they all are included in the summation in equation (3.41), the final time step becomes quite small. However, the examination of the numerical treatment of the processes revealed that actually a splitting is used between the advection/diffusion processes on the one hand and the cloud microphysical processes on the other hand. This means that intermediate values of the prognostic variables are determined after advection and diffusion are completed. Based on these intermediate values, the changes by cloud microphysics are calculated. This means that advection/diffusion and cloud microphysics are not simulated to act simultaneously but consecutively, which implies that the length of the total time step should only be limited by *either* the dynamic processes (\mathfrak{P}_D), advection and diffusion, *or* the cloud microphysical processes (\mathfrak{P}_C), accretion and sedimentation. This is accomplished by changing the time step calculation Equation (3.41) to

$$\Delta t = \min \left(\frac{1}{\sum_{\mathfrak{P}_D} \frac{1}{\Delta t_{\mathfrak{P}_D}}}, \frac{1}{\sum_{\mathfrak{P}_C} \frac{1}{\Delta t_{\mathfrak{P}_C}}} \right) \quad (3.42)$$

This approach reduces the computational costs by permitting larger time steps, and thus less time steps are needed to complete a simulation. Therefore, this approach was implemented for the operational HAMMER simulations.

Time split for cloud microphysics

A second optimisation manifested when investigating the values of different $\Delta t_{\mathfrak{P}}$ during realistic simulations. It became evident that the hardest constrain for the total time step is the sedimentation of rain droplets. This is calculated by an explicit scheme in METRAS; hence, small time steps are required. To overcome this limitation, a time splitting approach was introduced to METRAS. The idea is to separate the dynamic processes from the cloud microphysical processes in a way that time step constraints which are required for the cloud microphysical processes do not affect the time stepping of the dynamic processes. This means that the model time step is

determined only from the dynamic (dry) processes, \mathfrak{P}_D , advection and diffusion:

$$\Delta t = \Delta t_{dry} = \frac{1}{\sum_{\mathfrak{P}_D} \frac{1}{\Delta t_{\mathfrak{P}_D}}} \quad (3.43)$$

For those cases, when the cloud-microphysical equations require a shorter time step, e.g. during precipitation events, a second, smaller time step, Δt_{liq} , is introduced. This is used to integrate the calculations of the cloud microphysical processes in several smaller steps during one time step of the model.

This approach can be used because the cloud microphysical processes do not interact with the other processes on time scales smaller than the model time step. This means that the impact of the cloud microphysical processes on quantities like the temperature can be integrated over one model time step, Δt , and only then they are applied by other processes. For example, the heat that is released by the condensation of cloud droplets during one small time step, Δt_{liq} , increases the air temperature in the respective grid cell. At the next small time step, the condensation intensity might change because of the higher air temperature. In contrast, advection (non microphysical process) of this warmer air mass into another grid cell is so slow that it can be neglected that the condensation intensity would also be altered there. Only after one model time step, Δt , is completed, the total effect of condensation during all small time steps is considered in the advection process. This example clarifies the relation of cloud microphysical and non cloud microphysical processes by means of condensation and temperature advection. It is, nevertheless, also true for all other processes.

The length of the small time step, Δt_{liq} , is determined from the time step limitations of the cloud microphysical processes

$$\Delta t_{liq} \leq \frac{1}{\sum_{\mathfrak{P}_C} \frac{1}{\Delta t_{\mathfrak{P}_C}}} \quad (3.44)$$

such that the model time step $\Delta t = \Delta t_{dry}$ is a multiple of Δt_{liq} . Thereby, it is possible to calculate all equations connected to cloud microphysical processes $n = \Delta t / \Delta t_{liq}$ times using Δt_{liq} while the dynamical processes are only calculated once with $\Delta t = \Delta t_{dry}$. This approach ensures that the time step for every equation in the model never exceeds its allowed limit. However, as the small time step is not applied to all equations, computational costs can be saved nevertheless.

3.2.2.2 Performance tests

The suggested time split implementation was tested during its development in idealised simulations. Here, its application with HAMMER is analysed for the simulations of the experiment phase, which are shortly described in the second paragraph of Section 3.2.1.2. As the detailed setup of these simulations is not of relevance for the performance evaluation, it is disregarded here, and the reader is rather referred to Section 4.1. The simulations that were conducted operationally during the experiment phase (OPER-runs) are repeated without allowing METRAS to make use of the time split scheme, i.e. the time step is always calculated by Equation (3.42). These runs are named woTS-runs. As the weather was fairly nice during the test phase, there exist only 6 runs in which the time split feature actually is used in the operational runs (OPER-runs). These are listed, together with their given names, in Table 3.2.

Table 3.2: Start date and start time of those simulations of the HAMMER experiment phase in which the new time split scheme is used. The first column assigns a name which is used in following figures.

Assigned name	Start date of simulation	Start time of simulation
x0	21/03/2014	18 UTC
x1	22/03/2014	06 UTC
x2	22/03/2014	18 UTC
x3	23/03/2014	06 UTC
x4	24/03/2014	18 UTC
x5	25/03/2014	06 UTC

The first investigation shall quantify by how much the computational time can be reduced when applying the time splitting scheme. For this, the “SC Timer Lib”⁶ measured the wall-clock time needed for those periods of the OPER-runs in which the time splitting is active. For the woTS-runs, the wall-clock time is measured for those periods in which the time splitting would have been activated if this was not prohibited. These measurement periods are named TS-periods, and they match well between OPER-runs and woTS-runs. Usually, they differ by not more than ± 10 minutes, with one exception being 30 minutes. Thus, comparing the wall-clock times of these periods seems reasonable.

⁶provided by the Deutsches Klimarechenzentrum (DKRZ). Documentation was available on 2014/11/17 at <https://doc.redmine.dkrz.de/sct/html/>.

The achieved model speed-up is determined as follows: The SC Timer measures the wall-clock time that MESIM-METRAS needs to simulate the TS-periods, however excluding all IO-tasks and the coupling to HAMSOM because these could be influenced externally. Then, the wall-clock time is divided by the length of the TS-period to determine how many wall-clock seconds are needed per simulation second. The ratio between OPER-runs vs. woTS-runs of these values is given in Table 3.3.

Table 3.3: Ratio between computational speed (i.e. wall-clock seconds per simulation second) of OPER-runs and woTS-runs. Values are given separately for each run x0–x5 (Table 3.2) and for each simulation period defined by hours after simulation start. No value is shown if the time splitting approach was not activated (OPER) or would not have been activated (woTS) in the specified simulation period.

Name	0 h–6 h	6 h–24 h	24 h–66 h	66 h–102 h	102 h–138 h
x0	-	-	88%	90%	85%
x1	-	-	-	-	82%
x2	-	-	-	-	92%
x3	-	-	-	-	91%
x4	-	-	-	89%	-
x5	-	-	81%	87%	-

The results reveal that MESIM-METRAS is, in average, more than 10% faster during TS-periods when the time splitting approach is used. In other words: during one wall-clock second it is possible to advance the simulation by 11.7 model-seconds if the time splitting approach is used, compared to 10.0 model-seconds without the time splitting. This is only a moderate speed-up, which might be due to merely light rain in these simulations. As the rain rate is low, Δt_{liq} never becomes smaller than $0.5 \Delta t$. Thus, the time split cannot be taken full advantage of. Anyhow, the forecasts of HAMMER can be delivered a bit earlier using the new time split scheme.

The question arises whether the model results are altered by the use of the time split scheme. First of all, the simulated cloud and rain water contents are analysed as they could be affected most directly. SCHLÜNZEN and SOKHI (EDITORS) (2008) suggest to evaluate the cloud cover utilising BIAS and RMSE, hence these measures are applied here. Figures 3.6a and 3.6b show the BIAS between OPER-runs and woTS-runs of the vertically integrated cloud water content and vertically integrated rain water content, respectively. In the course of the simulations the BIAS values vary around zero. Also after short peaks for single runs, the solutions do not diverge. This means, that the use of the time split does not induce an increase or decrease of

cloud or rain activity. Peaks might be caused by clouds or rain appearing slightly earlier or later than in the reference run. However, no considerable shift is noticeable. Furthermore, the RMSE stays small compared to typical absolute values in cloud or rain areas.

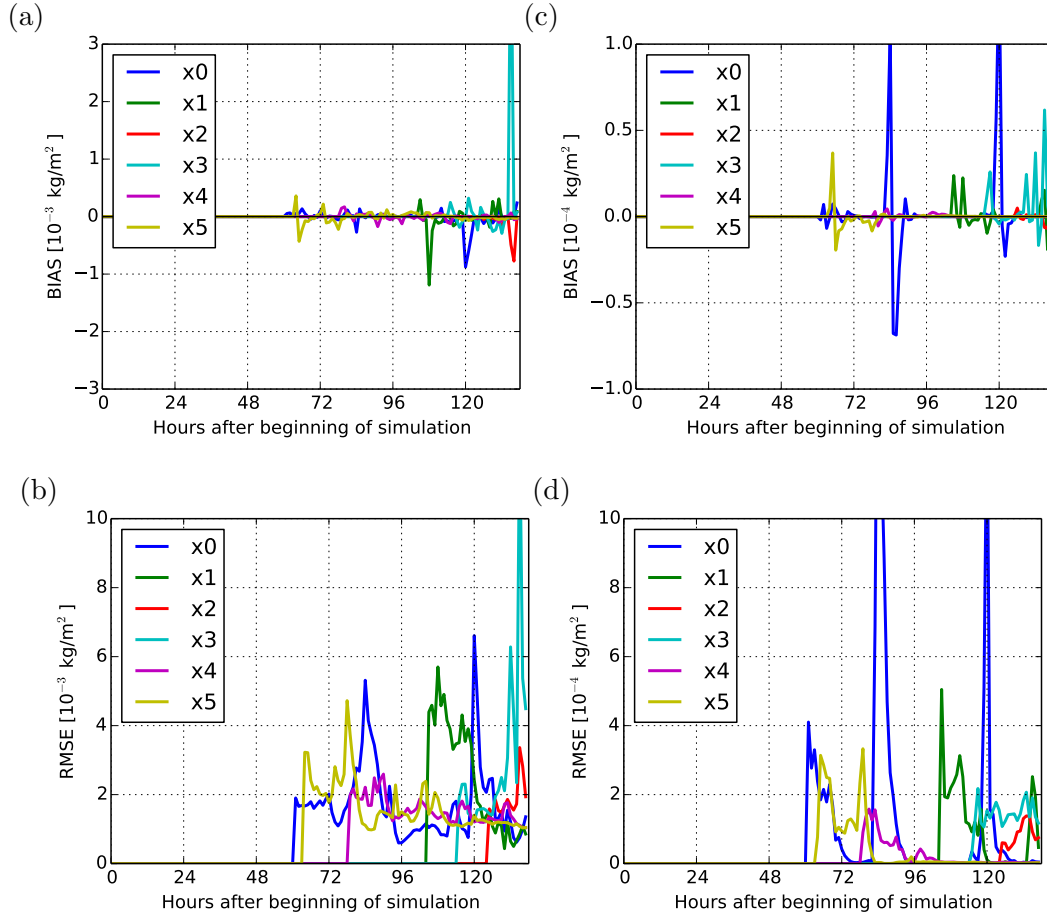


Figure 3.6: Comparison of model results for (a,b) vertically integrated cloud water content and (c,d) vertically integrated rain water content. The deviation between woTS-runs and OPER-runs is quantified by (a,c) BIAS, and (b,d) the 99-percentile of the absolute value of the differences. The development of these measures is shown for each run of Table 3.2.

Nevertheless, also the potential impact on sea ice properties should be checked. These quantities are mainly affected by the wind close to the surface. To evaluate the wind speed, SCHLÜNZEN and SOKHI (EDITORS) (2008) recommend to calculate a HITRATE. Using the formula given there together with the suggested tolerance limit of ± 1 m/s, the results are featureless. Thus, the limit to achieve a hit is reduced to 0.1 m/s here. The resulting HITRATE for the 10-m wind speed is shown in Figure 3.7a. It is mostly above 85%, which means that the pairs of OPER-runs and woTS-runs agree very well.

This agreement is also reflected by the sea ice properties ice concentration, A , and ice thickness, H : In analogy to Section 3.2.1.2, BIAS and 99-percentile of the differences are calculated. The time development is shown for each simulation in Figures 3.7b and 3.7d for ice concentration and in Figures 3.7c and 3.7e for ice thickness, respectively. The BIAS values are very small compared to typical values of these properties. The 99-percentile is largest for run x0, however it settles at a value that is still lower than what was caused by the new SOR-algorithm (Figure 3.5).

These evaluations lead to the conclusion that the application of the time splitting approach does not affect the simulation results considerably, while increasing the computational speed. For the analysed cases from the HAMMER experiment phase, the time splitting approach thus is practical. However, the sample of test simulations that is analysed here is very small, and further investigations are desirable. First tests have been carried out by SCHOETTER (2013, personal communication) based on cases from SCHOETTER (2013), which feature more intense rainfall events than simulated here. There, the effect of the time splitting becomes more relevant. The results indicate that the new time splitting approach can also be applied in these non-Arctic situations. Nevertheless, it should be considered to equip METRAS for Arctic simulations with an additional precipitation scheme that is capable of simulating snowfall instead of rain. This would, among others, alter the velocity of fall and thus the time step limitation.

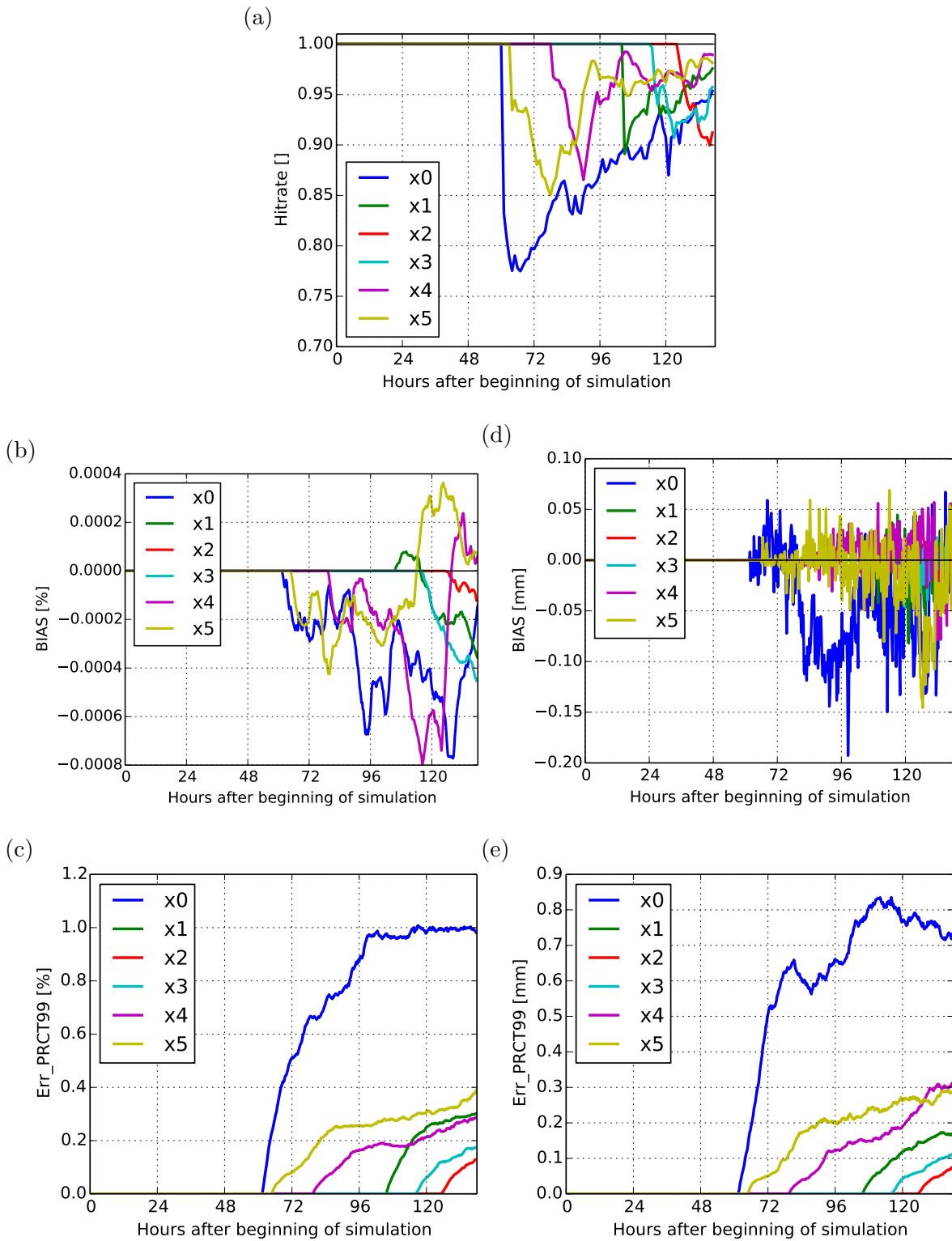


Figure 3.7: Comparison of model results for (a) 10-m wind speed, (b,c) ice concentration, A , and (d,e) ice thickness, H . The deviation between woTS-runs and OPER-runs is quantified by (a) HITRATE, (b,d) BIAS, and (c,e) the 99-percentile of the absolute value of the differences. The development of these measures is shown for each run of Table 3.2.

4 Application and evaluation of the model system

The model system HAMMER (Section 3.1) was developed in the project IRO-2 “Ice Forecast and Route Optimization” with the aim to forecast sea ice conditions in Arctic regions to support ship navigation. The long-term objective is to provide captains sailing in ice-covered waters with predicted ice charts as well as with routing suggestions. For a fast and timely delivery of the forecasts to the ships, several optimisations were applied to HAMMER, two of which are presented in Section 3.2.1 and Section 3.2.2. The improved model system was tested for the first time in March 2014: HAMMER was operationally simulating the ice conditions in the Barents Sea region, where the ice-going vessel R/V Lance was sailing along the suggested routes. At the beginning of this chapter, in Section 4.1, the setup of HAMMER for the modelling experiment is shown, supplemented by some exemplary simulation results. Afterwards, the model is evaluated using two different approaches: First, hit rates are used to evaluate the simulated ice concentration fields (Section 4.2). Then, the forecasted navigability of ship routes is evaluated by threat indices (Section 4.3).

4.1 Application of the model system during the IRO-2 experiment phase

HAMMER is applied in this thesis to the experiment phase of IRO-2. The specifics of this application, the model setup, and the used data are explained in Section 4.1.1. Subsequently, exemplary simulation results are shown in Section 4.1.2 to demonstrate the functionality of HAMMER and to give an impression of the conditions during the experiment phase.

4.1.1 Experiment and model setup

The components of the IRO-2 ice routing system, including the ice forecast model system HAMMER, were tested in an operational setup in the Barents Sea. Accordingly, the model domains are chosen as shown in Figure 4.1. Because the ocean model HAMSOM has a different grid type than the sea-ice/atmosphere model MESIM-METRAS, their model domains cannot be identical. HAMSOM covers the Barents Sea including the coast lines at its boundaries, which is advantageous for the numerical boundary conditions of the ocean model. This region is enclosed by the MESIM-METRAS model domain which completely includes the surrounding islands. In this way, it is avoided that orographic elevations are located at model boundaries where they would cause difficulties for METRAS. The topographic data for METRAS are prepared with the preprocessor GRITOP (SPENSBERGER and SCHLÜNZEN, 2010) from GTOPO30 data. The grid resolution of MESIM-METRAS is 5 km and the resolution of the underlying ocean in HAMSOM is about 1 nautical mile, represented in a longitude–latitude grid.

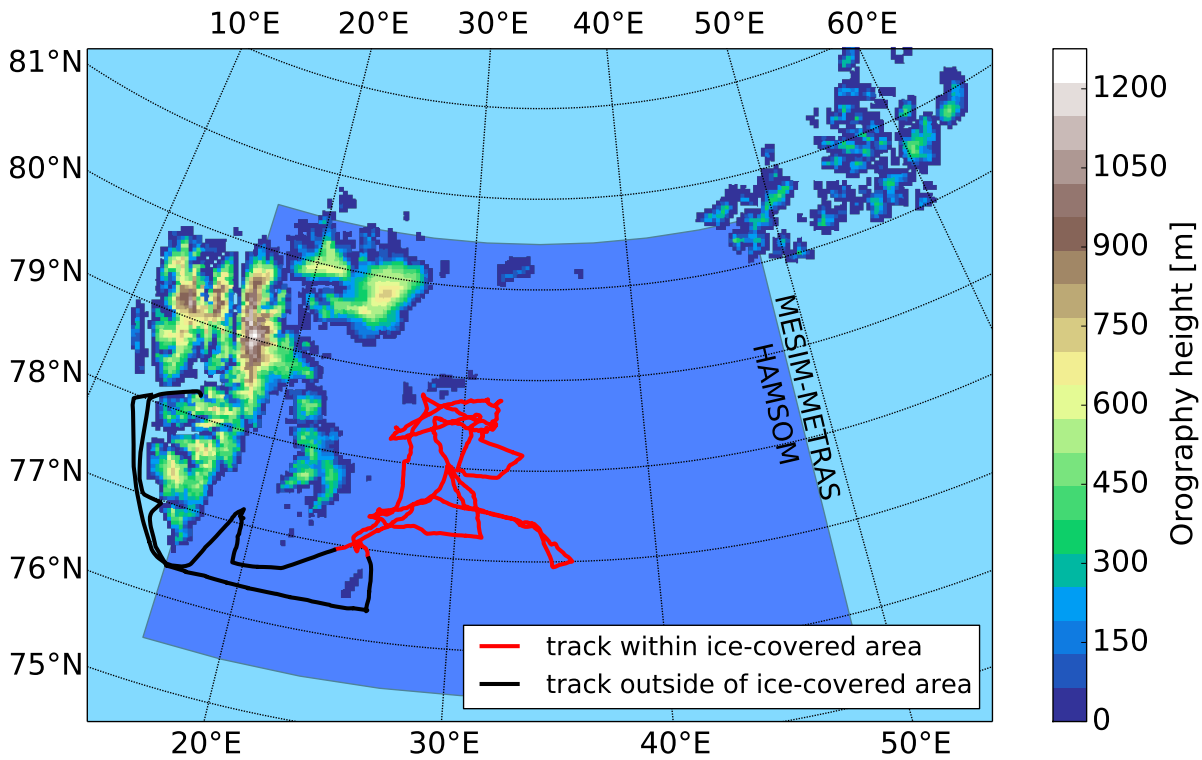


Figure 4.1: Model domain of the sea-ice/atmosphere model MESIM-METRAS with orography heights. The dark blue area depicts the model domain of HAMSOM. The line plot shows the track of R/V Lance from 15/03 until 28/03 in black if it passed areas without sea ice, and in red if it traversed sea ice.

Figure 4.1 also shows the track of the research vessel R/V Lance during the experiment phase in late March 2014. Since this is the only situation analysed in this thesis, the year will no longer be mentioned hereafter. When R/V Lance was in the ice-covered area (red track), it was guided by the navigation module of IRO-2, which utilised the sea ice forecasts of HAMMER. On 15/03, R/V Lance was put to sea from Longyearbyen in Svalbard. It met the ice edge in the southern Barents Sea on 17/03 and continued its cruise there until it left the ice on 26/03. On 28/03 it reached Isfjorden again. During these days, HAMMER was run operationally to forecast the sea ice conditions for R/V Lance. Thus, the model results will be analysed for Lance's sailing period and two preceding and succeeding days, i.e. from 13/03 until 30/03. HAMMER was controlled during the test by the automatic scheduling system ecFlow (ECMWF, 2014b) supervised by Björn H. Fock. The system prepared and managed all data (pre-)processing and started model simulations twice daily for 06 UTC and for 18 UTC. Thus, there is a total of 36 runs available, each of which includes 138 hours (>5 days) of forecast. More information about the automatic scheduling system can be found in FOCK (2014).

At the beginning of each simulation, all model components are initialised. Ice concentration data is provided by the Institute of Oceanography in Hamburg. They retrieve it from the Advanced Microwave Scanning Radiometer 2 (AMSR2) (BEITSCH et al., 2014). The product is available shortly before the 06-UTC-simulation is started and it contains the average ice concentration of the previous day. These data are prescribed at the beginning of the 06-UTC-simulation as well as at the 18-UTC-simulation assuming persistence of the ice concentration field due to lack of more recent data. The ice thickness is initialised from a SMOS product (TIAN-KUNZE et al., 2014), also provided by the Institute of Oceanography in Hamburg. As SMOS tends to underestimate the ice thickness in regions with little ice concentration (KALESCHKE, 2013, personal communication), a correction is applied that makes use of the AMSR2 data (Appendix D). Because the SMOS data are only available with a delay of 2 days, they are combined with the latest ice thickness forecast from ICEDAS. ICEDAS is run by O.A.Sys and FastOpt prior to each start of HAMMER, so its results can be used for initialisation after they have been interpolated onto the MESIM grid. After that, the corrected ice thickness from SMOS/AMSR2 is merged with results from ICEDAS to yield a high-resolution product as up-to-date as possible. In addition, ICEDAS is also used to initialise the thickness of the snow cover on top of the ice. The ice drift velocities are initialised from the preceding HAMMER run taking the values after 12 hours of forecast as the new initial values. The entire ocean model is also initialised from preceding simulations, as mentioned in Section 3.1.4.2. The state of the atmosphere is initialised from ECMWF forecasts using the 1D-version of METRAS. Each METRAS-simulation is started from the most recent ECMWF forecast, i.e. the 06-UTC METRAS-run is initialised by the 6-hour-forecast of the 00-UTC ECMWF-run, and the 18-UTC METRAS-run is initialised by the 6-hour-forecast of the 12-UTC ECMWF-run.

During the runs, boundary values are provided to HAMMER: METRAS is forced by the same large scale weather forecasts from ECMWF as it was initialised from. The used 'HRES product' of ECMWF provides 144-hour-forecasts with a time resolution of 3 hours. Boundary values for nesting MESIM and HAMSOM are provided by ICEDAS, which is run daily prior to the start of the 06-UTC HAMMER-run. The merging of ICEDAS-data with the tidal data of FES2004 is accomplished by the ecFlow scheduling system (ECMWF, 2014b).

The version of HAMMER that was used for the model calculations is defined by revision r1724 of the svn-repository <https://svn-zmk.zmaw.de/svn/metras/branches/iro/trunk> for HAMSOM and METRAS-1D and by revision r1724 of the svn-repository <https://svn-zmk.zmaw.de/svn/metras/branches/andrea/fixvalueBC> for MESIM and METRAS-3D, respectively.

Model output was generated every 15 minutes and saved in NetCDF format. During the experiment phase, these data were also provided to the Hamburgische Schiffbau-Versuchsanstalt

HSVA where the best sailing route suggestions were calculated (JOCHMANN et al., 2014) and delivered to the research vessel R/V Lance.

4.1.2 Exemplary results

Some of the simulation results generated by HAMMER are presented in this section. The intention is not to be exhaustive but to show selected features of HAMMER. Besides, the exemplary results shall give an impression about the ice- and weather-conditions during the experiment phase in late March 2014.

The first images show the ice concentration in the model domain and its development over time. Figures 4.2a and 4.2b depict the ice concentration as simulated by the 06-UTC run of 15/03. This represents the beginning of the experiment phase, when there was only relatively few ice in the Barents Sea. Starting from Figure 4.2a, that is valid for 00:00 UTC on 16/03, HAMMER forecasts a southward shift of the ice until 00:00 UTC on 19/03 (Figure 4.2b). This movement is caused by northerly winds, which were typical for the experiment phase. Its effect is e.g. well visible in the lee of (i.e. south of) islands, where large open water areas are predicted to emerge. These cannot freeze over in the simulation because of the missing thermodynamic part of MESIM.

The bottom row of Figure 4.2 shows simulation results of the 06-UTC run started on 29/03, that is towards the end of the experiment phase. Between Figure 4.2c (30/03, 00:00 UTC) and Figure 4.2d (31/03, 00:00 UTC) there is less ice movement predicted than in the previous example, but instead the formation of leads can be noticed. Conspicuous is also a general reduction of the ice concentration throughout the model domain. This feature is presumably caused by a numerical problem in MESIM that could not be solved despite all efforts.

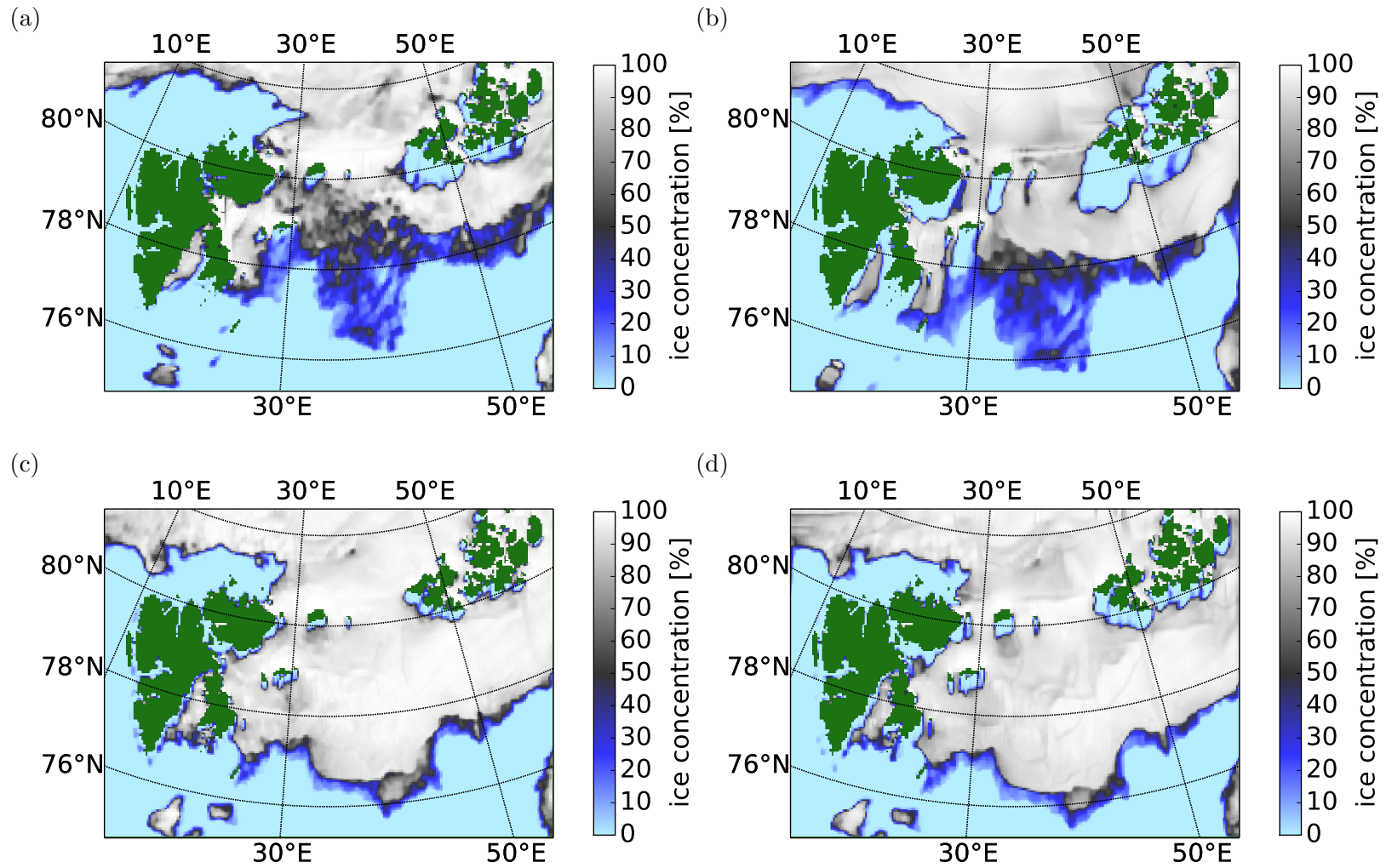


Figure 4.2: Simulated ice concentration on 4 exemplary days. Top row: 06-UTC run of 15/03 after (a) 18 hours simulation and (b) 3 days later than (a). Bottom row: 06-UTC-run of 29/03 after (c) 18 hours simulation and d) 24 hours later than (c). Land areas are coloured green.

In comparison to the previous situation early in the experiment phase (top row), there is a lot more ice present at the end (bottom row). Even though MESIM cannot simulate new ice formation, the results show an increased ice concentration. The reason is that the satellite whose data is used to initialise MESIM observes the newly formed ice. Ice formation is favoured during the experiment phase because of low temperatures. Figure 4.3 illustrates this with station data of the observation sites on the islands of Edgeøya, Kongsøya, and Kvitøya. These data were acquired from the eKlima-portal⁷ of the Norwegian Meteorological Institute. Just before the start of the experiment phase on 13/03, the temperature dropped below $-10\text{ }^{\circ}\text{C}$ and remained there almost until end of March. This gave rise to a period of intensive new ice formation.

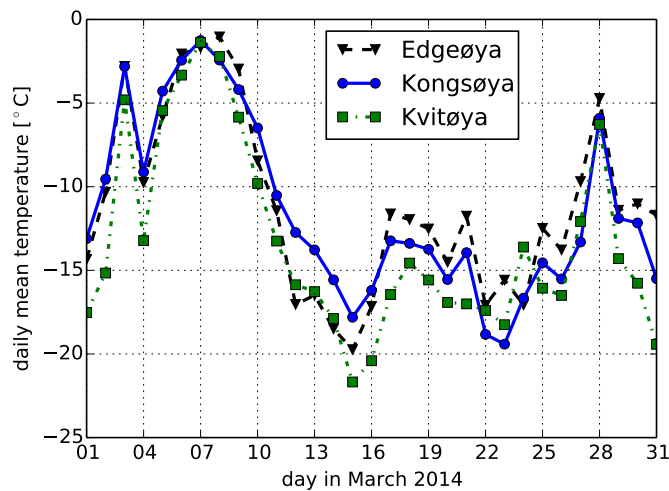


Figure 4.3: Daily mean temperatures at the stations on Edgeøya, Kongsøya, and Kvitøya during March 2014.

The simulation results in Figure 4.4 reveal what could be speculated from Figure 4.2 already: The ice drift is, at times, heavily controlled by the near-surface wind. The 06-UTC run of 19/03 features a small low pressure system that moves eastward across the Barents Sea. Snapshots of wind speed and direction are presented for 22/03 04:00 UTC and 22/03 14:00 UTC in Figure 4.4a and Figure 4.4b, respectively. Comparing these with Figure 4.4c and Figure 4.4d, which show the ice drift at the same times, demonstrates well that the ice movement clearly follows the wind in this situation.

⁷eklima.met.no, accessed on 14/07/2014.

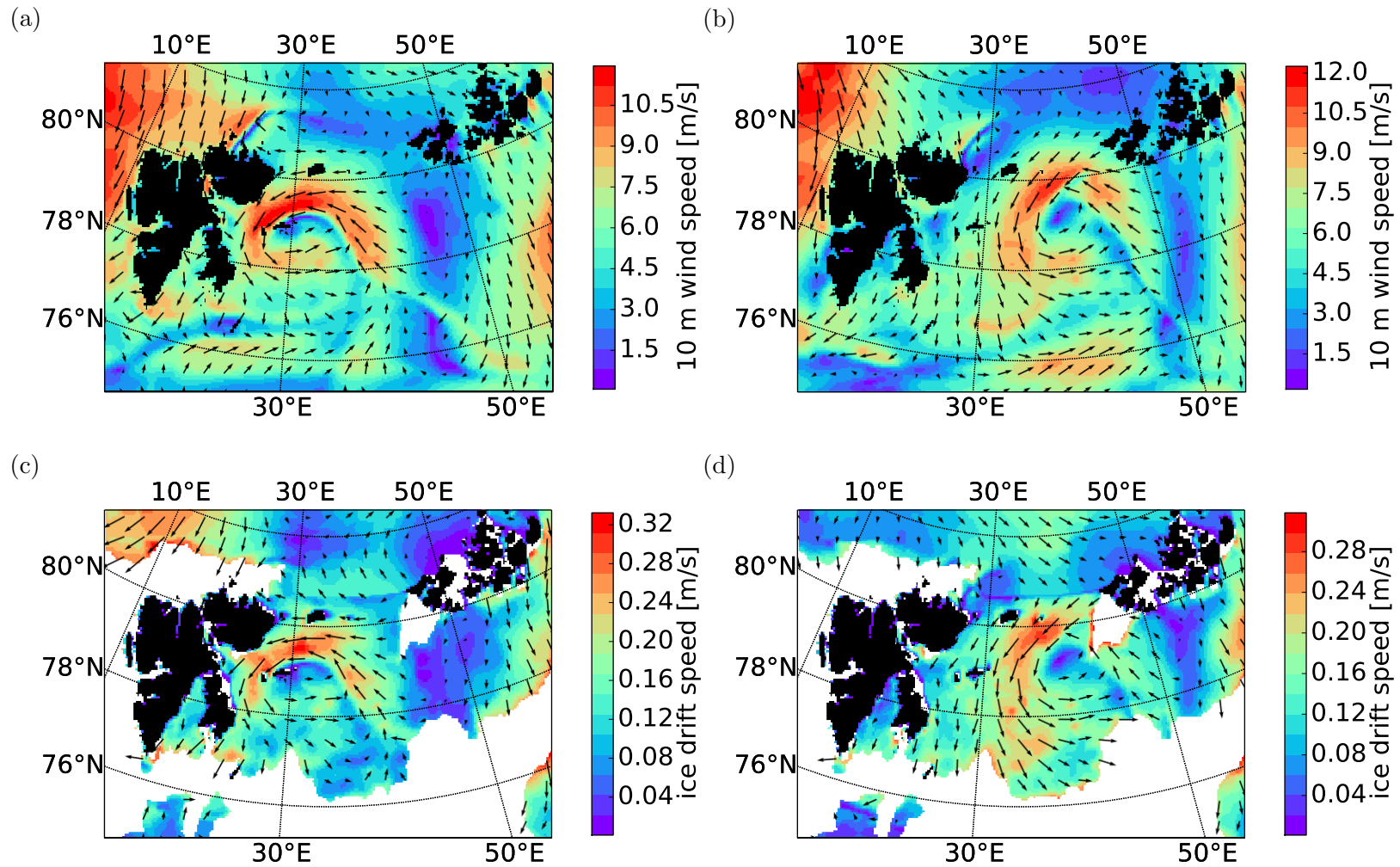


Figure 4.4: Simulated 10-m wind (top row) and ice drift (bottom row) from the 06-UTC run of 19/03. (a) and (c) show the state at 04:00 UTC on 22/03, and (b) and (d) show the state 10 hours later. Please note the changing colour scales! No values are shown in (c) and (d) for regions without ice. Land areas are blacked out.

The interaction between atmosphere and sea ice works, however, in both ways: Figure 4.5a shows the transport of temperature from the surface (be it land, ocean or ice) into the atmosphere. The snapshot is taken from the 06-UTC run of 28/03 and gives the values for 29/03 17:00 UTC, which is at about sunset. Light blue values over land indicate that the land cools the atmosphere because its surface temperature is low due to radiative cooling. Outside of land areas, the temperature transport is still positive meaning that the surface is warmer than the air above. This is consistent with the weather situation, with cold air above the warm ocean ($>-1.8\text{ }^{\circ}\text{C}$). Interestingly, the intensity of the heat transport varies locally, and the cause for this can be seen in Figure 4.5b: Those areas which are covered by sea ice exhibit less temperature transport than the open ocean. Thus, HAMMER is clearly able to simulate the insulating effect of sea ice for the heat exchange between ocean and atmosphere.

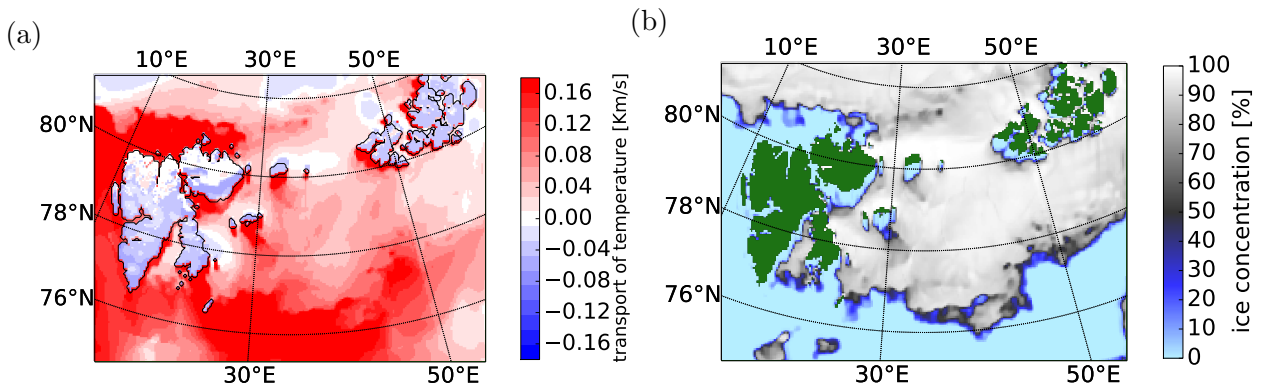


Figure 4.5: Simulated (a) temperature transport and (b) ice concentration on 29/03 at 17:00 UTC from 06-UTC run of 28/03. Land areas are shown as black contour line in (a) and are coloured green in (b).

Another exemplary result presents a feature of METRAS. During the experiment phase, the weather was often nice without any precipitation. Clouds, however, existed, and such an example is shown in Figure 4.6a from the 06-UTC run of 21/03 for 06:00 UTC on 22/03, i.e. shortly after sunrise. The vertically integrated cloud water content reveals clouds with different density in the model domain. In comparison, Figure 4.6b shows the net shortwave radiation that METRAS simulated for the same time: The shadowing effect of the clouds is clearly visible. Additionally, the influence of different albedo values of the surfaces can be noticed. The dark land absorbs most of the incoming shortwave radiation, while the sea ice reflects much, so that the net value is small. Open water areas are also well recognisable because they absorb much less shortwave radiation than land areas at this time. The sun is very low above the horizon so that the incident angle to the water surface is low, and most of the radiation is reflected. METRAS is capable of simulating this effect and reduces the net shortwave radiation.

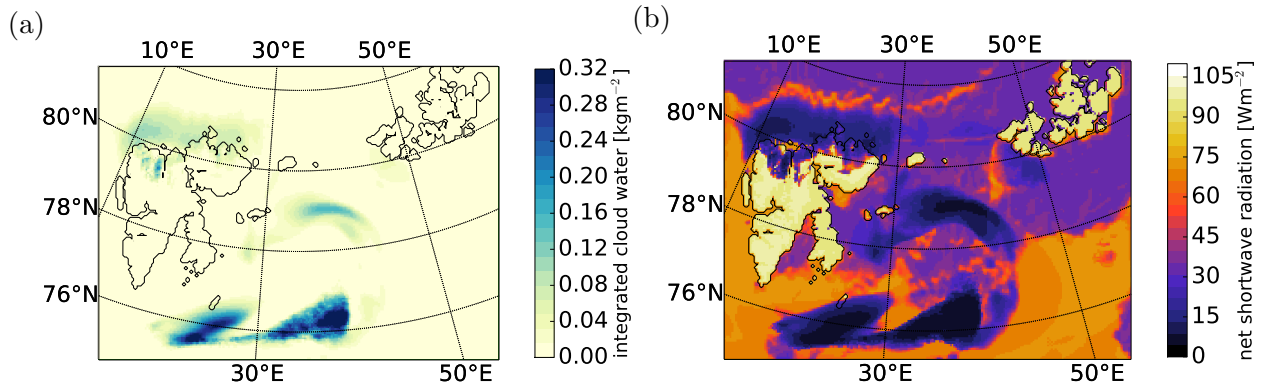


Figure 4.6: Simulated (a) vertically integrated cloud water content and (b) net shortwave radiation on 22/03 at 06:00 UTC from 06-UTC run of 21/03. Land areas are shown as black contour line.

The last paragraphs should have given some impression about the model features and physical conditions during the experiment phase. These simulations will serve as the standard application cases of HAMMER throughout the rest of the thesis, and they will be drawn upon again.

4.2 Predicted ice concentration

4.2.1 Calculation of hit rates

The quality of the model simulations during the experiment phase shall be evaluated against satellite data. The focus is on ice concentration because it is a key property for ship navigation. Forecasted ice concentration values are compared to the data set from AMSR2 which was also used to initialise the model. It is suitable for model evaluation (VAN WOERT et al., 2004)—even though it does not perfectly represent the 'truth'—because it eases the interpretation of the differences between model and satellite as no additional errors are introduced from an external reference data set.

When the ice concentration of global sea ice models is compared to satellite data, often integral values are used, for instance the total sea-ice area or the sea-ice extent (NOTZ, 2014). This practice seems appropriate for climate studies, where the overall ice coverage of the ocean is of interest. For the evaluation of a model with respect to ship navigation however, not only the total amount of sea ice but also its spatial distribution is crucial. A measure that would take into account the value at each single grid cell is the root mean square error (e.g. applied by TIETSCHKE et al. (2013)). However, it places the model at a disadvantage if the reference data are

subject to uncertainties. In order to take into account the uncertainty inherent to the AMSR2 data while evaluating the accuracy of each grid cell, the model quality is assessed by a hit rate.

A hit rate compares a model simulation with an observation field (in this case a satellite map) and states how many grid cells show a difference between model and observation that is smaller than a certain threshold, called a 'hit'. Often, this threshold is set according to the assumed desired accuracy of model results, i.e. in which range the simulated values of a "correct" model can be expected (as e.g. proposed by the model evaluation guidelines of COST728 (SCHLÜNZEN and SOKHI (EDITORS), 2008)). In our case, the uncertainty of the observations, to which the model is to be compared, is quite large. Thus, it seems appropriate to take the observational uncertainty as threshold and count a hit if the simulated value lies within the uncertainty range.

The hit rate is given in percent and specifies the fraction of the number of hits to the total amount of grid cells. It is calculated as

$$H = \frac{1}{N} \sum_{i=1}^N n_i \quad \text{for } n_i = \begin{cases} 1 & \text{if } |M_i - S_i| < \epsilon(S_i) \\ 0 & \text{if } |M_i - S_i| > \epsilon(S_i) \end{cases} \quad (4.1)$$

by evaluating the difference between the ice concentration M_i of the model and S_i of the satellite at each grid cell i and counting how often it is smaller than the uncertainty ϵ of the satellite. This sum is divided by the total number of grid cells N .

The uncertainty ϵ of the satellite data is given in SPREEN et al. (2008) as a function of ice concentration S_i . It is up to $\pm 25\%$ for low ice concentration and approaches $\pm 6\%$ for compact ice coverage. So, in regions with low ice concentration, the model is allowed to deviate by 25 percentage points from the satellite to achieve a hit while for high ice concentration a smaller difference than 6 percentage points is required for a hit.

In order to make the comparison possible, the model data have to be preprocessed: The AMSR2 ice concentration data (BEITSCH et al., 2014) are provided by BEITSCH (2014, personal communication) as daily average values. Accordingly, daily mean values are calculated for the modelled ice concentration. For this, the first hour of each model run is disregarded because the results are not reliable during this initialisation phase where the atmospheric forcing is not fully active yet. Likewise, values of grid cells either containing land or located at the model boundary are not taken into account.

Hit rates are calculated for each of the 18 model simulations between 13/03 and 30/03, for both the morning run fc06 (starting for 06:00 UTC) and the evening run fc18 (starting for 18:00 UTC). The daily average for each of the 6 forecasted days is compared to its corresponding satellite observation. The results—discussed in Section 4.2.2—are 18×6 hit-rate matrices for both fc06 and fc18.

Open water areas usually are very easy to forecast for the model, especially if they are far away from the ice edge. This would lead to inordinately high hit rates if the model domain includes much open water. Therefore, grid cells are excluded from the hit-rate calculation if they do not show any ice during the six days of forecast—neither in the model nor in the satellite maps. This means that the 'total number of grid cells' N is different for each of the 18-2 model runs.

4.2.2 Results

Figure 4.7a and Figure 4.7b show the resulting hit rates for the two simulations that are run at each day, namely the forecast fc06 that starts at 06:00 UTC and the forecast fc18 that starts at 18:00 UTC. The plots display six hit rate values for each model run (y-axis), one for each day of the 6-day-forecast (x-axis). The first column shows the hit rates for the day at which the model is initialised, or more precisely for the remaining 18 hours (fc06) and 6 hours (fc18) of this day, respectively. Here, for fc06, the maximum value of 75% can be found revealing that the model predicts an ice concentration value within the error range of the satellite for 75% of all grid cells. The hit rates decrease in the course of the simulations and in the worst case, after five days lead time, an acceptable ice concentration value is forecasted only for 23% of the grid cells. In general, such a decrease of the hit rate over time is expected, unless HAMMER were a "perfect model" with an absolutely correct initialisation. As this is not the case, the forecast will deviate more and more from the reality, as reflected by the hit rate values.

Besides this, there are some more features and questions concerning the hit rate charts that will be investigated in Sections 4.2.2.1–4.2.2.3:

1. What is the difference between the hit rates of fc06 and fc18 and how can it be explained? (Section 4.2.2.1)
2. How does the model compare to persistence-forecasts? (Section 4.2.2.2)
3. How can the day-to-day variability of the model quality be explained? (Section 4.2.2.3)

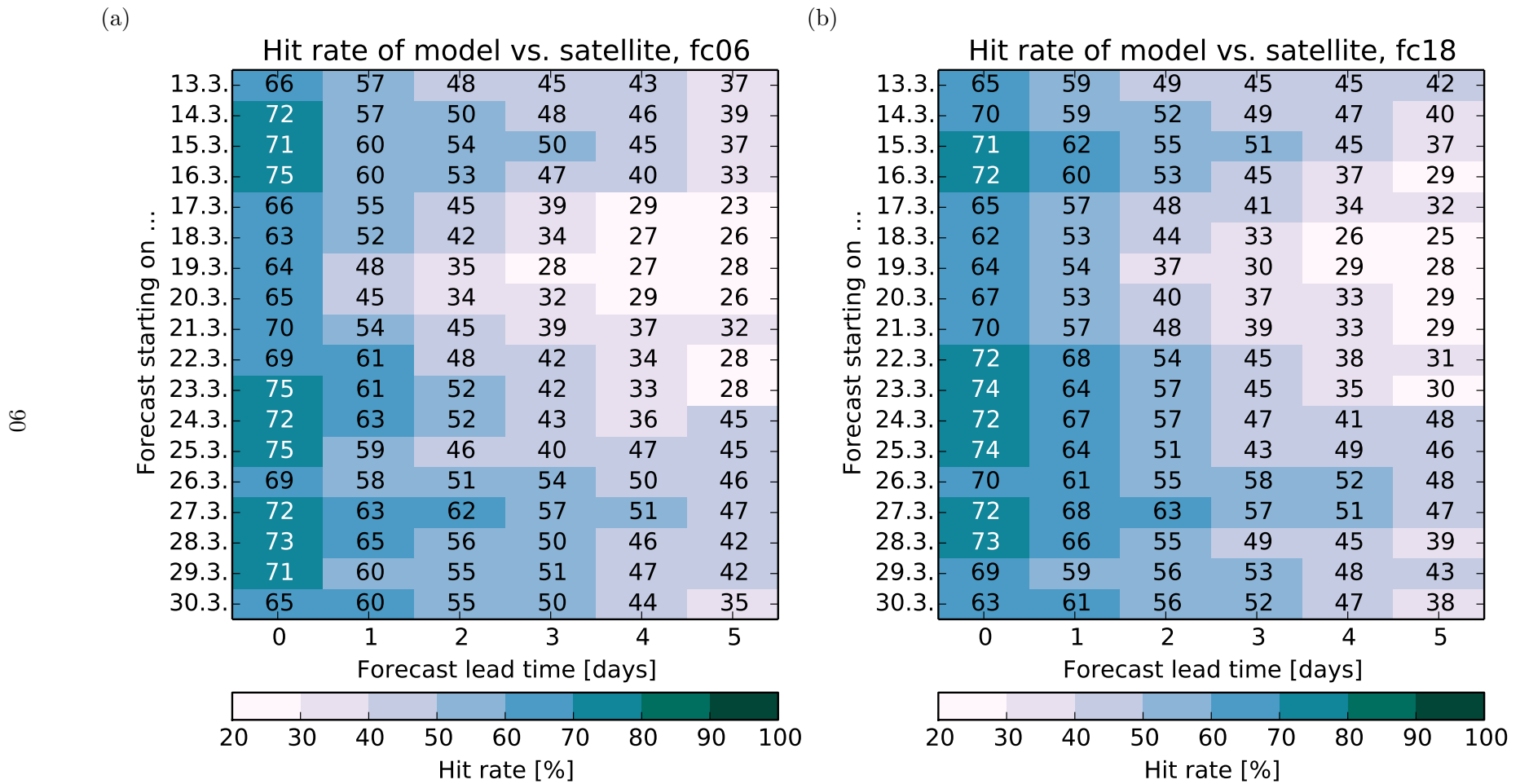


Figure 4.7: Hit rate of simulated ice concentration values compared to AMSR2 data for (a) fc06-runs and (b) fc18-runs.

4.2.2.1 Impact of the time of model initialisation on hit rates

The hit rate is determined separately for the model runs fc06, that started at 06:00 UTC (Figure 4.7a), and for those that started at 18:00 UTC (fc18, Figure 4.7b). The resulting maps are similar and contain the same features, so their differences were calculated and displayed in Figure 4.8. Positive values indicate higher hit rates for fc18 compared to fc06. In general, the differences do not exceed 5% except for few outliers. At the initialisation day—i.e. 0 days lead time—the differences are very close to zero but slightly negative in average over all runs. For forecasts lasting 1 day or longer, the differences are mostly positive as indicated by the reddish colour.

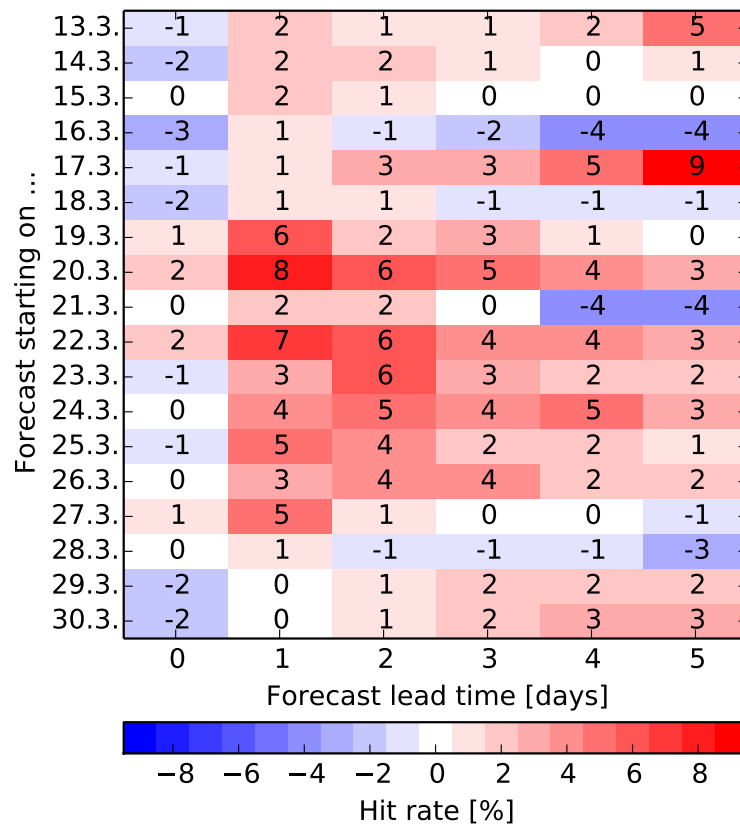


Figure 4.8: Difference of the hit rates of simulated ice concentration between fc18-runs and fc06-runs. Positive values indicate that the hit rate of the evening run fc18 is higher than that of the morning run fc06.

The fc06- and fc18-runs distinguish themselves by their initialisation time and correspondingly by their initialisation and forcing data. The fc18-run uses an atmospheric forcing from the 12-UTC-forecast of ECMWF instead of the 00-UTC-forecast used for fc06. Furthermore, more

recent satellite data of SMOS become available prior to the start of fc18 which are used for the ice thickness initialisation. This is not true, however, for the initialisation of ice concentration and the lateral forcing of ice variables by the large-scale sea ice model. These data sets are not updated between fc06 and fc18, thus both model runs rely on the same forecast-run of the large-scale model and are started with an identical ice concentration field.

The higher hit rates for fc18 than for fc06 that are shown in Figure 4.8 after the first forecast day can have multiple reasons: First of all, the model run for producing a forecast for a specific day is shorter for fc18-runs than for fc06-runs. Thus, model deficiencies cannot impair the model results as much due to the shorter run time. Furthermore, the newer atmospheric forcing used in fc18-runs can lead to a more realistic sea ice concentration forecast because newer weather forecasts usually are more correct than older ones. Also the more recent ice thickness initialisation could favour the fc18 run; its influence on the ice concentration field however is considered to be minor. That hit rates at the initialisation day are lower for fc18 compared to fc06 has yet another explanation: The daily average for the initialisation day is based on 17 hours of model forecast for fc06 and 5 hours⁸ for fc18. The low hit rate for fc18 indicates that only 5 hours of model simulation are not sufficient to represent the average of the whole day.

The general advantages of fc18 compared to fc06 are independent of the ice concentration initialisation as both runs are initialised with the same satellite data. The update takes place between fc18 and the fc06 of the next day (named fc06₊₁). So, in order to study the impact of renewed ice concentration initialisation data, the hit rate differences are calculated for the fc06₊₁-runs compared to their preceding fc18-runs. The results are averaged over all runs and presented in Figure 4.9 as solid line. For comparison purposes, the dashed line shows the averages of the previously discussed differences of fc18-runs compared to their preceding fc06-runs. The forecast lead time is given corresponding to the latter of the two runs that are compared to each other. Therefore, no hit rate difference of fc06₊₁ to its preceding fc18-run can be calculated for a lead time of 5 days because the preceding fc18-run is finished before this day. In contrast to the previously discussed results, the newer fc06₊₁-runs have a higher hit rate than their preceding fc18-runs, also at the beginning of the model runs: On average, they are higher by 9 percentage points. Over the course of the model runs, the average difference decreases but it never drops below 2.5 percentage points.

The two graphs in Figure 4.9 are similar in their shape except for the first value and an offset. There is no jump at the beginning of the solid line because all involved daily averages are determined from at least 17 hours of data. Except for this, both curves are located above the zero line which leads to the conclusion that a recent run is better than its preceding one. The

⁸fc06 starts at 06:00, fc18 starts at 18:00 UTC, and the first hour is disregarded because of the initialisation phase. Thus, there are $24-6-1=17$ and $24-18-1=5$ simulation hours left, respectively.

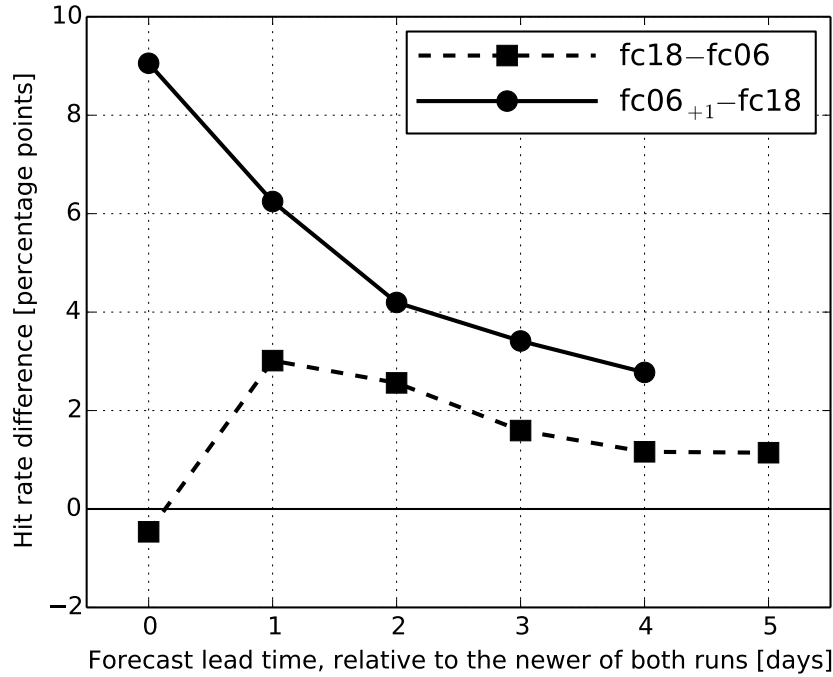


Figure 4.9: Hit rate difference between fc18 and fc06 (dashed) and between fc06₊₁ and fc18 (solid) averaged over all simulations. The subscript “+1” marks that the values of fc06₊₁ originate from the succeeding day compared to fc18. The forecast lead time is quantified based on the more recent run, i.e. fc06₊₁ (for solid) and fc18 (for dashed), respectively.

decline of both curves over time, however, shows that the advantage which is inherent to a later run decays during the course of a simulation. Moreover, the dashed line depicts that fc18 is only less than 2 percentage points better than fc06 after three days. Thus, when a timely forecast is required, it is not recommended to wait for the fc18-run.

Additionally, the offset of the two graphs indicates that the fc06₊₁-runs differ from their preceding fc18-runs much more than fc18-runs differ from their preceding fc06-runs. The different setup of fc18-runs in comparison to fc06-runs includes—as discussed above—a more recent atmospheric forcing and an updated ice thickness initialisation. For the succeeding fc06₊₁-run on the next day, again a new atmospheric forcing is applied. Therefore, this cannot explain the offset of the graphs because it affects both transitions, fc06→fc18 and fc18→fc06₊₁, equally. Discrepancies can only arise from different update times: Ice thickness initialisation data is updated between fc06 and fc18, while ice concentration initialisation data and lateral sea ice forcing data are updated between fc18 and fc06₊₁. The lateral sea ice forcing, however, is not supposed to have a large influence on the model results because sea ice properties from the

boundaries cannot be advected far into the model domain. Hence, it comes down to the update times of the initialisation data for ice concentration and for ice thickness. Ice concentration is updated between fc18 and fc06₊₁ (solid line), while ice thickness is updated between fc06 and fc18 (dashed line). Apparently, an update of ice concentration initialisation data improves the hit rates more effectively than an update of ice thickness initialisation data. In a way, this finding is not surprising considering that the hit rates assess the quality of the ice *concentration* forecast. Wrong ice thickness values should only have a minor impact on the ice concentration field.

4.2.2.2 Comparison of hit rates between model and persistence forecasts

The calculated hit rates state how well the forecasted ice concentration conditions compare with "reality" in the form of satellite observations. The resulting numbers, however, are not too informative in itself and the question arises which hit rate value has to be achieved to deem the model "good" or beneficial. The answer can be found by comparing the model to a reference, which could be climatology for long-range models and persistence for short-range models (VAN WOERT et al., 2004). HAMMER as a short-range forecasting system is thus compared to persistence here.

A persistence-forecast is the easiest prediction of future conditions, as it does not require any model: It is simply assumed that the current state *persists*, i.e. that there are no changes over time. The focus in this section is on ice concentration, so the current state is determined from the AMSR2-data that were previously used for model initialisation and model-hit-rate calculation. When the current state of some day is compared to the observational data of a later day which was targeted by the persistence-forecast, the quality of the persistence-forecast can be assessed for example by calculating a hit rate again. This can then be compared to the hit rate of the model forecast to investigate the advantage of the model over the persistence-forecast.

The hit rates for the persistence-forecasts are calculated in the same way as for the model-forecasts (Equation (4.1)), with the difference that outdated satellite observations are used instead of modelled data. In order to be able to compare the resulting persistence-hit-rates to the model-hit-rates later on, the grid points that are masked out because of open water are the same here as in the calculation of the model-hit-rates. Because there are different open-water-masks for the fc06 and fc18 runs, the persistence-hit-rates of fc18 differ slightly from those of fc06, albeit not enough to be shown separately. The hit rates are calculated for persistence-forecasts that use observed data of 12/03 and up to 29/03. The reason for investigating the forecast of 12/03 and not that of 30/03 as done before will become clear later on when the persistence-forecasts are compared to the model.

The resulting hit rates are shown in Figure 4.10 for daily persistence-forecasts with up to 6 days lead time each. For 0 days lead time, the hit rate invariably is 100% because the ice concentration field is compared to itself: The observed satellite data are used as reference-”truth“ as well as as forecast for the day of observation. After this first day, the hit rate drops by about 30% and further decreases creepingly for 2 and more days lead time. The predicted ice concentration after 6 days lies within the uncertainty range of the satellite data in 40–67% of the grid cells. In general, a decreasing hit rate over time is expected as the sea ice system develops and thus diverges from its previous state. However, certain variability can be seen: for example persistence-forecasts in the period 12/03 to 14/03 show a clearly worse skill than those in the period 21/03–23/03. The skill depends on the steadiness of the weather situation: If the day-to-day variation is low, persistence is a good predictor.

The persistence-hit-rates can serve as a reference when interpreting the hit rates achieved by the model. If the persistence-forecast achieved better results than the model, the benefit of the model would be contested. For the comparison, the model-hit-rates have to be compared to their *corresponding* persistence-hit-rates, i.e. the persistence-forecast that is based on the same data that are available at model start. Let us assume that a persistence-forecast had to be made due to absence of a model. The only data that were available then are the initialisation data, which would be used by the model to simulate the conditions of the first day (0 days lead time). These data were observed on the previous day. Thus, the corresponding persistence-forecast starts at the previous day and needs 1 day lead time to predict ice conditions for the day of model initialisation. Hence, the hit rate of the model-forecast for 0 days lead time has to be compared to the hit rate of the persistence-forecast starting one day earlier, but evaluated for 1 day lead time. More generally, the N -day forecast of the model that was started on day X is to be compared to the $(N+1)$ -day persistence-forecast based on data of day $X-1$. Thus, the model runs from 13/03 until 30/03 are compared to the persistence forecasts of 12/03 until 29/03.

The resulting differences between model- and persistence-hit-rates are shown in Figure 4.11. Positive values, which indicate a higher hit rate of the model than of the persistence-forecast, can almost only be found in the first column, which depicts the hit rate difference for the initialisation day. On that day, the model has a marginally better hit rate than the persistence-forecast, at maximum 4 percentage points. For 1 day lead time or more, the values are increasingly negative telling that the ice concentration is predicted less accurate by the model than by the persistence-forecasts. This is especially true between 17/03 and 25/03, where the persistence-forecasts show hits for at least 20% more grid cells than the model does.

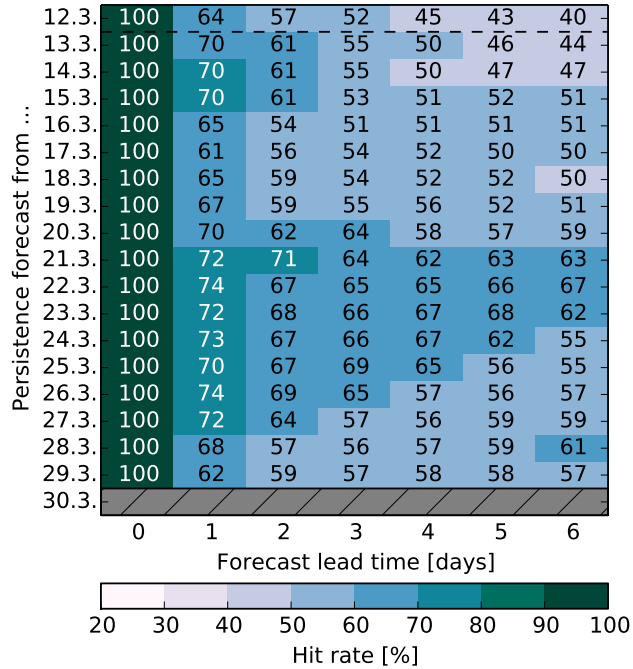


Figure 4.10: Hit rates for ice concentration values predicted by persistence-forecasts from AMSR2 data compared to most recent AMSR2 observations valid for each forecast day. Those grid cells that had been excluded in the fc06-runs due to open water have been excluded from the hit rate calculation.

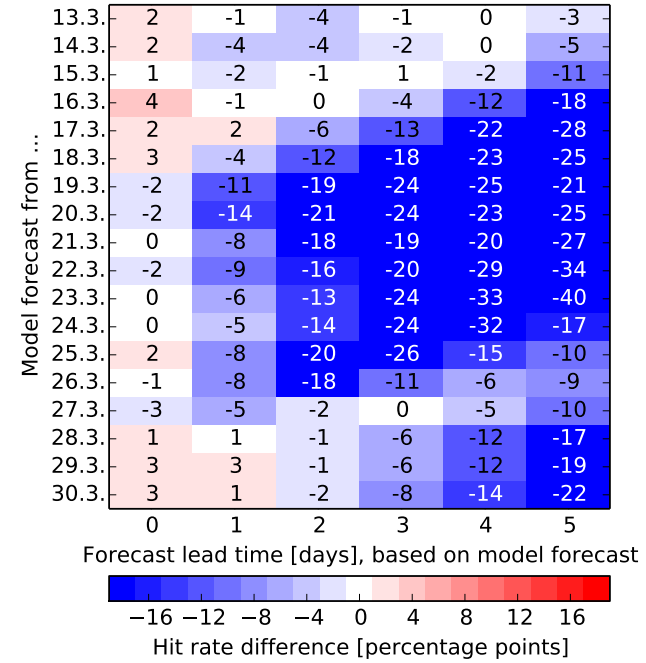


Figure 4.11: Difference between the hit rates from the model-forecasts (Figure 4.7a) and from the persistence-forecasts (Figure 4.10) for fc06-runs. Positive values indicate higher hit rates of the model than of the persistence-forecasts. Model-forecasts are compared to their preceding persistence-forecasts valid for the same day, i.e. with 1 day more lead time than the model-forecast.

The hit rate differences for 0 days lead time, that are close to zero, evince that the model-forecast for the initialisation day is not worse than persistence. Looking at it the other way round, the model has no actual chance to be better than persistence because it is initialised with the data from the previous day. This connotes an implicit application of persistence because the model misses 18 hours of ice development. As the hit rate drops within the first 24 hours of persistence by 30% (Figure 4.10), the seemingly low model hit rate of about 70% at the beginning (Figure 4.7a) is obviously caused by the initialisation procedure rather than by a deficiency of the model itself.

After more lead time, however, the hit rate of the model becomes worse than persistence—sometimes drastically. This is evidence of an incapacity of the model as it implies that the forecasted ice concentration is more correct if the initial fields were taken as the forecast result; so no model would be needed. One could argue that the satellite maps might contain features which the model is not able to capture nor to reproduce, hence favouring the persistence-forecast because in this case satellite data are compared with other satellite data and not with model data. However, the hit rate differences are too large to be caused only by this effect.

In order to investigate the reason for the poor model performance, the hit rates are calculated separately for those grid cells that show an sea ice concentration (SIC) below 5% and above 95% in the reference satellite data, respectively. The resulting persistence-hit-rates are subtracted from the model-hit-rates as explained above and the differences are presented in Figure 4.12a for $SIC < 5\%$ and in Figure 4.12b for $SIC > 95\%$. In contrast, Figure 4.12c depicts the hit rate difference for the remaining grid cells with an ice concentration between 5% and 95%.

The figures reveal that the hit rate difference is negative mostly for grid cells with less than 5% or more than 95% ice concentration. For the remaining grid cells, the difference is positive indicating that the model performs better than persistence-forecasts.

The largest (negative) impact on the total hit rate difference arises from the grid cells with $SIC > 95\%$, not only because there are many of these cells in the model domain but also because the model has an incredibly lower hit rate than a persistence-forecast (Figure 4.12b). The explanation for this behaviour is a deficiency of the sea ice model MESIM: Due to unknown reasons, the ice concentration in MESIM continually decreases during the simulations. Ice mass is not lost, however, because the ice thickness increases accordingly to the decreasing ice concentration. Some attempts have been made during this study to find and fix the cause of this unphysical feature, without any success though. The leakage of ice concentration is larger than the allowed deviation from the reference satellite observations of ± 6 percentage points, so the hit rate is very low for the model predictions.

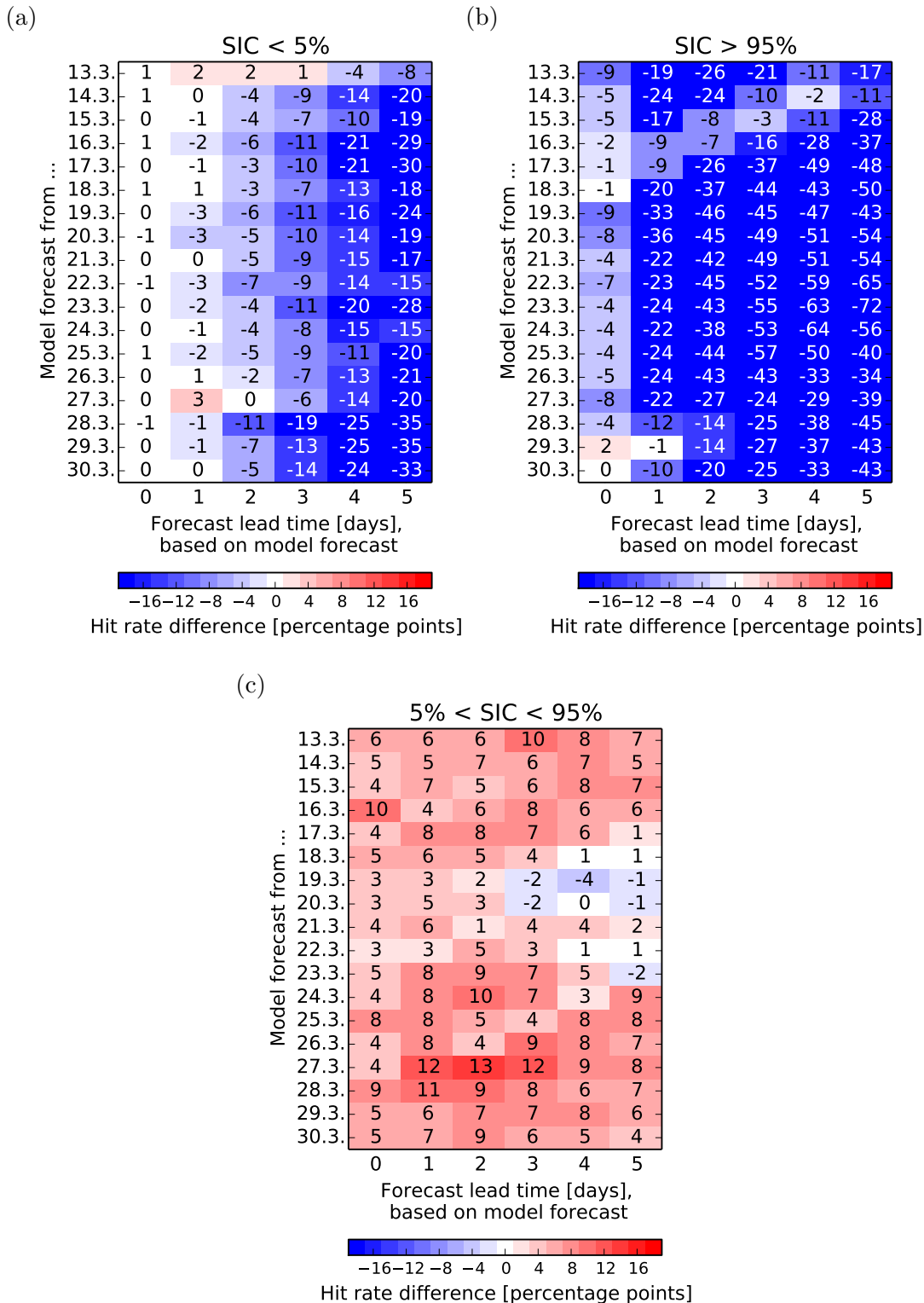


Figure 4.12: Difference between the hit rates from the model-forecasts and from the persistence-forecasts for fc06-runs, separated for grid cells with ice concentration (SIC) of the satellite observations (a) lower than 5%, (b) higher than 95%, and (c) between 5% and 95%. Positive values indicate higher hit rates of the model than of the persistence-forecasts.

A negative hit rate difference also evolves for grid cells with less than 5% ice concentration at the end of the forecasts (Figure 4.12a). The model, however, performs not particularly bad—also because the allowed deviation to achieve a hit is large (± 25 percentage points for this ice type)—but the persistence-forecast is even better. The reason lies in the general ice development during the investigated days at the end of March: The ice edge progresses southward most of the time due to low temperatures and ice drift from north. Hence, the area that is covered with ice of less than 5% concentration shrinks from day to day. This means that those grid cells in which the ice concentration is still below 5% after some days have most likely also been ice-free before. These are good preconditions for the persistence-forecast, which keeps the ice edge at its northerly position. Thus it predicts open water to the south of it where the only ice-free areas remain in reality. Hence, the hit rate for these ice-free regions is very high. The model, in contrast, translocates the existing ice, possibly moving it also into these regions that stay rather ice-free in the observations. Thus, the model-hit-rate drops.

For all remaining grid cells, the hit rate difference between model and persistence-forecasts is mostly positive, at least slightly (Figure 4.12c). This proves that the model indeed has some benefit over the persistence-forecast, in particular in the transition zone between open water and totally-ice-covered areas.

4.2.2.3 Day-to-day variability of the model quality

Figure 4.7a depicts that the hit rate of simulated ice concentration varies for each run and that it is higher for some forecast-runs (e.g. for 27/03) and lower for other forecast-runs (e.g. for 19/03). In other words, the model deviates varyingly strong from the observations, thus certain conditions seem to either promote or impede the model's ability to forecast the ice concentration conditions.

In order to ascertain the reason for the variability, it is necessary to investigate the particular hit rates for specific ice concentration categories. In preparation for this, the ice concentration distribution in the model domain as observed by the satellite is presented in Figure 4.13. It shows which fraction of all grid cells is covered by ice of which concentration. Grid cells that are never ice-covered are still excluded as described in Section 4.2.1. The grey error bars specify the standard deviation with respect to all observed days. The distribution is bimodal with one maximum at 0%-5% ice concentration and a second maximum at 95%-100% ice concentration: About 50% of all grid cells have an ice concentration of more than 85%, and 20% of all grid cells have an ice concentration of less than 5%. Thus, it seems reasonable to investigate the hit rates of these two groups of cells separately.

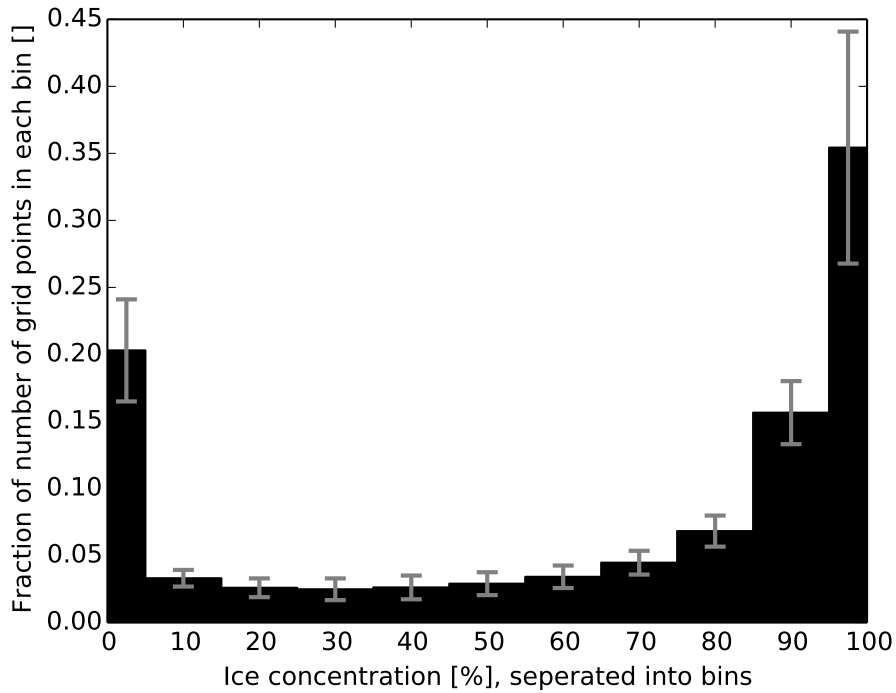


Figure 4.13: Distribution of ice concentration values in satellite observations. The bars show which fraction of the total number of grid points is covered with ice of the respective concentration. Drawn is the average over all days and the resulting standard deviation. Each day is included multiple times—videlicet for each model forecast that is to be compared with this day—because a different amount of only-water-covered cells is excluded from the satellite map for each model run.

The hit rate for the first group of cells with ice concentration below 5% is shown in Figure 4.14a. It is higher than 90% at the beginning of the model run, and rarely decreases below 75%. In contrast, the hit rate for the second group of cells with an ice concentration above 85% (Figure 4.14b) is mostly below 75% at the first day already. At some days, especially at the end of the investigation period, the further decrease is weak, but between 17/03 and 23/03 the hit rates decrease below 20% for 5-day-forecasts.

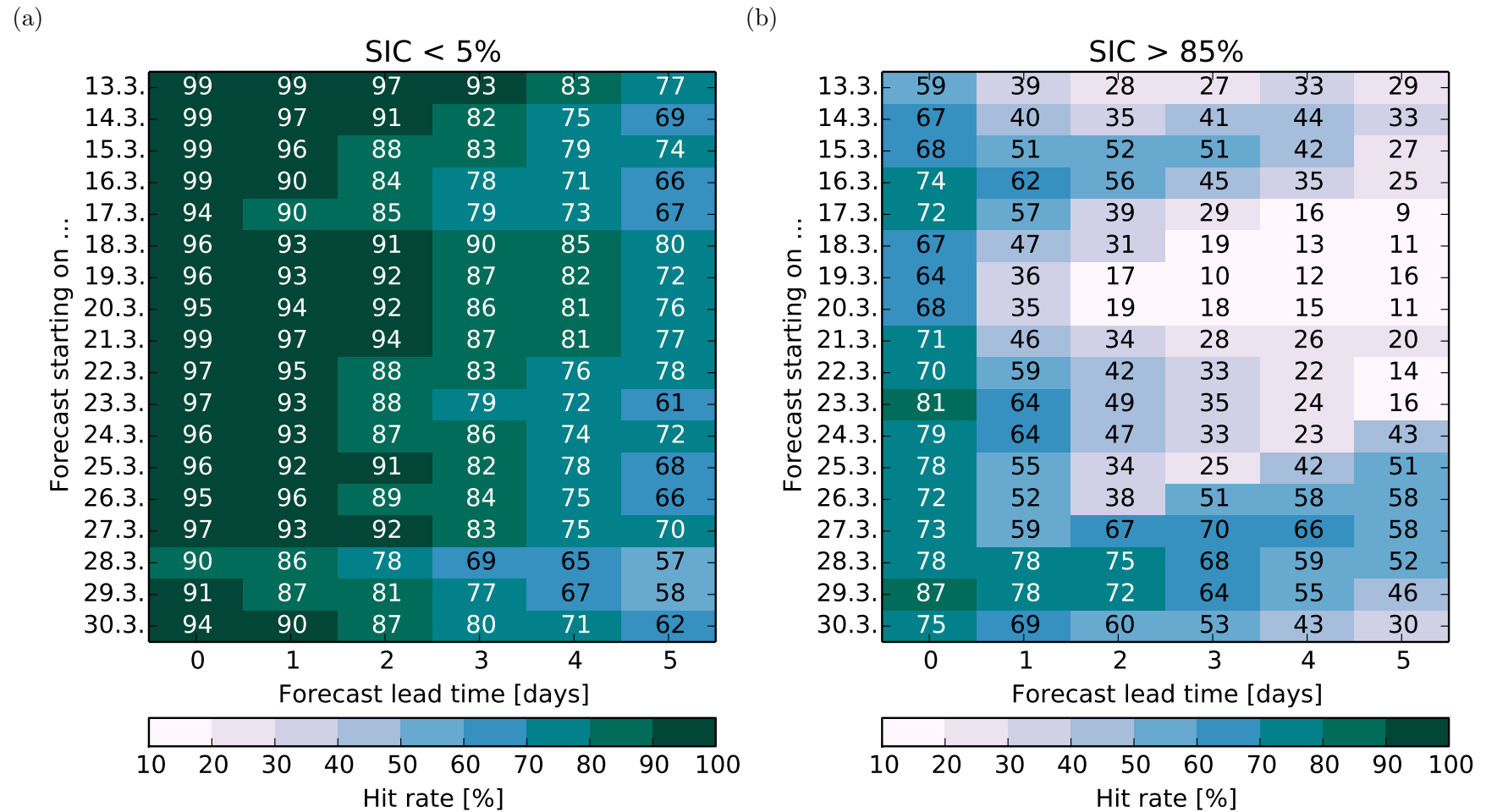


Figure 4.14: Hit rate of simulated ice concentration in fc06-runs in relation to AMSR2-data for grid cells with an ice concentration (SIC) as observed by AMSR2 of less than 5% (a) and more than 85% (b).

As the model performs so well for grid cells with low ice concentration, this cannot effect the drop of the overall hit rate seen in Figure 4.7a. On the contrary, the hit rate is very low for grid cells for which the satellite observed more than 85% ice concentration (SIC85_{SAT}-cells). This is caused in some part by the variable allowed deviation for scoring a hit $\epsilon(S_i)$, that is much more strict for high ice concentration than for low ice concentration. However, an assessment of the quantiles of the ice concentration errors (Appendix E.1) suggests that the low error tolerance cannot be the only reason for the low hit rates at SIC85_{SAT}-cells.

As SIC85_{SAT}-cells account for more than 50% of all grid cells (Figure 4.13), the poor model performance for them can impinge on the overall hit rate, and evidence for it is the resemblance of both hit rate patterns: Low hit rates are attained both in total and for SIC85_{SAT}-cells in the period 17/03 to 23/03, especially for long forecasts. So, the day-to-day variability of the overall hit rate in the investigation period seems to be induced by the variability of the SIC85_{SAT}-cells' hit rate.

The question arises which conditions prevent the model from achieving better hit rates for SIC85_{SAT}-cells between 17/03 and 23/03. A hint is given by the the number of SIC85_{SAT}-cells in the model domain or rather their fraction. However, the mechanism is not that a higher fraction of SIC85_{SAT}-cells leads to an increase of their negative impact on the overall hit rate. It is rather the *change* of the fraction of SIC85_{SAT}-cells that correlates with the hit rates: Figure 4.15 depicts the tendency of the fraction of these cells that are observed by satellite during the course of the model simulations. The figure shows the difference of the fraction of SIC85_{SAT}-cells for each forecast day compared to the day of initialisation. A red–white colour indicates that the amount of cells with high ice concentration has increased in the observations since the start of the model run. This occurs especially between 17/03 and 20/03. The blue–black colour reveals a decrease of SIC85_{SAT}-cells particularly towards the end of the investigation period and also slightly on 22/03 and 23/03.

The comparison of the plots for the tendency of the SIC85_{SAT}-cell fraction and for their hit rate reveals striking similarities, highlighted by the black–white colour scales: The pattern in both plots match quite well. Especially conspicuous are the following three time periods:

1. Between 17/03 and 20/03, the fraction of SIC85_{SAT}-cells increases from the initialisation day to the forecast day in every case. This is caused by dropping temperatures (Figure 4.3) leading to higher ice concentrations due to freeze-up. Additionally, strong southerly ice drift (Figure 4.16) transports compact ice from the north into ice-free regions. Coincidentally, the hit rate for SIC85_{SAT}-cells is very low (Figure 4.14b) . This suggests that the model is not capable of predicting an increase of ice concentration in form of SIC85_{SAT}-cells correctly. The main reason is that MESIM does not include sea ice thermodynamics.

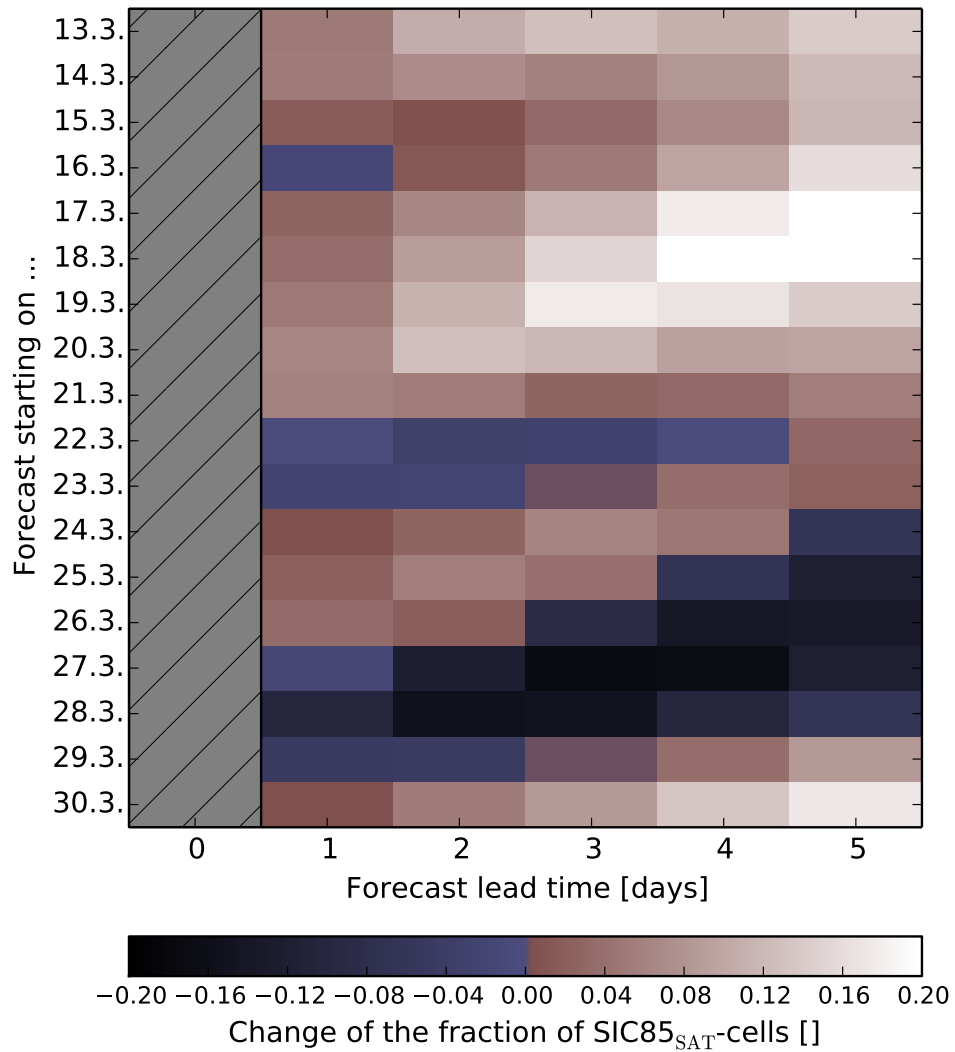


Figure 4.15: Satellite deduced tendency of fraction of grid cells with more than 85% ice concentration in the AMSR2 data (SIC85_{SAT}-cells). For each day of the forecast (1–5 days forecast lead time), the colour indicates the change of the fraction relative to the day of initialisation (0 days forecast lead time). For the calculation of the fraction of SIC85_{SAT}-cells, grid cells that are never ice-covered during the fc06-runs are excluded.

Hence, new ice formation cannot be modelled, whereas it certainly took place during these days because of low temperatures. Additionally, the lack of ice is amplified by the model issue already mentioned above, which wrongly reduces the ice concentration continually during all simulations. Due to these behaviours, the model cannot reproduce an increasing ice concentration.

2. On 22/03 and 23/03 the hit rate increases slightly while the fraction of SIC85_{SAT}-cells decreases, at least for the first forecast days. This happens despite steadily low temperatures (Figure 4.3), which could still promote freezing. The ice drift direction, however, turned slightly and the new eastward component favours loosening of the ice behind the islands of Svalbard. On average, the ice drift in regions with SIC85_{SAT}-cells is also divergent (Figure 4.16). The decrease of cells with high ice concentration is supported by an artefact within in the satellite data on which this analysis is based on. On 22/03, the ice concentration was overestimated due to clouds and high water vapour in the atmosphere (more details in Appendix E.2). Thus, the decrease between 22/03 and 23/03 (i.e. 1 day lead time for the forecast of 22/03) appears stronger than in reality. Nevertheless, these faulty satellite data are used both as reference for hit rate calculation and for model initialisation. Thereby, the model is affected adversely because either it is not able to forecast an unphysical increase of ice concentration caused by clouds, or it has to get rid of an excessive ice concentration after initialisation.
3. Between 27/03 and 29/03, as well as at the end of the simulations of the days before, the observed fraction of SIC85_{SAT}-cells decreases drastically. This time, warm weather conditions combined with increasing drift speed lead to break-up of the ice. At the same time, the hit rate for these cells is particularly high. To some extent, this could again be attributed to the model feature of continual loss of ice concentration. In these days however, it actually supports correct simulations.

In summary, the tendency of the fraction of SIC85_{SAT}-cells is a good indicator for the hit rate, which is low whenever the fraction of SIC85_{SAT}-cells increases. So, the day-to-day variability of the overall hit rate is mainly caused by variations of the ice concentration within highly-ice-covered regions. The model HAMMER can better handle conditions with decreasing ice concentrations than situations in which the ice concentration increases.

4.2.3 Discussion

In Section 4.2.2, the model quality of HAMMER has been evaluated using the measure hit rate with respect to AMSR2 ice concentration data. And yet, the obtained findings have to be

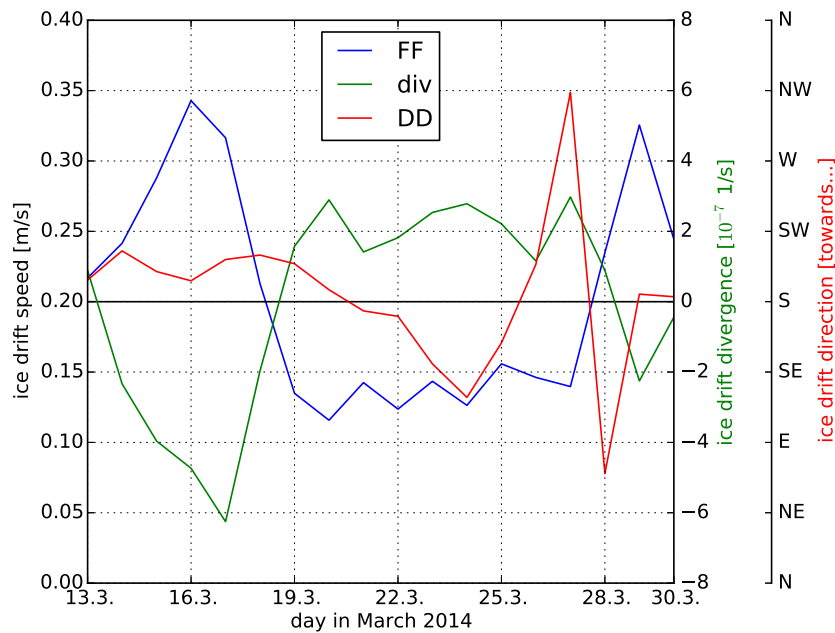


Figure 4.16: Daily mean ice drift speed (blue) and ice drift direction (red) as average of all grid cells in the model domain and divergency of ice drift (green) as average of those regions with more than 85% ice concentration in satellite observations.

treated with care. First of all, the results of the study are only valid for ice concentration; no other quantities like ice thickness were assessed. Furthermore, the conclusions are drawn based on only 36 model simulations for 18 days, which is not necessarily representative for other time periods especially not for other months than March.

The finding from the first question (Section 4.2.2.1) is that the morning simulations fc06 are only slightly better than the evening simulations fc18. A reason could be that no recent ice concentration data are available for the initialisation of fc18-runs. Thus, the same data are used as for fc06-runs implying that the ice conditions would have been persistent since then. The model results possibly could be improved, if the model simulations would be started earlier, so that they begin at the same time for which the ice concentration data are valid. As a consequence however, the simulation would take more time to finish, thus delaying the forecast results. The only alternative would be to use the information of single satellite swaths. These data are available soon after each satellite passage but they do not cover the whole model domain. Therefore, another technique would be required to merge swath data into a running model simulation both temporally and spatially.

The analysis in Section 4.2.2.2 suggested that the model is better than persistence-forecasts only in the transition zone between open water and totally-ice-covered areas. Of course, this can be

affirmed only for the examined time period in March 2014. Besides, only daily mean values of ice concentration are investigated both from the simulations and as average of all swaths of each day. The model is actually able to simulate intra-day variations, for example as effect of tides, within the whole model domain—unlike the persistence-forecast. The changing ice conditions during a day might, for example, be relevant for ship navigation. Thus, model simulations could in fact have an advantage over persistence-forecasts—despite the conclusion drawn from the analysis of daily averages. In order to test this hypothesis, the hit rates would have to be calculated and compared for both persistence and model forecasts with respect to single swaths as reference values.

In Section 4.2.2.3, the third question was discussed and it revealed that HAMMER can better handle conditions with decreasing ice concentrations than situations with increasing ice concentrations caused by missing thermodynamic effects in the model. During the analysis it became clear however, that the AMSR2 satellite data used as reference are affected by artefacts and do not reflect the true ice conditions. For low ice concentration, the known uncertainty of the satellite data is very high with up to $\pm 25\%$. It is desired, however, that the model predicts ice concentration conditions with a higher accuracy than that. Hence, the AMSR2-data are not completely suitable to evaluate the model quality, but data with less uncertainty are required. For high ice concentration, the uncertainty of AMSR2-data proposed by SPREEN et al. (2008) seems to be underestimated for certain situations. If this were not the case, the effect of atmospheric humidity and cloud water should have been comprised by the hit rate tolerance and no impact on the hit rate values would be expected. Hence, in order to improve the analysis results, the applied hit rate tolerance $\epsilon(S_i)$ has to be set dependent on the local and current cloud and humidity conditions. Possible tolerance values could be deduced from the sensitivity studies of BEITSCH (2014).

4.3 Predicted navigability of artificial ship routes

In Section 4.2, the model quality was evaluated using the measure 'hit rate'. For this measure, the model skill at each grid cell in the model domain is equally important. The aim for the development of the model system, however, was not primarily to produce sea ice maps that are accurate at each grid cell. But first of all, simulations should be produced that can provide support for ship navigation. Presumably, ship navigators are not so much interested in the sea ice conditions at *every* location but rather on their desired route. Certainly, it is important for them which speed the ship can reach under the predicted conditions. But first of all, it is crucial to know if the desired route is navigable at all or if the ship could get stuck there. Thus, the model system will be evaluated with regard to its navigability forecasts in this section.

4.3.1 Method for determining threat indices

In order to evaluate the predicted navigability, an adequate quality measure has to be defined. In contrast to sea ice concentration maps (Section 4.2), that represent continuous forecasts, the navigability of ship routes requires a *dichotomous* forecast. This kind of forecast states whether an event (e.g. a tornado) does or does not occur. Here, the event is defined as the non-navigability of a route because this is the event which navigators should be warned about by the forecasts.

An evaluation method for dichotomous forecasts is the calculation of threat indices. STEPHENSON (2000) has applied it to tornado forecasts, but VAN WOERT et al. (2004) also used it for the evaluation of the Polar Ice Prediction System, PIPS. The forecasted events are compared to observed events utilising a 2×2 contingency table (Table 4.1). This shows the number of events that are observed and have been forecasted (hit), the number of events that are observed but have not been forecasted (miss), the number of cases in which no event is observed but has been forecasted (false alarm), and the number of cases in which no event is observed and no event has been forecasted (correct rejection). The numbers in the contingency table can be combined in several ways to form different skill scores like the probability of detection or the false alarm ratio (ROEBBER, 2009). Each of these, however, has certain disadvantages, for example if the events are very rare (DOSWELL et al., 1990). Therefore, no combinations of hit, miss, false alarm, or correct rejection are calculated in this study, but their values are presented individually.

Table 4.1: 2×2 contingency table of forecasted and/or observed events.

	Event forecasted	No event forecasted
Event observed	hit	miss
No event observed	false alarm	correct rejection

4.3.1.1 Determination of random ship routes

To evaluate the model skill of HAMMER with respect to navigability, random routes are chosen in the model domain. For each of them it is checked whether it is navigable in satellite observations and if HAMMER had predicted the route to be navigable. Under which conditions a route is declared to be navigable will be discussed in Section 4.3.1.2. Random routes are selected with different starting points in the model domain to account for different ship positions. Thus, for

each grid cell as starting point, a random generator selects 150 routes. The number has been proven to be sufficient for revealing meaningful results, as the results with only 50 routes would be quasi-identical.

The random generator is set up to produce as realistic routes as possible. This means that routes should primarily lead into one direction, not preferring grid parallel tracks, but there should still be the possibility for directional changes and turns. To give a visual impression, five randomly generated routes with the same starting point are exemplarily shown in Figure 4.17 as red lines.

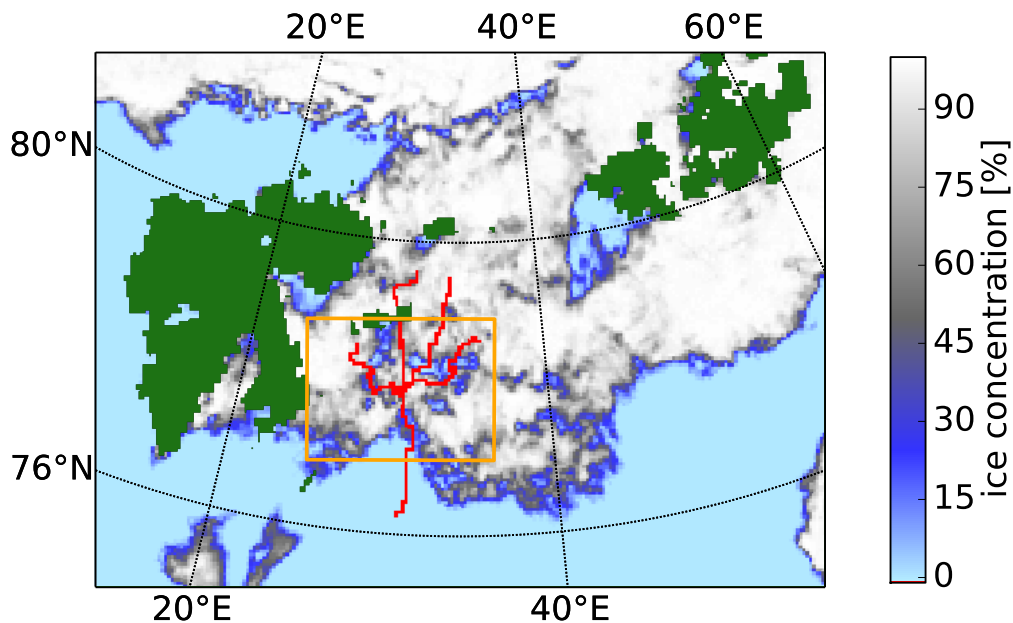


Figure 4.17: Five exemplary, randomly chosen artificial ship routes (red) starting at the same starting point. For orientation purposes, the observed ice concentration on 20/03 is depicted. Land areas as defined by the SMOS land mask are shown in green, and the orange frame indicates the evaluation area.

The area of interest for further evaluation is indicated by the orange frame in Figure 4.17. Within this area, every grid cell is used as starting point for 150 routes. The routes itself are allowed to lead outside of the orange evaluation area. The evaluation area is chosen to fully include the real track of R/V Lance in the ice. It also lies within the domain of the ocean model HAMSOM, and it covers a region where the ice conditions were quite variable during the field experiment.

Each generated route fulfils the following criteria:

- It consist of grid cells that are adjacent to each other in x-direction or y-direction of the model grid. Diagonal routes are not allowed.
- It has a length of 48 grid cells additional to the cell it starts from. Thus, it represents a route which can be completed in about 1 day travel time. With an assumed speed of 5.4 knots, which was typical for R/V Lance in partly ice-covered waters, the ship makes 10 km in 1 hour. In 24 hours it can travel 240 km and thus pass 48 grid cells of 5 km diameter. This is only a rough estimate as ships in reality would not follow the grid orientation and the speed would depend on ice conditions.
- It does neither cross nor meet itself at any grid cell. Especially, the imaginary ship is not allowed to turn around and proceed in its opposite direction. In the rare case that the imaginary ship gets trapped between its own track, this route is still used although it contains less than 48 grid cells.
- It is not allowed to exit the model domain of HAMSOM because the model results are regarded as less reliable where the coupled ocean model is missing.
- It is not allowed to enter land areas. Indeed, the land masks of MESIM and of the satellite data which are used as reference are not identical. Thus, the route is restricted by either of both land masks.

The random generator produces routes with these criteria (more details in Appendix F), however, a special treatment is applied to routes which lead onto land. An example for such a route is the upwards-directed route in Figure 4.17. Such routes are rejected from further assessment without replacing them by a correct route. Instead, the total number of 150 routes is decreased accordingly for this starting point. If a correct route were searched to replace the land-leading route, the final set of routes would contain overproportionally many routes with a direction away from the land. This effect is very pronounced for starting points close to the land. In this case, the navigability of the ice close to land would be examined more often than of ice around a starting point far away from land. To avoid this bias, land-leading routes are not replaced. Thus, the total number of routes is usually lower for starting points close to land areas compared to starting points far away from land.

4.3.1.2 Definition of navigability

The generated random routes are checked for their navigability. Whether a ship is able to pass through the ice depends on many factors. An important one is the ice concentration: ships can easily navigate through sea ice with low concentration because it can travel in the open water between the ice floes. If the ocean is fully ice-covered, the ice thickness becomes relevant as it determines if the ship can break through it. In addition, also several other factors play a role. For example the passage can be hindered by pressure ridges or a thick snow layer on top of the ice. These properties, however, are either not simulated or no observation data exist for their evaluation. Thus, the navigability is determined only by ice concentration, A , and ice (floe) thickness, H .

Which combinations of A and H allow a ship to pass through the ice is ascertained utilising the real route of R/V Lance during the field experiment (Section 4.1.1). Figure 4.18 shows the values of ice concentration and ice thickness that R/V Lance met on her track. One pair of values is drawn for each grid cell that was traversed by R/V Lance. In Figure 4.18a, the data of A and H are taken from the most recent model simulation and from the output time which is closest to the time when R/V Lance entered the respective grid cell. In Figure 4.18b, the data are from satellite observations of AMSR2 and SMOS. As the same satellite data are used as reference (observation) during the threat-index calculation, the processing of these data is described in detail in Section 4.3.1.3.

The scatter plots in Figure 4.18 reveal that R/V Lance traversed grid cells with very high ice concentration only if the ice thickness was lower than 0.3-0.4 m. If the ice concentration was less, however, R/V Lance could also handle thicker ice. Thus, navigability limits are proposed as $A \cdot H = 0.3$ m (solid line) and $A \cdot H = 0.4$ m. Unfortunately, the maximum values of $A \cdot H$ differ a bit between model and satellite data. Therefore, manual ice observation data are consulted additionally: During the cruise, the ice conditions around the ship were permanently observed and noted according to WMO standards. This data set, which was postprocessed by TEGTMEIER from the Bundesamt für Seeschifffahrt und Hydrographie (2014, personal communication), is used to detect those grid cells in which R/V Lance evidently met heavy ice conditions or even got stuck. The according model and satellite values are highlighted red in Figure 4.18. As they do not exceed the limit of $A \cdot H = 0.3$ m, this threshold is used here to define navigability. If for *every* grid cell of a route the product of A and H is less than 0.3 m at the time when the imaginary ship traverses the grid cell, the whole route is declared to be 'navigable'. Since this threshold certainly depends on the actual ship type, this study also examines the sensitivity of the threat-index results to an increase of the threshold to $A \cdot H = 0.4$ m.

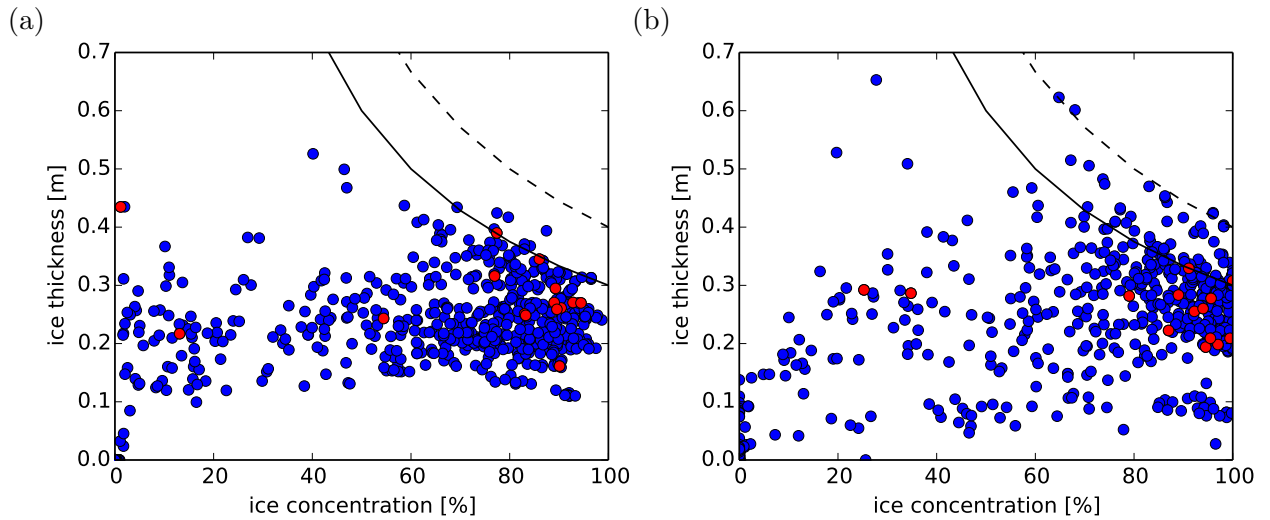


Figure 4.18: Ice thickness, H , vs. ice concentration, A , on Lance’s track (a) as simulated by HAMMER’s most recent run and (b) as observed by satellite (AMSR2 and SMOS). The red data points represent the conditions at those locations where Lance got stuck or met heavy ice conditions. The black lines specify the chosen navigability-thresholds $A \cdot H = 0.3$ m (solid) and $A \cdot H = 0.4$ m (dashed).

4.3.1.3 Used model data, observation data, and comparison data

The navigability of routes is determined for three different data sets of ice concentration and ice thickness. The threat-index calculation requires forecast (model) data and observation data (Table 4.1). In order to compare the obtained model skill to a reference, namely persistence as motivated in Section 4.2.2.2, the threat indices are also calculated from persistence data relative to the observation data.

As model data, the simulations conducted during the field experiment (Section 4.1.1) are used. Only the 06-UTC-runs are considered because the 18-UTC-runs are initialised with ice concentration and ice thickness data of a different age. Furthermore, the hit rate analysis indicated that the 18-UTC-runs do not offer much additional value compared to the 06-UTC-runs. All forecasts between 13/03 and 30/03 are evaluated. At every day, the imaginary ship starts its cruise on every route at 7:00 UTC and travels for 24 hours with a predefined speed of 10 km per hour, thus reaching the next grid cell of the route every 30 minutes. Therefore, the ice concentration and ice thickness data are taken from the 30-minute-output of the model forecasts.

Unfortunately, the observation data are not available exactly every 30 minutes. The highest possible time resolution of satellite data can be achieved by analysing every single satellite

transit (swath) separately. For ice concentration, such a product became available recently (BEITSCH et al., 2014) as provided by BEITSCH (2014, personal communication). Thus, for each grid cell along the artificial routes the ice concentration value is taken from the most recent AMSR2-swath which covered the respective grid cell. The observed ice thickness is based on daily average fields observed by SMOS. Single swath data are not used here because of too large uncertainties in the SMOS-swaths which balance out only in daily average (KALESCHKE, 2014, personal communication). Hence, SMOS ice thickness values for the 30-minute-steps along the artificial routes are found by linear interpolation in time between two daily maps. These can be assumed to be valid for 12:00 UTC (KALESCHKE, 2014, personal communication). As the SMOS ice thickness values represent rather a kind of ice volume per unit area, they are transformed to the actual ice thickness by using the corresponding AMSR2-swath ice concentration value. The applied transformation method is the same as used for the model initialisation (Section 4.1.1), and it is described in Appendix D.

Analogously to the threat indices calculated from model and observation data, threat indices are also calculated from a data set representing persistence. For this, the same data are used as for model initialisation, i.e. one day old maps of ice concentration as observed by AMSR2, and two days old ice thickness maps calculated from a combination of daily SMOS observations and daily ice concentration data. The additional merging of this ice thickness data with model output from ICEDAS, as mentioned in Section 4.1.1, is omitted here. The reason is that no model at all is wanted to be necessary for producing the persistence data. One exception from this procedure was applied for 25/03: During the operational experiment, recent SMOS data were not available on this day for model initialisation, so that the simulation was started with SMOS data from the day before. Thus, the persistence data for 25/03 are produced analogously with old SMOS data.

4.3.1.4 Calculation of threat indices

With this preparatory work, the threat indices can be calculated. They are determined for every starting point in the evaluation area separately. First, 150 random routes are generated that originate from the given starting point. After rejecting land-leading routes, each remaining route is tested for its navigability, once using model data and once using satellite observations. Depending on the resulting combination of navigability identifications the route is counted either as hit, as miss, as false alarm, or as correct rejection according to Table 4.1. After summing up all hits, misses, false alarms and correct rejections of one starting point, these values are divided by the total number of tested routes (up to 150) to yield the threat indices HIT [%], MIS [%], FAL [%], and COR [%]. Finally, the resulting HIT, MIS, FAL, and COR values of all

starting grid points can be combined into four maps illustrating the evaluation area. The entire procedure is repeated for the persistence data instead of the model data.

4.3.2 Results and discussion

An example of resulting maps of the four threat indices HIT, MIS, FAL, and COR for 25/03 is shown in Figure 4.19. The grey area enclosing the evaluation area is added to display the surrounding islands (black) in order to provide a better orientation. The maps reveal that the threat indices strongly depend on the location of the starting point of the routes. If a ship starts a random route in the north-west of the evaluation area, the model would correctly declare the route to be not navigable (HIT). If the ship starts in the south-west, however, the model is mostly correct with forecasting the route to be navigable. Recalling the general ice situation at the end of March 2014 (Figure 4.2) brings out that this causes the location-dependency. Much ice is located in the north, while the ocean is mostly ice-free in the south. South of islands, the ice conditions are also mostly lighter because of offshore winds. In contrast, very thick ice (not shown) is located north and east of Edgeøya (island west of the evaluation area). This picture fits well to the locations of HIT and COR: Where the ice conditions are certainly too heavy to be passed, it is easy for the model to correctly declare routes starting there as non-navigable (HIT). Analogously, if the ocean is ice-free at the starting point, only few routes lead into the ice, thus the model often forecasts navigable routes correctly (COR).

Difficulties for the model arise, wherever the ice conditions are close to the navigability-threshold. Then, small changes in the ice cover can alter the navigability of a route. On 25/03, the model has problems to correctly forecast routes starting south of Kongsøya (island north of the evaluation area). There, the model is too strict and rises false alarms telling ships not to navigate their routes even if it would be possible. In contrast, it misses to warn about non-navigable routes if the ship starts in the south-east. There, the development of a non-passable ice accumulation is registered by the satellite observations, which the model could not reproduce.

Whether these discussed features are generally valid during the experiment phase is revealed by Figure 4.20, which shows the average threat indices for the period 13/03–30/03. The distribution of HIT and COR is recognisable from the previous example, and it can again be ascribed to the general sea ice conditions. The average fields of MIS and FAL, however, differs from the example in Figure 4.19. They are much more homogeneous with values of about 10%–20%. Only in the region directly east of Edgeøya, FAL is very small. This is caused by very heavy ice conditions so that routes starting there are never observed to be navigable. Thus, no false alarm can be risen by the model. Summing up the HIT and COR values, which represent the

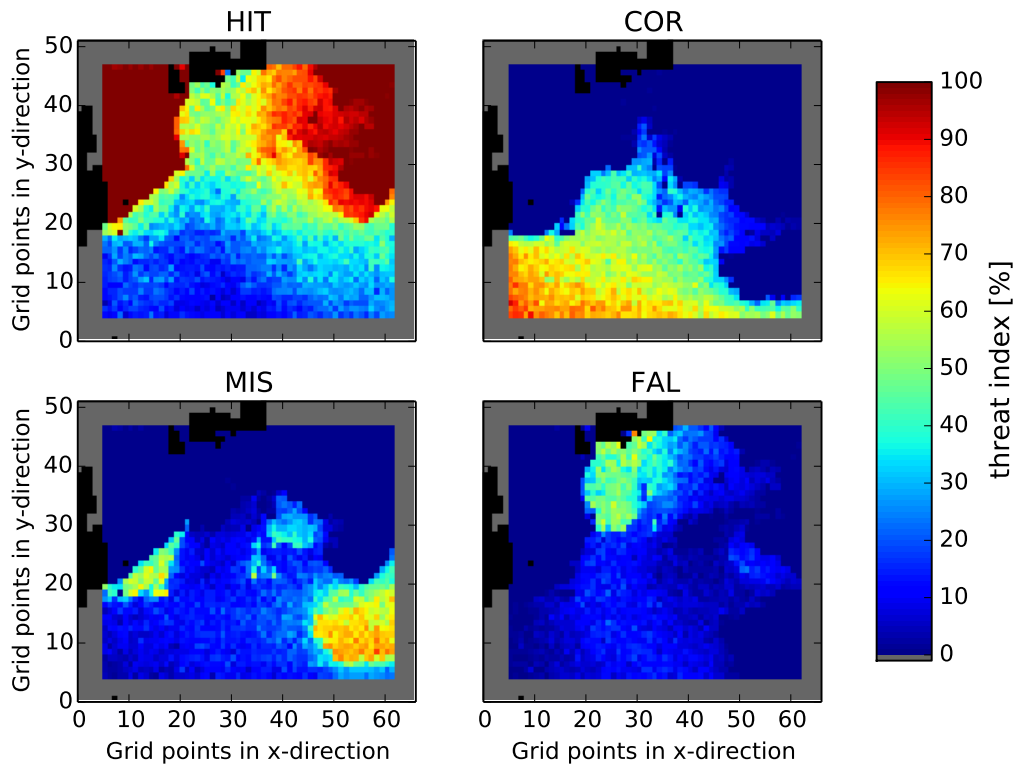


Figure 4.19: Threat indices HIT, COR, MIS, and FAL (following Table 4.1) for the forecasted navigability of random ship routes on 25/03. A larger area (grey) than the evaluation area is depicted for better orientation by land areas (black).

cases in which the model is correct, reveals that a correct forecast is given for at least 70% of all routes, mostly for more than 80% of all routes (not shown). This seems to be an acceptable value when bearing in mind all imperfection of the model, for example that it does not include thermodynamic processes. Obviously, the neglected formation of new ice does not affect the navigability of routes because ships can easily break through thin ice.

The actual benefit of the model can be evaluated by comparing its skill to persistence forecasts. Those express which performance would be possible without any model. Figure 4.21 shows the difference of the threat indices between model and performance forecasts as average for the experiment phase. Red values indicate a higher threat index for the model. Desirable would be more hits and correct rejections and, in turn, less misses and false alarms. Indeed, on average the model features a higher value of HIT compared to persistence. However, COR is lower so that, accordingly, the model rises more false alarms. A reason for this behaviour might be that the ice thickness in the model is initialised to be at least as high as in ICEDAS. Thus, the model might be more conservative than the persistence, which relies solely on the SMOS observations.

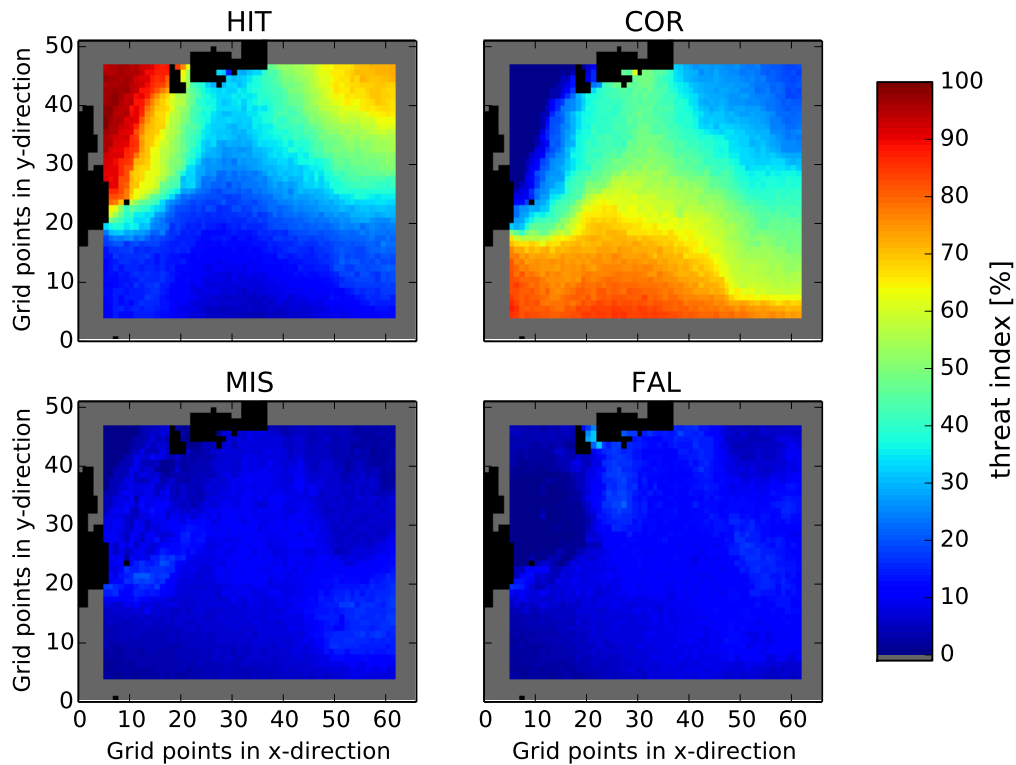


Figure 4.20: Threat indices HIT, COR, MIS, and FAL (following Table 4.1) for the forecasted navigability of random ship routes as average over 13/03 to 31/03. A larger area (grey) than the evaluation area is depicted for better orientation by land areas (black).

The local distribution of the differences is fairly homogeneous. Except in the areas north-west and south-west, where the ice conditions are distinct, either very heavy or very light, there are no differences in the performance of model and persistence.

As the time-averaged differences are spatially homogeneous, the time development of the spatial averages is analysed in Figure 4.22a. It confirms the results of Figure 4.20 for each single day: The model forecasts non-navigable routes correctly (HIT) at least as often as the persistence does. However, it also forecasts less navigable routes to actually be navigable (COR). The values for MIS and FAL are not shown because they are mathematically the negative value of HIT and COR, respectively. The model would be abundantly better than persistence if both shown curves were positive. With the HIT-difference being positive and the COR-difference being negative, the model forecasts are at least as safe as persistence forecasts when used for ship navigation: On each day, the model detects more dangerous non-navigable routes, with the drawback that it also rejects more navigable routes than the persistence forecast does.

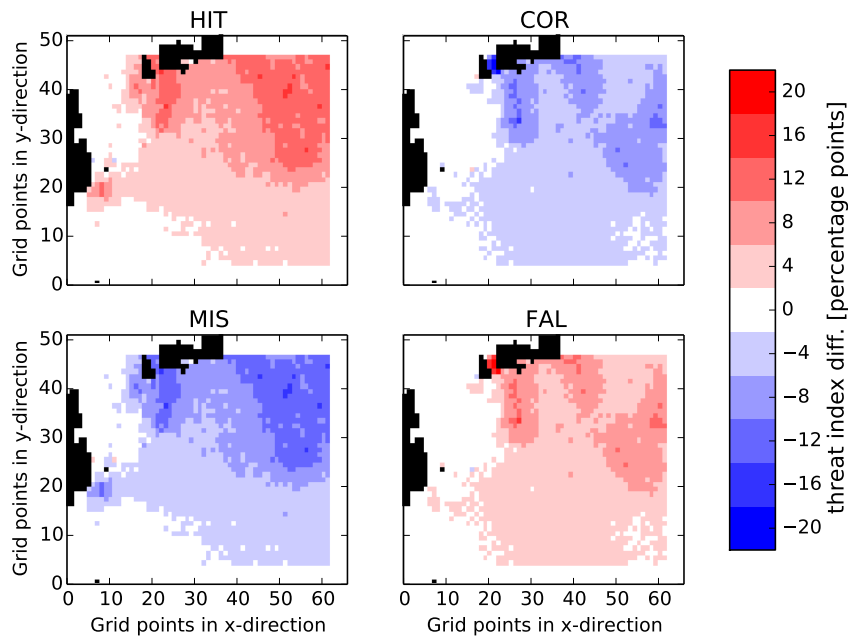


Figure 4.21: Difference of the threat indices HIT, COR, MIS, and FAL (following Table 4.1) for the forecasted navigability of random ship routes as average over 13/03 to 31/03 between HAMMER forecasts and persistence forecasts. Positive values indicate a higher threat index for HAMMER forecasts. A larger area (white) than the evaluation area is depicted for better orientation by land areas (black).

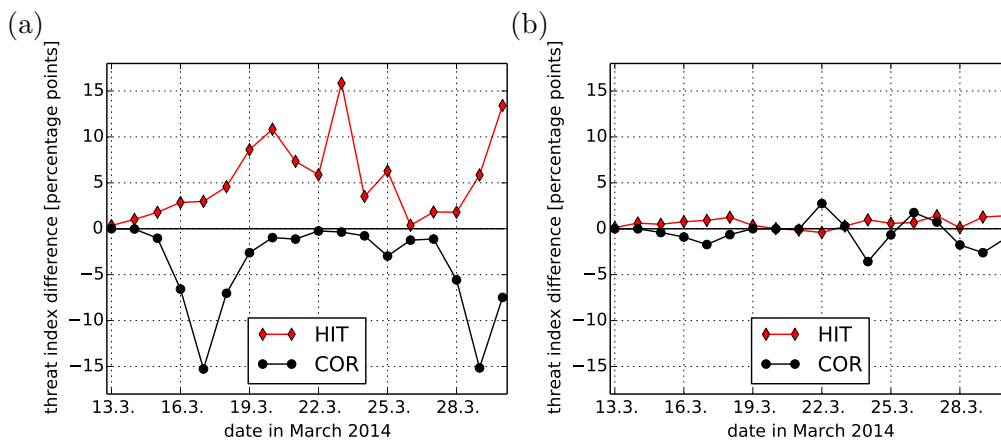


Figure 4.22: Development of the threat index difference between HAMMER forecasts and persistence forecasts for HIT and COR (following Table 4.1) as spatial average over the evaluation area. The navigability threshold is set to $A \cdot H=0.3$ m for (a) and to $A \cdot H=0.4$ m for (b). Positive values indicate a higher threat index for HAMMER forecasts.

Up to here, all results are based on a navigability-threshold of $A \cdot H=0.3$ m. How they change for $A \cdot H=0.4$ m, is shown in Figure 4.22b. Here, the benefit of the model is only marginal; the difference to persistence forecasts is very low. The reason is that with the increased threshold, a lot more routes are navigable, and the transition to non-navigable routes is quite distinct in the chosen evaluation domain. Because here the area, in which ice conditions are around the threshold value, is much smaller, the variability is low so that persistence becomes a good predictor. This leads to the conclusion that the benefit of the model when forecasting the navigability of routes strongly depends on the type of the ship in combination with the ice conditions in the operation area. However, no damage is done by the model in this case either; it just cannot really outperform persistence forecasts.

5 Conclusions & Outlook

With increasing ship traffic in the Arctic, short-range sea ice forecasting becomes more and more important. In order to design an appropriate sea ice forecast model, the involved physical processes were analysed regarding their relevance and variability. For this, all processes are assumed to be independent from each other. The relevance of processes that affect ice drift speed, ice concentration, or ice thickness is rated by their impact-timescale in Chapter 2. The summary given in Figure 2.3 can be used for the optimisation of various sea ice models as it indicates that some processes could be disregarded during model simulations. This applies, for instance, to the lateral melt of ice floes and the open water production due to shear. Chapter 2, furthermore, presents a new method to determine the update-timescale of processes. Its application revealed that the intensity of processes varies in time with different rates. Thus, some processes can be treated as constant for some time period during the model calculations, as summarised in Table 2.8.

A mesoscale sea ice forecast model is presented in Chapter 3: HAMMER is one of few models designed for short-range forecasts that applies an online coupling to both ocean and atmosphere models. Because it, hence, accounts for all important interactions and feedbacks between the system components, it is thus highly applicable for the high-accuracy forecasts that are required for navigation purposes.

In order to reduce computational costs of the forecasts and to complete them earlier, HAMMER has undergone an optimisation process. Two of these optimisations are presented in this thesis: First, a time-split approach was implemented in the atmosphere model METRAS. It reduces the computational time during precipitation events. As such, it will be of benefit also for future non-Arctic applications of METRAS. Second, for solving the ice drift equation in MESIM, a new numerical algorithm was developed. By more frequent coupling of the ice drift components u and v during the solution process, numerical instabilities could be avoided. This reduces the number of required iteration cycles enormously and, thus, decreases the computational costs. Efficiency tests show that the fraction of computational time that is used by the sea ice model relative to the atmosphere model is decreased from 50% to 5% by the new algorithm. The simulation results, however, remain basically unchanged.

With these optimisations, HAMMER was applied to realistic cases in an operational setup. For two weeks it has produced sea ice forecasts twice daily for routing the ice-going vessel R/V Lance in the Barents Sea. Analyses of these simulations in Chapter 4 show HAMMER's ability to simulate involved processes realistically. The skill of HAMMER to forecast sea ice concentration was investigated utilising hit rates. In general, persistence yields better results than forecasts by HAMMER. A detailed analysis revealed that especially conditions with high

ice concentration pose a problem to HAMMER. This can be ascribed to a deficiency in the sea ice model MESIM which leads to an unexplained reduction of ice concentration during the simulation. Despite this poor performance regarding ice concentration hit rates, HAMMER proved its benefit in the last part of Chapter 4. As the application of HAMMER targets ship navigation, a new evaluation technique was contrived. It allows to rate the benefit of a model for ships by addressing the navigability of randomly chosen ship routes. The model skill is represented by threat indices. These indicate that HAMMER mostly correctly forecasts whether a route is navigable or not. Only rarely it would advise ships to not use routes that are actually navigable, or it would recommend non-navigable routes. The actual value of HAMMER is manifested by the comparison to persistence forecasts: HAMMER is able to reduce danger for ships because it forecasts non-navigable routes better than persistence. As drawback, however, it also raises more 'false alarms' for actually navigable routes. The eventual benefit of HAMMER also depends on the navigability-threshold of the routed ship.

The studies in this thesis show that short-range sea ice forecasts with regard to navigability are possible with the coupled model system HAMMER. Even though thermodynamic processes are not considered in the current version, the errors for the evaluated 1-day-navigability-forecasts are assumed to be small: The reason is that the timescale analysis in Chapter 2 stated that the growth of thick ice and the lateral melt of ice floes is not relevant for 1-day-forecasts. Although Chapter 2 showed, in contrast, that new ice formation might be important, it can not produce so much ice that a route would be rendered non-navigable.

Experiences made aboard the vessel R/V Lance during the experiment phase showed that there is, nonetheless, still potential for improvement. The determining factors whether a ship is able to navigate through the ice are not only ice thickness and ice concentration. First of all, the snow layer on top of the ice exerts high resistance to the ship's hull decreasing the ship speed. Also any pressure ridge can hinder the passage enormously. In contrast, navigation can be highly facilitated if the ice cover is broken up in very small ice floes. All these features should be included in sea ice forecasts in order to provide best support for navigation decisions. Furthermore, the resolution of the model grid of 5 km is quite coarse compared to the size of the ship. An increase of the resolution could be useful because then features on smaller scales could be resolved. This would, however, not only infer to reconsider the currently used ice dynamics approach because the continuum assumption becomes invalid; but it would also require more detailed data for the model initialisation, which are not available on an operational basis up to now. As navigators anyway follow leads or apparently light ice within sight, they might not require very high-resolution forecasts. Rather, they could be interested in the distribution of ice thicknesses within one grid cell or the probability of pressure ridge occurrences. Thus, further developments of the sea ice forecast system should be discussed with ship navigators to optimally meet their requirements.

Acknowledgements

First of all, I want to thank my first supervisor K. Heinke Schlünzen for her guidance during my PhD. Thanks for your various support ranging from interesting discussions and new ideas, to travel support and proof-reading. I am grateful not only for your Fortran program which you provided so I could use it as a basis for the hit rate analyses conducted with Python. But I also appreciate that you supported me to participate in the cruise on R/V Lance.

Lars Kaleschke and Frank Lunkeit from my Advisory Panel are acknowledged for their helpful discussions and their availability whenever I had open questions.

Many members of the IRO-2 project contributed directly or indirectly to this work. Especially, I want to mention Björn H. Fock and thank him for all the innumerable aspects of his support: Efforts in model maintenance, improvement, and coupling; controlling the operational ecFlow setup during the experiment phase; hints and tips concerning programming, including code snippets; downloading of data from ECMWF; spotting and emphasising my achievements; various discussions and ideas; and much more. Further, I acknowledge Mikhail Dobrynin for his work to couple MESIM and HAMSOM, or his help to correctly set up the simulations, and for converting Lance's track to the model grid. Thanks to David Bröhan and Xiangshan Tian-Kunze, and to Alex Beitsch for providing the satellite data of SMOS and AMSR2, respectively. Alex is further acknowledged for his Python-script to calculate the hit rate error limits, the preprocessing and providing of the AMSR2 swath data, and discussions for instance about the impact of clouds on the AMSR2 data. I thank Nils Reimer for collecting and preprocessing the NMEA navigation data of R/V Lance and Jan Tegtmeier for preprocessing the sea ice observation data collected during the cruise. Also, I want to thank the whole cruise-team under the direction of Gerd Müller for the great time aboard R/V Lance.

A special thanks to all members of the MeMi group not only for a very good time but also for various technical and scientific advice. I am very grateful for Marita's sympathetic ear, her helpfulness and mental support, and her great ideas and comments in general. I want to thank my office colleagues Ronny and Jana for a very nice time; Jana especially for her help with Python, and Ronny for great scientific discussions, writing advice, and others. I acknowledge Robert for profound discussions about the time splitting approach. Also with David I had nice discussions that sometimes scrutinised my work, which helped to improve my approaches. My thanks also go to Volker, who provided advice and assistance during every programming issue.

I want to acknowledge Hendryk Bockelmann for his assistance when setting up the HAMMER system, for the development of a parallelised version of the pressure solver in METRAS, and

for providing the SC Timer Lib. I thank Dirk Notz for fruitful discussions about the time scale analyses and Laura Niederdrenk for providing the LaTeX template for this thesis.

I was supported by the SICSS, not only by their guidance and advice but also with travel support. Thanks for this. Further travel support was provided by CliSAP. I acknowledge funding by the Bundesministerium für Wirtschaft und Technologie (BMW, Federal Ministry of Economics and Technology) through the project “Ice-Route-Optimization-2” (IRO-2, U-4-6-03-BMW-11-02) in the framework of the program “Shipping and ocean engineering for the 21st century”, and its predecessor project IRO. The model simulations were made possible by the contingent of the University of Hamburg for the supercomputer at DKRZ. For general IT support I acknowledge CIS, and particularly Andreas Bock for his help with diverse issues.

Regarding data of 10-m-windspeed over sea ice, “we thank our colleagues in the SHEBA Atmospheric Surface Flux Group, Ed Andreas, Chris Fairall, Peter Guest, and Ola Persson for help collecting and processing the data. The National Science Foundation supported this research with grants to the U.S. Army Cold Regions Research and Engineering Laboratory, NOAA’s Environmental Technology Laboratory, and the Naval Postgraduate School.” Data from observation stations around the Barents Sea were provided by the Norwegian Meteorological Institute through the eKlima-portal. ASI Algorithm SSMI-SSMIS sea ice concentration data, originally computed at and provided by IFREMER, Brest, France, were obtained as 5-day median-filtered and gap-filled product for 2014-09-17 from the Integrated Climate Data Center (ICDC, <http://icdc.zmaw.de/>), University of Hamburg, Hamburg, Germany. Most plots were produced with Python which uses the Global Self-consistent, Hierarchical, High-resolution Geography Database for illustrating countries.

I thank my brother, Flo, for very helpful discussions about the structure of my thesis and for converting the MESIM-VICE-table into LaTeX. Further, I am very grateful to Heinke, Nils, Ronny, Marita, and Carsten for reading parts of earlier versions of my thesis and giving valuable feedback. Last but not least, I want to express my sincere gratitude to my family and all my friends for their perpetual mental support.

A Derivation of the ice thickness equation from equations of ice concentration and ice volume

The conservation equation of ice volume Equation (2.22) can be rewritten in the following way:

$$\frac{\partial AH}{\partial t} + \nabla(AH\vec{v}) = S_h \quad (\text{A.1})$$

$$A \cdot \frac{\partial H}{\partial t} + H \cdot \frac{\partial A}{\partial t} = -AH \cdot (\nabla \cdot \vec{v}) - H\vec{v} \cdot (\nabla A) - A\vec{v} \cdot (\nabla H) + S_h \quad (\text{A.2})$$

$$\frac{A}{A} \cdot \frac{\partial H}{\partial t} + \frac{H}{A} \cdot \frac{\partial A}{\partial t} = -\frac{A}{A}H \cdot (\nabla \cdot \vec{v}) - \frac{H}{A}\vec{v} \cdot (\nabla A) - \frac{A}{A}\vec{v} \cdot (\nabla H) + \frac{S_h}{A} \quad (\text{A.3})$$

$$\frac{\partial H}{\partial t} + \frac{H}{A} \cdot \frac{\partial A}{\partial t} = -H \cdot (\nabla \cdot \vec{v}) - \frac{H}{A}\vec{v} \cdot (\nabla A) - \vec{v} \cdot (\nabla H) + \frac{S_h}{A} \quad (\text{A.4})$$

A.1 Case I: Divergent ice drift or partly ice covered sea

In the case of divergent ice drift or if the ocean is only partly ice covered, the empirical equation for ice concentration (Equation (2.23)) is valid. It is rewritten as:

$$\frac{\partial A}{\partial t} + \nabla(A\vec{v}) = S_A \quad (\text{A.5})$$

$$\frac{\partial A}{\partial t} = -A \cdot (\nabla \cdot \vec{v}) - \vec{v} \cdot (\nabla A) + S_A \quad (\text{A.6})$$

$$-\frac{H}{A} \frac{\partial A}{\partial t} = +\frac{H}{A}A \cdot (\nabla \cdot \vec{v}) + \frac{H}{A}\vec{v} \cdot (\nabla A) - \frac{H}{A}S_A \quad (\text{A.7})$$

Adding Equation (A.7) to Equation (A.4) yields the prognostic equation for H in case I:

$$\frac{\partial H}{\partial t} = -\vec{v}\nabla H + \frac{1}{A}S_h - \frac{H}{A}S_A \quad \text{if } A < 1 \quad (\text{A.8})$$

A.2 Case II: Convergent ice drift of unbroken ice cover

In the case that $A=1$, the ice concentration is not allowed to increase further even though the ice drift is convergent. Therefore,

$$\frac{\partial A}{\partial t} \stackrel{!}{=} 0 \quad (\text{A.9})$$

is applied in Equation (A.4). This yields the prognostic equation for H in case II:

$$\frac{\partial H}{\partial t} = -\vec{v}\nabla H - H \nabla \cdot \vec{v} - \frac{\vec{v}H}{A} \nabla A + \frac{1}{A}S_h \quad \text{if } A=1 \quad (\text{A.10})$$

B Derivation of the characteristic values for internal forces, INT, and open water production due to shear, OWS

B.1 Internal forces, INT

The characteristic value for the expression $(\rho h)^{-1} \nabla \underline{\sigma}$ arises from Equation (2.6). Replacing P by Equation (2.7) yields:

$$\sigma_{ij} = 2\eta \epsilon_{ij} + \delta_{ij} \left\{ (\zeta - \eta) (\epsilon_{11} + \epsilon_{22}) - \frac{P^* h C(A)}{2} \right\} \quad \text{for } i, j \in \{1, 2\} \quad (\text{B.1})$$

According to LEPPÄRANTA (2011b), the last term, that contains the fraction, governs the characteristic value of internal forces. So, the final expression can be found by using this last term of Equation (B.1) in $(\rho h)^{-1} \nabla \underline{\sigma}$, after which both h cancel in the nominator and the denominator. Then, the ∇ -Operator is estimated as $1/\mathcal{L}_\sigma$ (a characteristic value for horizontal changes of σ), and the characteristic value \mathcal{A} is used for A (Table 2.1). With this, the characteristic value for $(\rho h)^{-1} \nabla \underline{\sigma}$ becomes:

$$\frac{1}{\rho h} \nabla \underline{\sigma} \rightarrow \frac{P^* C(\mathcal{A})}{2 \mathcal{L}_\sigma \rho} \quad (\text{B.2})$$

B.2 Open water production due to shear, OWS

The parameterisation of open water production due to shear is given by Equation (2.15). In order to find a characteristic value of this expression, it is assumed that both invariants of the strain rate tensor, $\dot{\epsilon}_I$ (divergence) and $\dot{\epsilon}_{II}$ (shear), are of the same order. This assumption is supported by a case study of two leads conducted by SCHULSON (2004). Thus, $\dot{\epsilon}_I$ is replaced by $\dot{\epsilon}_{II}$. Furthermore, the aspect ratio of the yield curve ellipse e is set to 2 as given by H79. With this, Equation (2.15) can be rewritten as

$$Q_S = \frac{\sqrt{5} - 2}{4} \cdot \dot{\epsilon}_{II} \cdot C(A) =: \lambda \dot{\epsilon}_{II} \cdot C(A) \quad (\text{B.3})$$

By using $\dot{\mathcal{E}}_{II}$ as a characteristic value for the strain rate invariant $\dot{\epsilon}_{II}$, the open water production term Q_S has a characteristic value of

$$\lambda \dot{\mathcal{E}}_{II} C(\mathcal{A}) \quad (\text{B.4})$$

C Comparison of sea ice models MESIM and VICE

Table C.1: Comparison of different features of the sea ice models MESIM and VICE, which were discussed to be used in HAMMER. Continued on the next page.

	MESIM	VICE
Thermodynamics		
Thermodynamic scheme	accurate but slow thermodynamic: approach of MAYKUT and UNTERSTEINER (1971)	fast but inexact thermodynamic: approach of SEMTNER (1976)
Number of layers in the ice	varying number of ice and snow layers	up to 3 (1 snow, 2 ice)
Surface temperature	energy budget with heat conduction and heat storage, or force-restore method	time-dependent diagnostically: Newtonian iteration method
Numerics		
Grid	Arakawa B	Arakawa C
Discretisation approach	Eulerian, finite difference	Eulerian, finite difference
Solution of momentum equation	SOR (2 colours), 2 iteration procedures per time step	SOR (like in HAMSOM), many iteration procedures per time step
Advection scheme	NICe-scheme of v. D. EMDE (1992)	componentwise upstream
Resolution	5 km	10 km
Time step	same as METRAS	same as HAMSOM
Computational speed	"2 days in 1 day" with METRAS time step	"3 months in 1 day" with HAMSOM time step

Table C.1 (cont.): Comparison of different features of the sea ice models MESIM and VICE, which were discussed to be used in HAMMER. Continued on the next page.

	MESIM	VICE
Included processes		
Atmospheric surface drag force	yes, calculation of u^*	yes, bulk approach with constant drag coefficient
Atmospheric form drag force	yes, integration of logarithmic wind profile over freeboard	no
Oceanic surface drag force	yes, bulk approach with constant drag coefficient	yes, bulk approach with constant drag coefficient
Oceanic form drag force	yes, integration of logarithmic current profile over draft height	no
Lead formation due to shear	yes	no
Rafting/piling-up	yes	yes
Ridging	no	no, but calculation of deformation energy
Drift of newly formed ice	drift calculated from wind speed	collection up to demarcation thickness as function of wind speed
Ice formation in leads	yes	yes

Table C.1 (cont.): Comparison of different features of the sea ice models MESIM and VICE, which were discussed to be used in HAMMER. Continued on the next page.

	MESIM	VICE
Included processes		
Melting at surface	yes, but without freshwater runoff	yes, including freshwater runoff
Flooding	yes, but without energy conservation	no
Evolution of salinity in the ice	prescribed C-profile for “relative depth”	no, constant in time and depth
Dependence of ice properties on temperature and salinity	yes for heat conductivity and heat capacity	no
Melting at bottom of ice floes	yes, but without freshwater runoff	yes
Salt/freshwater flux to the ocean	no	yes
Surface fresh water freezing	no	no
Penetration of short-wave radiation into the ice	yes	yes
Lateral ice floe melt	yes, parametrised from ocean temperature	yes, parametrised as portion of bottom melt

Table C.1 (cont.): Comparison of different features of the sea ice models MESIM and VICE, which were discussed to be used in HAMMER.

	MESIM	VICE
Parameterizations		
Rheology	Hibler: viscous-plastic	Hibler: viscous-plastic, modified Coulomb, flexible modified Coulomb and trimmed ellipse
Oceanic heat flux	bulk approach with u_w^* (from logarithmic ocean current profile) and $T_{wat} - T_{ice}$	bulk approach with $v_{ice} - v_w$
Sensible heat flux at ice top	calculation from u^* and θ^* (flux aggregation method)	bulk approach with constant transfer coefficient
Ice albedo	dependent on ice thickness, snow and clouds	dependent on ice surface temperature
Variables		
Number of ice classes	4	1
Prognostic variables	$h_c, A_c, \vec{v}, T_{ice,c}, T_{snow,c}, L_{f,c}$	$h, A, \vec{v}, T_{ice}, T_{snow}$
Temperature of oceanic surface layer	constant	from HAMSOM
Temperature profile in the ice	yes ($\Delta z = 10$ cm)	poorly resolved (2 layers)
Snow thickness	not built up, but considered if present	built up & considered
Assumptions	isotropic, continuous, 2D	isotropic, continuous, 2D

D Correction method for SMOS ice thickness data

Since SMOS tends to underestimate the ice thickness in regions with little ice concentration (KALESCHKE, 2013, personal communication), a correction is applied. The input data that are required by MESIM must represent the actual ice thickness, H , and not an ice volume per unit area, h . Following KALESCHKE (2013, personal communication), the ice thickness provided by SMOS can be interpreted like an ice volume per unit area, h , for ice concentrations $A > 50\%$ and for ice thinner than 5 cm. Due to the lack of better knowledge, this matter of fact is assumed to be valid for all ice thicknesses. Therefore, *for high ice concentration*, the SMOS ice thicknesses can be converted to the actual ice thickness, H , by Equation (2.1). Rearranging its terms yields

$$H = \frac{h}{A} \quad (\text{D.1})$$

In order to transform SMOS ice thicknesses, h_{SMOS} for *any* ice concentration, a transformation function, $g(A)$, is to be contrived that can be applied like

$$H_{corr} = h_{SMOS} \cdot g(A) \quad (\text{D.2})$$

to generate the corrected ice thickness, H_{corr} . For this, $g(A)$ has to fulfil the following requirements:

1. $g(A)$ is continuous. This is necessary to avoid discontinuities in the H_{corr} field.
2. $g(A)$ yields 1 for $A=1$.
3. $g(A)$ is close to $1/A$ for large A .
4. $g(A)$ approaches 1 for $A \rightarrow 0$ in order to leave h_{SMOS} unchanged for small A .

Empirical tests revealed that this behaviour is well represented by the function

$$g(A) = A^{-2.5 \cdot A} \quad (\text{D.3})$$

This function is similar to $1/A$ for $A > 40\%$ as can be seen in Figure D.1. Even though it is not perfect, it at least seems to improve the original data and, thus, is applied in HAMMER. The ice concentration data required for $g(A)$ is taken from AMSR2.

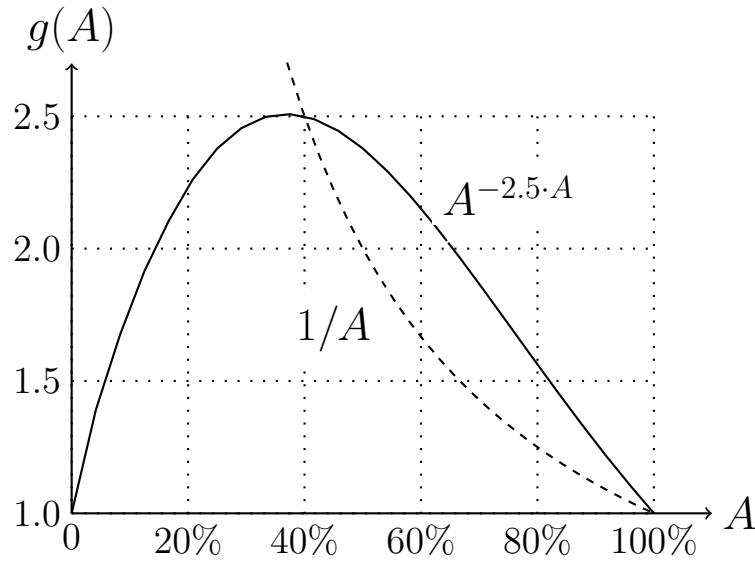


Figure D.1: Values of the transformation function $g(A)$ (solid line) in dependence of ice concentration A , as used to transform ice thickness data of SMOS, h_{SMOS} , into actual ice thickness, H_{corr} . The dotted line depicts $1/A$, to which $g(A)$ should be similar for large ice concentrations.

E Supplementary material to the hit rate analysis

In Section 4.2.2, the ice concentration simulated by HAMMER is evaluated utilising hit rates with respect to ice concentration values observed by the AMSR2 satellite. In order to not interrupt the text, two special aspects of the analysis are discussed here separately.

E.1 Assessment of the error tolerance using quantiles

When calculating hit rates, the error tolerance $\epsilon(S_i)$ is relevant for determining whether a certain deviation between model and satellite data is considered a hit. $\epsilon(S_i)$ depends on the current ice concentration because it is deduced from the uncertainty of the satellite. For cells with high ice concentration above 85% (SIC85_{SAT}-cells), the uncertainty and thus the tolerated deviation is less than 7 percentage points. For cells with an ice concentration below 5% (called SIC5_{SAT}-cells hereinafter) however, the uncertainty—and thus the tolerance—increases to 25 percentage points. This raises the hypothesis that solely the smaller tolerance for SIC85_{SAT}-cells causes their lower hit rate: Figure 4.14b shows a lower hit rate for SIC85_{SAT}-cells compared to SIC5_{SAT}-cells (Figure 4.14a). In this subsection, the hypothesis will be tested by assessing the quantiles of the ice concentration deviations.

If solely the error tolerance were responsible for the lower hit rate of SIC85_{SAT}-cells, then these cells should not show larger differences between forecasted and observed ice concentration values than other cells do. So, the approach is to calculate the absolute value of the difference between the forecasted and the observed value for each grid cell. For the difference-distribution over the whole grid area the 80%-quantile is calculated. It specifies which deviation between model and satellite has to be allowed so that 80% of all grid cells exhibit a smaller difference value. In other words, if the error tolerance for the hit rate is set to the 80%-quantile-value, the resulting hit rate is 80% because 80% of all cells meet the tolerance criterion.

The quantile analysis is done for cells with less than 5% ice concentration (SIC5_{SAT}-cells) and cells with more than 85% ice concentration (SIC85_{SAT}-cells) separately. The results are shown in Figure E.1 for calculations based on the fc06-runs; results for fc18-runs are similar. The 80%-quantile for SIC5_{SAT}-cells (Figure E.1a) is very low at the beginning of all simulations and increases to more than 25% at the simulation end. For SIC85_{SAT}-cells (Figure E.1b), the 80%-quantile is larger than 4% at the beginning and increases heavily only in the first part of the investigation period until 22/03.

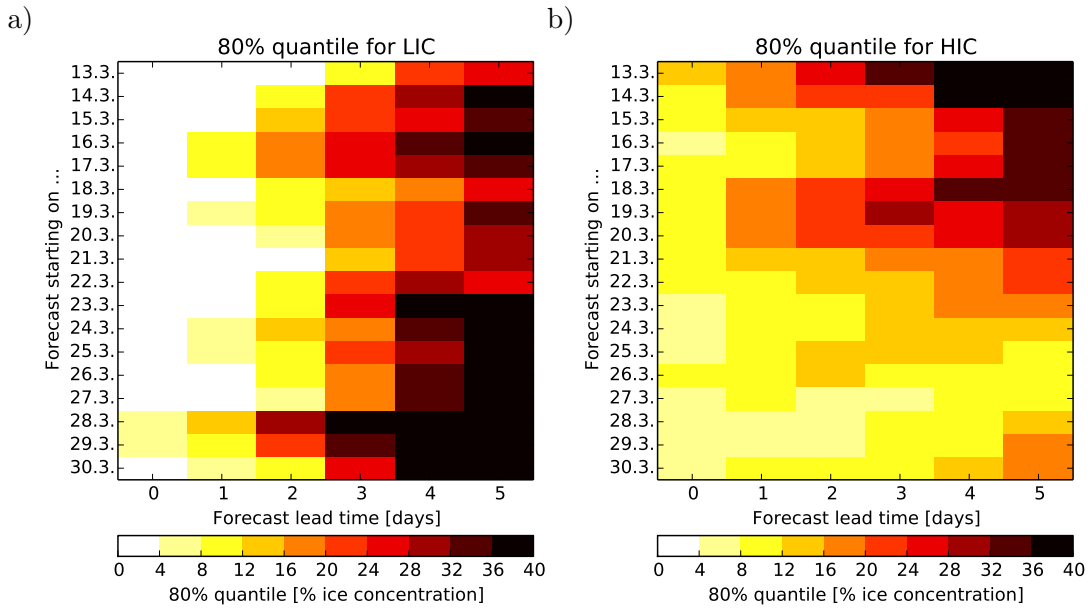


Figure E.1: 80%-quantiles of the absolute value of the differences between simulated and observed (AMSR2) ice concentration for all grid cells at which AMSR2 observed a) less than 5% (SIC5_{SAT}-cells) and b) more than 85% ice concentration (SIC85_{SAT}-cells), respectively. The results are shown for each forecast day of the fc06-runs.

In the period after 23/03, the 80%-quantile is lower for SIC85_{SAT}-cells than for SIC5_{SAT}-cells after the second forecast day. This means, for high ice concentration, the simulation results differ less from the observation. The hit rate of SIC85_{SAT}-cells, however, is lower than for

SIC5_{SAT}-cells. This supports the hypothesis: SIC85_{SAT}-cells have a low hit rate only because of the stricter error tolerance.

The situation is different, however, during the first two days of each simulation: Not only is the hit rate is lower for SIC85_{SAT}-cells (Figure 4.14), but also their 80%-quantile is higher. This indicates that the simulation indeed differs more from the observations for cells with high ice concentration. Thus, the hypothesis cannot be confirmed for the first period of each simulation.

The conclusion that the hypothesis cannot be confirmed in general, is also supported by the findings from a slightly different approach: The hit rate for SIC85_{SAT}-cells is recalculated using the less strict error tolerance of the SIC5_{SAT}-cells. The resulting hit rates are higher for SIC85_{SAT}-cells than for SIC5_{SAT}-cells after 23/03. At the beginning of the simulations, however, the hit rates are still lower. This affirms that the strict error tolerance is not the only reason why the hit rate of SIC85_{SAT}-cells is low.

E.2 Influence of clouds and water vapour on observed sea ice concentration

The sea ice concentration that was observed by AMSR2 in the Barents Sea shows a suspicious behaviour between 21/03 and 23/03 (Figure E.2): The grid cells in the red-framed regions belong to the group of SIC85_{SAT}-cells only on 22/03 but neither on 21/03 nor on 23/03. This means the ice concentration in this regions is observed to be less than 85% on 21/03, then it increases to more than 85% on 22/03, whereupon it drops again on 23/03. Certainly, such a behaviour is normal to occur for single cells, but it seems odd that the ice concentration varies that much in a coherent area.

In order to understand what is going on, the synoptic situation on these days has to be considered. On 22/03, a small low pressure system quickly moved across the southern Barents Sea from west to east. This low brings with it not only clouds but also an air mass containing more water vapour than the environment. The average conditions between 0 UTC and 12 UTC on 22/03 are shown in Figures E.3a,b as vertically integrated cloud water and water vapour, respectively. The data originate from the 00-UTC-run on 22/03 of the HRES-simulation by the IFS model run at ECMWF (ECMWF, 2014c). The downloaded 3-hourly time steps of 'total column water vapour' and 'total water column' (ECMWF, 2014a) are interpolated to the MESIM grid and averaged over 0-12 UTC. This time period was chosen because it covers most of the overflights of AMSR2 (swaths) from which the ice concentration map is generated. The total column *cloud water* is calculated as the difference between the *total water* column minus the total column *water vapour*. Thus⁹, the calculated total column cloud water also contains cloud ice.

⁹Definition of "total column water" from ECMWF(http://tigge.ecmwf.int/tigge/d/show_object/table=parameters/name=total_column_water/levtype=sfc/): Vertical integral from the ground to the nominal top of the atmosphere expressing the total amount of water (vapour + cloud water + cloud ice), but no precipitation included.

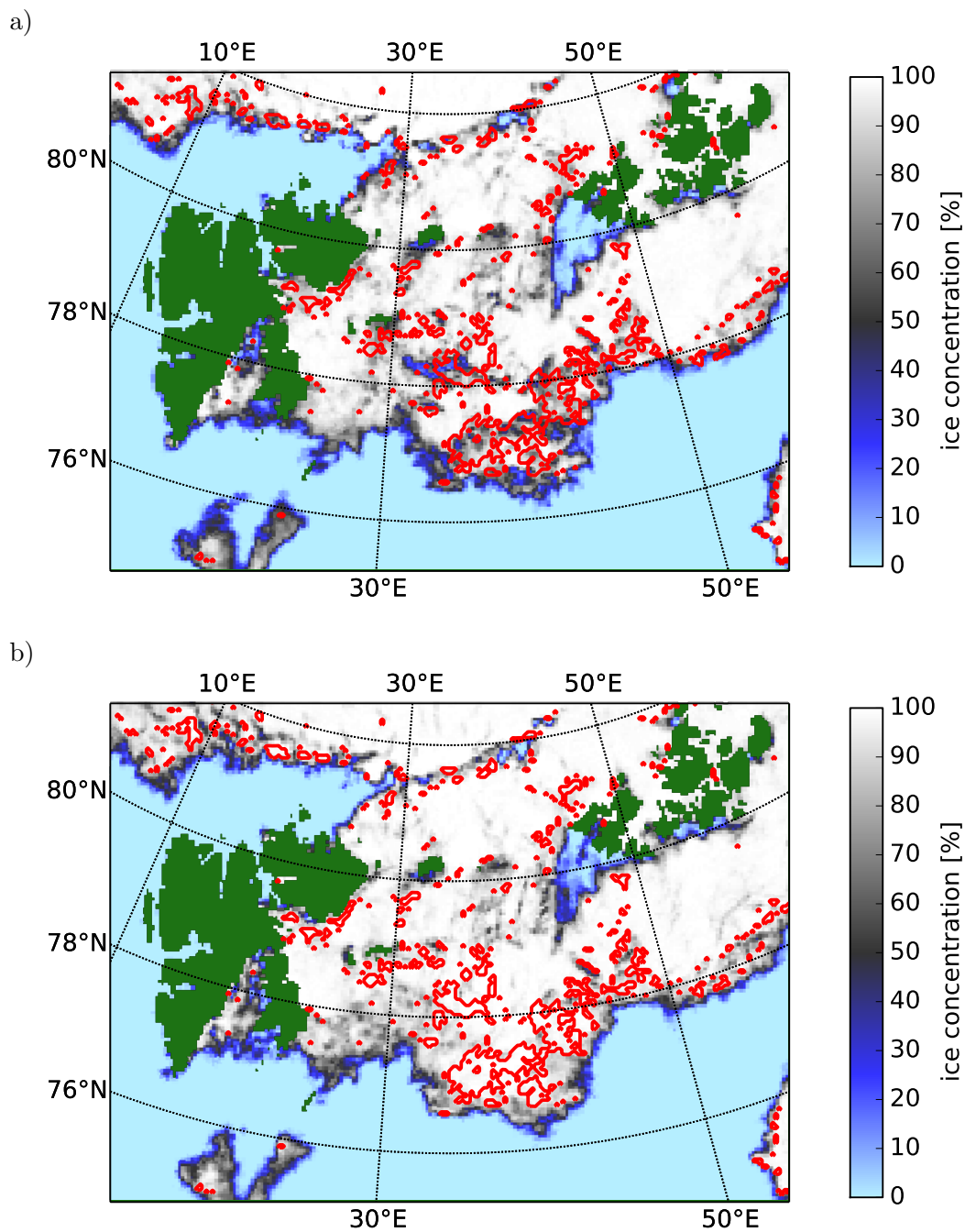


Figure E.2: Ice concentration observed by AMSR2 on a) 21 March 2014, b) on 22 March 2014, and c) on 23 March 2014. Red lines frame those regions in which the ice concentration is lower than 85% on 21/03, increases above 85% on 22/03, and decreases again below 85% on 23/03. Green areas depict land.

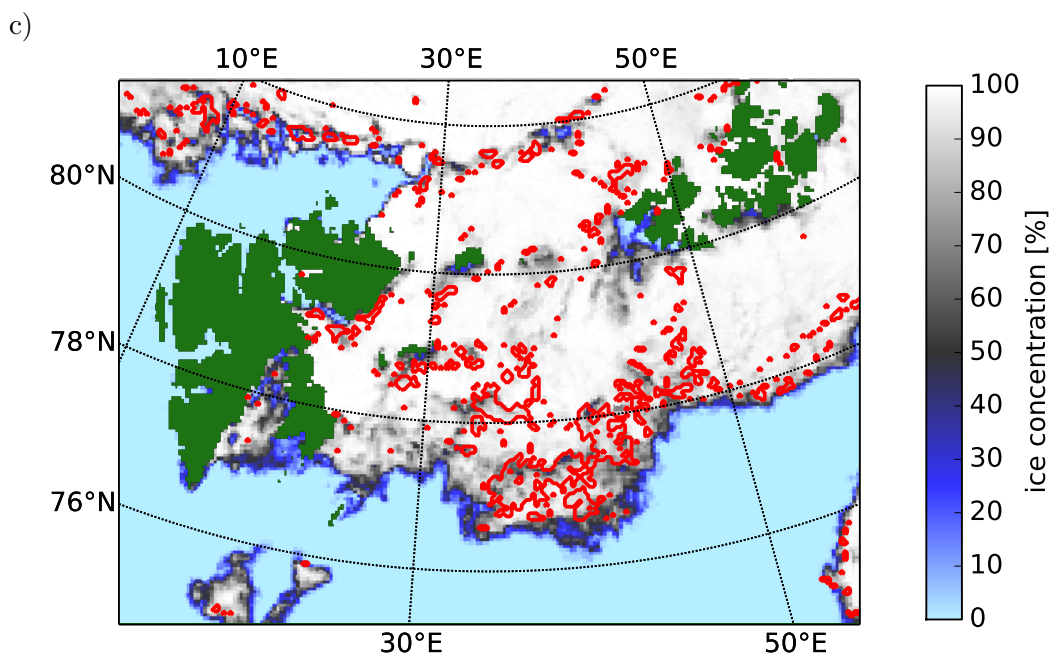


Figure E.2 (cont.): Ice concentration observed by AMSR2 on a) 21 March 2014 (previous page), b) on 22 March 2014 (previous page), and c) on 23 March 2014. Red lines frame those regions in which the ice concentration is lower than 85% on 21/03, increases above 85% on 22/03, and decreases again below 85% on 23/03. Green areas depict land.

Comparing the location of dense clouds and high water vapour (Figure E.3) to the ice concentration development (Figure E.2) suggests that clouds and high water vapour values occur in the same regions as the variations of ice concentration: Where there are clouds or water vapour above high-concentrated sea ice, the red frames indicate that the affiliation to the group of SIC85_{SAT}-cells changes from day to day. Clouds and water vapour, however, would hardly affect the ice concentration by physical means in such a short time. It is rather that they alter the signal which is received by the satellite: Clouds and water vapour interact with radiation at a frequency of 89 GHz and reduce its depolarisation. Unfortunately, the applied retrieval algorithm for AMSR2-data (SPREEN et al., 2008) uses the 89 GHz-channel to distinguish between sea ice and open water by the level of polarisation: Sea ice emits less polarised microwave radiation than the open sea surface does. Thus, radiation that is altered by clouds or water vapour during its path to the satellite pretends that there would be more sea ice than actually exists, so the ice concentration can be overestimated. A sensitivity study by BEITSCH (2014)

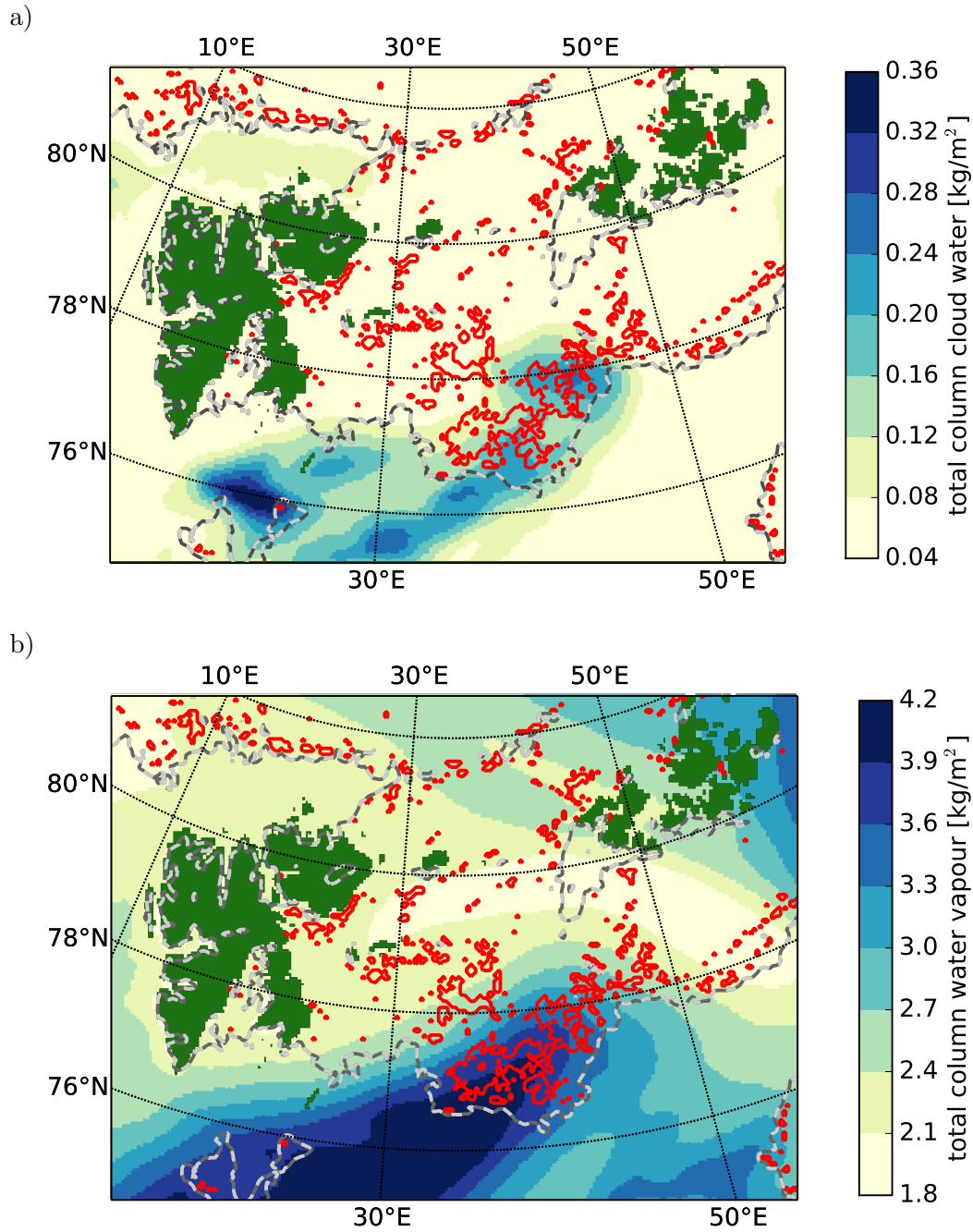


Figure E.3: a) Total column cloud water and b) total column water vapour from the ECMWF 00-UTC HRES-simulation on 22/03, average from 00 UTC until 12 UTC. Gray dashed lines mark the 50%-ice-concentration line from the AMSR2-observations on 22/03. Red lines frame those regions in which the ice concentration is lower than 85% on 21/03, increases above 85% on 22/03, and decreases again below 85% on 23/03. Green areas depict land.

revealed¹⁰ that the observed cloud intensity and water vapour amount could indeed induce the ascertained variations of ice concentration.

For small ice concentrations, the depolarisation effect of clouds and water vapour causes larger artefacts in the observations than for high ice concentration. Thus, the retrieval algorithm includes a weather filter which assures that no spurious ice is detected in open water areas. This filter is intended to apply only for ice with less than 15% ice concentration in order to retain the observed ice edge (SPREEN et al., 2008).

For higher ice concentrations—like studied here—, the influence of clouds and water vapour is included in the specified data uncertainty. As the hit rate calculation takes into account exactly this uncertainty as the error tolerance, no influence of clouds or water vapour is expected to be identifiable in the hit rates. For this, the observed cloud impact had to be smaller than the given uncertainty of less than 7 percentage points (SPREEN et al., 2008) for SIC85_{SAT}-cells. Investigating the ice concentration variations between 21/03 and 23/03 however reveals that more than half of the red-framed grid cells show changes of more than 7 percentage points¹¹.

The discrepancy suggests that the proposed uncertainty value is not extensive enough for the investigated situation. One reason is that the uncertainty value was rather intended as standard deviation by SPREEN et al. (2008). Hence, exceptional cases are to be expected. Another reason can be that this standard deviation was determined from two field experiments during which the optical thickness of the atmosphere was recorded (SVENDSEN et al., 1987). If these experiments did not cover the total range of possible atmospheric states—including the extremes—, the measured range of the optical thickness could be underestimated. This would lead to a too small uncertainty value.

In order to reduce the impact of clouds and water vapour on the hit rate analyses presented in Section 4.2.2, a more sophisticated approach, thus, would include...

1. to determine the actual total cloud and water vapour values at each grid cell,
2. to calculate the expected error from it by applying the sensitivities found by BEITSCH (2014)
3. to use the expected error as space- and time-dependent uncertainty by adding it to the error tolerance for the hit rate analysis.

¹⁰ If the so-called 'brightness temperature polarisation difference', which is a measure for the polarisation intensity, is reduced by 3 K, the ice concentration is overestimated by about 4 percentage points. Thereby, a total column cloud water of $0.1 \frac{\text{kg}}{\text{m}^2}$ can cause a change of 1.8–2.9 K in the brightness temperature polarisation difference, and a total column water vapour of $1.0 \frac{\text{kg}}{\text{m}^2}$ can cause a change of 0.9–2.3 K.

¹¹For each grid cell the smaller of both changes was chosen: either between 21/03 and 22/03 or between 22/03 and 23/03.

F Random generator for artificial ship routes

The route generator is a method to find random, artificial ship routes. Routes are built up step by step: Starting from a given starting grid cell, new adjacent grid cells are chosen and added to the already existing route part. The final routes should be as realistic as possible. This means that the route should mainly follow one direction while still allowing for direction changes. This is achieved by maintaining a list of the cardinal directions (north, east, south, west; relative to the model grid) in which the artificial ship has moved already at each step. This serves as a kind of memory so that the ship will mainly move in the same direction. Thus, the cardinal direction for each next step is chosen from the present members of this memory-list. An exception is introduced in order to still allow the ship to leave the old course and to pursue a new direction: The next cardinal direction can instead of from the list also be chosen randomly. The probability for choosing this additional cardinal direction is twice as high as for each member of the memory-list. Thus, the additional cardinal direction is more likely chosen at the beginning of the route, where the list is short, than at the end, where the list is long and, hence, the probability for each member is low. This produces relatively straight routes which, however, are not grid orientated. If the selected cardinal direction—either randomly or from the list—represents a grid cell that already belongs to the route, it is disregarded. Instead, a new cardinal direction is selected using the same procedure. In the rare case that the route blocks itself because it convolutes, the generation process is stopped and this route is applied although it is too short. Otherwise, further grid cells are added to the route until it reaches a length of 49 grid points.

More systematically, the route generator procedure is represented by following instructions:

1. Set up an empty list (memory-list).
2. Choose a random cardinal direction, \mathcal{D} .
3. Calculate the coordinates of the grid cell that is adjacent to the starting cell in direction \mathcal{D} and add it to the route.
4. Append \mathcal{D} to the memory-list.
5. Choose a cardinal direction, \mathcal{D} , from the memory-list, or—with twice the probability of each list member—take \mathcal{D} as random cardinal direction.
6. Calculate the coordinates of the grid cell that is adjacent to the previously chosen grid cell in direction \mathcal{D} .
7. If the new grid cell does *not* already belong to the route: Add it to the route and append \mathcal{D} to the memory-list.
8. Repeat steps 5–7 until the route has a length of 49 grid cells.

List of Symbols

\mathcal{A} [%]	characteristic value for ice concentration
A [%]	ice concentration
A_c [%]	ice concentration in ice class c
c	index specifying a variable specific to the ice class c
C^* [-]	ice strength parameter determining the dependency of ice strength on ice concentration
$C(A)$ [-]	empirical function for modelling dependencies on A
C_a [-]	drag coefficient between air and sea ice
$c_{sd,w}$ []	surface-drag coefficient between ice and ocean, $c_{sd,w}=4 \cdot 10^{-3}$
C_w [-]	drag coefficient between sea water and sea ice
e [-]	aspect ratio of the yield curve ellipse
\mathcal{E}_{II} [s^{-1}]	characteristic value for ice drift divergence (strain rate invariant)
$E(t)$	error development of target variable if forcing variables are set constant
$\hat{E}(t)$	development of the maximally allowed error for a target variable
E_{max}	maximally allowed error for a target variable at the end of a simulation
f [s^{-1}]	Coriolis parameter
$f(0)$ [$m s^{-1}$]	growth rate of new ice ($H=0$)
$f(H)$ [$m s^{-1}$]	growth or melt rate of existing ice with thickness H
\mathcal{F}_i	set of forcing variables ψ that belongs to the process P_i
g [$m s^{-2}$]	gravitational constant

\mathcal{H} [m]	characteristic value for ice thickness H
H [m]	mean ice thickness of all ice floes in a grid cell
h [m ³ m ⁻²]	ice volume per unit area; interpreted as the fictive ice thickness that would result if all ice in the grid cell was evenly redistributed over the whole grid area
h_0 [m]	demarcation ice thickness. It is used by H79 to differentiate between “thin ice” and “thick ice”. “Thin ice” includes open water and ice floes with an ice thickness H lower than h_0 . For consistency reasons with literature, the demarcation thickness is named h_0 although it specifies an ice thickness (H) rather than an ice volume per unit area (h).
h_c [m ³ m ⁻²]	ice volume per unit area in ice class c
$H_{d,c}$ [m]	height of ice floe draught in ice class c
$H_{f,c}$ [m]	height of ice floe freeboard in ice class c
K_{hor} [m ² s ⁻¹]	horizontal diffusion coefficient in METRAS
K_{ver} [m ² s ⁻¹]	vertical diffusion coefficient in METRAS
\vec{k} [-]	unit vector normal to the surface
\mathcal{L}_A [m]	characteristic length scale for changes of ice concentration
\mathcal{L}_H [m]	characteristic length scale for changes of ice thickness H
\mathcal{L}_i [m]	characteristic value for length of ice floes
L_i [m]	length of ice floe
$L_{i,c}$ [m]	length of ice floes in ice class c
\mathcal{L}_U [m]	characteristic length scale for changes of ice drift speed
$L_{w,c}$ [m]	distance between ice floes in ice class c
\mathcal{L}_σ [m]	characteristic length scale for changes of the internal stresses

List of Symbols

M [kg m ⁻²]	ice mass per unit area
m_1 [m s ⁻¹ K ^{-1.36}]	parameter for lateral melt rate: $m_1=2.85 \cdot 10^{-7} \text{ m s}^{-1} \text{ K}^{-1.36}$
m_2 [-]	parameter for lateral melt rate: $m_2=1.36$
M_r [m s ⁻¹]	lateral melt rate
P [N m ⁻¹]	ice strength
P^* [N m ⁻²]	ice strength parameter: compressive strength of compact ice of unit thickness
p_a [Pa]	atmospheric pressure at the water surface
P_i	characteristic strength of process P_i
P_i	process (collective term for all processes affecting χ)
Q_F [kg s ⁻¹ m ⁻²]	fresh water flux into the ocean at its surface
Q_H [W m ⁻²]	heat flux into the ocean at its surface
Q_L [% s ⁻¹]	reduction of ice concentration by lateral melt of ice floes
Q_{L_h} [% s ⁻¹]	parametrisation of H79 for reduction of ice concentration by lateral melt of ice floes
Q_{L_j} [% s ⁻¹]	parametrisation of J79 for reduction of ice concentration by lateral melt of ice floes
Q_N [% s ⁻¹]	increase of ice concentration by new ice formation
q_r [kg kg ⁻¹]	rain water content
Q_S [% s ⁻¹]	reduction of ice concentration by creation of open water during shear
S_A [% s ⁻¹]	source and sink terms of ice concentration
$S_{A,c}$ [% s ⁻¹]	source and sink terms of ice concentration in ice class c
S_h [m ³ m ⁻² s ⁻¹]	source and sink terms of h , the ice volume per unit area

List of Symbols

$S_{h,c}$ [$\text{m}^3 \text{m}^{-2} \text{s}^{-1}$]	source and sink terms of h_c , the ice volume per unit area in ice class c
S_o [ppt]	salinity profile in the ocean
t [s]	time
T_o [K]	temperature profile in the ocean
t_{sim}	duration of a model simulation, i.e. the forecast range
T_W [K]	temperature of the ocean surface layer
\mathcal{U} [m s^{-1}]	characteristic value for ice drift speed
u [m s^{-1}]	x-component of the ice drift velocity \vec{v}
u_1, u_2 [m s^{-1}]	components of the ice drift velocity \vec{v}
u_a [m s^{-1}]	x-component of the wind vector
\mathcal{U}_{ag} [m s^{-1}]	characteristic value for geostrophic wind speed
$u_{*,c}$ [m s^{-1}]	friction velocity over an ice surface of class c
$u_{*,w}$ [m s^{-1}]	friction velocity over a water surface
\mathcal{U}_{wg} [m s^{-1}]	characteristic value for geostrophic ocean current speed
v [m s^{-1}]	y-component of the ice drift velocity \vec{v} ; valid in Chapter 3
v [m s^{-1}]	ice drift speed (i.e. absolute value of \vec{v}); valid in Chapter 2
v_a [m s^{-1}]	y-component of the wind vector
$V_{existice}$ [$\text{m}^3 \text{m}^{-2} \text{s}^{-1}$]	change of h , the ice volume per unit area, by accretion or melting of existing ice
$V_{existice \leftrightarrow}$ [$\text{m}^3 \text{m}^{-2} \text{s}^{-1}$]	change of h , the ice volume per unit area, by melting ice laterally
$V_{existice \updownarrow}$ [$\text{m}^3 \text{m}^{-2} \text{s}^{-1}$]	change of h , the ice volume per unit area, by melting ice at its top or bottom
V_{newice} [$\text{m}^3 \text{m}^{-2} \text{s}^{-1}$]	change of h , the ice volume per unit area, by new ice formation

List of Symbols

\vec{v} [m s^{-1}]	ice drift velocity
\vec{v}_{ag} [m s^{-1}]	geostrophic wind velocity
$\vec{v}_{a,s}$ [m s^{-1}]	horizontal wind velocity close to the surface
\vec{v}_{wg} [m s^{-1}]	geostrophic ocean current velocity
$\vec{v}_{w,s}$ [m s^{-1}]	horizontal ocean current velocity close to the surface
W [$\text{kg m}^{-2} \text{s}^{-1}$]	abbreviation for $\rho_w C_w \vec{v}_{wg} - \vec{v} $
w []	weighting factor used in the SOR-algorithm
w_a [m s^{-1}]	z-component of the wind vector
$z_{0,oc}$ [m]	roughness length of ice with respect to water, $z_{0,oc}=0.1$ mm
$z_{0,w}$ [m]	roughness length of a water surface
β [m m^{-1}]	tilt of the sea surface
Δ [s^{-1}]	expression for total deformation $\sqrt{\epsilon_I^2 + (\epsilon_{II}/e)^2}$
Δt [s]	time step
Δt_{dry} [s]	length of time step determined from dynamic processes advection and diffusion
Δt_{liq} [s]	length of time step determined from cloud microphysical processes accretion and sedimentation
$\Delta \mathcal{T}_w$ [K]	characteristic value for elevation of water temperature above the freezing point
ΔT_w [K]	elevation of water temperature above the freezing point
Δx [m]	resolution of the grid in x-direction
Δy [m]	resolution of the grid in y-direction
Δz [m]	resolution of the grid in z-direction
δ [m]	fictive width of 1D ice floe

List of Symbols

δ_{ij} [-]	Kronecker delta
$\Delta\chi$	change of a target variable χ
ϵ_I [s^{-1}]	invariant <i>divergence</i> of the strain rate tensor ϵ_{ij}
ϵ_{II} [s^{-1}]	invariant <i>shear</i> of the strain rate tensor ϵ_{ij}
ϵ_{ij} [s^{-1}]	component of the strain rate tensor
ζ [N s m^{-1}]	bulk viscosity (Chapter 2)
ζ [m]	sea surface height (Chapter 3)
η [N s m^{-1}]	shear viscosity
θ_a [$^\circ$]	turning angle between sea ice drift and wind direction
θ_w [$^\circ$]	turning angle between sea ice drift and ocean current direction
κ []	von-Karman constant
λ [-]	constant, $\lambda = \frac{\sqrt{5}-2}{4}$
ρ [kg m^{-3}]	density of sea ice
ρh [kg m^{-2}]	ice mass per unit area
ρ_a [kg m^{-3}]	density of air
ρ_s [kg m^{-3}]	reference air density, $\rho_s = 1.29 \text{ kg m}^{-3}$
ρ_w [kg m^{-3}]	density of sea water
$\underline{\sigma}$ [N m^{-1}]	stress tensor of internal forces within the ice pack
σ_{ij} [N m^{-1}]	component of the stress tensor of internal forces within the ice pack; $i, j \in 1, 2$
$\tau_{a,f,c}$ [N m^{-2}]	form drag contribution of wind stress acting on ice of ice class c
$\tau_{a,s,c}$ [N m^{-2}]	surface drag contribution of wind stress acting on ice of ice class c

List of Symbols

$\vec{\tau}_a$ [N m^{-2}]	wind stress
$\vec{\tau}_{a,c}$ [N m^{-2}]	wind stress acting on ice of ice class c
$\vec{\tau}_w$ [N m^{-2}]	ocean stress
$\vec{\tau}_{w,c}$ [N m^{-2}]	ocean stress acting on ice of ice class c
χ	target variable (collective term for v , A , and H)
Ψ	characteristic value for a forcing variable ψ
ψ	forcing variable (collective term)
$\dot{\Psi}$	value for a characteristic temporal change of a forcing variable ψ
$\psi_{m,w}$ []	stability function of the atmospheric boundary layer over water surfaces for momentum
$\pi/\alpha L$ [-]	perimeter-to-area ratio for 2D ice floes (nomenclature of STEELE, 1992)
\mathfrak{I}_i	impact timescale of process P_i

List of Acronyms

ADV	Process: Advection of ice concentration or ice thickness, or acceleration of drifting ice by advection of momentum
AST	Process: Acceleration of drifting ice by atmospheric stress (wind)
COR	Process: Acceleration of drifting ice by the Coriolis force
DIV	Process: Change of ice concentration or of ice thickness by convergent/divergent drift
GRW	Process: (Vertical) melt or accretion of ice
H79	HIBLER (1979)
INT	Process: Acceleration of drifting ice by internal forces caused by the interaction of ice floes
J79	JOSBERGER (1979)
LAMh	Process: Parametrisation of HIBLER (1979) for the reduction of ice concentration by lateral melt of ice floes
LAMj	Process: Parametrisation of JOSBERGER (1979) for the reduction of ice concentration by lateral melt of ice floes
NEW	Process: Increase of ice concentration by new ice formation or associated change of the mean floe thickness, H .
OST	Process: Acceleration of drifting ice by ocean stress (current)
OWS	Process: Open water creation due to shear, altering ice concentration or ice thickness
TIL	Process: Acceleration of drifting ice by the downhill force caused by the tilted sea surface

References

- AARI, 2014: Review ice charts for the Arctic Ocean. Center <<Sever>>. Arctic and Antarctic Research Institute. St. Petersburg. Russia.. http://www.aari.ru/odata/_d0015.php, accessed on 14/11/2014.
- BACKHAUS, J. O., 1985: A Three-Dimensional Model for the Simulation of Shelf Sea Dynamics. – *Deutsche Hydrografische Zeitschrift* **38**(4), 165–187.
- BEITSCH, A., 2014: Uncertainties of a near 90 GHz sea ice concentration retrieval algorithm, Ph.D. thesis, Staats- und Universitätsbibliothek Hamburg, 123 pp.
- BEITSCH, A., L. KALESCHKE, S. KERN, 2014: Investigating High-Resolution AMSR2 Sea Ice Concentrations during the February 2013 Fracture Event in the Beaufort Sea. – *Remote Sensing* **6**(5), 3841–3856.
- BIRNBAUM, G., 1998: Numerische Modellierung der Wechselwirkung zwischen Atmosphäre und Meereis in der arktischen Eisrandzone= Numerical modelling of the interaction between atmosphere and sea ice in the Arctic marginal ice zone. – *Berichte zur Polarforschung (Reports on Polar Research)* **268**, 176 pp.
- BITZ, C. M., 2008: Numerical modeling of sea ice in the climate system. Lecture notes of the IPY Sea Ice Summer School in Svalbard, 22 pp. www.atmos.washington.edu/~bitz/Bitz_draftchapter.pdf, accessed on 2014/05/09.
- BJORNSSON, H., A. J. WILLMOTT, L. A. MYSAK, M. A. M. MAQUEDA, 2001: Polynyas in a high-resolution dynamic-thermodynamic sea ice model and their parameterization using flux models. – *Tellus A* **53**(2), 245–265.
- BOUILLON, S., M. MORALES MAQUEDA, V. LEGAT, T. FICHEFET, 2009: An elastic-viscous-plastic sea ice model formulated on Arakawa B and C grids. – *Ocean Modelling* **27**(3-4), 175–176.
- BRÜMMER, B., G. MÜLLER, H. HOEBER, 2003: A Fram Strait cyclone: Properties and impact on ice drift as measured by aircraft and buoys. – *J. Geophys. Res.* **108**(D7), 4217, ACL 6 1–13.
- BUDGELL, W., 2005: Numerical simulation of ice-ocean variability in the Barents Sea region. – *Ocean Dynamics* **55**(3), 370–387.
- CHMEL, A., V. N. SMIRNOV, I. B. SHEIKIN, 2010: Variability of scaling time series in the Arctic sea-ice drift dynamics. – *Ocean Sci.* **6**(1), 213.

- CONNOLLEY, W. M., J. M. GREGORY, E. HUNKE, A. J. MCLAREN, 2004: On the Consistent Scaling of Terms in the Sea-Ice Dynamics Equation. – *J. Phys. Oceanogr.* **34**(7), 1776–1780.
- DEARDORFF, J. W., 1978: Efficient prediction of ground surface temperature and moisture, with inclusion of a layer of vegetation. – *Journal of Geophysical Research* **83**(C4), 1889–1903.
- DIERER, S., K. H. SCHLÜNZEN, 2005: Influence parameters for a polar mesocyclone development. – *Meteorologische Zeitschrift* **14**(6), 781–792.
- DIERER, S., K. H. SCHLÜNZEN, G. BIRNBAUM, B. BRÜMMER, G. MÜLLER, 2005: Atmosphere–Sea Ice Interactions during a Cyclone Passage Investigated by Using Model Simulations and Measurements. – *Mon. Wea. Rev.* **133**(12), 3678–3680.
- DIERER, S. C., 2002: Untersuchung von groß- und mesoskaligen Einflüssen auf die Entwicklung polarer Mesozyklonen mit Hilfe des Modells METRAS. – *Berichte aus dem Zentrum für Meeres- und Klimaforschung, ZMK Universität Hamburg, Meteorologisches Institut* **35**, 13–47.
- DINESSEN, F., T. CARRIERES, L. TOUDAL, L. JANSSEN, F. AXELL, 2011: An inventory and description of ice forecasting models at ice centers, 41 pp. https://nsidc.org/noaa/iicwg/docs/IICWG_2011/An_Inventory_and_Description_of_Ice_Forecasting_Models_at_Ice_Centers.pdf, accessed on 2014/05/09.
- DOSWELL, C. A., R. DAVIES-JONES, D. L. KELLER, 1990: On Summary Measures of Skill in Rare Event Forecasting Based on Contingency Tables. – *Weather and Forecasting* **5**(4), 576–578.
- DURRAN, D., 2010: *Numerical Methods for Fluid Dynamics: With Applications to Geophysics* 32. – Springer New York, page 40.
- ECMWF, 2014a: Dataset I-i Atmospheric fields — high-resolution forecast. Webpage by the European Centre for Medium-Range Weather Forecasts (ECMWF): <http://www.ecmwf.int/en/forecasts/datasets/dataset-i-i-atmospheric-fields-high-resolution-forecast>, accessed on 31/07/2014.
- ECMWF, 2014b: ECFLOW USERS GUIDE, 96 pp. Published by the European Centre for Medium-Range Weather Forecasts (ECMWF) as https://software.ecmwf.int/wiki/download/attachments/13207146/user_manual_2014.pdf, accessed on 06/06/2014.
- ECMWF, 2014c: IFS DOCUMENTATION – Cy40r1. Operational implementation 22 November 2013. Published by the European Centre for Medium-Range Weather Forecasts (ECMWF) at <http://old.ecmwf.int/research/ifsdocs/CY40r1/index.html>, accessed on 06/06/2014.

- FISCHER, H., 1995: Vergleichende Untersuchungen eines optimierten dynamisch-thermodynamischen Meereismodells mit Beobachtungen im Weddellmeer. Comparison of an optimized dynamic-thermodynamic sea ice model with observations in the Weddell Sea. – *Berichte zur Polarforschung* **166**, 7–21.
- FLATO, G. M., 1995: Spatial and temporal variability of Arctic ice thickness. – *Annals of Glaciology* **21**, 323–329.
- FOCK, B. H., 2014: Hamburg system for mesoscale sea ice forecasting for ship routing. Technical report, CEN, University of Hamburg, version 2014-06-13, 24 pp.
- HAAPALA, J., N. LÖNNROTH, A. STÖSSEL, 2005: A numerical study of open water formation in sea ice. – *J. Geophys. Res.* **110**(C9), C09011, 1–17.
- HALLER, M., B. BRÜMMER, G. MÜLLER, 2013: Results from the DAMOCLES ice-buoy campaigns in the transpolar drift stream 2007–2009. – *The Cryosphere Discussions* **7**(4), 3749–3781.
- HALLER, M., B. BRÜMMER, G. MÜLLER, 2014: Atmosphere–ice forcing in the transpolar drift stream: results from the DAMOCLES ice-buoy campaigns 2007–2009. – *The Cryosphere* **8**(1), 275–288.
- HARDER, M., 1994: Erweiterung eines dynamisch-thermodynamischen Meereismodells zur Erfassung deformierten Eises. Master’s thesis, Berichte aus dem Fachbereich Physik 50, Alfred-Wegener-Institut für Polar- und Meeresforschung, Bremerhaven. Diplomarbeit, Universität Bremen, Fachbereich Physik/Elektrotechnik, 145 pp.
- HARDER, M., 1996: Dynamik, Rauigkeit und Alter des Meereises in der Arktis—numerische Untersuchungen mit einem großskaligen Modell. Dynamics, roughness, and age of Arctic sea ice—Numerical investigations with a large-scale model. – *Berichte zur Polarforschung* **203**, 19–25.
- HEBBINGHAUS, H., K. H. SCHLÜNZEN, S. DIERER, 2007: Sensitivity studies on vortex development over a polynya. – *Theoretical and Applied Climatology* **88**(1-2), 1–16.
- HEDSTRÖM, K. S., 2009: Technical Manual for a Coupled Sea-Ice/Ocean Circulation Model (Version 3). Arctic Region Supercomputing Center University of Alaska Fairbanks, U.S. Department of the Interior Minerals Management Service, Anchorage, Alaska. 169 pp. https://www.myroms.org/wiki/images/3/3b/Manual_2010.pdf, accessed on 19/05/2014.
- HIBLER, W. D., 1979: A dynamic thermodynamic sea ice model. – *Journal of Physical Oceanography* **9**, 815–846.

- HIBLER, W. D., 1984: The Role of Sea Ice Dynamics in Modeling CO₂ Increases. – In: J. HANSEN and T. TAKAHASHI (Eds.), *Climate Processes and Climate Sensitivity*, Geophysical Monograph 29 (Maurice Ewing Volume 5), American Geophysical Union, 238–253.
- HUNKE, E. C., J. K. DUKOWICZ, 1997: An Elastic–Viscous–Plastic Model for Sea Ice Dynamics. – *J. Phys. Oceanogr.* **27**(9), 1849–1867.
- HUNKE, E. C., W. H. LIPSCOMB, A. K. TURNER, 2010: Sea-ice models for climate study: retrospective and new directions. – *Journal of Glaciology* **56**(200), 1162–1172.
- HUNKE, E. C., W. H. LIPSCOMB, A. K. TURNER, N. JEFFERY, S. ELLIOTT, 2013: CICE: the Los Alamos Sea Ice Model, Documentation and Software User’s Manual, version 5.0. Tech. Rep. LA-CC-06-012. Technical report, Los Alamos National Laboratory, Los Alamos, New Mexico. 115 pp., <http://oceans11.lanl.gov/drupal/CICE>, accessed on 19/05/2014.
- IICWG, 2007: Ice Information Services: Socio-Economic Benefits and Earth Observation Requirements. http://nsidc.org/noaa/iicwg/docs/IICWG_2007/IICWG_SE_2007_Update_Final_.pdf, accessed on 20/06/2013. Published by The International Ice Charting Working Group in Sept. 2004, updated Sept. 2007.
- JOCHMANN, P., N. REIMER, L. KALESCHKE, G. MÜLLER, B. H. FOCK, F. KAUKER, J. ASSENG, J. HOLFORT, 2014: Ice Routing Optimization IRO-2. Validation Trial. – *HSVANewswave* **2014/1**, 2–5, (http://www.hsva.de/10_downloads_content/downloads_pics/newswave2014_1.pdf, accessed on 06/06/2014).
- JOSBERGER, E. G., 1979: Laminar and turbulent boundary layers adjacent to melting vertical ice walls in salt water. Ph.D. thesis, Dep. of Oceanogr., University of Washington.
- KALESCHKE, L., C. LÜPKES, T. VIHMA, J. HAARPAINTNER, A. BOCHERT, J. HARTMANN, G. HEYGSTER, 2001: SSM/I Sea Ice Remote Sensing for Mesoscale Ocean-Atmosphere Interaction Analysis. – *Canadian Journal of Remote Sensing* **27**(5), 526–537.
- KARCHER, M. J., R. GERDES, F. KAUKER, C. KÖBERLE, 2003: Arctic warming: Evolution and spreading of the 1990s warm event in the Nordic seas and the Arctic Ocean. – *J. Geophys. Res.* **108**(C2), 3034, 16 1–16.
- KAUKER, F., R. GERDES, M. KARCHER, C. KÖBERLE, J. LIESER, 2003: Variability of Arctic and North Atlantic sea ice: A combined analysis of model results and observations from 1978 to 2001. – *Journal of Geophysical Research Oceans* **108**(C6), 3182, 13 1–10.
- KHON, V., I. MOKHOV, M. LATIF, V. SEMENOV, W. PARK, 2010: Perspectives of Northern Sea Route and Northwest Passage in the twenty-first century. – *Climatic Change* **100**(3-4), 757–768.

- KLEINE, E., S. SKLYAR, 1995: Mathematical features of Hibler's model of large-scale sea-ice dynamics. – In: DINESSEN et al. (2011), 179–230 DOI: 10.1007/BF02736204.
- KOENTOPP, M., O. EISEN, C. KOTTMEIER, L. PADMAN, P. LEMKE, 2005: Influence of tides on sea ice in the Weddell Sea: Investigations with a high-resolution dynamic-thermodynamic sea ice model. – *J. Geophys. Res.* **110**, C02014, 1–12.
- KOTOVIRTA, V., R. JALONEN, L. AXELL, K. RISKKA, R. BERGLUND, 2009: A system for route optimization in ice-covered waters. – *Cold Regions Science and Technology* **55**(1), 52 – 62.
- KWOK, R., M. COON, 2006: Introduction to special section: Small-Scale Sea Ice Kinematics and Dynamics. – *J. Geophys. Res.* **111**, C11S21, 1–2.
- KWOK, R., J. MORISON, 2011: Dynamic topography of the ice-covered Arctic Ocean from ICESat. – *Geophysical Research Letters* **38**(2), 3–4.
- KWOK, R., G. SPREEN, S. PANG, 2013: Arctic sea ice circulation and drift speed: Decadal trends and ocean currents. – *J. Geophys. Res. Oceans* **118**(5), 2420–2423.
- LEPPÄRANTA, M., 2011a: *The Drift of Sea Ice*. Springer Praxis Books. Geophysical Sciences Series. – Springer, 266 pp.
- LEPPÄRANTA, M., 2011b: *The Drift of Sea Ice*, chapter 5, 109–139 Springer Praxis Books. Geophysical Sciences Series. Springer.
- LYARD, F., F. LEFEVRE, T. LETELLIER, O. FRANCIS, 2006: Modelling the global ocean tides: modern insights from FES2004. – *Ocean Dynamics* **56**(5-6), 394–415.
- LÜPKES, C., T. VIHMA, G. BIRNBAUM, U. WACKER, 2008: Influence of leads in sea ice on the temperature of the atmospheric boundary layer during polar night. – *Geophys. Res. Lett.* **35**, L03805, 1–5.
- MARSAN, D., H. STERN, R. LINDSAY, J. WEISS, 2004: Scale Dependence and Localization of the Deformation of Arctic Sea Ice. – *Phys. Rev. Lett.* **93**, 178501, 1–4.
- MASLANIK, J. A., C. FOWLER, J. STROEVE, S. DROBOT, J. ZWALLY, D. YI, W. EMERY, 2007: A younger, thinner Arctic ice cover: Increased potential for rapid, extensive sea-ice loss. – *Geophysical Research Letters* **34**, L24501, 1–5.
- MAYKUT, G., D. PEROVICH, 1987: The role of shortwave radiation in the summer decay of a sea ice cover. – *Journal of Geophysical Research* **92**(C7), 7032–7044.
- MAYKUT, G., N. UNTERSTEINER, 1971: Some results from a time-dependent thermodynamic model of sea ice. – *Journal of Geophysical Research* **76**(6), 1550–1575.

- MELLOR, G. L., S. HÄKKINEN, 1994: A Review of Coupled Ice-Ocean Models. – In: Geophys. Monogr. Ser., volume 85, AGU, Washington, DC, 21–31.
- MELLOR, G. L., L. KANTHA, 1989: An Ice–Ocean Coupled Model. – J. Geophys. Res. **94**(C8), 10937–10954.
- NOTZ, D., 2009: The future of ice sheets and sea ice: Between reversible retreat and unstoppable loss. – Proceedings of the National Academy of Sciences **106**(49), 20590–20595.
- NOTZ, D., 2014: Sea-ice extent and its trend provide limited metrics of model performance. – The Cryosphere **8**(1), 229–243.
- NSIDC, 2012: Arctic Sea Ice Age. NSIDC courtesy J. Maslanik and M. Tschudi, University of Colorado.. <http://nsidc.org/arcticseaicenews/files/2012/04/Figure5.png>, accessed on 14/11/2014.
- ÓLASON, E. O., 2012: Dynamical modelling of Kara Sea land-fast ice, Ph.D. thesis, Staats- und Universitätsbibliothek Hamburg, p. 19–24.
- ÓLASON, E. O., I. HARMS, 2010: Polynyas in a dynamic-thermodynamic sea-ice model. – The Cryosphere **4**(2), 147–160.
- OVERLAND, J., R. COLONY, 1994: Geostrophic drag coefficients for the central Arctic derived from Soviet drifting station data. – Tellus A **46A** 1(1), 75–85.
- PIELKE SR, R. A., 2002: Mesoscale meteorological modeling. International Geophysics Series, Volume 78. – Academic press, Department of Atmospheric Science, Colorado State University, Fort Collins, Colorado, p. 33–34.
- POHLMANN, T., 1996: Predicting the thermocline in a circulation model of the North sea – part I: model description, calibration and verification. – Continental Shelf Research **16**(2), 131–146.
- POHLMANN, T., 2006: A meso-scale model of the central and southern North Sea: Consequences of an improved resolution. – Continental Shelf Research **26**(19), 2367–2385.
- ROEBBER, P. J., 2009: Visualizing Multiple Measures of Forecast Quality. – Weather and Forecasting **24**(2), 601–603.
- RØED, L., J. DEBERNARD, 2004: Description of an integrated flux and sea-ice model suitable for coupling to an ocean and atmosphere model. – Met. no. report **4**, 48 pp., <http://met.no/filestore/MI-IM-Documentation.pdf>, accessed on 2014/11/10.

- SCHLÜNZEN, K. H., R. S. SOKHI (EDITORS), 2008: Overview of Tools and Methods for Meteorological and Air Pollution Mesoscale Model Evaluation and User Training. Joint Report of COST Action 728 and GURME. – GAW Report No. 181 WMO/TD - No. 1457, p. 22–23, 70–72.
- SCHLÜNZEN, K. H., 1990: Numerical studies on the inland penetration of sea breeze fronts at a coastline with tidally flooded mudflats. – *Contributions to atmospheric physics* **63**(3-4), 243–248.
- SCHLÜNZEN, K. H., D. D. FLAGG, B. H. FOCK, A. GIERISCH, C. LÜPKES, V. REINHARDT, C. SPENSBERGER, 2012: Scientific Documentation of the Multi-scale Model System M-SYS (METRAS, MITRAS, MECTM, MICTM, MESIM). – MEMI Technical Report 4, Meteorologisches Institut KlimaCampus, Universität Hamburg, 138 p., http://www.mi.uni-hamburg.de/fileadmin/files/forschung/techmet/nummod/metras/M-SYS_Scientific_Documentation_2012-02-09.pdf, accessed on 2014/05/09.
- SCHOETTER, R., 2013: Can local adaptation measures compensate for regional climate change in Hamburg Metropolitan Region? Ph.D. thesis, Staats- und Universitätsbibliothek Hamburg, p. 69–77.
- SCHRÖDER, D., 2005: Wirkung von Zyklonen auf das Meereis in der Framstraße : Modellrechnungen und Beobachtungen Ph.D. thesis, Staats- und Universitätsbibliothek Hamburg, 161 pp.
- SCHULSON, E. M., 2004: Compressive shear faults within arctic sea ice: Fracture on scales large and small. – *J. Geophys. Res.* **109**, C07016, 1–23.
- SEMTNER, A.J., J., 1976: A model for the thermodynamic growth of sea ice in numerical investigations of climate. – *J. Phys. Oceanogr* **6**(3), 379–389.
- SKAMAROCK, W. C., J. B. KLEMP, 1994: Efficiency and Accuracy of the Klemp-Wilhelmson Time-Splitting Technique. – *Mon. Wea. Rev.* **122**(11), 2623–2630.
- SPENSBERGER, C., K. H. SCHLÜNZEN, 2010: GRITOP - Preprozessor zur Initialisierung von Topographiedaten für das Modell METRAS. – Meteorologisches Institut, Universität Hamburg. METRAS Technical Report **8**, 31 pp.
- SPREEN, G., L. KALESCHKE, G. HEYGSTER, 2008: Sea ice remote sensing using AMSR-E 89-GHz channels. – *J. Geophys. Res.* **113**, C02S03, 1–14.
- STEELE, M., 1992: Sea ice melting and floe geometry in a simple ice-ocean model. – *J. Geophys. Res.* **97**(C11), 17729–17738.

- STEELE, M., J. ZHANG, W. ERMOLD, 2010: Mechanisms of summertime upper Arctic Ocean warming and the effect on sea ice melt. – *J. Geophys. Res.* **115**, C11004, 1–12.
- STEPHENSON, D. B., 2000: Use of the "Odds Ratio" for Diagnosing Forecast Skill. – *Weather and Forecasting* **15**(2), 221–223.
- STEWART, E. J., S. E. L. HOWELL, D. DRAPER, J. YACKEL, A. TIVY, 2007: Sea Ice in Canada's Arctic: Implications for Cruise Tourism. – *Arctic* **60**(4), 370–380.
- SVENDSEN, E., C. MATZLER, T. C. GRENFELL, 1987: A model for retrieving total sea ice concentration from a spaceborne dual-polarized passive microwave instrument operating near 90 GHz. – *International Journal of Remote Sensing* **8**(10), 1484.
- THORNDIKE, A. S., D. A. ROTHROCK, G. A. MAYKUT, R. COLONY, 1975: The Thickness Distribution of Sea Ice. – *J. Geophys. Res.* **80**(33), 4501–4513.
- TIAN-KUNZE, X., L. KALESCHKE, N. MAASS, M. MÄKYNEN, N. SERRA, M. DRUSCH, T. KRUMPEN, 2014: SMOS-derived thin sea ice thickness: algorithm baseline, product specifications and initial verification. – *The Cryosphere* **8**(3), 997–1018.
- TIETSCHKE, S., D. NOTZ, J. H. JUNGCLAUS, J. MAROTZKE, 2013: Assimilation of sea-ice concentration in a global climate model – physical and statistical aspects. – *Ocean Sci.* **9**(1), 19–36.
- V. D. EMDE, K., 1992: Solving Conservation Laws with Parabolic and Cubic Splines. – *Mon. Wea. Rev.* **120**(3), 482–492.
- VAN WOERT, M. L., C.-Z. ZOU, W. N. MEIER, P. D. HOVEY, R. H. PRELLER, P. G. POSEY, 2004: Forecast Verification of the Polar Ice Prediction System (PIPS) Sea Ice Concentration Fields*. – *J. Atmos. Oceanic Technol.* **21**(6), 944–957.
- VANCOPPENOLLE, M., T. FICHEFET, H. GOOSSE, S. BOUILLON, G. MADEC, M. A. M. MAQUEDA, 2009: Simulating the mass balance and salinity of Arctic and Antarctic sea ice. 1. Model description and validation. – *Ocean Modelling* **27**(1–2), 33–53.
- VINJE, T., Å. S. KVAMBEKK, 1991: Barents Sea drift ice characteristics. – *Polar Research* **10**(1), 59–68, Norsk Polarinstitutt Contribution No. 275.
- VON SALZEN, K., M. CLAUSSEN, K. SCHLÜNZEN, 1996: Application of the concept of blending height to the calculation of surface fluxes in a mesoscale model. – *Meteorologische Zeitschrift*, N.F. **5**, 60–66.
- WILHELMSSON, T., 2002: Parallelization of the HIROMB Ocean Model. Licentiate Thesis, Royal Institute of Technology, Department of Numerical Analysis and Computer Science,

References

Stockholm, 120 pp. http://msi.ttu.ee/~elken/HIROMB_Parallelization.pdf, accessed on 2014/05/09.

WMO, 1970: WMO SEA-ICE NOMENCLATURE, TERMINOLOGY, WMO/OMM/BMO - No.259 &bull Edition 1970-2004, Ice terms arranged in alphabetical order. <http://www.aari.ru/gdsidb/XML/volume1.php?lang1=0&lang2=1&arrange=1>, accessed on 03/11/2013 Published by World Meteorological Organization, 1970 (http://library.wmo.int/opac/index.php?lvl=notice_display&id=6772).

Erklärung

Hiermit erkläre ich, Andrea Gierisch, an Eides statt, dass ich die vorliegende Dissertationsschrift selbst verfasst und keine anderen als die angegebenen Quellen und Hilfsmittel benutzt habe.

Einer Veröffentlichung dieser Arbeit stimme ich zu.

Hamburg, den 18. November 2014